AD-A042 554 UNITED TECHNOLOGIES RESEARCH CENTER EAST HARTFORD CONN F/G 20/4
INVESTIGATION OF THE AIRFLOW OF A HOVERING MODEL HELICOPTER AT --ETC(U)
JUL 77 A J LANDGREBE, J C BENNETT DAA21-76C-0151
UNCLASSIFIED UTRC-R77-912573-15 NL

1 OF 2
ADA042554

1 OF 2

DA042554

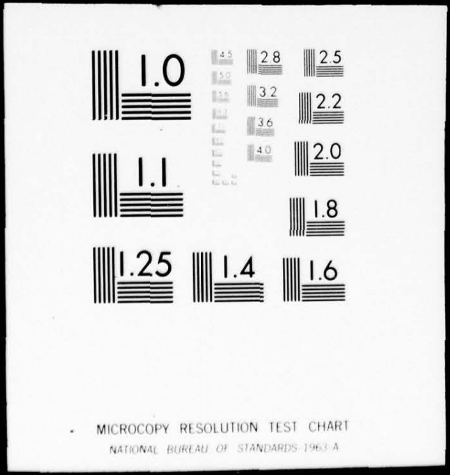

MICROCOPY RESOLUTION TEST CHART
NATIONAL BUREAU OF STANDARDS-1963-A

UTRC Report No. R77–912573–15

(12)

INVESTIGATION OF THE AIRFLOW OF A HOVERING MODEL HELICOPTER AT ROCKET TRAJECTORY AND WIND SENSOR LOCATIONS

Application of model helicopter testing, laser velocimetry, flow visualization, and rotor wake theory to investigate the aerodynamic interference of a hovering helicopter at rocket trajectories and wind sensors.

Anton J. Landgrebe and John C. Bennett, Jr.

United Technologies Research Center
East Hartford, Conn. 06108

July 1977

Final Report for Period March 1976–June 1977

APPROVED FOR PUBLIC RELEASE; DISTRIBUTION UNLIMITED

Prepared for
DEPARTMENT OF THE ARMY
U.S. Army Armament R&D Command
Dover, N.J. 07801

UNCLASSIFIED
SECURITY CLASSIFICATION OF THIS PAGE (When Data Entered)

REPORT DOCUMENTATION PAGE		READ INSTRUCTIONS BEFORE COMPLETING FORM
1. REPORT NUMBER R912573-15	2. GOVT ACCESSION NO.	3. RECIPIENT'S CATALOG NUMBER (9)
4. TITLE (and Subtitle) (6) Investigation of the Airflow of a Hovering Model Helicopter at Rocket Trajectory and Wind Sensor Locations. (Subtitle on reverse side)		5. ~~TYPE OF REPORT~~ & PERIOD COVERED Final Report. March 1976 — June 1977,
		6. ~~PERFORMING ORG. REPORT NUMBER~~ (14) UTRC-R77-912573-15
7. AUTHOR(s) (10) Anton J. Landgrebe John C. Bennett, Jr.		8. ~~CONTRACT OR~~ GRANT NUMBER(s) (15) DAAA21-76-C-0151 new
9. PERFORMING ORGANIZATION NAME AND ADDRESS United Technologies Research Center East Hartford, Connecticut 06108		10. PROGRAM ELEMENT, PROJECT, TASK AREA & WORK UNIT NUMBERS
11. CONTROLLING OFFICE NAME AND ADDRESS Department of the Army U. S. Army Armament R&D Command Dover, New Jersey 07801		12. ~~REPORT DATE~~ (11) July 1977
		13. NUMBER OF PAGES 166 (12) 168p.
14. MONITORING AGENCY NAME & ADDRESS (if different from Controlling Office)		15. SECURITY CLASS. (of this report) Unclassified
		15a. DECLASSIFICATION DOWNGRADING SCHEDULE

16. DISTRIBUTION STATEMENT (of this Report)

Approved for public release; distribution unlimited.

17. DISTRIBUTION STATEMENT (of the abstract entered in Block 20, if different from Report)

18. SUPPLEMENTARY NOTES

The investigation reported herein is being extended to include low speed forward flight under Dept. Army Contract DAAG29-77-C-0013.

19. KEY WORDS (Continue on reverse side if necessary and identify by block number)

Helicopter Hover Performance
Helicopter Rotor Airflow
Model Helicopter Testing
Laser Velocimetry
Wind Sensor
2.75 In. Rockets
Flow Visualization
Rotor Wake Theory
Induced Velocities
Aerodynamic Interference
AH-1G Helicopter

20. ABSTRACT (Continue on reverse side if necessary and identify by block number)

An investigation was conducted to determine the airflow characteristics in the vicinity of a model helicopter to determine representative flow velocities at the rocket trajectory and wind sensor locations of a hovering Army AH-1G "Cobra" helicopter. Laser velocimetry and flow visualization techniques were applied to provide flow velocity and wake geometry data for correlation with thecry and for a systematic determination of the total and separate influence of each of the aircraft components (rotor, fuselage, and → next page

DD FORM 1 JAN 73 1473 EDITION OF 1 NOV 65 IS OBSOLETE

409252

UNCLASSIFIED
SECURITY CLASSIFICATION OF THIS PAGE (When Data Entered)

20. ABSTRACT (Cont'd)

wing), and significant operating condition parameters (rotor thrust, tip speed, and ground effect) on the airflow influencing rocket trajectories. In addition, the flow velocities at potential locations for a fire control system wind sensor, mounted on the aircraft, were determined to assist in identifying wind sensor locations for accurately measuring flow velocities at hover.

4. TITLE (Cont'd)

Subtitle: Application of model helicopter testing, laser velocimetry, flow visualization, and rotor wake theory to investigate the aerodynamic interference of a hovering helicopter at rocket trajectories and wind sensors.

SUMMARY

As investigation was conducted to determine the airflow characteristics in the vicinity of a model helicopter to determine representative flow velocities at the rocket trajectory and wind sensor locations of a hovering Army AH-1G "Cobra" helicopter. Laser velocimetry and flow visualization techniques were applied to provide flow velocity and wake geometry data for correlation with theory and for a systematic determination of the total and separate influence of each of the aircraft components (rotor, fuselage, and wing), and significant operating condition parameters (rotor thrust, tip speed, and ground effect) on the airflow influencing rocket trajectories. In addition, the flow velocities at potential locations for a fire control system wind sensor, mounted on the aircraft, were determined to assist in identifying wind sensor locations for accurately measuring flow velocities at hover.

Time-averaged and peak-to-peak values of flow velocity components, measured with a laser velocimeter (LV), are presented and compared for the model test configurations and conditions. Also, the cyclic time-variant flow velocities, related to blade azimuth position, are presented for points on a rocket trajectory for the reference model AH-1G configuration and condition. The measured model flow velocities are scaled to representative full-scale values, and the applicability of scaling procedures to rotor thrust and tip speed variations is demonstrated. Rotor wake theory was applied to selected model and full-scale configurations and conditions. The predicted flow velocities are compared with LV test data and used in combination with wake geometry data for interpretation of the airflow results. The location of the rotor wake (particularly the tip vortices at the wake boundary) relative to the rocket trajectories and wind sensors is shown to be a major determinant of their flow velocities. The presence of either the fuselage, modified canopy, or ground is shown to produce significant flow velocity increments; however, the influence on the rocket flight trajectory and resulting aim bias requirements remain to be determined from a separate aeroballistics investigation.

PREFACE

This investigation was sponsored by the U.S. Army Armament R&D Command, Dover, New Jersey under Contract DAAA21-76-C-0151. Efforts under this contract were initiated in March 1976 and completed in July 1977. An extension of this investigation to include low speed forward flight conditions was initiated in April 1977 under Contract DAAG29-77-C-0013 from the U.S. Army Research Office.

The Contract Project Officer was Mr. Saul Wasserman of the U.S. Army Armament R&D Command. The interest and project support provided by Mr. Wasserman and Mr. Robert W. Bergman of the U.S. Army Missile Command is gratefully acknowledged. Also acknowledged is the support provided in various phases of the investigation by Mr. P. A. M. Spierings, Mrs. Dawn Anderson, and personnel of the Test Facilities Section of UTRC. Particular acknowledgement is given to the technical assistance provided by Mr. T. Alan Egolf of the Rotary Wing Technology Group, UTRC, in the theoretical phase of the contract.

The program manager for the contract was Mr. Anton J. Landgrebe, Supervisor, Rotary Wing Technology Group, UTRC. Dr. John C. Bennett, Jr., Senior Research Engineer, Aeroacoustics Group, UTRC, was responsible for the acquisition and data processing of the laser velocimeter data.

TABLE OF CONTENTS

Page No.

TABLE OF CONTENTS (Cont'd)

LIST OF FIGURES

LIST OF TABLES

INTRODUCTION

The accurate determination of the flow field in the vicinity of a helicopter is required when a helicopter is used as a weapons platform. Since a free-flight projectile such as a rocket, when fired from a helicopter, initially travels at a speed which is the same order of magnitude as the flow velocities, the flow field induced by the rotor wake system can have a significant effect on the rocket trajectory. This can necessitate some form of aiming compensation or special firing techniques--particularly at the low helicopter flight speeds at which rockets are to be fired in accordance with current Army nap-of-the-earth, tactical concepts. The shortage of information on helicopter airflow and its influence on free flight rockets for the purpose of achieving an effective fire control is a major concern of the Army, as stated in Ref. 1. Current Army doctrine calls for employment of helicopters such as the AH-1 and the AAH in hover, pop-up, and terrain flying modes. The requirement for investigation of rocket aerodynamic interference for helicopters operating in such modes and recommendations for such investigation are well documented in the Army Missile Command memo (Ref. 1), included herein as Appendix A. The requirement is also discussed in the Proceedings of the Conference on the Effects of Helicopter Downwash on Free Projectiles (Ref. 2), particularly in the presentations of Army representatives Marner (Ref. 3), Morse (Ref. 4), and Bergman (Ref. 5).

To assess the influence of the rotor/wake flow field on the flight path of a 2.75 inch rocket fired from the Army AH-1G (Cobra) helicopter when hovering or flying at low forward speeds, an analytical investigation was performed at the United Technologies Research Center, UTRC (formerly the United Aircraft Research Laboratories), to predict the induced flow velocities at the rocket trajectories. UTRC computer analyses which have the capability to calculate tip vortex geometry and rotor wake induced velocities were used to calculate the time-averaged and time-varying (instantaneous) induced flow velocities along the rocket trajectories for helicopter flight speeds of 0, 15, and 30 kts. The results of this investigation were reported in 1975 in the following reference (Ref. 6):

> Prediction of Rotor Wake Induced Flow Velocities Along the Rocket Trajectories of an Army AH-1G Helicopter, by A. J. Landgrebe and T. A. Egolf, United Technologies Research Center, U.S. Army Picatinny Arsenal Technical Report 4797, March 1975.

The results were presented on August 12, 1975 at the Conference on the Effects of Helicopter Downwash on Free Projectiles, organized by the U.S. Army Aviation Systems Command, and summarized in a paper entitled "Rotor Wake Induced Flow Along Helicopter Rocket Trajectories" (Ref. 7). Since this investigation was the immediate forerunner of the investigation reported herein, the summary, conclusions, and recommendations from Ref. 7, which are the same as those of Ref. 6, are included as Appendix B. The induced velocity results from this investigation have been used by Wasserman in a trajectory analysis at the Army Picatinny Arsenal to predict the influence of the aerodynamic interference of the rotor wake on rocket trajectories (Ref. 8). It was concluded that this influence is significant and must be compensated for when establishing aiming techniques. This conclusion has been substantiated in Army flight tests such as those reported for the UH-1 and the AH-1 in Refs. 9 and 10.

Although the analytical investigation provided a significant amount of information regarding induced velocities along the AH-1G rocket trajectories, it was limited in scope to three flight conditions, and the interference effects of the fuselage, wing and ground on the predicted velocities were not included. It was concluded that model helicopter testing should be conducted to provide systematic experimental data for correlation, investigation of other operating conditions and neglected interference effects, and determination of wind sensor locations. It was thus suggested that the model hovering and wind tunnel facilities, and experimental flow measurement and visualization techniques, available at UTRC, be used to measure the flow velocities and wake boundaries in the regions of the rocket trajectories and potential wind sensor locations and to compare them with theoretical predictions. Model rotor flow measurement using a laser velocimeter had recently been demonstrated at UTRC as reported in Ref. 11. Techniques used at UTRC for model helicopter testing, flow visualization, and theoretical rotor airflow predictions had previously been developed as reported in Refs. 12 through 23. A contract (DAAA21-76-C-0151) was awarded by the Army Picatinny Arsenal (now the U.S. Army Armament R&D Command) on March 1, 1976 to use the UTRC model rotor hover test facility to conduct such an investigation for the hover mode of operation. The results of this contract investigation are reported herein. An additional contract (DAAG29-77-C-0013) was awarded to UTRC by the U.S. Army Research Office (with the cooperation of the Army Armament R&D Command, the Army Air Mobility Research and Development Laboratory, and the Army Missile Command) on May 25, 1977 to expand the experimental investigation to the low speed forward flight mode of operation. The test program for this investigation is being conducted using UTRC wind tunnel facilities.

The objective of the investigation reported herein was to determine, through an experimental program, the airflow characteristics in the vicinity of a model representative of the AH-1G "Cobra" helicopter at zero forward air velocity (hover). Model helicopter hover test facilities and experimental flow measurement and visualization techniques were used to measure the flow velocities and rotor wake characteristics in the regions of rocket trajectories and potential wind sensor locations. Schematics of the AH-1G showing rocket trajectories, tested wind sensor locations, and reference axis systems used in the investigation are presented in Figs. 4 and 5. Model rotor-fuselage-wing testing, application of laser velocimeter techniques to measure flow velocities, and application of flow visualization techniques to determine wake geometry were included in the test program. It was the objective of the experimental program to provide flow velocity and wake geometry data for correlation of theory and for the systematic determination of the total and separate influence of each of the aircraft components (rotor, fuselage, and wing), and significant operating condition parameters (aircraft weight, tip speed, and ground effect) on the airflow influencing rocket trajectories. In addition, the measurement of flow velocities at and in the vicinity of potential locations for a fire control system wind sensor, mounted on the aircraft, was included in the requirements of the experimental program to assist in evaluating wind sensor locations for accurately measuring flow velocities at hover. The experimental data is also intended for use in determining the aim bias necessary for rocket firings at hover. In addition to providing rocket trajectory and wind sensor information, analysis of the test data was directed toward providing information on the fundamentals of hovering helicopter airflow and wake characteristics.

DESCRIPTION OF TEST

MODEL HELICOPTER HOVER TEST FACILITY

The test program was conducted at the UTRC Model Helicopter Hover Test Facility. Photographs and associated schematics of the facility and equipment, as used in this test program, are presented in Figs. 6 through 13. As shown in Fig. 6, the test facility consists of a model helicopter test rig, flow velocity measurement equipment (laser velocimeter), flow visualization equipment, and a movable ground plane, all located in a large enclosed area. The test control area, located below and forward of the test area, is shown in Fig. 7. The model rotor test rig is mounted to an overhead supporting structure (Fig. 6) such that rotor thrust and torque can be measured with a strain-gauged load cell and calibrated bending beam. Smoke flow visualization equipment includes a variable-position smoke rake (Fig. 8), high intensity light sources, and cameras and electronic time-delay controls for synchronizing the camera and lighting system to the rotor rotation. Schlieren equipment (Fig. 6), consisting of a light source, optical system, and cameras, is also available for recording rotor tip vortex patterns on film. A laser velocimeter system was installed at the hover test facility for this test program. The laser velocimeter, shown in Figs. 9 and 10, had the capability for measuring the component of flow velocity in the plane normal to the axis of the emitted laser beams. Two components could be measured, one-at-a-time, by rotation of the optics. Measurement of the third component (relative to the model) was achieved by rotation of the model.

SELECTION OF MODEL HELICOPTER COMPONENTS

In order to minimize cost and time requirements, available model components were selected to represent the Army AH-1G helicopter. An existing 1/8th scale AH-1G fuselage model was loaned by the Government from the Bell Helicopter Company for the test program. UTRC provided two model rotor blades and an existing hub system to represent the AH-1G rotor. The rotor radius was 28.5 in. A photograph of the model used to simulate the AH-1G helicopter is presented in Fig. 8.

The primary model rotor design values are compared with those of the full-scale AH-1G rotor in Table 1.

TABLE 1. MODEL AND FULL-SCALE ROTOR DESIGN VALUES

	Full-Scale AH-1G	Available Model
Rotor Radius, R	22 ft	28.5 in.
Blade Chord, c	27 in.	2.94 in.
Aspect Ratio	9.78	9.69
Number of Blades	2	2
Rotor Solidity Ratio, σ	0.0651	0.0657
Taper Ratio	1.0	1.0
Linear Twist	-10 deg	-8 deg
Airfoil Section	modified NACA 0009	NACA 0012
Hub	Teetering	Articulated (flapping)

Although the model rotor values do not exactly duplicate the full-scale values, they are regarded to be sufficiently close so as not to significantly compromise the accomplishment of the objectives of the experimental program.

The rotor parameters of most significance to this test (number of blades, solidity ratio, aspect ratio, and taper ratio) were identically or very closely scaled. The effects of the relatively small differences in twist and airfoil section, indicated in Table 1, on the rotor wake and flow velocities were minimized through test operation at full-scale thrust coefficient. The use of an available hub with flapping articulation rather than a teetering hub is, in itself, of no consequence for a hover test provided that the full-scale rotor hovers at the built-in precone angle and the articulated blade mass factor (Lock number) is such to produce the same coning angle. The model rotor coning angle (approximately 0.3 deg), achieved through articulation, was less than the full-scale AH-1G precone angle (2.75 deg) due to the lower Lock number of the proportionately heavier, available model blades. The coning angle difference is generally insignificant for the magnitude of flow velocities at flow field points near rocket trajectories and wind sensors. It will be shown that it has an effect on the time phasing of the flow velocities at specific field points.

Theoretical substantiation of the generally small anticipated effects of scaling differences on the flow velocites, as mentioned above, was achieved through application of the rotor hover analysis used for the results presented in Ref. 12. It will be shown that, where model rotor scaling differences are significant, theoretical and experimental results can be used in combination to account for the differences and improve the prediction of the full-scale rotor flow field. Comparison of predicted model and full-scale flow velocities and experimental model flow velocities are presented in a later section of this report.

The available AH-1G fuselage model was 1/8th full-scale size. The ratio of the model rotor diameter to the full-scale rotor diameter was 1/9.26. Although the resulting rotor-fuselage scaling was somewhat inconsistent (the fuselage was 14 percent too large), the anticipated effect of this inconsistency, on the data to be measured, was anticipated to be small when the following were considered:

1. The contribution of the fuselage interference to the velocities at rocket trajectory points is small compared to the influence of the rotor.

2. The narrow width of the AH-1G (only 7 percent of the rotor diameter) results in a scaling inaccuracy of the model fuselage width of less than 2 percent of the model rotor diameter.

3. The model fuselage was positioned under the model rotor such that the primary distances for rotor/fuselage flow interference at rocket trajectories and wind sensor locations were scaled to be consistent with full-scale AH-1G values. Considering the importance of the rotor as the flow velocity producing device, the primary distances selected were measured relative to the rotor hub center and scaled to the rotor radius.

Regarding the above, several scaling selections should be mentioned. First, the fuselage was positioned relative to the rotor hub such that the vertical distance between the canopy roof (at the pylon junction) and the rotor was appropriately scaled to the full-scale value (0.18 R). This was important for both canopy interference on the flow at rocket trajectory locations beneath the canopy and for selected wind sensor locations aside of the top of the canopy. The hub was moved forward over the fuselage to better simulate the full-scale nose to hub distance (0.65 R). (The forward portion of the fuselage was of importance for this rocket trajectory, wind sensor test.) This scaling was slightly compromised to 0.70 R to prevent the hub center from moving forward of the pylon (see Fig. 8). Model stub wings were specially designed to be scaled to the rotor. Following fabrication, they were mounted on the fuselage such that their relative position to the rotor hub was scaled equivalent to that of the full-scale wing to rotor position. In addition to being sized and positioned correctly for the rotor flow field, scaling the wings to the rotor permitted rocket trajectory locations relative to the wing to be representative of full-scale and correctly positioned in the flow field. A summary of the primary scaling values are presented in Table 2.

TABLE 2. SCALING OF RELATIVE POSITIONS OF ROTOR, FUSELAGE, AND WING

	Model*	Full-Scale AH-1G*
Canopy Roof to Rotor (Vertical Positioning of Fuselage)	z = -0.18	z = -0.18
Nose to Rotor Hub Center (Horizontal Positioning of Fuselage)	x = 0.70	x = 0.65
Wing Trailing Edge (@ Root) to Rotor Hub Center	x = -0.06 z = -0.37	x = -0.06 z = -0.37
Wing Semi-Span	y = ±0.23	y = ±0.23

---

* All values are scaled to the rotor radius (i.e., nondimensionalized by R)

A modified canopy for the model fuselage was scaled from the alternate flat sided canopy of the AH-1G, shown in Fig. 3, and fabricated for use in a "modified canopy" portion of the test.

SELECTION OF TEST CONFIGURATIONS AND CONDITIONS

Four model configurations were selected for the test program. A configuration consisting of the model rotor, fuselage, and wing was selected as the reference configuration. In order to investigate the independent effects of the rotor, fuselage and wing, additional isolated rotor and rotor-fuselage (without wing) configurations were selected. The fourth configuration consisted of the rotor, fuselage with modified canopy, and wing.

TABLE 3. TEST CONFIGURATIONS AND CONDITIONS

		Test Condition			
Abbreviated Name	Model Configuration	Thrust Coefficient C_T (±2%)	Tip Speed ΩR, fps	OGE or IGE H/R	h/R
Reference	Rotor-Fuse-Wing	0.00472	497	OGE	
Isolated Rotor	Rotor	0.00472	497	OGE	
Rotor-Fuselage	Rotor-Fuselage	0.00472	497	OGE	
Modified Canopy	Rotor-Fuse (w/Mod. Canopy)-Wing	0.00472	497	OGE	
Modified Thrust	Rotor-Fuse-Wing	0.00354	497	OGE	
Modified Tip Speed	Rotor-Fuse-Wing	0.00472	373	OGE	
IGE (H = 18.5 ft)	Rotor-Fuse-Wing	0.00472	497	0.84	1.42
IGE (H = 10 ft)	Rotor-Fuse-Wing	0.00472	497	0.46	1.04
IGE (H = 0 ft)	Rotor-Fuse-Wing	0.00472	497	0	0.58

Six test conditions (model operating conditions) comprising different combinations of rotor thrust coefficient, tip speed, and ground effect were selected as follows. A thrust coefficient (C_T = 0.00472) representative of the AH-1G gross weight (9500 lbs) and a tip speed (ΩR = 497 fps) equivalent to two-thirds of the AH-1G tip speed (ΩR = 746 fps) were selected in combination with out-of-ground-effect operation as the reference operating condition. The reference thrust coefficient of 0.00472 corresponds to a thrust coefficient/solidity ratio (C_T/σ) of 0.072. The selection of the lower reference tip speed (2/3 full-scale) was based on structural considerations for the available model blades. The selection was justified on the basis that both available theoretical and experimental results have substantiated the general independence of hovering rotor wake geometry to tip speed and the linear scaling of flow velocities with tip speed when the rotor is operated at a constant thrust coefficient. Several sets of substantiating test data from different investigators for tip speeds between 450 and 700 fps are compared with theoretical predictions in Ref. 12.

Independent variations of each of the test condition parameters (thrust coefficient, tip speed and ground effect) from the single combination of the reference condition were selected as the remaining five conditions. A single independent variation of thrust coefficient (C_T = 0.00354), which is three-fourths of the reference value, was selected to simulate a change in the direction of the helicopter empty weight. The thrust coefficient variation was achieved by reducing the blade collective pitch setting at the reference tip speed. A single independent variation of tip speed (ΩR = 373 fps), which is three-fourths of the reference condition value and one-half the full-scale value, was selected. This value and the extent of the variation is obviously not typical of full-scale rotor operation. It was selected on the basis of providing a variation equivalent to the tip speed increment between the reference value and the full-scale operational value. The reference thrust coefficient was retained for the modified tip speed condition by maintaining collective pitch essentially constant. Three in-ground-effect conditions were selected to provide a comparison with the reference out-of-ground-effect condition. Three distances between the full-scale AH-1G landing gear skids and the ground (H = 0, 10, and 18.5 ft) were scaled by the rotor radius (H/R = 0, 0.46, and 0.84) and converted to scaled distances between the rotor hub and the ground (h/R = 0.58, 1.04, and 1.42) to establish distance settings between the movable ground plane (Fig. 6) and the model rotor. The reference rotor tip speed and thrust coefficient was retained (the latter by reducing collective pitch) for all three in-ground-effect conditions.

The selected model test configurations and conditions were combined to result in the nine test configuration/condition combinations listed in Table 3. Abbreviated names, assigned to the nine combinations, are included in Table 3 and will be used to simplify configuration/condition identification throughout the remainder of this report. As indicated in Table 3, each of the four test configurations were tested at the reference condition, and each of the five test conditions representing modifications from the reference condition were tested using the reference configuration.

In summary, in addition to testing the reference configuration and operating condition, the separate influence of the fuselage, wing, and modified canopy on the flow velocities and wake patterns were measured by testing the isolated rotor, rotor-fuselage (without wing) and rotor-modified canopy fuselage-wing at the reference operating condition. Independent variations of each of the operating condition parameters (thrust coefficient, tip speed, and ground effect) were then tested for the reference configuration.

SELECTION OF TEST DATA

Flow velocity (laser velocimeter) data and flow visualization (smoke and/or schlieren) data were acquired for all test configurations and conditions. Considering the contractual scope of the test program, the number of configurations and conditions, and the potential number of flow velocity locations and component combinations to completely investigate all rocket trajectory and wind sensor locations, a limited but judicious selection of laser velocimeter measurements was necessary. Also, priority configurations and conditions were established for the analysis of the flow visualization data. The selection of test data and the bases thereof are discussed below. The flow velocity locations and components are summarized in Tables 4 through 6.

Flow Velocity (Laser Velocimeter) Data

The 2.75 in. rocket trajectories in the vicinity of the AH-1G helicopter are shown in Fig. 4. Two sets of axis systems (x, y, z and x_T, y_T, z_T), used during the test program, are also shown in this figure. The first (x, y, z) is a horizontal-vertical axis system with the rotor hub as the origin. The second (x_T, y_T, z_T) is oriented with respect to the rocket trajectories with the intersection of the line joining the launch points and the fuselage plane of symmetry as the origin. For convenience, both axes systems were selected to result in left-handed coordinate systems. In Table 4, the locations for rocket trajectory Nos. 1 through 4 correspond to those of the full-scale

TABLE 4. ROCKET TRAJECTORY LOCATIONS

Rocket Trajectory No.	Launch Point Coordinates						Launch Attitude
	x	y	z	x_T	y_T	z_T	γ, Deg
1	0.035	-0.22	-0.39	0	-0.22	0	7
2	0.035	-0.16	-0.39	0	-0.16	0	7
3	0.035	0.16	-0.39	0	0.16	0	7
4	0.035	0.22	-0.39	0	0.22	0	7
5	0.035	0.16	-0.39	0	0.16	0	9

TABLE 5. WIND SENSOR LOCATIONS

Wind Sensor Location No.	x	y	z
1	0.27	0.133	-0.185
2	0.27	-0.083	-0.185
3	0.27	-0.107	-0.185
4*	0.27	-0.133	-0.185
5	0.27	-0.183	-0.185
6	0.77	0	-0.40
7	0.835	0	-0.40

---

*Primary wind sensor location

TABLE 6. LASER VELOCIMETER DATA -- COMPONENTS AND LOCATIONS

Test Configuration/ Condition	Flow Velocity Component, fps	LV Data Locations			
		Rocket Trajectory			Wind Sensor No.
		Trajectory No.	y_T	γ Deg	
Reference	v_{z_T}	2,3,4	-0.16,0.16,0.22	7	
	v_{z_T}	5	0.16	9	
	v_{x_T}	3	0.16	7	
	v_{y_T}	2,3	-0.16,0.16	7	
	v_y, v_z				1-5
	v_x, v_z				6,7
Isolated Rotor	v_{z_T}	-	0	7	
	v_{z_T}	3,4*	0.16,0.22	7	
	v_{z_T}	4	0.22	7	
	v_y, v_z				1-5
Rotor - Fuselage	v_{z_T}	3,4	0.16,0.22	7	
Modified Canopy	v_{z_T}	3,4	0.16,0.22	7	
	v_y, v_z				1-5
Modified Thrust	v_{z_T}	3,4	0.16,0.22	7	
	v_y, v_z				1-5
Modified Tip Speed	v_{z_T}	3,4	0.16,0.22	7	
IGE (H = 18.5 ft)	v_{z_T}	3,4	0.16,0.22	7	
IGE (H = 10 ft)	v_{z_T}	3	0.16,0.22	7	
	v_y, v_z				1-5
IGE (H = 0 ft)	v_{z_T}	3	0.16		

---

*Transformed from data taken at $y_T = 0$

AH-1G indicated in Fig. 4 .* Rocket trajectory No. 5 is a trajectory launch attitude variation. Flow velocities were measured with the laser velocimeter at rocket trajectory Nos. 2-5. Primary emphasis was placed on trajectories 3 and 4 which were located on the starboard side of the model at $y_T = 0.16$ and 0.22, respectively. These were given priority to provide data for side-by-side inboard and outboard (relative to the fuselage) trajectories, and thereby detect the anticipated difference in fuselage flow interference. Thus, trajectories 3 and 4 were investigated for most all of the test configuration/condition combinations.** In addition, velocity measurements at selected points on rocket trajectory No. 5 representing a trajectory attitude variation of No. 3 from 7 to 9 degrees and rocket trajectory No. 2 on the opposite side of the fuselage were taken for the reference configuration and condition. Also, for the isolated rotor, LV measurements were made parallel to the rocket trajectories but at $y_T = 0$. Recognizing the flow symmetry of the hovering rotor in the absence of the fuselage, these measurements could be transformed, through appropriate geometric relations, to represent other parallel trajectories. Transformations to the rocket trajectories of interest were made, and the results will be presented and compared in a later section of this report. All of the above LV data locations for rocket trajectories are presented in Table 6.

Flow velocity components at rocket trajectories were measured in the trajectory axis system (v_{x_T}, v_{y_T}, v_{z_T}). That is, v_{y_T} and v_{z_T} were measured normal to the rocket trajectory, and v_{x_T} was measured in the direction of the rocket trajectory. Primary emphasis was placed on the measurement of the velocity component in the vertical plane and normal to the rocket trajectory, v_{z_T}, since for hover it is this component which generally is of much larger magnitude than the other two components and, with regard to flow interference, it is the most influential on the attitude and thus the range of the rocket. Thus, as indicated in Table 6, v_{z_T} was measured for the rocket trajectories of all configurations and conditions. The velocity components in the lateral direction, v_{y_T}, and the direction of the rocket trajectory, v_{x_T}, were measured for the reference configuration and condition at selected points.

---

* The rocket launch points were assumed to be beneath the wing tip leading edge (@ x = 0.035). The actual front openings of the 2.75 in. rocket launchers are somewhat forward of this point.

**The IGE (H = 0 and 10 ft) conditions were limited scope additions to the original test program, and LV measurements were thus limited to rocket trajectory 3.

In addition to rocket trajectory points, flow velocity measurements were taken at and in the vicinity of wind sensor locations under consideration by the Army at the time of the test program. The seven tested wind sensor locations are shown in Fig. 5 and their coordinates relative to the rotor hub center and nondimensionalized by the rotor radius are presented in Table 5. The wind sensor locations were properly scaled to those of the full-scale AH-1G rotor. The scaling difference between the model and full-scale fuselages with respect to their respective rotor radii resulted in slight inconsistencies between the wind sensor locations when scaled to the model and full-scale fuselages, as indicated in Fig. 5. Note that the double points are only shown to indicate relative scaling differences in the distances between the model and full-scale fuselages. Actual measurements were taken only at the model scaled points which were properly located in the rotor flow field. Wind sensor location Nos. 1 through 5 were selected to provide data at, in the vicinity of, and on the opposite side of the fuselage from primary wind sensor location No. 4 as prescribed by the Army technical representative for this investigation. Wind sensor Nos. 6 and 7 were located ahead of the nose of the model by 7 and 14 percent of the rotor radius, respectively. Wind sensor data (v_y and v_z) were measured at locations 1 through 5 for the reference, isolated rotor, modified canopy, modified thrust, and IGE (H = 10 ft) test configurations/conditions. At locations 6 and 7, v_x and v_z velocities were measured for the reference configuration and condition. The test combinations of test configuration, condition, velocity component and wind sensor locations are included in Table. 6.

FLOW VISUALIZATION AND WAKE GEOMETRY DATA

Flow visualization results are presented prior to the LV results to provide a familiarization with the rotor wake characteristics associated with the various test configurations and conditions which will assist in the interpretation of the LV data.

INTRODUCTORY WAKE INFORMATION

To introduce the procedures used in reducing the flow visualization data, a brief discussion of the fundamental characteristics of the hovering rotor wake and the interpretation of these characteristics from previous tests (Refs. 14 and 15) is presented. A schematic of the wake from one blade is shown in Fig. 14. The wake contains two primary components. The first, and most prominent, is the strong tip vortex which arises from the rapid rolling up of the portion of the vortex sheet shed from the tip region of the blade. The second feature is the vortex sheet shed from the inboard section of the blade. This sheet does not roll up but generally remains in the form of distributed vorticity. The vertical or axial transport velocity near the outer end of the inboard vortex sheet is much greater than that of the tip vortex. The vertical velocity of the inboard sheet also increases with radial position, resulting in a substantially linear cross section of the inboard sheet at any specific azimuth position as shown in Fig. 14. These characteristics result directly from the velocities induced by the strong tip vortex. The radial extent of the vortex sheet is depicted in Fig. 14 as ending abruptly. This is attributable to the absence of wake circulation strength there. The radial distribution of trailing vorticity emanating from the blades is directly related to the gradient of the blade spanwise lift distribution. The blade lift reaches a maximum near the tip of the blade which results in a local zero gradient and thus zero wake strength. Outboard of this region, the trailing vorticity forms a rolled-up tip vortex with the rotational circulation direction indicated in Fig. 14. Inboard, the blade lift gradient is opposite in sign, and thus the circulation sense of the inboard vortex sheet is opposite to that of the tip vortex. It is the local circulation sense of a wake element which determines the direction of its induced velocity contribution at a point in the flow field. In addition to the wake structure shown in Fig. 14 for one blade, similar wake structures for other blades also exist, with the aggregate forming the complete wake representation.

A computerized analytical representation of the hovering rotor wake is presented in Fig. 15. The wake of each blade is divided into the tip vortex and inboard vortex sheet as represented by the finite vortex filaments shown in the figure. This representation was used for the previous theoretical flow study for rocket trajectories (Refs. 6 and 7), and for the theoretical results presented in a later section of this report. A schematic of the tip vortex pattern and rocket trajectories is presented in Fig. 16.

Smoke and schlieren flow visualization techniques were used during the test program. These two techniques complement one another in that, as applied, the schlieren technique provides visualization of the three-dimensional tip vortex patterns, and the smoke provides two-dimensional cross sections of the tip vortices and inboard vortex sheet. Sample flow visualization results are presented in Figs. 17 through 31.

SCHLIEREN WAKE VISUALIZATION

Sample frames from schlieren movies of the rotor tip vortices are shown in Fig. 17. The photographic quality in Fig. 17 has been somewhat compromised by the reproduction of enlarged photographs from movie frames. To more clearly depict the schlieren results, tracings from projections of selected movie frames associated with several test configurations and conditions are presented in Figs. 18 through 22.

Reference Configuration/Condition

In Fig. 18, the tip vortices for the reference rotor and condition are shown relative to the blade, fuselage, and rocket trajectory. The selected movie frame for this figure had the two blades over the fuselage (ψ = 180 deg for the blade shown). The start of the second revolution of the tip vortex from the blade at ψ = 180 deg is shown to be near the rocket trajectories on the starboard side of the fuselage. Using smoke data it was determined that, for the reference configuration/condition, the tip vortex intersects with rocket trajectory no. 4 ($y = 0.22$, $\gamma = 7$ deg) at the intersection point shown ($x = 0.78$; $x_T = 0.75$) when the blade is at approximately 215 deg. The vortex age, at this point, is approximately 415 deg.

In addition to wake geometry, the schlieren data was useful in determining tip vortex core size for use in the hovering rotor computer analysis. Since the schlieren technique results in a recorded visualization of the density gradients in the air, the tip vortex core is made visible due to the significantly different density within the core in relation to the surrounding air. The vortex core diameter was measured from several schlieren movie frames, and was found to be one-tenth of the blade chord ($0.1c \pm 30\%$). The variation of approximately thirty percent was found from data for various blade azimuths (ψ) and tip vortex age (ψ_w). In terms of blade radius, the vortex core diameter was 0.01R.

Isolated Rotor

The tip vortex pattern for the isolated rotor is compared with that of the reference configuration in Fig. 19. The vortex patterns were found to be closely similar considering that Figs. 18 and 19 were acquired from single movie frames and do not exactly indicate the mean locations recognizing some vortex unsteadiness. The primary difference that did occur, that was verified by the smoke data, was a slightly greater radial extent of the tip vortices (wake boundary) due to the presence of the fuselage. The intersection of the isolated rotor tip vortex with rocket trajectory no. 4 was determined to occur at $x = 0.76$ ($x_T = 0.73$) when the blade azimuth, ψ, was approximately 200 deg. At this point the vortex age, ψ_w, was approximately 400 deg.

The unsteadiness of the tip vortices increases with vortex age. The vortices were generally found to be fairly stable above and in the region of the rocket trajectories. However, the vortex stability deteriorated appreciable below the rocket trajectory as shown in Fig. 19 (at $\psi_w = 540$ deg). The smoke data indicated that the tip vortices become very unstable at a vortex age, ψ_w, of approximately 720 deg. This is consistent with the results of Ref. 14. If anything, the presence of the fuselage appeared to increase the tip vortex stability.

Modified Thrust Condition

The tip vortex pattern for the modified thrust condition, presented in Fig. 20, indicates that a reduction of the thrust coefficient results in a reduction in the vertical wake transport velocity, as expected. This reorients the tip vortices relative to the rocket trajectories. This wake reorientation with respect to blade azimuth will be shown to have an impact on the blade azimuth phasing of the rocket interference flow velocities.

Modified Tip Speed Condition

The results of the tip speed variation were somewhat surprising. Earlier flow visualization results (Ref. 14) have indicated the general independence of wake geometry on tip speed for the same rotor and thrust coefficient. As shown in Fig. 21, the location of the tip vortices for the two-blades (1 and 2) at the modified tip speed condition did not repeat at the same vortex age as the vortices approached and travelled below the rocket trajectories. Also, they departed significantly from the reference condition location at a vortex age, ψ_w, of 540 deg. The possibility of unequal and incorrect blade pitch settings was eliminated on the basis that the vortex geometry of the two blades was in agreement within the first wake revolution, and the midpoint between the two vortex locations at the same vortex age was close to that of the reference rotor. It is possible that the presence of the fuselage in combination with the low tip speed tested (350 fps) reduced the wake stability, but this should be investigated further.

In-Ground-Effect Conditions

Placement of the model in-ground-effect resulted in the expected expansion of the wake boundary as shown for the simulated 10 ft skid height condition in Fig. 22.

SMOKE FLOW VISUALIZATION

Flow Visualization Techniques and Sample Wake Photographs

To obtain smoke flow visualization data, smoke was injected into the flow by movable smoke rakes located above and to the side of the rotor (Fig. 8). The smoke rakes were positioned by remote control to insure a clearly defined tip vortex. The wake patterns were recorded on film with remotely operated cameras. A time-delay system was used to trigger the cameras and microflash units when the rotor was at a desired azimuth position. The delay system used a one/rev signal from the rotor shaft as a reference, and the delay time (manually adjusted) was measured on an electronic counter. For each test condition, photographs were taken at preselected azimuth positions of a reference blade with respect to the plane of the smoke. Photographs were generally taken at azimuth angles of 0, 30, 60, 90, 120, and 150 deg as shown in Fig. 23 for the reference configuration and condition. Several photographs were normally taken at each azimuth position.

The schematic in Fig. 14 is representative of the three-dimensional wake pattern which would be observed if smoke were emitted from the blade (i.e., in the rotating system). To take advantage of the symmetrical nature of the wake of a hovering rotor as well as to facilitate the acquisition of quantitative data, the wake for this investigation was observed by emitting smoke externally from the blades (i.e., in the nonrotating system). Smoke was emitted from smoke rakes in a single plane and the flow patterns were photographed, as shown for the two-bladed rotor in Figs. 23-31. In this manner, a two-dimensional cross section of the wake was recorded. The cross sections of the tip vortices appear as circles in which the central regions are clear of smoke due to the local centrifugal field which forces the smoke particles radially outward. The center of the circular cross sections are interpreted as the centers of the vortex core. The vortex sheet cross sections are indicated by the discontinuities present in the smoke filaments passing through the inner region of the rotor wake.

Sample smoke flow visualization photographs for comparison of wake cross sections of various test configurations and conditions are presented in Fig. 24. Enlarged photographs are presented in Figs. 25-31. Particularly noteworthy are Figs. 30 and 31 which clearly show the expansion of the wake boundary relative to the reference out-of-ground effect condition (Fig. 25) when the aircraft is operated close to the ground.

Wake Geometry Data

The photographic wake data were analyzed for selected test conditions to determine the principal wake geometry characteristics. The conditions were selected so as to permit assessment of the effects of the primary test parameters and to provide wake geometries for the computerized prescribed wake hover theory. Radial and axial wake coordinates were determined from the photographs as functions of the wake azimuth angle (ψ_w), which is equivalent to the blade azimuth travel ($\psi = \Omega t$) from the time it generates the vortex cross section. For example, in Figs. 24 to 31, the uppermost tip vortex and vortex sheet cross section were shed by a blade which has traveled 180 deg from the time it passed through the plane of smoke. The following tip vortex and vortex sheet cross section were shed by the blade shown the previous time it passed through the reference side of the smoke plane, and thus the wake azimuth angle for these cross sections is 360 deg. Likewise, the azimuth angle of the third cross section is 540 deg. It should be noted that the cross sections in the visible wake near the rotor remain approximately in the same plane (rotor wake tangential velocities are small). The azimuth angle, ψ_w, was used as the third coordinate in the wake geometry analysis. For an idealized, stable, hovering rotor wake, the radial and axial coordinates at a given azimuth angle are equivalent for each blade due to symmetry. Thus the complete coordinate system of the wake for a given test condition was determined by the following procedure.

Using special negative film projection equipment and computerized coordinate identification equipment, the radial and axial coordinates of the wake from several blades in a single photograph were determined. This was repeated for a sequence of photographs taken with the rotor at a series of prescribed rotational positions. A sample sequence is presented in Fig. 23, in which the rotor rotational positions relative to the smoke plane are designated by the azimuth positions, ψ_s, of the two blades. Considering the known azimuth positions of the reference blade and relating each vortex cross section to the appropriate blade, the radial and axial coordinates were obtained in terms of the wake azimuth (age), ψ_w. The coordinate results from the series of photographs were then plotted as functions of ψ_w as shown in Figs. 32 to 34. To facilitate the comparison of wake geometries from varying rotors and test conditions, the radial and axial coordinates were nondimensionalized by the rotor radius, and differences in axial coordinates due to blade coning were eliminated by generally using the blade tip as the reference (z_{TIP} instead of z). The range of wake azimuth angles for which data could be acquired was limited by the visibility of the smoke. For example, for two-bladed rotors, generally only 1½ to 2 tip vortex revolutions per blade, are visible. However, rotor performance is mainly sensitive to the near wake geometry, and knowledge of the exact positioning of the far wake elements below the rocket trajectories was not essential to the objectives of this study. However, further investigation of the far wake instability is warranted for refinement of the prescribed wake geometry used in the hover theory to predict rocket flow interference.

The tip vortex coordinates for the isolated rotor are presented in Fig. 32. An indication of the steadiness of the tip vortex geometry is indicated by the extent of the measured data from different blades and photographs at each wake azimuth.

The general features of the tip vortex geometry are evident in Fig. 32. When an element of the tip vortex is shed from a blade, its rate of axial displacement is very low until it passes beneath the following blade (at ψ_w = 360 deg/b). At that point, the tip vortex element lies radially inboard of the tip vortex of the following blade and thus experiences a large downward induced velocity from that vortex and the blade. The axial transport velocities before and after the passage of the following blade are fairly constant in the near wake, as can be seen from the substantially linear variations of the axial displacement, z_{TIP} with wake azimuth angle in these regions. The radial displacement, r, of the tip vortex decays in an apparently exponential manner as the wake azimuth is increased. The fairings of the tip vortex data in Figs. 32 and 33 are based on these general wake characteristics.

The tip vortex coordinates for various test configurations and conditions are compared in Fig. 33. The vertical coordinates of the isolated rotor were slightly different from the reference rotor, but within the degree of experimental scatter. As expected, the vertical coordinates for the modified tip speed condition were similar to the reference condition, and those for the modified thrust condition were significantly reduced. The radial tip vortex coordinates were similar for the three conditions with the fuselage. However, they were slightly further out from those of the isolated rotor indicating a slight wake expansion due to the fuselage.

It should be noted that the fuselage may create a dissymmetry in the wake, and thus to completely describe the wake in the presence of a fuselage, the wake coordinates should be measured at numerous azimuth locations. This was beyond the scope of the test program reported herein. Results of comparison of the smoke and schlieren results, taken at two different rotor azimuths (ψ = 90 and 180 deg) suggest that the effects on the tip vortex geometry are small, but this and particularly the azimuthal dependence of the inboard wake remain to be investigated further.

Since the cross sections of the vortex sheet from each blade are essentially lines rather than discrete points, as is the case for the tip vortex cross sections, the procedure of Ref. 14 for transforming the photographic data for the vortex sheets to coordinate form was found to be convenient. Assuming the vortex sheet cross sections to be linear, the axial position of a vortex sheet at a given azimuth can be defined by two points. For simplicity, the two points selected were the imaginary extensions of the cross section to $r = 0$ at on end and to $r = 1.0$ at the other end. These two points establish the intercept at the axis of rotation and the slope of the vortex sheet. Tip vortex transport velocities described in Ref. 14 can be derived from this information to provide the necessary wake parameters for the prescribed wake theory.

The inboard wake coordinates, as described above, are presented in Fig. 34 for the reference and isolated rotor configurations. The unsteadiness of the inboard wake is generally greater than that of the tip vortex, and thus lines representing the boundaries of the inboard wake data are presented in Fig. 34. The coordinates for the isolated rotor and reference configuration/condition were similar within the indicated boundaries.

DESCRIPTION OF LASER VELOCIMETRY TECHNIQUES

Laser Velocimetry (LV) is uniquely suited for acquiring velocity measurements on helicopter model tests. While the ability of the technique to provide data as a function of blade position is not unique (e.g., hot wires or hot films), it does have advantages over other techniques. For example, the output is always linear with particle velocity. This may be contrasted with hot wires which change calibrations as velocities get small. Also, implementation never requires introduction of any probe at the measurement location. This is of obvious importance in regions near a tip vortex, for example, where the presence of a probe might alter the flow. These LV advantages are particularly important for the current rotor hover simulation.

The basic principles associated with LV together with the details specific to the present application will be discussed in this section. The basic principles are included only as an outline to serve as an introduction to the specifics. Details to be discussed will include optics, seeding, data processing, and data editing.

BASIC LV PRINCIPLES

The Doppler principle is most commonly illustrated through the apparent change in train whistle pitch as it passes by a stationary observer (i.e., a frequency shift due to a moving object). Applied to laser beams, one finds that the frequency (or wavelength) of scattered laser light from a moving target is shifted relative to the incident frequency. This shift is dependent upon the index of refraction of the test medium, n; the wavelength of the incident beam, λ; the velocity of the target, U; and the collection angle, ϕ, relative to the incident direction. Items such as incident power, target size, and target optical properties (e.g., index of refraction, shape) influence the amplitude of the scattered light, not the frequency shift. Since the test medium of interest is air at standard conditions, the index of refraction is essentially constant with value $n = 1$. It will be assumed constant and no further reference will be made to it.

The specific application of the Doppler principle to LV involves beating (or heterodyning) two signals to produce a signal with frequency corresponding to the shift only. In principle one could observe the frequency of the scattered (reflected) light directly. In practice, this frequency is too high ($\sim 10^{15}$ Hz) for most equipment to respond accurately; in addition, the percentage change in frequency due to the velocity of the target relative to this incident frequency (typically a maximum of $1/10^7$) is so small as to preclude adequate resolution of the data. Historically, the first techniques utilized the scattered light together with a small fraction of the incident light (so called "reference beam" LV).

While certain applications are best suited to reference beam probing (e.g., flows with many particles), the current test was conducted with the "fringe mode" or "dual-scatter" LV optics (Fig. 35). With this arrangement, scattered light is collected from light incident from two directions, $\hat{e}_1$ and $\hat{e}_2$. As such the frequency shift f_D, is related to relevant parameters by

$$f_D = \frac{\vec{U} \cdot (\hat{e}_1 - \hat{e}_2)}{\lambda} = \frac{2U \sin(\Theta/2)}{\lambda} \qquad (1)$$

where Θ, as shown in Fig. 35, is the angle between the beams. In general, the target velocity will not be in the direction shown. The measured velocity is that component in the direction shown (i.e., in the plane of the two beams, perpendicular to the bisector of the two beams). The velocity component of solid particles moving through a "probe volume", which is the intersection of the two incident beams, at focal length, d, is measured.

Several items should be noted with regard to the dual-scatter arrangement. First, note the lack of dependence in Eq. (1) of f_D upon the scattering (reflection) direction. As such, the reflected light collection angle is prescribed to meet the requirements of the available equipment and/or test facility. To maximize the signal/noise ratio, the collection solid angle is typically made as large as possible by using a sufficiently large collecting lens. Although f_D is independent of scattering direction, the amplitude of the signal is not. In general, where possible, collection as close to the forward direction as practical, maximizes the signal/noise ratio. Also, note that, for a given wavelength, the frequency-velocity relationship is linear and dependent upon the angle Θ only.

The LV system cannot distinguish between $\pm f_D$ in Eq. (1) because of the mixing characteristics of the photomultiplier used to convert the scattered light into an electrical signal for subsequent processing. As such, the system cannot distinguish velocity direction (i.e., $\pm U$). For applications with flow reversal, this restriction is severe. However, unlike hot-wire anemometry for example, LV optics can be modified to allow direction to be determined over a limited range of velocities. By installing a Bragg cell (or similar frequency-shifting device) into one of the incident beams, its wavelength is changed very slightly. The net result is a nonzero Doppler shift for zero velocity; i.e., Eq. (1) becomes

$$f_D = f_B + \frac{2U \sin(\Theta/2)}{\lambda} \qquad (2)$$

where f_B is the frequency offset due to the Bragg cell. The effect can be seen in Fig. 36. Note that the slope of the frequency-velocity calibration, α, is defined by

$$a = \tan^{-1}\left(\frac{2\,\mathrm{Sin}(\Theta/2)}{\lambda}\right) \qquad (3)$$

and is independent of the use of a Bragg cell. As mentioned previously, unless the direction can be inferred from other sources, given a measured f_D with no Bragg Cell, only the velocity magnitude can be calculated from Eq. (1). With a Bragg Cell, note that the frequency-velocity relationship is unique for any $U > U_{min}$. To the extent that f_B can be varied, U_{min} (velocity at which $f_D = 0$) can be selected to be less than any velocity anticipated.

HOVER FACILITY LV SYSTEM

The application of laser velocimetry to helicopter flow documentation required special considerations to address flow and geometric features peculiar to the problem. Specifically, the system had to include (1) sensing approximately five feet from the optics, (2) backscatter collection, (3) artificial seeding, (4) velocity direction sensitivity, and conditional sampling relative to rotor position. Previous experience at UTRC in applying LV techniques to a model helicopter rotor (described in Ref. 11) was used to develop the LV system and procedures for this test program. Details of the system used to meet the above requirements for the hover test program are discussed in the following paragraphs.

A general view of the optics system together with the seedant probes and the first-stage signal processing equipment are shown in Fig. 9. The optics, including transmitting components, collecting lens, laser head, and photomultiplier are shown mounted on a single-direction, remotely controlled traversing system. This system had the capability for aligning the traversing direction along the rocket trajectories. Two seedant probes are shown in Fig. 9: one above the rotor plane which moved with the traversing system, and one mounted in the vertical plane outside the wake (r = 1.4). Each probe had two outlets to increase the seeding coverage while reducing the seed exit velocities from the probe. The electronic instrumentation shown in Fig. 9 were used to adjust the value of f_B in Eq. (2) and to amplify the signal before transmission via cable to the control room. The model is shown in the position used for wind sensor measurements. (The model was rotated 90 degrees for rocket trajectory measurements.)

The LV optics are shown in greater detail in Figs. 10 and 11. Fig. 11 shows schematically the LV optical arrangement shown photographically in Fig. 10. The laser beam was emitted from the upper end of the laser head as shown in these figures. After the beam was turned 90 degrees with a mirror, it entered the transmitting optics where the beam was divided into two beams, passed through a Bragg Cell, and focused with the transmitting lens. The beams had a 55 mm separation at the transmitting lens and were focused 1600 mm (63 inches) from the lens surface. With the f_B = 2 MHz used for the tests, the velocity range was from -60 ft/sec to 160 ft/sec. The sign of the velocity was selected to meet requirements of testing. For vertical velocity measurements for example, the largest velocities were expected downward from the rotor. Thus, for the purposes of processing, positive velocity is indicative of downwash. For the purposes of data analysis and reporting, the sign of the velocity was changed to conform to more typical helicopter convention. Scattered light was collected 15 degrees off the direct backward scatter direction. Backward scatter was dictated by the remote-control requirement for testing. Collection off axis reduced the effective measuring volume ("probe volume") to an acceptable size (approximately 0.05 inches in diameter by 0.10 inches long). The collected light was redirected by a mirror to focus on the photomultiplier aperture. The collection lens had a four inch diameter and 24 inch focal length. The magnification of the collection optics was approximately 1.0.

As is often the case with any LV application, seeding was of prime importance for the current program. LV is a technique which measures the velocity of particles, not gas molecules. As such, the particles must accurately track the flow velocities to yield reliable results. Artificial seeding was introduced into the flow pattern using the two probes shown in Fig. 9. Positioning of the probes was based on results of flow visualization testing so as to seed all areas which contributed to the flow at any given measurement point. This is particularly important for the current application. At many locations the flow represented contributions from many sources; failure to seed all sources would preclude accurate sampling of all velocities at the measurement location, thus introducing a bias to the results. Union Carbide Bakelite Phenolic "Microballoon" particles were selected for seeding. These seedant particles have the advantage of a relatively low density (0.15 g/cc). As such their larger size (average diameter of 0.0017 inches) did not preclude their following the flow accurately. The larger size was helpful in maximizing the signal/noise ratio given the small collection solid angle imposed by the necessity of testing at large distances from the collection lens. Particles were injected by using compressed air passing through a fluidized bed seeder. Measurements at the seedant probe exits with the seeders operating at test conditions showed the particle velocities to be less than one ft/sec. This was necessary given that the seeding was being introduced in essentially ambient air; large particle exit velocities would increase the probability of data biasing through particles not tracking the local flow accurately. Most of the particles did track the sometimes large velocity and direction changes. The largest particles would not always do so,however. Fortunately in these instances, the large particle velocities were quite different from the gas velocities (obtained from the more numerous smaller particles) and were discarded during data editing.

LV DATA PROCESSING

LV data were processed utilizing a single realization counter connected directly to an on-line PDP 11/10 computer (Figs. 12 and 13). The counter/processor performed several tasks on the photomultiplier-signal. The photomultiplier signal (Fig. 37a) has a Gaussian shape because of the Gaussian variation of the incident intensity across the beam cross-section. Each particle generates a similar signal. As the voltage exceeds a preset trigger level (allowing discrimination from the background electronic noise), the signal is processed in the counter. In addition to bandpass filtering and amplifying the input signal (Fig. 37b), the processor does a validity check on the Doppler frequency samples from individual particles. Briefly, two 125 MHz clocks are started by the scope trigger. One counts five zero crossings; the other counts eight zero crossings. The times are required to agree (multiplied appropriately by the factor 8/5) within a preset tolerance. For the hover tests, the agreement was required to be within 1.5 percent. This validation insures that data is acquired from a single particle (one particle at a time). Valid signals are transmitted digitally to the Mode Control Interface (Fig. 12).

The Mode Control Interface (MCI) has two primary functions. The first is to take the processor output signal and input it to the computer. In addition, for each valid sample, the interface has the capability to read the sample arrival time relative to some external marker. For the present hover tests, the external marker was generated by a once/revolution induction pickup attached to the rotor shaft. This permitted all velocity measurements to be related in time to rotor blade azimuth position, ψ. The once/revolution signal was converted to an acceptable pulse utilizing the Pulse Detector on the console and fed to the MCI. The "clock" actually counts pulses from an internal frequency generator. The MCI can accurately time flows with periods ranging from 100 μseconds up to 60 seconds. Although the MCI can accommodate three processor signals simultaneously, additional computer interfacing is required. This hardware is currently under construction at UTRC, but the hover tests were limited to a single channel (one velocity component measurement at a time).

Helicopter LV data is most valuable when presented relative to given rotor orientation. For this test, data were repeatedly acquired for twenty time increments per each rotor revolution. Each time increment corresponded to 18 degrees of blade azimuth travel ($\Delta\psi$) and was appropriately related to the rotor azimuth reference ($\psi = 0$) which corresponded to a blade azimuth position over the tail of the model helicopter.

The computer was used to organize the data and calculate the mean velocity, $\bar{v}_i$, for each blade azimuth segment, $\Delta\psi_i$, as related to each of the 20 blade positions, ψ_i. Also calculated were the overall time-averaged velocity, $\bar{v}$, and RMS value for both all data irrespective of rotor position and weighting the data for each azimuth segment equally (a more accurate representation of the overall time-average). If each azimuth segment had the same number of velocity samples (seedant particles), the two overall time-averaged values would agree. The velocity calculations are described in greater detail below.

The two digital words from each valid sample, Doppler period and arrival time, are inputted into the computer buffer. The program calculates the velocity and catalogs it in the appropriate $\Delta\psi_i$ location. As mentioned above, $\Delta\psi_i$ is a segment of the blade 360° azimuth travel, and twenty segments were used (i.e., $\Delta\psi_i = 18^\circ$). For each segment, the mean velocity

$$\bar{v}_i = \frac{1}{N_i} \sum_{j=1}^{N_i} v_j(\Delta\psi_i) \qquad (4)$$

and root-mean-square velocity

$$v_i' = \left\{ \frac{1}{N_i} \sum_{j=1}^{N_i} \left(v_j(\Delta\psi_i) - \bar{v}_i \right)^2 \right\}^{1/2} \qquad (5)$$

were calculated. The N_i are the actual number of seedant particle samples for the i^{th} segment (typically, 25). After the $\bar{v}_i$ are calculated the overall time-averaged velocity

$$\bar{v} = \frac{1}{20} \sum_{i=1}^{20} \bar{v}_i \qquad (6)$$

was calculated. Data outputs included N_i, $\bar{v}_i$, and v'_i for each of the twenty segments as well as the overall time-average values. The more meaningful time-average velocity, $\bar{v}$, of Eq. (6) was used for the data presented herein.

All data samples (Doppler period and arrival time) were stored on cassette tapes (Figs. 12 and 13) for subsequent editing. Two main sources of unacceptable data are occasionally inputted into the computer. The first is samples from particles not accurately tracking the flow. As mentioned previously, the wide range in particle sizes (especially with some agglomeration) results in occasional bad samples (usually less than 10 percent of the total number of samples). Since the LV measures only particle velocity, it cannot distinguish between particles following or not following the flow. Also, with any electronic system, occasional samples from the noise signal will be validated and inputted to the computer.

Data editing was conducted to remove these unacceptable samples. Editing was performed at a later time so as not to slow the data acquisition progress. For each LV data segment, $\Delta\psi_i$, a histogram (plot of number of samples vs. velocity) is displayed on the computer oscilloscope. Since most of the samples accurately reflect the airflow velocity, the unacceptable samples will not fit within the histogram. The operator instructs the computer to ignore these samples and an edited set of results are calculated. For future reference, the edited and the unedited results are printed as outputs.

For the hover test, the velocity component v_{z_T}, perpendicular to the rocket trajectory was the primary measurement. For selected cases (including wind sensor locations) the other velocity components were measured. Typically 500 samples were taken for each location/flow condition combination. Accuracy is dependent upon local turbulence level and number of samples: as turbulence intensity decreases and/or number of samples increases, accuracy is improved. Accuracy is usually stated in terms of probable error. Probable error is defined as the error band around the true value within which 68 percent of the statistical results would fall, given N samples. Specifically, for the mean value,

$$\left| \frac{\bar{v}_i\,(\text{meas}) - v_i\,(\text{true})}{v_i\,(\text{true})} \right| < \left(\frac{v'_i}{\bar{v}_i} \right) \frac{1}{\sqrt{N_i}} \qquad (7)$$

and for the RMS value

$$\left| \frac{v'_i\,(\text{meas}) - v'_i\,(\text{true})}{v'_i\,(\text{true})} \right| < \frac{1}{\sqrt{2}} \quad \frac{1}{N_i - 1} \qquad (8)$$

The right-hand side of (7) and (8) represent the probable errors; again, this means that 68 percent of the time repeated sets of N_i samples at one location would result in (7) and (8) being satisfied. For the hover test, the probable error for the mean velocities at any segment $\Delta\psi_i$, from (7), ranged from 1 percent for low turbulence-high sample segments to 20 percent for high turbulence-low sample segments. The probable error for most of the segments was near the lower limit of the range. This is evident in the repeatability of the data in Fig. 39 (to be discussed). Based upon (8), the probable error in RMS was typically 15 percent or higher; thus any RMS results are presented only to indicate trends (i.e., high or low fluctuations) and should not be taken as absolute RMS profiles. It will be shown that the general repeatability of the time-averaged flow velocity data was within approximately 3 fps.

FLOW VELOCITY (LASER VELOCIMETER) DATA

In this section, the laser velocimeter data is presented and compared for rocket trajectory and wind sensor locations. Presentation of the LV data is preceded by the following description of the flow velocity scaling procedure applied to the model LV data to transform the data to be representative of the operational hover condition of the full-scale AH-1G.

FLOW VELOCITY SCALING

As mentioned earlier, the model rotor tip speed (497 fps) was two-thirds of the full-scale AH-1G value (746 fps). In order to present flow velocity data representative of full-scale values, appropriate velocity scale factors were applied.

The fundamental relation used for scaling is the following equation for the uniform induced velocity at a hovering rotor based on momentum principles:

$$v_{i_{mom}} = \Omega R \left(\frac{C_T}{2}\right)^{1/2} \tag{9}$$

Equation (9) indicates that the induced flow velocity is proportional to rotor tip speed and the square-root of the thrust coefficient. A velocity scale factor, defined in Eq. (10), was thus applied to the data.

$$v_2 = \left[\text{Velocity scale factor}\right] v_1 = \left[\frac{(\Omega R)_2}{(\Omega R)_1}\left(\frac{(C_T)_2}{(C_T)_1}\right)^{1/2}\right] v_1 \tag{10}$$

The model LV data for the reference rotor, isolated rotor, modified canopy, and in-ground-effect configurations/conditions were scaled to the full-scale tip speed with a Velocity Scale Factor of 1.5. For consistency and purposes of comparison, the model LV data for the modified thrust coefficient and modified tip speed conditions were also scaled to the reference full-scale condition representing the AH-1G gross weight and operational tip speed. This permitted a check on the scaling procedure through direct comparison of velocity plots. It should be recognized that the actual flow velocities measured for the model rotor operation can be reconstructed by dividing by the scale factor.

Also, the flow velocities representative of full-scale operation at the reduced thrust and tip speed conditions can be determined by dividing by 1.15 (from 1.73/1.5) and 1.33 (from 2.0/1.5), respectively.

As mentioned earlier, the above scaling procedure has been examined in past investigations as described in Refs. 12 and 14. A summary of the Velocity Scale Factors is presented in Table 7. Also included in Table 7 are the momentum induced velocity values ($v_{i_{MOM}}$ from Eq. 11) for the model test conditions. The value of $v_{i_{MOM}}$ for the full-scale AH-1G operating condition ($C_T = 0.00472$, $\Omega R = 746$ fps) is 36.2 fps.

TABLE 7. Flow Velocity Scale Factors

Test Configuration/Condition	Velocity Scale Factor (For Scaling to Full-Scale AH-1G Condition)	Model $V_{i_{MOM}}$ fps
Reference	1.5	24.1
Isolated Rotor	1.5	24.1
Modified Canopy	1.5	24.1
IGE (All Conditions)	1.5	24.1
Modified Thrust	1.73	20.9
Modified Tip Speed	2.0	18.1

ROCKET TRAJECTORY LV DATA

Prior to presenting the LV data for all configurations, conditions and rocket trajectory locations, the data for one rocket trajectory of the reference configuration operating at the reference condition is presented to describe the fundamental flow velocity characteristics. The LV data substantiated the rocket trajectory flow characteristics identified theoretically in Refs. 6 and 7, and the following observations are consistent with those presented in these references.

Time-averaged and time history data for the velocity component in the vertical plane and normal to the rocket trajectory (v_{Z_T}) are presented in Figs. 38 through 40. The variation of the time-averaged v_{Z_T} velocity component at rocket trajectory No. 4 is presented in Fig. 38 along with peak-to-peak limits at each point. The peak-to-peak limits for each rocket trajectory point correspond to the peaks of the mean time variation (rotor azimuth variation) such as those of Fig. 39.* Since the effect of the stub wing was found to be insignificant, except in the immediate vicinity of the wing, the test data in this figure have been supplemented with rotor-fuselage data in the outer wake area. The time-averaged v_{z_T} velocity component increases from appropriately 35 fps to 70 fps (downward) going from the rocket launch position ($x_T = 0$) to the intersection of the trajectory with the wake boundary. The wake boundary, where the tip vortices intersect rocket trajectory No. 4, was determined from the flow visualization results to be at approximately $x_T = 0.75$ for the reference configuration/condition. The increasing downwash trend over the inner wake portion of the rocket trajectory is consistent with the fact that the rocket launch position is near the center of the wake in hover, and the downwash in the hovering rotor wake is known to increase with radial position (Ref. 12). Moving from inside to outside the wake boundary, an abrupt change in velocity occurs in both magnitude and direction (downflow to upflow). The upflow is not nearly as severe as the downflow because the contributions of the tip vortices and the inboard wake are opposing outside of the wake, whereas they are additive just inside the wake boundary. As the rocket moves away from the wake, the velocity decreases as expected and is close to zero beyond $x_T = 1.2$.

The flow velocities at each rocket trajectory point vary with time even in hover due to the rotation of the blades and the associated passage of the wake elements by the points. The periodic time variation of the flow velocity at points on the rocket trajectory are indicated in Figs. 38 and 39 by the peak-to-peak limits and the time-history variations with rotor azimuth, respectively.

In Fig. 39, the time variation of the v_{z_T} velocity component is presented for the reference configuration and condition at selected points along rocket trajectory No. 4 (x_T = 0.025, 0.2, 0.6, 0.68, 0.73, 0.8, and 1.2). The mean of the instantaneous velocities (measured velocities of individual seedant particles) is indicated at each blade azimuth by a symbol. Since ideally, the flow velocities at a point below a two-bladed rotor are periodic with each half-rotor revolution (2 per rev), the LV time-history data are plotted over a 180 deg rotor azimuth range. The azimuth positions for both blades are indicated, and different symbols are used to distinguish between data taken for the first and second half of the rotor revolution. Data were taken

---

*In determining the peaks, individual mean LV data points were used instead of the faired curves, to show the maximum measured mean deviations from the time-averaged values.

for many revolutions (normally until the velocities of 500 seedant particles were measured), and the symbols represent the mean value at each rotor azimuth position. The RMS deviation, indicating the unsteadiness (nonperiodicity) of the flow for numerous rotor revolutions is indicated in Fig. 39 by the brackets.

For rocket trajectory points well inside the rotor wake (see Fig. 38 and x_T = 0.025, 0.2, and 0.6 in Fig. 39), the time variation of the mean velocity is relatively small. As the wake boundary intersection ($x_T \cong 0.75$) is approached, the peak-to-peak velocity variation increases (see x_T = 0.68 in Figs. 38 and 39), and near the wake boundary (x_T = 0.73) the peak-to-peak variation increases significantly. In the vicinity of the wake boundary, a v_{z_T} velocity of approximatley 100 fps was measured when the tip vortex passed by the rocket trajectory point. It is possible that somewhat greater velocities might have been measured in this region if the centrifuging effect of the tip vortex didn't limit the number of seedant particles passing through the LV probe volume (discussed below). It is noted that the 100 fps flow velocity is similar in magnitude to the initial 2.75 in. rocket launch velocity.

The cyclic nature of the induced flow at a frequency of once-per-blade-passage (2 per rev) is a direct result of the passage of the tip vortices, and to a lesser extent the inboard vortex sheets, past the trajectory point. The peak downward velocity occurs when the tip vortex is close to the point. Where the magnitude of the velocity is low near the wake boundary (e.g., @ ψ = 90 deg for x_T = 0.73 in Fig. 39), the trajectory passes approximately mid-way between the tip vortices at this rotor position.

The peak-to-peak velocity variation decreases as the rocket trajectory points extend beyond the wake, and as shown in Fig. 39 at x_T = 1.2, the velocity time variation is small. In fact, the variation that did occur was found to be essentially the random turbulence in the ambient air as influenced somewhat by the rotor operation.

As noted above and indicated in Fig. 39 (at x_T = 0.73), the extent of the LV data was somewhat limited in the vicinity of the tip vortices. In Fig. 40 (a) and (b), the number of flow seedant particles that passed through the LV focal point ("probe volume") during the period of time their velocities were being measured at x_T = 0.65 and 0.73 is plotted along with the flow velocity azimuth variation. Although the velocities of 250 to 500 particles were normally measured for each focal point position (rocket trajectory position), it is shown in these figures that the distribution of particles was not always uniform with blade azimuth position. At points away from the wake boundary, the azimuth distribution of seedant particles was fairly uniform. Near the wake boundary, very few particles passed through the "probe volume" when a tip vortex was in close proximity. This is evident near $\psi = 90$ deg in Fig. 40. Although the velocity data generally appeared to be reasonable, even for blade azimuths with few particles, acknowledgement of this particle variation led to the requirement for additional editing of the LV data. Also, for points in the immediate vicinity of the wake boundary, there was a complete absence of particles at some azimuth locations which influenced the accuracy of the peak-to-peak and time-averaged velocities in this region. One possible cause of this problem, the centrifuging of seedant particles by the tip vortices, could possibly be eliminated through the use of smaller, lighter seedant particles. This shall be investigated for the forthcoming wind tunnel test program. In addition, the sensitivity to seedant source location shall be investigated further.

The scaled LV data representing the time-averaged and peak-to-peak flow velocities at the rocket trajectories for all model test configurations and conditions are presented in Figs. 41 to 62. Comparisons of the time-averaged velocity data for various rocket trajectory locations, test configurations, and conditions are presented in Figs. 63 through 70. A discussion of the LV data as presented and compared follows below.

Isolated Rotor LV Data

LV data along a line parallel to and in the plane of rocket trajectories 1 through 4 were taken beneath the centerline of the rotor (at $y_T = 0$) in the early portion of the test program. With the exception of the small tilt angle (rocket attitude = 7 deg), this line represents a radial line at the trajectory elevation below the rotor. Neglecting the generally insignificant contributions of the small slipstream rotation components (v_x and v_y) to the tilted v_{z_T} component, the v_{z_T} velocities were anticipated to be symmetrical* (independent of azimuth and equivalent at equal radial positions). This allowed the LV data at $y_T = 0$ to be transformed to other locations at the same elevation, and thus transformation to the rocket trajectory locations of interest. Plots of the scaled time-averaged and peak v_{z_T} velocity component at the $y_T = 0$ line, rocket trajectory no. 4 ($y = 0.22$ -- transformed and non-transformed data) and rocket trajectory no. 3 (transformed data) are presented in Figs. 41 through 45 for the isolated rotor as operated at the reference condition.

In Figs. 41 and 42, it is noted that the data are incomplete at points near the wake boundary. This is to indicate that the earlier described seedant particle limitation at azimuths corresponding to a close tip vortex passage applied at the noted wake boundary points. The peak-to-peak data, in particular,

---

*It was recognized that flow symmetry applies only to the isolated rotor configuration. The fuselage presence can produce a dissymmetry.

should be considered as approximate for such points. This generally applies to most data taken at the wake boundary, and thus identification of such points will not be repeated in subsequent figures. To compare the repeatability of the LV data, repeat data taken at $y_T = 0$ and transformed to rocket trajectory no. 4 are presented for the vicinity of the wake boundary in Fig. 43. Away from the wake boundary, the data repeats well. However, near the wake boundary, where the large v_{z_T} gradient occurs, the repeatability is not as good. This is attributable to both the seedant limitation mentioned above and unsteadiness of the flow in this region. Deviations were even greater than those of Fig. 43 for some of the other configurations and conditions. Although the deviations should be recognized and their sources investigated further in future test programs, the overall data, when faired and compared, satisfied the objectives of the test program.

In Fig. 63, the fairings of the time-average data of Figs. 41 through 45 are compared to show both the effects of rocket trajectory location and transformation of data from $y_T = 0$ for the isolated rotor. A direct comparison of the transformed LV data fairing from Fig. 42 with the data fairing from Fig. 44, taken directly at rocket trajectory no. 4 ($y = y_T = 0.22$*), is presented in Fig. 63. The general agreement of the data substantiates the transformation procedure discussed above.

A comparison of the faired LV data for $y = 0$ with the transformed data for the various rocket trajectories is also included in Fig. 63. The downflow from the isolated rotor decreases from the outboard to the inboard rocket trajectories, and the difference is the greatest at the launch points ($x_T = 0$). For $y = 0$, an upflow of 2 fps is indicated at $x_T = 0$, and at the rocket launch points downflow velocities of 17 and 27 fps are indicated for trajectory nos. 2 and 3 ($y = \mp 0.16$) and 1 and 4 ($y = \mp 0.22$), respectively. This is attributed to the following. For the $y = 0$ data, $x_T = 0$ lies almost directly beneath the rotor hub center (there $r = x - 0.035$), whereas the rocket launch points are further out radially from the axis of the rotor ($r = 0.164$ and 0.226, respectively). The differences in the rotor downwash at the trajectories decrease as the wake boundary is approached due to the decreasing differential of the radial coordinates. It is also shown in Fig. 63 that the intersections of the wake boundary with the trajectory lines occur slightly further in on the outboard trajectories. This is consistent with the relative geometry of the wake and rocket trajectories as shown for one rotor azimuth in Fig. 16.

---

*The coordinates y and y_T are equivalent and are used interchangeably herein.

Comparisons of the isolated rotor LV data with rotor-fuselage and rotor-fuselage-wing (reference configuration) data are presented in Fig. 64 and discussed below.

Rotor-Fuselage LV Data

Scaled LV data for the rotor-fuselage configuration, as tested at the reference condition, are presented in Figs. 46 and 47. The fairings of the time-average v_{z_T} data are compared with those of the isolated rotor and reference configurations in Fig. 64. Considering the demonstrated insignificance of the effect of the small stub wing at remote points, the data in Fig. 47 were supplemented with data from the reference configuration (with wing) at and beyond the wake boundary.

The comparison of the rotor-fuselage and isolated rotor data in Fig. 64 (a) and (b) indicates that the effect of the presence of the fuselage on the time-average velocity is most significant in the vicinity of the rocket launch points where the fuselage apparently increases the downflow by approximately 10 fps. The fuselage influence decreases as the wake boundary is approached. Some tendency toward an outward shift in the LV data indicative of an outward shift in the wake boundary, produced by the fuselage, is indicated in Fig. 64. A slight shift was anticipated from analysis of the flow visualization data (Fig. 33). Shown in Fig. 64(d) is the effect of rocket trajectory location for the rotor-fuselage configuration.

Rotor-Fuselage-Wing (Reference Configuration/Condition) LV Data

Scaled LV data for the rotor-fuselage wing configuration, as tested at the reference condition, are presented in Figs. 48 through 52. The associated data fairings for this reference configuration/condition are compared in Figs. 64 through 66.

In Fig. 64, the close agreement of the rotor-fuselage-wing and rotor-fuselage data indicates that, with the exception of a small effect in the vicinity of the launch point which approximates the repeatability of the test data, the effect of the wing is negligible. As expected, the flow directly beneath the wing (behind the launch point) is unsteady and influenced strongly by the presence of the wing. This is shown by the LV data in Fig. 71, which were measured at several vertical locations beneath the wing. This reinforces the well recognized concept of mounting the rocket launchers such that the rocket enters the airstream in front of the wing.

LV data for a rocket trajectory (No. 2) on the opposite side of the fuselage from the two primary trajectories (Nos. 3 and 4) of the test program were acquired for the reference configuration/condition. The data are presented in Fig. 50 and compared with the LV data of the primary test trajectories in Fig. 64. In the latter figure, a significant flow velocity difference is indicated between this trajectory on the port side of the model and those on the starboard side. As shown in Fig. 50, this difference is mainly based on two data points, and thus, this finding should be considered preliminary. If future investigation substantiates this finding, it may be concluded that a dissymetry in the flow between the port and starboard sides is produced by the flow interference of the fuselage.

As mentioned earlier, the v_{z_T} velocity component was of primary concern in this test program. However, in order to demonstrate the relatively lower magnitudes of the other velocity components, v_{x_T} and v_{y_T} data were acquired at several rocket trajectory points for the reference configuration/condition. The data are presented in Fig. 51 and compared to the v_{z_T} (AVG) data in Fig. 66. The lower magnitudes for the v_{x_T} and v_{y_T} components are consistent with the theoretical results presented in Ref. 6.

Results for a rocket attitude variation from the reference 7 deg (trajectory No. 3) to 9 deg (trajectory No. 5) are shown in Figs. 52 and 65. Since the rotor operating condition and wake geometry are unchanged, the time-averaged velocity components do not change extensively with the small reorientation in elevation of the rocket trajectory to the time-averaged wake geometry. However, consistent with the results shown in Ref. 6, the velocity time variation in the vicinity of the wake boundary was found to experience a phase shift with rotor azimuth position due to the rotational reorientation of the tip vortices with respect to the trajectory.

LV Data for the Modified Canopy Configuration

Scaled LV data for the modified (flat) canopy configuration as tested at the reference condition are presented in Figs. 53, 54, and 67. As shown in Fig. 67, relative to the reference configuration, the canopy modification tends to increase the time-averaged downflow by up to 5 fps at the portion of the rocket trajectories aside of the fuselage without significantly influencing the wake boundary data.

LV Data for the Modified Thrust Condition

Scaled LV data for the reference configuration tested at the modified thrust condition are presented in Figs. 55, 56, and 68. Although the data were measured at three-fourths the thrust level (C_T = 0.00354) of the reference condition (C_T = 0.00472), the data were scaled to represent the reference full-scale thrust level. This permits a direct comparison of the data with the reference data, as presented in Fig. 68, and thereby a valuation of the scaling procedure. The close agreement of the data, particularly at rocket trajectory No. 4 (y = 0.22), confirms the applicability of the velocity scaling procedure to rotor thrust level.*

In addition to influencing the magnitude of the flow velocities, a change of the rotor thrust coefficient influences the phasing of the velocity time variation as related to rotor azimuth. This is attributable to the change in the rotor wake geometry which results in a reorientation of the wake relative to each rocket trajectory point, as previously shown in the flow visualization results of Figs. 20, 28, and 33. The wake data can be used to estimate the phase increments from one thrust level to another. For example, in the region of the wake boundary where the velocity time variation is of greatest significance,the phasing increment can be derived by relating the increment in tip vortex spacing to the blade azimuth position.

LV Data for the Modified Tip Speed Condition

Scaled LV data for the reference configuration tested at the modified tip speed condition are presented in Figs. 57, 58, and 69. Although the data were measured at three-fourths the tip speed (373 fps) of the reference test condition (497 fps), and one-half the full-scale AH-1G value (746 fps), the data were scaled to represent the full-scale tip speed. This permits a direct comparison of the data with the scaled reference condition data, as presented in Fig. 69, and thereby a valuation of the velocity scaling procedure. Considering that the velocity scaling factor of 2.0,used for the modified tip speed condition, results in increments in v_{z_T} (AVG) ranging from 8 to 36 fps, and that agreement of the scaled data is within 0 to 7 fps, the following assessment is made. The flow velocity scaling procedure for rotor tip speed generally applies as has previously been demonstrated in other experimental and theoretical programs (described in Ref. 12). However, the low value of the modified tip speed (373 fps) and/or the presence of the fuselage resulted in a somewhat greater difference in the scaled time-averaged velocities than anticipated, particularly at the inboard rocket trajectory (y = 0.16). This may be related to the unanticipated dissimilarty between the

---

*The small difference at rocket trajectory No. 3 (y = 0.16) indicates a possible small deviation from the scaling procedure due to the proximity to the fuselage. However, it is recognized that the difference, approximately 3 fps, is about the extent of the repeatibility of the LV data.

wake geometry of the two rotor blades evident in the schlieren flow visualization data described earlier and presented in Fig. 21. Although further investigation of this observation is required, it is conjectured that the measured differences of the scaled data are associated with the low tip speed value, and that the scaling procedure is more accurate within the higher tip speed range between the reference test condition and full-scale operation.

Since, ideally, the rotor wake coordinates (nondimensionalized by R) are independent of tip speed for a specific rotor design and thrust coefficient, there is no phase shift in the time variation of the airflow between different tip speed conditions. Of course, dissimilariities due to vortex unsteadiness, far wake instability, or fuselage influence would cause some phase differences. The similar mean wake characteristics between the reference and the modified tip speed conditions were shown in Fig. 33. The effect of the inter-blade vortex dissimilarity shown in Fig. 21 was evident in producing a related dissimilarity in the LV time history data.

LV Data for In-Ground-Effect Conditions

Scaled LV data for the reference configuration tested at the three in-ground-effect (IGE) conditions are presented in Figs. 59 through 62 and Fig. 70. The three conditions simulate skid heights above ground of 18.5, 10 and 0 ft. The elevations of the skids and rotor, nondimensionalized by the rotor radius, are included in Table 3. No outstanding differences are noted between the peak-to-peak velocity increments of like points for the IGE and OGE conditions. However, substantial differences are observed in the time-averaged data.

The fairings of the time-averaged data are compared with the reference OGE condition in Fig. 70. Inside the rotor wake, the downflow at the rocket trajectories is shown to decrease with decreasing height. Also, the outward shift of the velocity profile with decreasing height is indicative of the wake expansion observed in the IGE flow visualization data. The flow characteristic variations with ground height are nonlinear. The airflow near the launch point of rocket No. 3 ($y = 0.16$) is shown to be most effected between OGE and the 18.5 ft skid height condition. The velocities in the vicinity of the wake boundary are most effected during operation in very close proximity to the ground (i.e., skid heights between 10 ft and 0 ft). The latter results in the retention of the high time-average downflow of approximately 60 fps near the wake boundary until the skid height becomes less than 10 ft. However, for skid heights below 10 ft, the reduced effect on the rocket of the lower downflow is somewhat compromised by the longer time period the rocket is in the wake downflow.

Overall, the results indicate that a rocket will experience relatively lower downflow velocities for in-ground-effect operation, and thus should be less effected by the rotor wake.

WIND SENSOR LV DATA

LV data for the seven wind sensor locations, described previously, are presented in Figs. 72 through 76. As shown in Fig. 5, wind sensor location Nos. 1 through 5 are aside the canopy, and wind sensor location Nos. 6 and 7 are in front of the fuselage nose. The wind sensor coordinates were presented in Table 5. The velocity components measured at the wind sensor locations were in the vertical (v_z) and horizontal (v_x and v_y) directions.

LV Data for Wind Sensor Locations Aside of Canopy

In Fig. 72, the scaled time-averaged downflow at wind sensor location Nos. 1 through 5 is presented for the isolated rotor, reference, and modified canopy configurations as operated at the reference condition. Comparison of the downflow at the primary location No. 4 and its counterpart, No. 1, on the opposite side of the fuselage indicates close agreement for each configuration. The generally linearly increasing downflow from location Nos. 2 to 5 corresponds to the general hovering flow velocity pattern. That is, the downflow increases as the wake boundary is approached. Consistent with the rocket trajectory data, the presence of the fuselage and the modified canopy each add an increment to the downflow. The wind sensor must be located at least as far out as location No. 5 before the fuselage effects become small. The flow velocity at location No. 2 departed from the general trend due to its extreme close proximity to the corner of the modified canopy. Lastly, comparing the magnitudes of the downflow between that at the wind sensor elevation and that at points directly beneath on inboard rocket trajectory Nos. 2 and 3 (from prior figures), indicates a significantly lower downflow velocity (approximately 10 fps) at the wind sensor elevation for all configurations in Fig. 72. It will be necessary to account for this when the calibration of wind sensor measurements to acquire representative flow velocities at rocket trajectories is attempted.

The LV data for the time-averaged lateral velocity component is presented in Fig. 73 for the same configurations. The flow direction for all measurements is in the direction of the port side of the aircraft (negative v_y). This is consistent with the anticipated direction of the lateral component induced by the circulation of the inboard wake. Also, the magnitude of the sideflow, for the fuselage included configurations, differs on opposide sides of the fuselage.

The wind sensor LV data for the modified thrust condition, presented in Fig. 74, has been scaled for direct comparison with the reference condition data. Similar to the rocket trajectory results, the general agreement of the data indicates that the thrust coefficient scaling procedure is valid.

The wind sensor LV data for the IGE (skid height = 10 ft) condition is compared with the reference OGE data in Fig. 75. As was observed in the rocket trajectory data, the IGE velocity components are much lower in magnitude than the OGE values.

LV Data for Wind Sensor Locations in Front of the Fuselage Nose

The scaled, time-averaged, vertical and longitudinal flow velocity components at wind sensor locations 6 and 7 are presented in Fig. 76. As shown, these wind sensor locations are near the central line at $y = 0$ and parallel to the rocket trajectories for which LV data for the isolated rotor were previously presented in Fig. 41. The vertical component data of the wind sensor compares favorably with the data of the central line included in Fig. 76. Data were also measured at the wind sensor locations without the fuselage and included in Fig. 76. These data also indicate that the wind sensor locations are sufficiently forward to be away from the major flow interference of the fuselage. However, the selected wind sensor locations are undesirable for they are in the immediate vicinity of the rotor wake boundary for hover operation.

Assessment of Wind Sensor Locations for Hovering Flight

Of the tested wind sensor locations, the location aside and removed from the fuselage canopy by 18 percent of the rotor radius (location No. 5) was found to be most favorable for avoiding fuselage aerodynamic interference and the wake boundary. It is recognized that the support required for placement this far out would be of concern, particularly for forward flight drag. If reducing the distance is considered a serious compromise, placement ahead of the wing tip may be preferable (providing it is sufficiently removed from the aerodynamic interference of the rocket launcher).

THEORETICAL RESULTS AND COMPARISON WITH TEST DATA

Available hovering rotor theory was applied for the reference and modified thrust conditions to compare predicted flow velocities with the LV data, and to assess the applicability of the model test results and associated scaling procedures to simulate full-scale airflow.

BRIEF DESCRIPTION OF THEORETICAL METHODS

The UTRC Prescribed Wake Hover Performance Analysis and a Sikorsky Aircraft derivative, the Circulation Coupled Hover Analysis Program (CCHAP), were used in this investigation. Brief descriptions of these computer analyses are presented below. More details on the contents, assumptions and applications of the methods are contained in Refs. 12 through 16 and 21. The Prescribed Wake Hover Performance Analysis is a component of the Rotorcraft Wake Analysis described in Refs. 12 and 13. This analysis was applied using a generalized wake to predict the rocket trajectory airflow presented in Refs. 6 and 7.

The function of the UTRC Prescribed Wake Hover Performance Analysis is to compute the circulation and induced velocity distributions along the rotor blades and in the wake that are compatible with a prescribed set of blade section operating conditions and a prescribed wake geometry. Each blade is represented by a segmented lifting line, and the wake is represented by a finite number of segmented vortex filaments trailing from the blade segment boundaries as shown in Fig. 15. The fundamental relations of blade circulation to lift coefficient, angle of attack, blade motions, control settings, induced velocity, and wake geometry are used in this analysis. Once the circulations are computed, the velocities induced at and away (e.g., at rocket trajectories) from the rotor disc by the bound and trailing vorticity of the rotor are determined through application of the Biot-Savart law which relates the induced velocity at a point in space to the circulations and wake geometry. The induced velocity is proportional to the summation of the products of the circulation strength and the geometric influence coefficient of each element of vorticity in the rotor-wake system. The geometric coefficient is related only to the relative geometry between a wake element and the point at which the induced velocity is being computed. Since the wake geometry is prescribed, the wake may vary from an undistorted wake model to a complex experimental or distorted analytical wake model with tip vortex roll-up and vortex core effects mathematically modeled. The experimental model rotor wake was used for this investigation.

The Circulation Coupled Hover Analysis Program (CCHAP) internally defines the hovering rotor wake geometry through coupling of the wake geometry solution to the blade loading solution. This analysis is described in Ref. 21, and has demonstrated good correlation with the hover performance test data of many rotors.

TIME-AVERAGED FLOW VELOCITIES

The theoretical methods are for an isolated rotor. Although some progress has been made for forward flight to include the influence of the fuselage in the Rotorcraft Wake Analysis, as described in Refs. 21 and 24, methodology for the fuselage aerodynamic interference has not yet been included for hovering flight. Thus the methods were first applied, in this investigation, to the isolated rotor configuration. The scaled time-averaged v_{z_T} velocity component predicted at rocket trajectory Nos. 3 and 4 are compared with the scaled model test data for the isolated rotor in Figs. 77 and 78. The model rotor wake geometry (Figs. 32 and 34) was used in the Prescribed Wake Analysis for this application. The favorable correlation indicates the capability of the analysis to predict the rotor time-averaged flow when the associated wake geometry is known.

Also included in Fig. 77 are the theoretical predictions from both methods for the full-scale AH-1G rotor using the prescribed model rotor wake and the circulation coupled wake, respectively. The small differences between the velocities of the model and full-scale rotors, predicted by the prescribed wake analysis, are due to differences in the operational airfoil data range (differences in Mach No. and Reynolds No.), the small differences in the rotor design characteristics described earlier (Table 1), and model tip speed scaling.

Similar comparisons for the modified thrust condition are presented in Fig. 79. It is noted that for this condition the model LV data were acquired with the fuselage and wing, whereas the theory is for the isolated rotor. It is also noted that the results in this figure are for the reduced thrust coefficient, (i.e., they have not been scaled to the reference thrust coefficient). The degree of correlation is again generally favorable and similar to that of the reference condition.

Comparisons of the model rotor theoretical results with test data for the refence configuration (rotor-fuselage-wing), at rocket trajectory Nos. 2 and 3 on opposite sides of the model, are presented in Fig. 80. Differences which are mainly attributable to the presence of the fuselage are evident. Although the theoretical results for the isolated rotor predict no significant velocity difference on opposite sides, differences exist in the test data.

As discussed earlier, this flow dissymmetry is based on a limited amount of data and should be investigated further.

Comparisons similar to those of Fig. 80, except that the data are for the other two velocity components, are presented in Fig. 81. For these components the theory predicts small velocity magnitudes similar to the test data.

TIME-VARIANT FLOW VELOCITIES

The time variation of the scaled v_{z_T} flow velocity component, at several points on rocket trajectory No. 4, are presented in Fig. 82. Shown are comparisons of the theoretical predictions, based on the prescribed model rotor wake, with the mean LV data corresponding to specific rotor azimuth positions of the isolated rotor. Away from the wake boundary (i.e., between x_T = 0 to 0.6 and 1.0 to 1.4), the time variation is small as is evident in both the theory and test results. The theory predicts the 2 per rev character and amplification of the peak-to-peak velocity increments near the wake boundary.

The time variation of the velocity components is mostly due to the periodic passage of the tip vortices past the point on the rocket trajectory. The relation between the phasing of the peak velocities and the relative positioning of the tip vortex geometry with the points where the rocket trajectories intersect the forward wake boundary may be derived by relating the azimuth locations of the peak velocities to the orientation of the tip vortices. The more negative peak values generally occur when a tip vortex passes closest to the point, and the more positive peak values generally occur when the point is approximately midway between two successive tip vortices. The greatest magnitudes of velocity correspond to the more negative peak values of the point just inside the wake boundary produced by the presence of the tip vortex. Small geometric increments of the tip vortex can produce large velocity phase shifts. This is recognized when it is considered that the tip vortex spacing in the vicinity of the rocket is 0.18R for the reference condition. Since this corresponds to an azimuth cycle of 180 deg, each one percent displacement of the tip vortex corresponds to a 10 deg phase shift. This indicates the importance of accurately representing the wake if the time variation of the instantaneous velocities at the rocket trajectory are of interest.

The phase differences at x_T = 0 and x_T = 0.7 were found to be due to the high sensitivity of the results to small changes in the wake geometry data, and both were essentially accountable and correctable within the experimental scatter in the experimental inboard vortex sheet and tip vortex geometry, respectively. That is, a 15 percent change of the inboard wake transport velocities (see Fig. 34) in the theory, reoriented the wake to the rocket launch point (x_T = 0) such that the phasing was in agreement to that of the LV data. Similarly, a change in the input wake parameters which moved the tip vortex coordinates (Fig. 32) down by $\Delta z_{TIP} = -0.015$ in the vicinity of the vortex-rocket trajectory intersection ($\psi_w \cong 400$ deg) was sufficient to produce a 15 deg phase shift toward the test data. It was thus concluded that the analysis is capable of predicting the induced velocity time variation at the rocket trajectories. However, the degree of correlation is very dependent on an accurate wake geometry representation.

The theoretical time variations of the v_{z_T} velocity component for the model rotor and the full-scale AH-1G rotor are presented in Figs. 83 and 84. The phase differences in the vicinity of the wake boundary ($x_T = 0.7$ and 0.8) are primarily due to the differences in coning angle between the model and full-scale rotor (0.3 and 2.75 deg, respectively) which produces an azimuthal reorientation of the tip vortices relative to the rocket trajectory. Additionally, the peak-to-peak velocity magnitude is predicted to be higher at $x_T = 0.7$ for the full-scale rotor. This is also due primarily to the small displacement of the rotor tip vortex relative to this point near its intersection with the rocket trajectory caused by the coning angle increment. Since, the scaled wake circulation strength was predicted to be the same for the model and full-scale rotors, it was concluded that this amplitude difference at $x_T = 0.7$ is of little consequence. That is, considering the extreme sensitivity of the peak velocities to small changes in location near the wake boundary, the theoretical peak-to-peak amplitudes would agree following a small shift of the rocket trajectory point of the model rotor (e.g., to $x_T \cong 0.71$).

More significant is the fact that the theory predicts a somewhat larger peak velocity near the tip vortex than that indicated by the LV data (e.g., 117 fps in Fig. 84 vs 97 fps in Fig. 42). This may be attributable to the high sensitivity of the theoretical results in close proximity to a tip vortex to the input core size and analytical vortex representation. However, the previously discussed seedant limitation and use of the mean velocity over an 18 deg azimuth interval, may result in reducing the measured peak velocity of the LV data from the absolute instantaneous peak at the intersection of the tip vortex and rocket trajectory.

SUGGESTED PROCEDURES FOR APPLYING AIRFLOW VELOCITY RESULTS

At each point in time along their trajectories, the rockets are affected by the instantaneous induced velocity components associated with the particular rotor position at that instant of time. Thus, to be accurate when performing the rockect trajectory calculations, the procedure should be to determine the rotor position for each point along a trajectory and use the corresponding induced velocity components. However, the problem arises that the rotor positions are not known due to the fact that the firing time is currently determined by the gunner irrespective of rotor position. Without rotor position synchronization, the correspondence of rocket position with rotor position, is unknown. However, to evaluate the impact of this problem, the following suggested procedures from Ref. 6 are repeated for the rocket trajectory calculations:

1. Perform the rocket trajectory calculations using the time-averaged induced velocity components at each point.
2. Perform the calculations assuming that the rockets pass in close proximity to a tip vortex. In accordance with this assumption, select the peak velocity components (emphasize v_{z_T} in the selection) at the trajectory point nearest and inside the wake boundary. Using an assumed rocket velocity (e.g., the launch velocity of approximately 100 fps), determine the time increment and corresponding rotor rotation interval between points along the trajectory. Based on the rotor rotation interval, determine the rotor positions for each point along the trajectory and interpret the flow velocity data accordingly to obtain the velocity components at each point to be used in the calculation of the rocket trajectory.
3. Perform the calculations using instantaneous velocities corresponding to a few other selected rotor position sequences.

Using the above procedures, the maximum and minimum deviations of the rocket trajectories based on the instantaneous induced velocities relative to the trajectories based on the time-averaged velocities should generally result. With these results, the range of possible trajectories produced at indiscriminate firing times would be established.

CONCLUSIONS

The following conclusions are based on the application of model test results to a full-scale hovering helicopter. Where values or locations are indicated, they are representative of the full-scale AH-1G helicopter.

1. The flow velocities of the hovering helicopter simulation model, measured with the laser velocimeter, substantiated the general airflow characteristics at rocket trajectories of the AH-1G helicopter predicted in the previous theoretical investigation.*

2. The application of laser velocimetry to measure hovering rotor airflow was successful. LV proved to be a valuable technique for acquiring both the time-average and time variation of flow velocity components at rocket trajectory and wind sensor locations inside and outside of the rotor wake.

3. Flow visualization techniques (smoke and Schlieren) were valuable to identify wake geometry, wake stability, and vortex core size in the vicinity of the rocket trajectory and wind sensor locations. The influence of the fuselage, modified canopy, thrust level, tip speed, and ground effect on wake geometry, determined from analysis of the flow visualization data, were useful for interpretation of the flow velocity data.

4. The total and separate influence of each of the aircraft components (rotor, fuselage, modified canopy, and wing), and significant operating condition parameters (rotor thrust, tip speed, and ground effect) on the airflow influencing rocket trajectories were successfully measured.

5. The presence of the fuselage produces a small but possibly significant effect on rocket trajectory airflow. On the starboard side of the aircraft, the fuselage effect is most noteworthy in the vicinity of the rocket launch points where it contributes additional downflow. A possible fuselage produced flow dissymmetry, which requires further verification, was indicated in a comparison of LV data from opposite sides of the fuselage. The presence of the stub-wing does not significantly add to the aerodynamic interference of the fuselage at rocket trajectories. The modified flat-sided canopy of the AH-1G produces an additional downflow increment along the portion of the rocket trajectories aside of the fuselage.

---

*Primary airflow characteristics are listed in the conclusions from the theoretical investigation in Appendix B.

6. The effects of rotor thrust and tip speed increments on the rocket trajectory airflow are scalable using momentum induced velocity as the scaling parameter. For large tip speed increments, a possible deviation from the scaling procedure at points near the fuselage remains to be substantiated through further investigation.

7. Operation near the ground results in a significant reduction in the magnitude of the downflow along the extent of rocket trajectories in the rotor wake. For simulated AH-1G skid heights above ground of less than approximately 20 ft, time-averaged upflow was measured in the vicinity of the launch point of an inboard rocket trajectory.

8. In the rotor wake, consistent with rotor hovering downflow patterns, the downflow at the outboard rocket trajectory is generally greater than that of the inboard trajectory.

9. Of the three velocity components, the downward component normal to the rocket trajectory is substantially larger in magnitude than the others.

10. A rocket attitude variation of 2 deg does not significantly influence the time-averaged flow velocities at the rocket trajectory, but does result in a phase shift of the time variant velocities relative to rotor azimuth position.

11. The airflow inside the rotor wake is fairly steady; however, large induced velocity variations with small increments of distance and time occur at points on a rocket trajectory near a wake boundary. These variations are caused by the close passage of the tip vortices. The magnitude of the mean time-variant downflow associated with each rotor azimuth position is generally within approximately ±10 fps of the time-average value for points on the rocket trajectories within the rotor wake. This peak-to-peak variation increases substantially (e.g., ±30 fps) in the vicinity of the wake boundary. The RMS deviations from the mean downflow values for specific rocket trajectory points and rotor azimuth positions, representative of flow unsteadiness, are generally within 10 fps, away from the wake boundary.

12. Of the tested wind sensor locations, a location aside and removed from the fuselage canopy by 18 percent of the rotor radius, was found to be most favorable for avoiding fuselage aerodynamic interference and the wake boundary. If the distance must be compromised, based on forward flight drag considerations, placement ahead of the wing tip may be preferable.

13. Neglecting fuselage interference effects, the results of the limited correlation study indicate that the UTRC Prescribed Wake Hover Performance Analysis can accurately predict the airflow characteristics at rocket trajectories. The time-averaged downflow within the rotor wake was generally predicted within 5 fps for the isolated rotor. (Fuselage aerodynamic interference is not currently included in the analysis.) The capability of the analysis to accurately predict the time-variation of the flow velocities is dependent on the accuracy of the wake geometry.

14. The model test data for rocket trajectory and wind sensor flow velocities can be appropriately scaled to represent full-scale aircraft operating conditions (thrust level and tip speed). Refinements for the full-scale AH-1G representation, to account for remaining differences in configuration design, airfoil characteristics (Reynolds number, Mach number), and coning angle can be determined using predicted increments between model and full-scale theoretical results as a guide. Theoretical indications are that the effects of the latter scaling differences are generally small, particularly for time-averaged velocities and the magnitudes of the time variant velocities. Any influence on the positioning and/or timing of the tip vortices, such as blade coning differences or aircraft and wake motions associated with full-scale helicopter operation, would result in a phase shift in the flow velocity *time variation* at a rocket trajectory or wind sensor location. Corrections for phase shifts associated with coning angle can be determined. The determination of corrections for random shifts associated with ambient winds, helicopter motion, or wake unsteadiness would be much more difficult, if not impractical.

RECOMMENDATIONS

1. As planned, the effect of the rotor wake induced velocities determined in this investigation on the rocket trajectories should be calculated using the Army rocket dynamic response analysis and the procedures described herein. Using these procedures, the deviations of the rocket trajectories can be determined, and the degree of accuracy required of the induced effects for rocket trajectory calculations would be established.

2. Analysis of the time-variant flow velocity data to present and interpret the results for all configurations and conditions relative to rotor azimuth position was beyond the scope of the investigation reported herein. The results of the above recommended aeroballistics investigation should be used to assess the requirement for additional data analysis in the time history format (in addition to the time-averaged and peak-to-peak format presented).

3. Considering the demonstrated usefulness of laser velocimetry for rocket trajectory flow measurements, the model helicopter experimental program is being extended to apply the LV technique to low speed forward flight conditions in a wind tunnel. It is suggested that several tasks beyond the scope of the planned program be considered, such as the testing of yawed flight, sideward flight, in-ground-effect, and gust conditions.

4. Additional hover testing to further investigate the extent of the flow dissymmetry produced by the fuselage is recommended.

5. Considering the favorable correlation of the hovering wake theory for the isolated rotor, and the usefulness of the theory for interpretation of the model data for full-scale aircraft, it is recommended that analytical refinements be included to improve the scope and accuracy of the analysis. Recommended refinements include provisions for ground effect, vertical climb, and fuselage aerodynamic interference. Wake modeling refinements should be incorporated as guiding experimental data become available.

6. Application and evaluation of hovering rotor wake theory for other aircraft (for example, AAH and UTTAS) over a wide range of operating conditions, and generalization of the predicted flow velocities is recommended.

7. Flow velocity data for full-scale aircraft should be acquired, at least for a limited number of flow field points and test conditions, to compare with the model test data and to determine the relative flow unsteadiness between full-scale operation and model testing in a controlled environment.

8. The model testing, laser velocimetry, and flow visualization techniques, as demonstrated in combination in this investigation for the specific rocket/wind sensor application, are recommended for use in a more general investigation of hovering rotor aerodynamics and associated performance. In addition to further defining fundamental characteristics, such an experimental program would provide comprehensive data for validation of theory and the further generalization of the aerodynamics and performance of hovering rotors.

LIST OF REFERENCES

1. Bergman, R.: Helicopter Air Flow Analysis at Hover and Low Air Speeds. Memo from U. S. Army Missile Command to the U. S. Army Aviation Systems Command, April 21, 1975. (Enclosed as Appendix A).

2. Proceedings of the Conference on the Effects of Helicopter Downwash on Free Projectiles. U. S. Army Aviation Systems Command, St. Louis, MO., November 1975.

3. Marner, G. R.: The Effects of Helicopter Downwash on Free Projectiles, Introduction and Assessment of the Problem. Proceedings of the Conference on the Effects of Helicopter Downwash on Free Projectiles, November 1975.

4. Morse, H. A.: Some Practical Aspects of Rotor Wake Effects on Rocket Accuracy. Proceedings of the Conference on the Effects of Helicopter Downwash on Free Projectiles, November 1975.

5. Bergman, R. : Interaction of Air Flow and Helicopter Characteristics on the 2.75 Inch Rocket System. Proceedings of the Conference on the Effects of Helicopter Downwash on Free Projectiles, November 1975.

6. Landgrebe, A. J. and T. A. Egolf: Prediction of Rotor Wake Induced Flow Velocities Along the Rocket Trajectories of an Army AH-1G Helicopter. United Technologies Research Center, Picatinny Arsenal Technical Report 4797, U. S. Army Picatinny Arsenal, Dover, New Jersey, March 1975.

7. Landgrebe, A. J. and T. A. Egolf: Rotor Wake Induced Flow Along Helicopter Rocket Trajectories. Proceedings of the Conference on the Effects of Helicopter Downwash on Free Projectiles, November 1975. (Summary, Conclusions, and Recommendations enclosed as Appendix B).

8. Wasserman, S., and R. Yeller: Preliminary Analysis of the Effect of Calculated Downwash Distributions on the Flight Performance of the 2.75 Inch Rocket. Proceedings of the Conference on the Effects of Helicopter Downwash on Free Projectiles, November 1975.

9. Jenkins, B. Z.: The Perturbed Flow Environment About Helicopters and Its Effect on Free Rockets. Proceedings of the Conference on the Effects of Helicopter Downwash on Free Projectiles, November 1975.

REFERENCES (Cont'd)

10. Boirun, B. H. and E. E. Bailes: AH-1G Helicopter Flow Field Survey. Proceedings of the Conference on the Effects of Helicopter Downwash on Free Projectiles, November 1975.

11. Landgrebe, A. J. and B. V. Johnson: Measurement of Model Helicopter Rotor Flow Velocities with a Laser Doppler Velocimeter. Journal of American Helicopter Society, Vol. 19, No. 3, July 1974.

12. Landgrebe, A. J. and T. A. Egolf: Rotorcraft Wake Analysis for the Prediction of Induced Velocities. United Technologies Research Center, USAAMRDL Technical Report 75-45, U. S. Army Air Mobility Research and Development Laboratory, Fort Eustis, Virginia, January 1976.

13. Landgrebe, A. J. and T. A. Egolf: Prediction of Helicopter Induced Flow Velocities Using the Rotorcraft Wake Analysis. Proceedings of the 32nd Annual National Forum of the American Helicopter Society, March 1975.

14. Landgrebe, A. J.: An Analytical and Experimental Investigation of Helicopter Rotor Hover Performance and Wake Geometry Characteristics. United Aircraft Research Laboratories, USAAMRDL Technical Report 71-24, Eustis Directorate, U. S. Army Air Mobility Research and Development Laboratory, Fort Eustis, Virginia, June 1971, AD728835.

15. Landgrebe, A. J.: The Wake Geometry of a Hovering Helicopter Rotor and Its Influence on Rotor Performance. Journal of the American Helicopter Society, Vol. 17, No. 4, October 1972 (Also preprint No. 620, 28th Annual National Forum of the American Helicopter Society, May 1972).

16. Jenney, D. S., J. R. Olson and A. J. Landgrebe: A Reassessment of Rotor Hovering Performance Prediction Methods. United Aircraft Corporation, Journal of the American Helicopter Society, Vol. 13, No. 2, April 1968, pp. 1-26.

17. Bellinger, E. D.: Experimental Investigation of Effects of Blade Section Camber and Planform Taper on Rotor Hover Performance. United Aircraft Research Laboratories, USAAMRDL Technical Report 72-4, Eustis Directorate, U. S. Army Air Mobility Reserach and Development Laboratory, Fort Eustis, Virginia, March 1972, AD743232.

REFERENCES (Cont'd)

18. Landgrebe, A. J. and E. D. Bellinger: Experimental Investigation of Model Variable-Geometry and OGEE Tip Rotors. AHS Paper No. 703, 29th Annual National Forum of the American Helicopter Society, May 1973.

19. Landgrebe, A. J. and E. D. Bellinger: A Systematic Study of Helicopter Rotor Stall Using Model Rotors. AHS Paper No. 804, 30th Annual National Forum of the American Helicopter Society, May 1974.

20. Landgrebe, A. J. and M. C. Cheney: Rotor Wakes - Key to Performance Prediction. AGARD-CP-111, AGARD Conference Proceedings No. 111 on Aerodynamics of Rotary Wings, Fluid Dynamics Panel Specialists Meeting, September 1972 (Also, paper presented at the Symposium on Status of Testing and Modeling Techniques for V/STOL Aircraft, Mideast Region of the American Helicopter Society, October 1972).

21. Landgrebe, A. J., R. Moffitt, and D. R. Clark: Aerodynamic Technology for Advanced Rotorcraft. Journal of the American Helicopter Society, Part I: Vol. 22, No. 2, April 1977; Part II: Vol. 22, No. 3, July 1977.

22. Landgrebe, A. J. and E. D. Bellinger: An Investigation of the Quantitative Applicability of Model Helicopter Rotor Wake Patterns Obtained From a Water Tunnel. United Aircraft Research Laboratories, USAAMRDL Technical Report 71-69, Eustis Directorate, U. S. Army Air Mobility Research and Development Laboratory, Fort Eustis, Virginia, December 1971, AD739946.

23. Landgrebe, A. J.: An Analytical Method for Predicting Rotor Wake Geometry. Journal of the American Helicopter Society, Vol. 14, No. 4, October 1969. (Also, AIAA Paper No. 69-196, AIAA/AHS VTOL Research, Design and Operations Meeting, Atlanta, Georgia, February 1969.)

24. Sheehy, T. H.: A Simplified Approach to Generalized Helicopter Configuration Modeling and the Prediction of Fuselage Surface Pressures. Paper presented at the National Symposium on Helicopter Aerodynamic Efficiency, American Helicopter Society - Northeast Region, March 1975.

APPENDIX A

DEPARTMENT OF DEFENSE UNITED STATES OF AMERICA

DEPARTMENT OF THE ARMY
HEADQUARTERS UNITED STATES ARMY MISSILE COMMAND
REDSTONE ARSENAL, ALABAMA 35809

APR 21 1975

MEMO FOR RECORD

SUBJECT: Helicopter Air Flow Analysis at Hover and Low Air Speeds

1. Reference is made to United Aircraft Research Laboratories[1] Final Report "Prediction of Rotor Wake Induced Flow Velocities Along the Rocket Trajectories of an Army AH-1G Helicopter," dated March 1975.

2. The US Army Training and Doctrine Command (TRADOC) has determined that the appropriate attack helicopter tactic for the mid-intensity or mid-east battle scenarios will be low level flight, known as "Terrain Flying." The need to engage targets with sophisticated air defense elements results in a major concern with aircraft survivability. Maximum survivability is achieved by engaging targets at the maximum effective range of the helicopter weapon, while minimizing closure on the target during the engagement. These tactical requirements have been instrumental in formulating aircraft/weapon specifications which place major emphasis on firing rockets, cannon, and missiles from a hover as a worst case condition. The most stringent hover technique involves the capability to start from a low level hover behind a masking terrain feature, "pop-up" with some minimum vertical rate of climb, engage the target, and retain sufficient aircraft performance to recover from a vertical rate of descent just in case no portion of the ordnance load is expended.

3. Ordnance which can be fired with initial high velocities, such as cannon rounds, or which can be given terminal guidance, such as a missile, are the least affected by local air flow in the hover, pop-up or low air speed regimes. Since the free aerial rocket has a relatively low initial velocity and receives no terminal guidance, it is significantly affected by the helicopters rotor down wash during these maneuvers. The Advanced Attack Helicopter (AAH) specifications call for a major portion of the mission time to be conducted at the hover. However, the AAH Primary weapons are considered at this time, to be the TOW missile and 30 mm cannon; therefore, the 2.75 Inch Rocket System performance at the hover has not been a major concern.[2] The performance of helicopters during these maneuvers has been the main concern of the aeronautical laboratories and major research is being pursued to determine the parameters of hover dynamics. Relatively little emphasis has been placed on the effects on weapon performance during these same maneuvers. Although the AAH and the AH-1 helicopters are expected to have at least some of the major components of rocket fire control, very little

applied research is being pursued to develop a solution to the user requirement for an effective aircraft/weapon system at low air speed.

4. This Office sponsored the 2.75 Inch Rocket/AH-1G System Baseline Accuracy Test which was a detailed analysis of the helicopter/rocket system performance at airspeeds of 90 and 120 knots. The major conclusion of the test was that helicopter rocket fire control was needed to accomplish a significant improvement in system effectiveness. The lack of appropriate instrumentation was a prime factor in not acquiring the same type of data for hover and low forward air speeds. Currently, instrumentation has still not advanced sufficiently to provide adequate experimental data on airflow under the Cobra rotor disc throughout the weapon launch envelope at low airspeeds. Discussions with the aeronautical laboratories revealed that no definitive data existed on the area of interest. Rocket ballistic simulations had to be performed utilizing assumed data generated with standard momentum theory based on the size of the rotor and gross helicopter weight. Airflow perturbations within the rotor down wash were unknown.

5. After determining that there existed a large gap in data on airflow in the rocket launch envelope at low airspeeds, the 2.75 Inch Rocket Project Manager's Office took advantage of a proposal from United Aircraft Research Laboratories (UARL) to acquire basic information utilizing computer simulation. Mr. Jack Landgrebe and his associates at UARL have exhibited considerable expertise and dedication in deriving the degree of data presented in the reference report, particularly when one considers the size of the Picatinny Arsenal contract. The computer simulation techniques developed by UARL are unique in the capability to provide instantaneous and time-averaged airflow vectors in both distorted and undistorted rotor wakes.

6. Mr. Saul Wasserman[3] of the Aeroballistics section at Picatinny Arsenal is currently following through with the data presented in the report to calculate the effects of the airflow on the rocket ballistic trajectory. The rocket will normally be influenced by the passage of approximately two rotor blades during its exit from the weapon launch envelope. During preliminary simulations with a six degree of freedom rocket ballistic simulation, it was found that at ranges below 2000 meters, a variation in impact distance could be detected as a function of the blade position and instantaneous velocities depicted in Fig. 15 of the reference report. At ranges greater than 2000 meters, the rocket was not influenced sufficently by variation in firing time to be detected in changes in the simulated ground impact. In actual hover firing tests at Yuma Proving Ground in 1974, the 2.75 Inch Rocket achieved a mean point of impact at 4500 meters while at 30 feet above target with a three degree nose-up angle. Firings from 90 knots at 300 feet required a 7 degree climb to achieve 4000 meters. The rocket is highly stable and weathervanes up into the rotor down wash, therefore, the effect on the trajectory of the rocket is significant.

7. As mentioned in the report, a number of the assumed variables have yet to be confirmed and refinement will probably have some effect on the performance characteristics of the helicopter/rocket system. It must be noted that these simulations are conducted at specific airspeeds of 0, 15 and 30 knots, without representation of fuselage effects. A review of the report will result in the impression that the airflow under rotor is very dynamic and velocity predictions at any one point are not necessarily representative of the total launch envelope. An additional consideration is that in the tactical situation the helicopter will rarely be in a stationary hover without a velocity vector in some direction.

8. New techniques of airflow measurements, such as Laser Doppler Velocimeter (LDV) have been developed in recent years. United Aircraft is capable of LDV measurement, both on a hover stand and in wind tunnels. The advantage of the LDV technique is the ability to measure airflow from a remote position, thereby, eliminating the disturbance effects normally involved with mounting a sensing device directly in the airflow. Ultimately, the LDV may become a tool for helicopter instrumentation and be flight qualified for full scale flight research.

9. The reference report is viewed as only the initial step in achieving data to properly evaluate the characteristics of helicopter/rocket systems when fired at a hover. A number of recommended tasks to continue development of airflow simulation and data acquisition techniques are as follows:

a. An AH-1G flight test to accurately determine the rotor control, flapping and disc angles assumed in Table I of the reference report.

b. A Laser Doppler Velocimeter (LDV) survey of a scale model of each helicopter gunship to determine the optimum location for an operational fire control relative wind sensor on each aircraft.

c. A LDV survey of the weapon launch envelope of each helicopter gunship at hover and forward airspeeds to provide experimental data and analysis to support the findings of the reference report.

d. Determine the feasibility of packaging the LDV concept so that it can be used as instrumentation on-board a gunship for detection of airflow characteristics under actual flight conditions.

e. Further development of airflow simulation techniques to include fuselage configuration effects and the resultant effect in the weapon launch area.

f. Adaptation of the airflow simulation to determine flight dynamics during the pop-up maneuver.

g. Initiation of 6.2 and 6.3 research into instrumentation and operational air data sensor devices.

h. Funding for aeroballistics analysis of the airflow effects on weapon performance and evaluation of courses of action to compensate for airflow effects.

10. Helicopter stability must be improved during hover in order to provide an effective weapons platform. This is particularly true when a large number of rockets are to be fired in the shortest possible time. It is expected that helicopter control systems will eventually provide this characteristic. Parallel research efforts are necessary so that a combination of platform stability, fire control, and rocket design can accomplish accurate rocket delivery during hover, pop-up and low speed flight as the helicopter transitions. These integrated tasks must be performed in order that the user can be provided with the effective helicopter system he desires.

Robert W. Bergman
ROBERT BERGMAN
AMCPM-RK2[4]

1977 Updates:

[1] United Aircraft Research Laboratories (UARL) is now United Technologies Research Center (UTRC)

[2] The AAH primary weapon system is the Hellfire system. The 2.75 Inch Rocket and 30 mm cannon are secondary weapons systems.

[3] Mr. Saul Wasserman is now with U. S. Army Armament R&D Command.

[4] Mr. Robert Bergman is now at DRCPM-RK, MIRADCOM, Redstone Arsenal.

APPENDIX B

SUMMARY, CONCLUSIONS AND RECOMMENDATIONS

FROM

ROTOR WAKE INDUCED FLOW ALONG HELICOPTER ROCKET TRAJECTORIES

(Paper from the Proceedings of the Conference
on the Effects of Helicopter Downwash
on Free Projectiles,
A. J. Landgrebe and T. A. Egolf, Nov. 1975)

SUMMARY

An analytical investigation was conducted to predict the rotor wake induced flow velocities along the trajectories of rockets fired from an Army AH-1G helicopter. The three components of both the time-averaged and instantaneous induced velocities were predicted at selected points along the trajectories of rockets fired from four wing locations. Three flight conditions with helicopter flight speeds of 0, 15, and 30 knots were investigated. The sensitivity of the predicted induced velocities to rotor wake model, rocket launch attitude, and rocket launch position was also investigated. Velocities induced by tip vortices near the intersections of the rocket trajectories with the wake boundary were found to be similar in magnitude to the launch velocities of the 2.75 in. rocket currently in use on AH-1G aircraft. Values of the downward induced velocity component as high as 70 fps (time-averaged) and 130 fps (instantaneous) were predicted for the hover condition, and the velocities decrease with increasing flight speed. For flight speeds greater than approximately 30 kts, the rotor wake passes behind the rocket launch position which significantly reduces the wake induced effects. The location of the rotor wake boundary relative to the rocket trajectories is a major determinant of the induced velocity distribution along the trajectories. Thus, the use of an accurate wake geometry was found to be important for accurate calculations of the induced velocities at the rocket.

The results of this analytical investigation were published in March 1975 in U. S. Army Picatinny Arsenal Technical Report 4797, "Prediction of Rotor Wake Induced Flow Velocities Along the Rocket Trajectories of an Army AH-1G Helicopter." This paper, presented on August 12, 1975 at the Conference on the Effects of Helicopter Downwash on Free Projectiles sponsored by the U. S. Army Aviation Systems Command, is a condensation of that report.

APPENDIX B (Cont'd)

CONCLUSIONS FROM REFERENCE 7

The following conclusions apply to the AH-1G helicopter operating at hover and low speed flight conditions:

1. The magnitude of the predicted induced velocity components at the trajectories can exceed the rocket launch velocity. Values of the downward induced velocity component as high as 70 fps (time-averaged) and 130 fps (instantaneous) were predicted.

2. Of the three velocity components, the greatest induced velocities were predicted for the downward component normal to the rocket trajectory. The component along the rocket trajectory was generally next in order of magnitude, and the smallest velocity magnitudes were predicted for the lateral component.

3. As the rocket moves from its launch position, the downward velocity component increases as the wake boundary is approached. As the rocket moves to the outside of the rotor wake the magnitude of the downward velocity decreases abruptly, and becomes insignificant within a distance of one rotor diameter from the launch position.

4. The position of the intersection of a rocket trajectory with the wake boundary is most influential for it determines the length of time that the rocket remains in the higher induced velocity region inside the wake. It also determines the location where the close proximity to a tip vortex can result in a high induced velocity. The importance of the wake boundary location establishes the importance of accurately determining the items which establish the wake skew angle -- flight speed, rotor and aircraft attitude, and aircraft gross weight (rotor thrust).

5. Considering the variation of the predicted induced velocities with flight speed, the influence of the wake aerodynamic intereference on the rocket trajectories is expected to decrease with increasing flight speed. In hover, the predicted velocities are the highest, and the rocket remains in the wake for the longest period of time. For flight speeds greater than approximately 30 kts, the rotor wake generally passes behind the rocket launch position which significantly reduces the wake induced effects.

6. Large impulsive type, induced velocity variations with time occur at points on the rocket trajectory near the wake boundary. These variations are caused by the passage of the tip vortices. If the high

impulsive type velocities induced by the close passage of a tip vortex are found to significantly alter the flight path of the rocket, a mechanism for synchronizing the rocket firing time with the rotor position for minimum tip vortex interference could be considered.

7. The variation of the predicted time-averaged induced velocity components between the four rockets of the AH-1G helicopter is within ± 10 fps at similar points along the trajectories.

8. It is necessary to use an accurate rotor wake model in calculations directed toward predicting induced velocities at rocket trajectories. The use of an undistorted wake model rather than a realistic distorted wake model results in significant differences in predicted induced velocities.

9. Small variations (4 degrees) in rocket launch attitude produce small induced velocity changes at the rocket trajectories except near the wake boundary where the variations produce a difference in the phasing of the velocities associated with the relation between rotor position and the passage of a tip vortex. This is generally also true for small variations in rocket launch point. However, vertical and/or longitudinal variations in launch point produce significant variations in induced velocities near the launch point at approximately 30 kts due to the movement of the point from inside to outside of the rotor wake or vice versa. The relative position of the rocket launch point to the wake boundary could also be varied by changes in any of the factors which determine the wake boundary (flight speed, aircraft gross weight, and rotor/fuselage attitude).

RECOMMENDATIONS FROM REFERENCE 7

1. Several factors which were approximated or neglected in the analytical calculations, should be considered. These are wake instability and dissipation, vortex core size, the selection of the finite spatial and temporal increments used in the analyses, and wing and fuselage interference effects. Also, the possible requirement for iterating between the induced velocities and the rocket trajectory should be considered.

2. Calculations of the effect of the rotor wake induced velocities determined in this investigation on the rocket trajectories should be continued.

3. The rotor wake effects for flight conditions other than the three discussed herein should be determined. In particular, calculations for specific flight conditions for which flight test rocket trajectory data become available should be performed for correlation purposes. Also, the sensitivity of the results to variations of the significant parameters in actual aircraft operation which influence the wake strength and wake/rocket positioning should be investigated, and procedures for generalizing the results should be determined.

4. Model helicopter tests should be conducted to acquire systematic experimental data on this rocket aerodynamic interference problem. Model hovering and wind tunnel facilities and experimental flow measurement and visualization techniques should be used to measure the wake boundaries and flow velocities in the regions of the rocket trajectories. Combined model rotor-fuselage-wing testing, application of flow visualization techniques, and application of laser velocimeter techniques (as reported in Reference 9*) to measure flow velocities, should be conducted. The results of such an experimental program would provide data for correlation with theory and for a systematic determination of the total and separate influence of each of the aircraft components (rotor, fuselage and wing) and significant parameters (flight speed, gross weight, aircraft attitude, etc.). In addition, the determination of the velocity field at potential locations for wind sensors mounted on the aircraft would assist in solving the problem of accurately measuring flow velocities at the low aircraft flight speeds required in accordance with current rocket firing tactics.

---

* Reference 11 of this report.

LIST OF SYMBOLS

b	Number of rotor blades
c	Blade chord, ft
C_T	Rotor thrust coefficient, rotor thrust/$\rho \pi R^2 (\Omega R)^2$
$\hat{e}_1$, $\hat{e}_2$	Unit vectors in direction of incident laser beams
f_B	Bragg cell offset frequency (adjustable)
f_D	Doppler frequency
h	Height of rotor above ground, ft
H	Skid height above ground, ft
IGE	In-ground-effect
n	Index of refraction of test medium (assumed $n = 1$)
N	Number of data samples
OGE	Out-of-ground-effect
r	Radial coordinate from rotor axis $\div R$
R	Rotor radius, ft
T	Rotor thrust, lbs
T_D	Doppler period ($T_D = 1/f_D$)
$\vec{U}$	Particle velocity vector
u, U	Particle velocity component in plane of incident beams and perpendicular to the bisector of the beams
U_{MIN}	Velocity at which $f_D = 0$
v	Local flow velocity, fps

LIST OF SYMBOLS (Continued)

$v_{i_{MOM}}$	Momentum induced velocity (see Eq.9), fps
v_x, v_y, v_z	Horizontal and vertical flow velocity components in the x, y, z coordinate axis system; same sign convention as x, y, z, fps
v_{x_T}, v_{y_T}, v_{z_T}	Flow velocity components in rocket trajectory coordinate system (x_T, y_T, z_T); sign convention is consistant with coordinate definition, fps
$v_{x_{T_{AVG}}}$, $v_{y_{T_{AVG}}}$, $v_{z_{T_{AVG}}}$	Time averaged flow velocity components in rocket trajectory coordinate system (x_T, y_T, z_T); same sign convention as v_{x_T}, v_{y_T}, v_{z_T}, fps
x, y, z	Hub centered axis system coordinates nondimensionalized by R, x-y plane parallel to rotor tip path plane, left-handed coordinate system (see Fig. 4)
x_T, y_T, z_T	Rocket trajectory axis system coordinates nondimensionalized by R, centered at intersection of axis of rocket launch positions and fuselage centerline, left handed coordinate system with positive x_T in direction of rocket travel (see Fig. 4)
α	Slope of frequency-velocity calibration
γ	Rocket launch attitude, positive nose up, deg
Θ	Angle between incident laser beams, deg
λ	Wavelength of incident laser light
ρ	Air density, lb-sec^2/ft^4
σ	Rotor solidity, $bc/\Pi R$
ϕ	Angle between incident and collection directions,deg
ψ	Blade azimuth angle measured from negative x axis, positive in the direction of rotation, deg

LIST OF SYMBOLS (Continued)

ψ_s	Blade azimuth angle relative to plane of smoke, deg
ψ_w	Wake azimuth angle (wage age related to blade rotation), deg
Ω	Rotor rotational frequency, rad/sec
Superscripts	
$(\bar{\ })$	Average or mean value
$(\ )'$	RMS value
Additional Subscripts	
$(\ )_{AVG}$	Average
$(\ )_i$	Value for ith segment of ψ
$(\ )_j$	Value for jth data sample
$(\ )_{REF}$	Reference configuration and condition
$(\ )_{TIP}$	Relative to tip of blade
$(\ )_T$	Relative to rocket trajectory coordinate system
$(\ )_{PTP}$	Peak-to-peak value
$(\ )_{MEAN}$	Mean value

Figure 1. AH-1G Helicopter Firing 2.75 In. Rockets.

Figure 2. Forward Section of AH-1G Helicopter With 2.75 In. Rocket Launcher.

Figure 3. AH-1 Helicopter with Modified (Flat) Canopy.

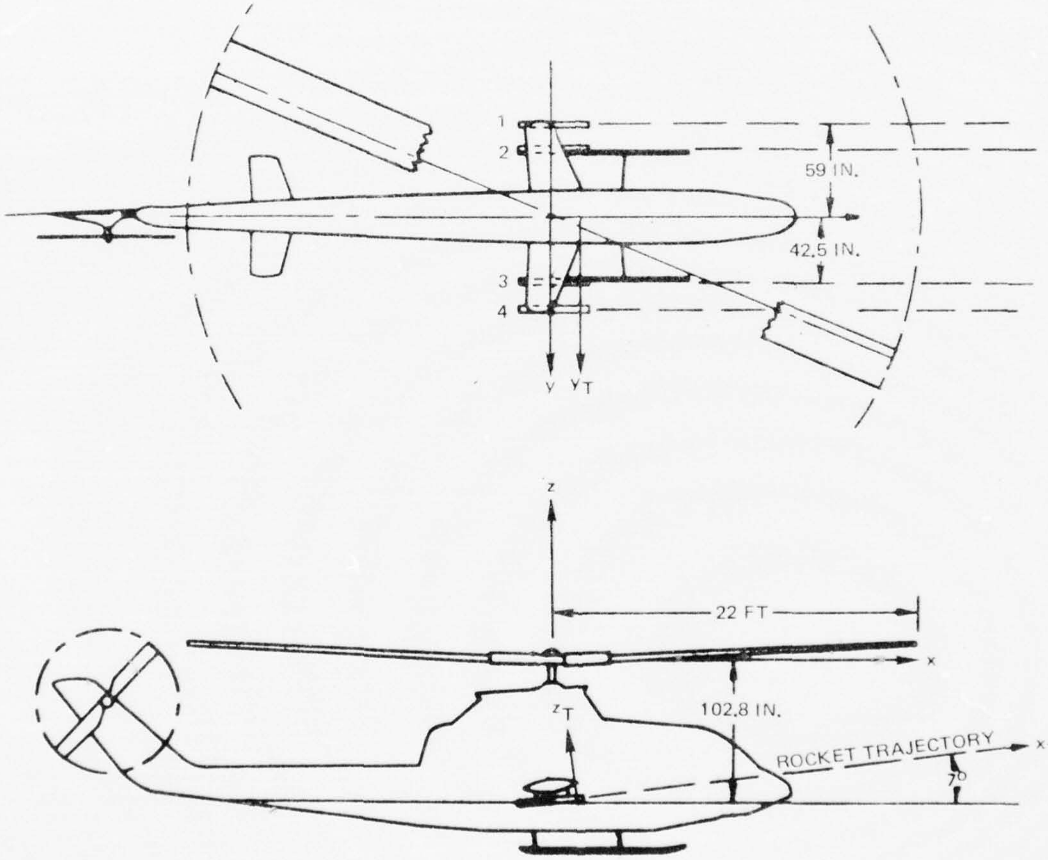

Figure 4. Schematic of AH-1G Helicopter Showing Rocket Trajectories and Axis Systems.

77-06-233-6

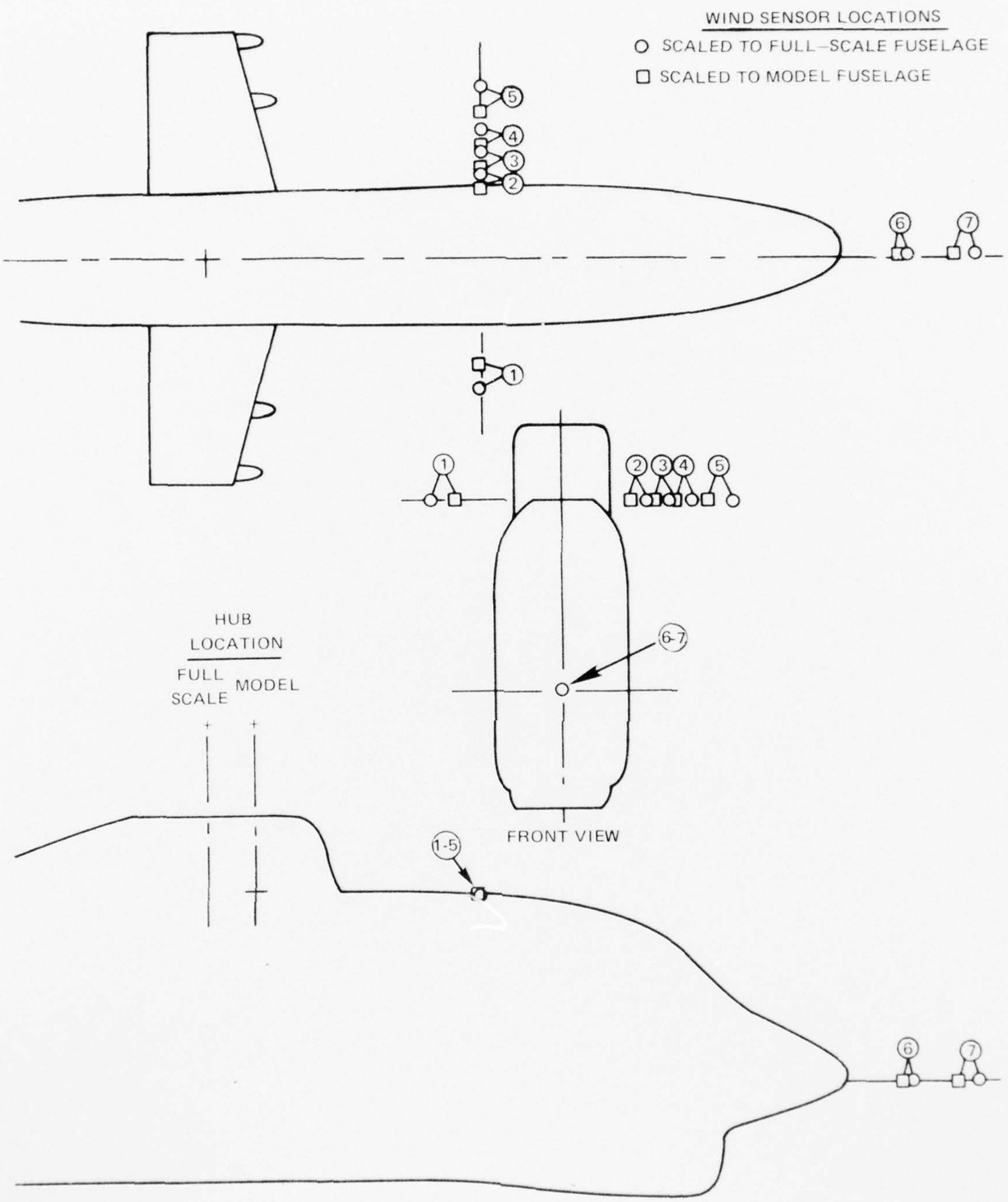

Figure 5. Schematic of Test Wind Sensor Locations Scaled Relative to Model and Full-Scale AH-1G Fuselage.

77-06-214-10

1 HELICOPTER MODEL (AH–1G)
2 ROTOR POWER AND BALANCE SYSTEM
3 LASER VELOCIMETER SYSTEM
4 MOVABLE GROUND PLANE
5 SMOKE RAKE
6 CAMERA FOR SMOKE PHOTOS
7 SCHLIEREN MOVIE CAMERA
8 SCHLIEREN MIRROR AND KNIFE EDGE
9 SCHLIEREN MIRRORS

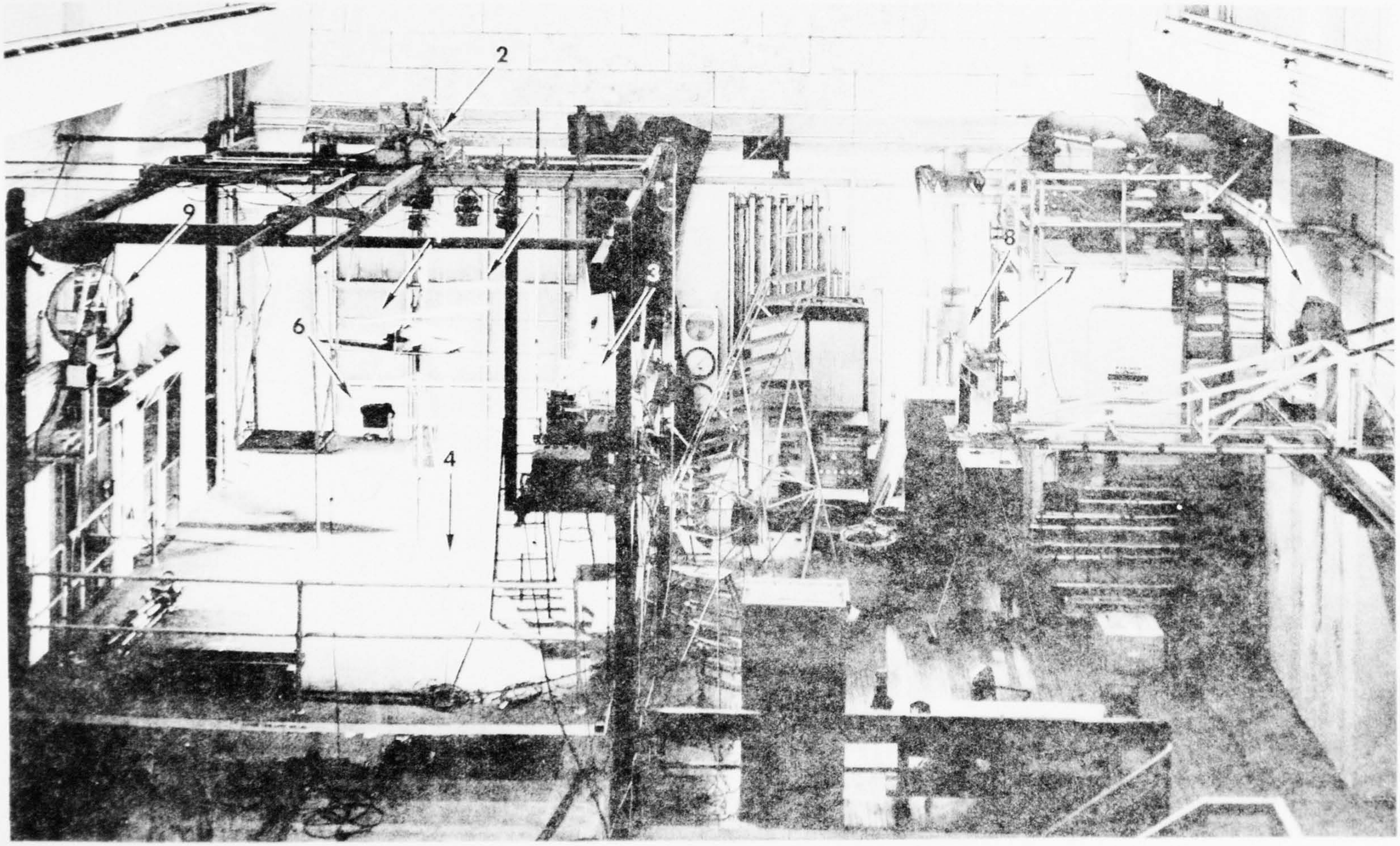

Figure 6. UTRC Model Helicopter Hover Test Facility.

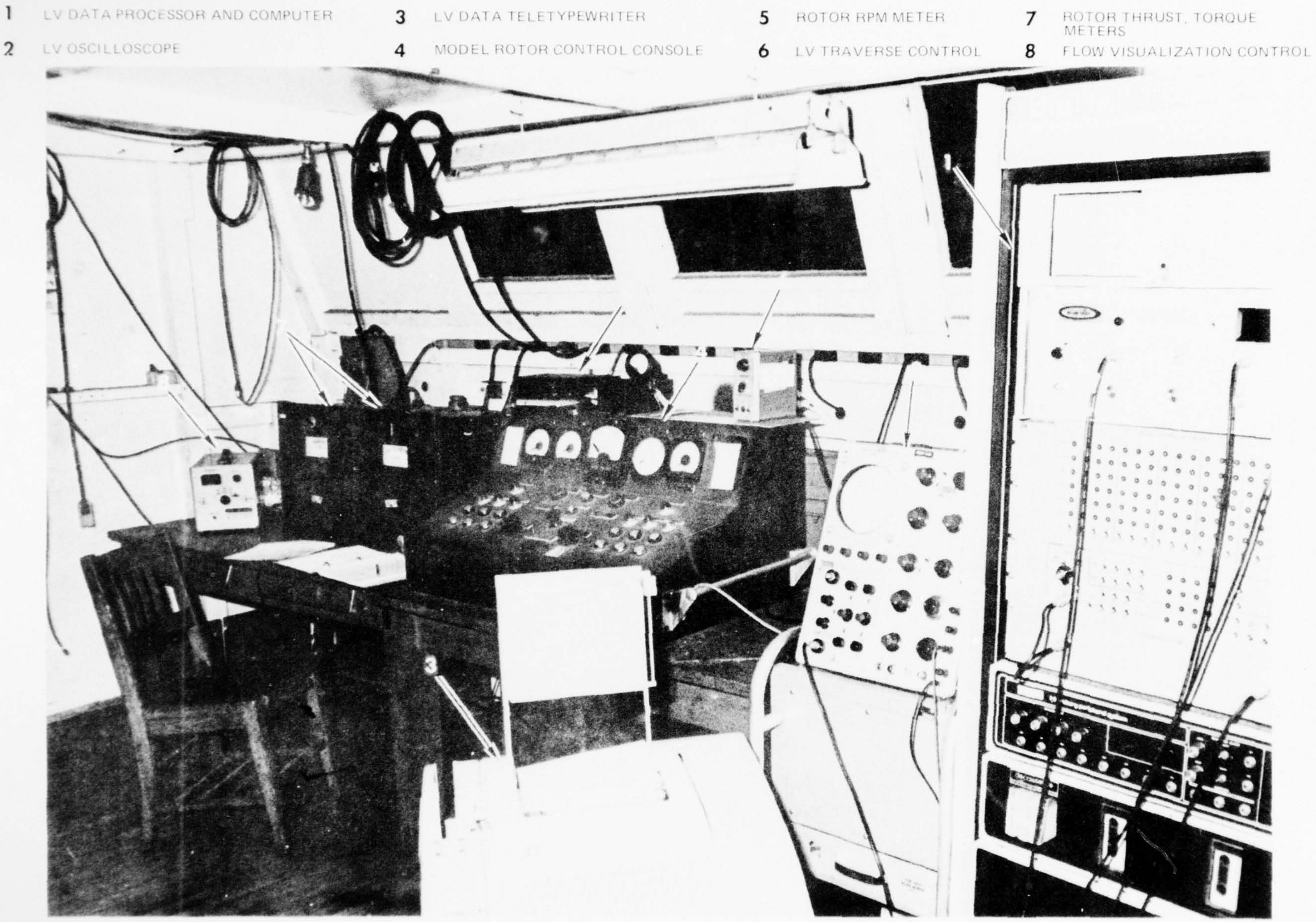

Figure 7. Control Area of UTRC Model Helicopter Hover Test Facility.

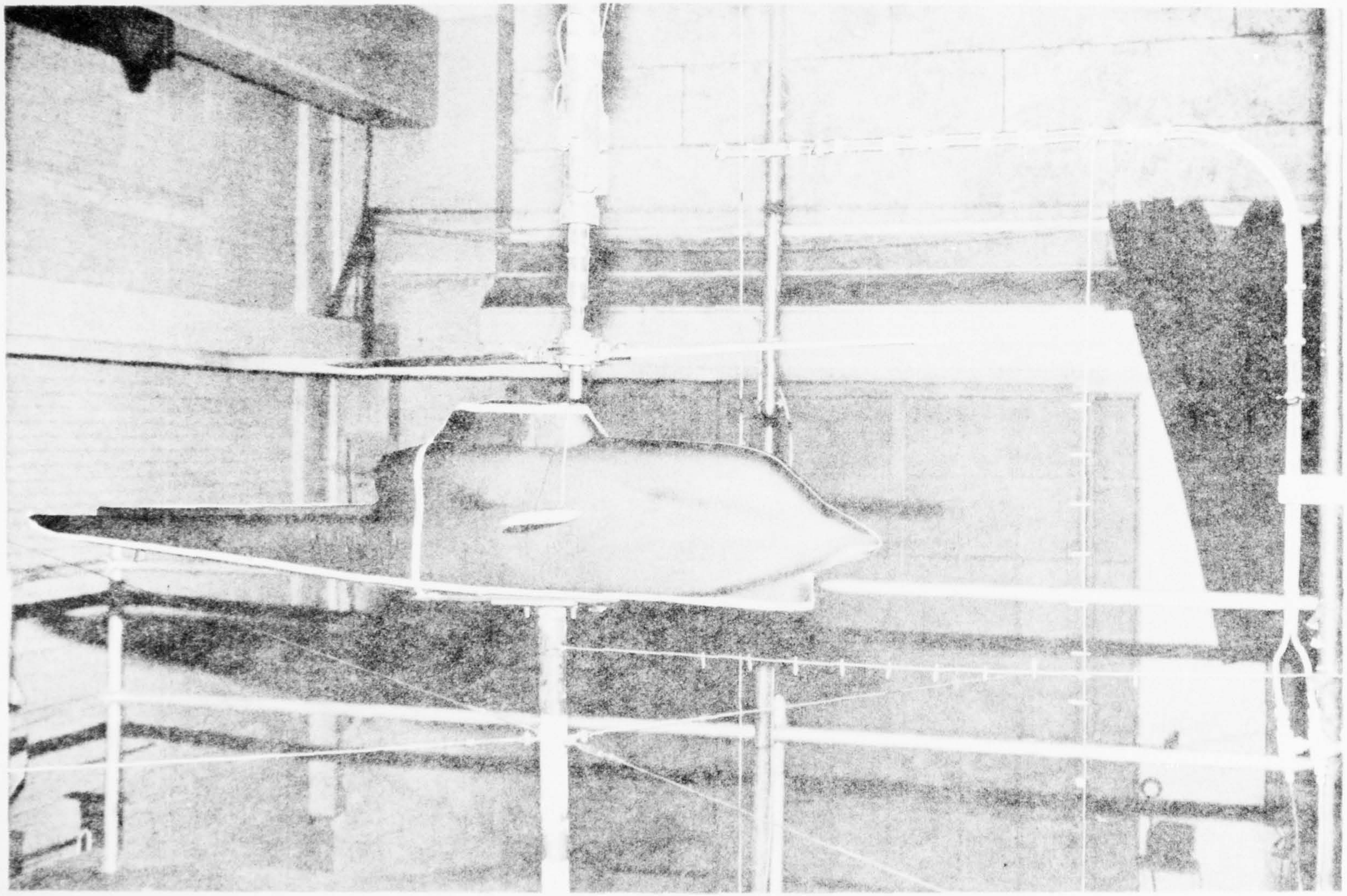

Figure 8. AH-1G Model Helicopter.

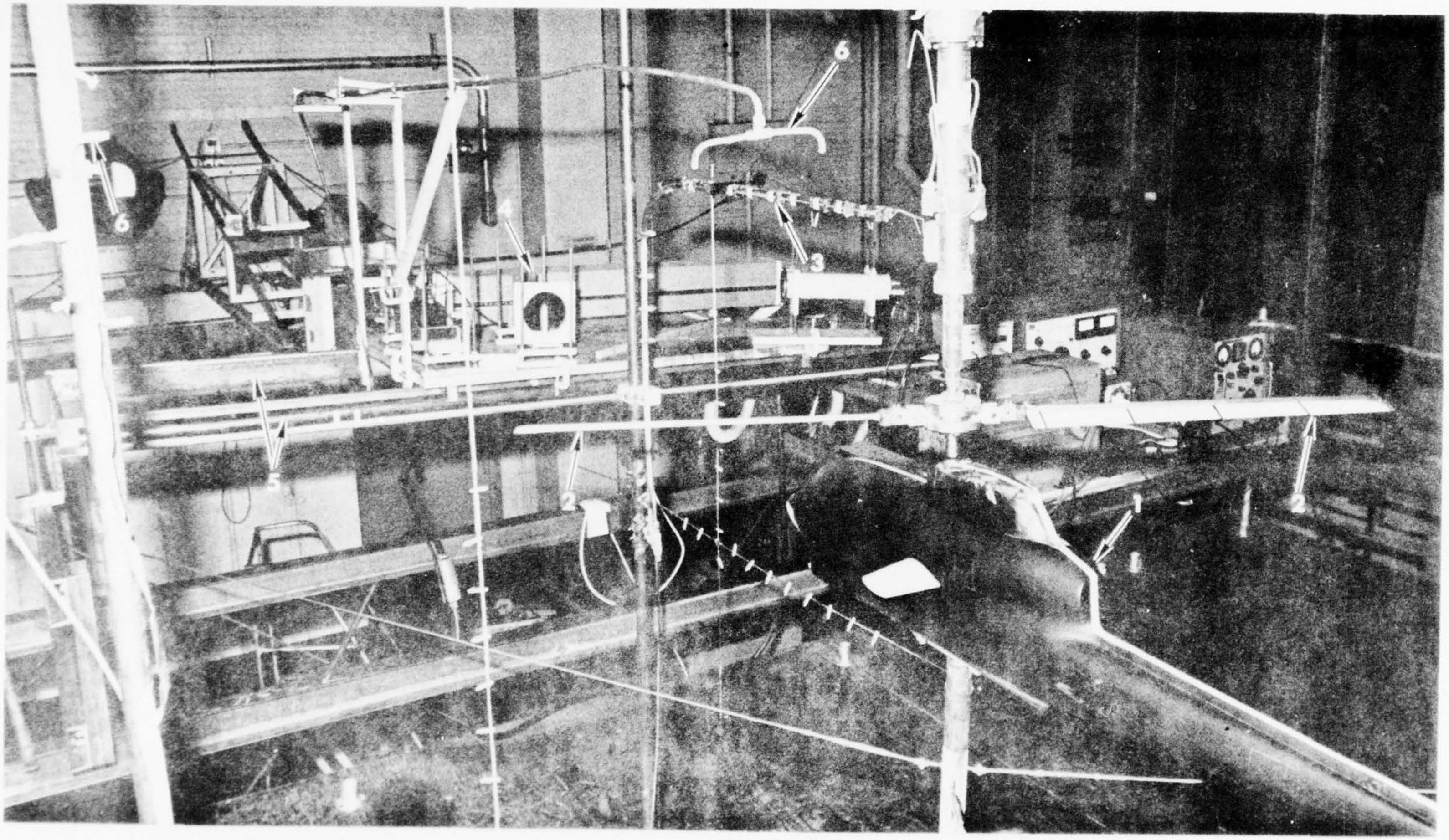

1 MODEL AH-1G FUSELAGE
2 MODEL BLADES
3 SMOKE RAKE
4 LASER VELOCIMETER SYSTEM
5 TRAVERSE RAILS
6 DUAL FLOW SEEDANT PROBES

Figure 9. AH-1G Model Helicopter With Laser Velocimeter and Traverse Equipment.

1 LASER
2 DIAGONAL MIROR
3 SENDING OPTICS AND BRAGG CELL
4 SENDING BEAM PATHS
5 COLLECTING LENS
6 DIAGONAL MIRROR
7 PHOTOMULTIPLIER
8 TRAVERSE TABLE
9 DRIVE SCREW AND MOTOR

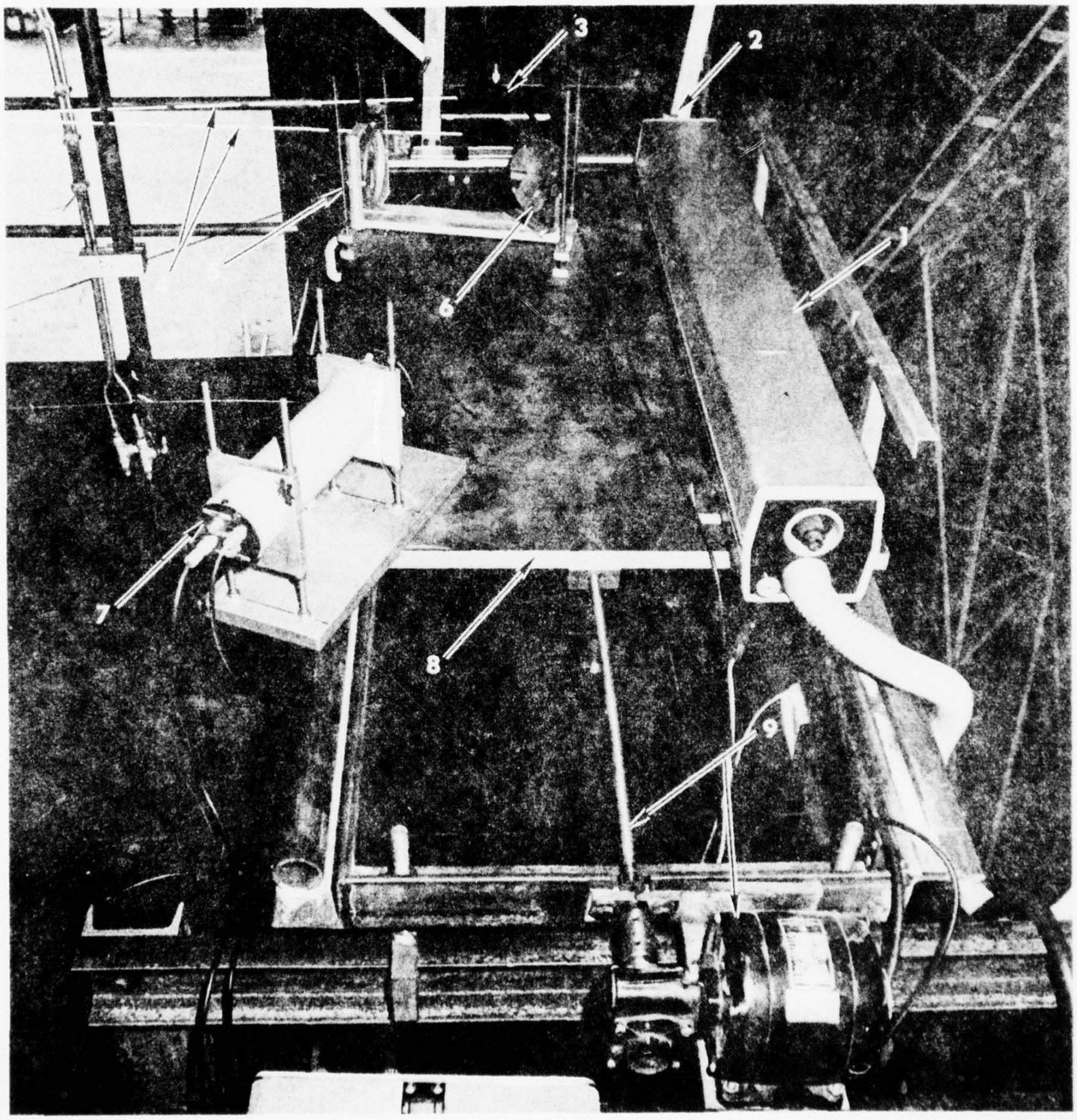

Figure 10. Laser Velocimeter and Traverse.

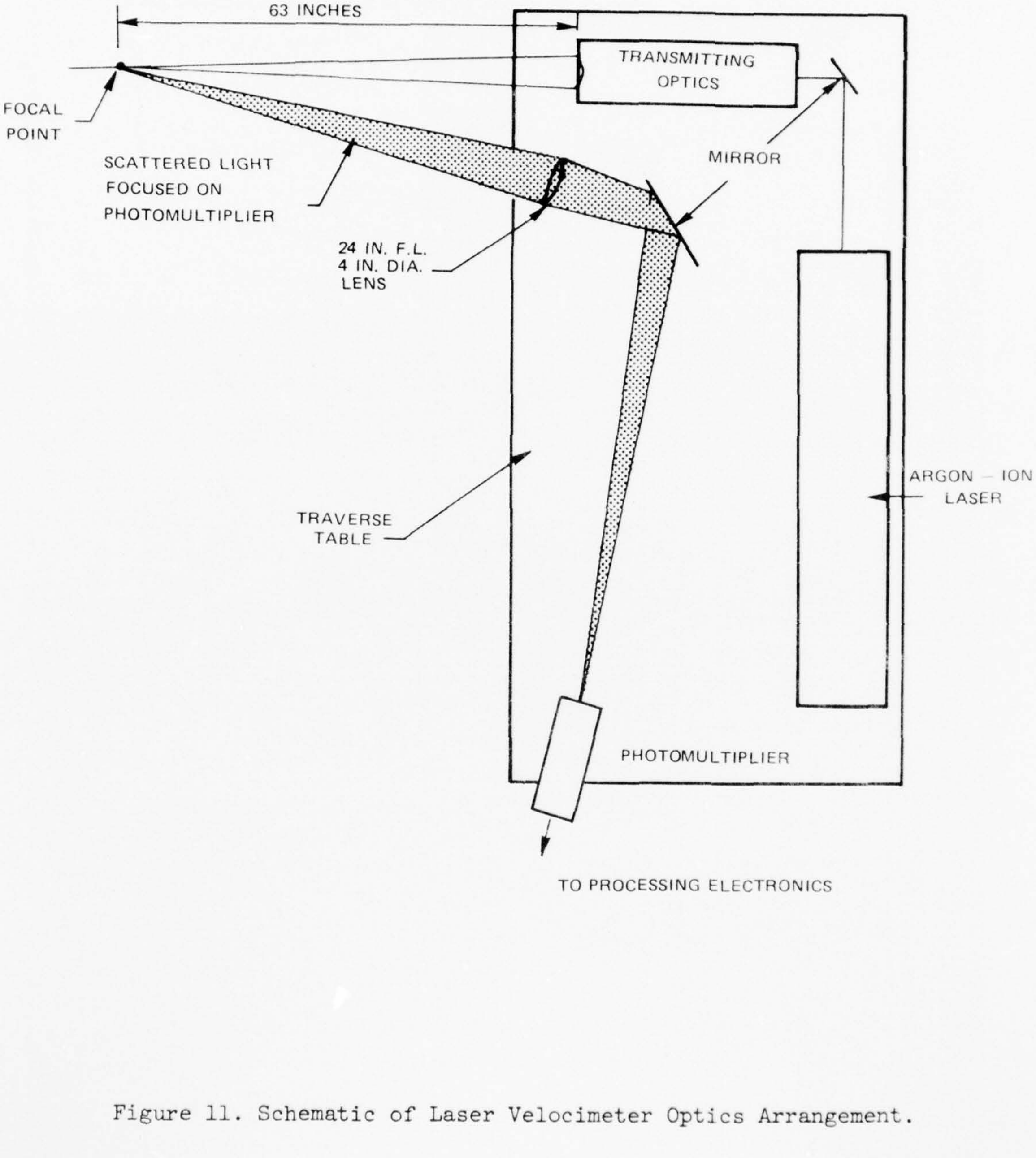

Figure 11. Schematic of Laser Velocimeter Optics Arrangement.

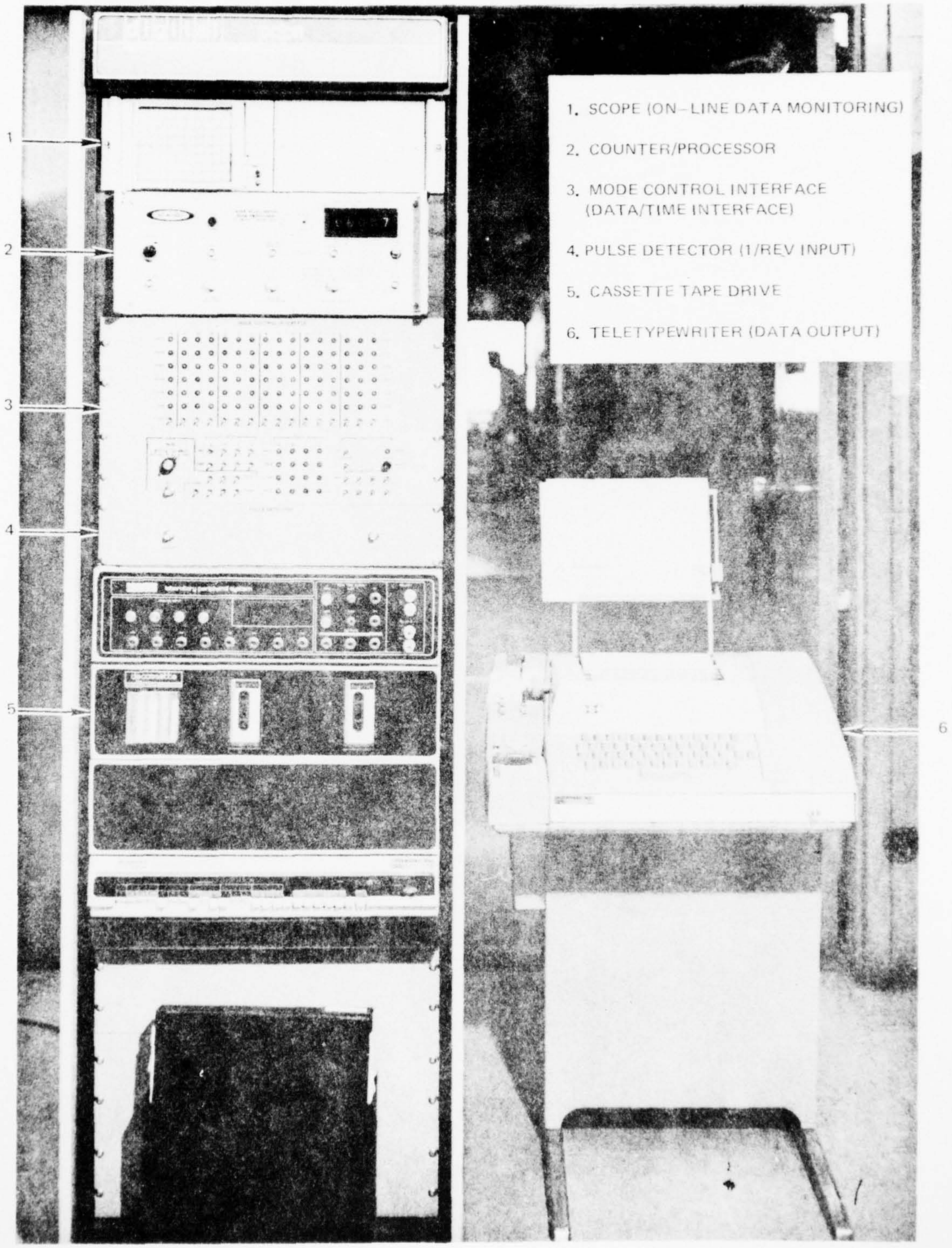

Figure 12. Laser Velocimeter Data Processing Equipment.

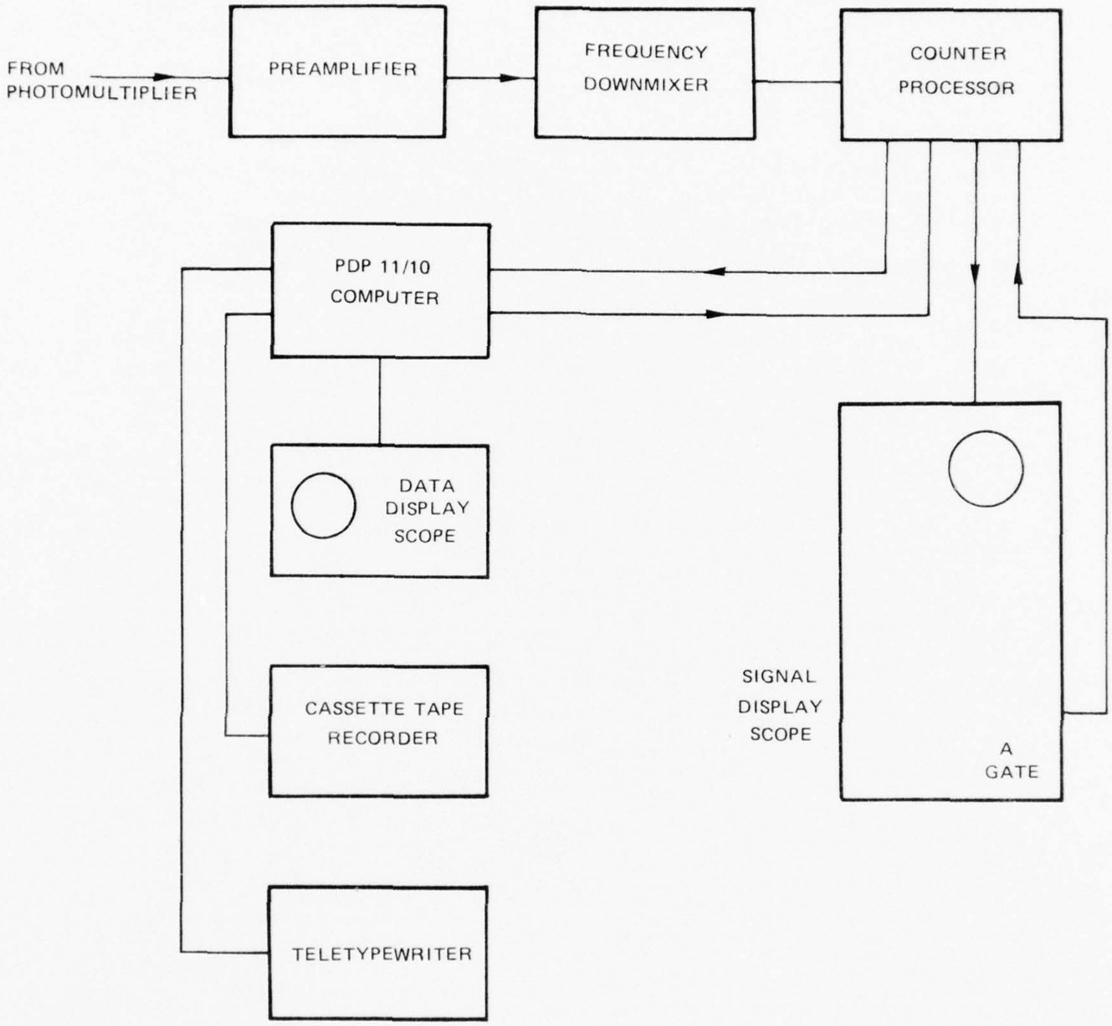

Figure 13. Schematic of Laser Velocimeter Data Processing Components.

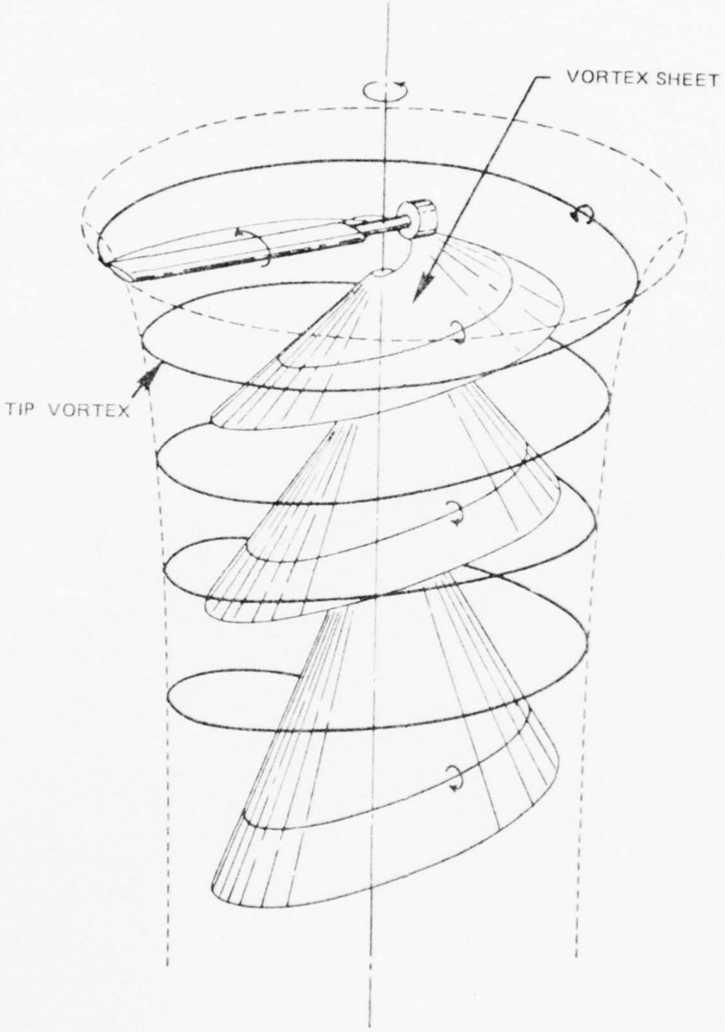

Figure 14. Structure of Hovering Rotor Wake from One Blade.

FROM DR. R.B. GRAY
GA. INST. OF TECHNOLOGY

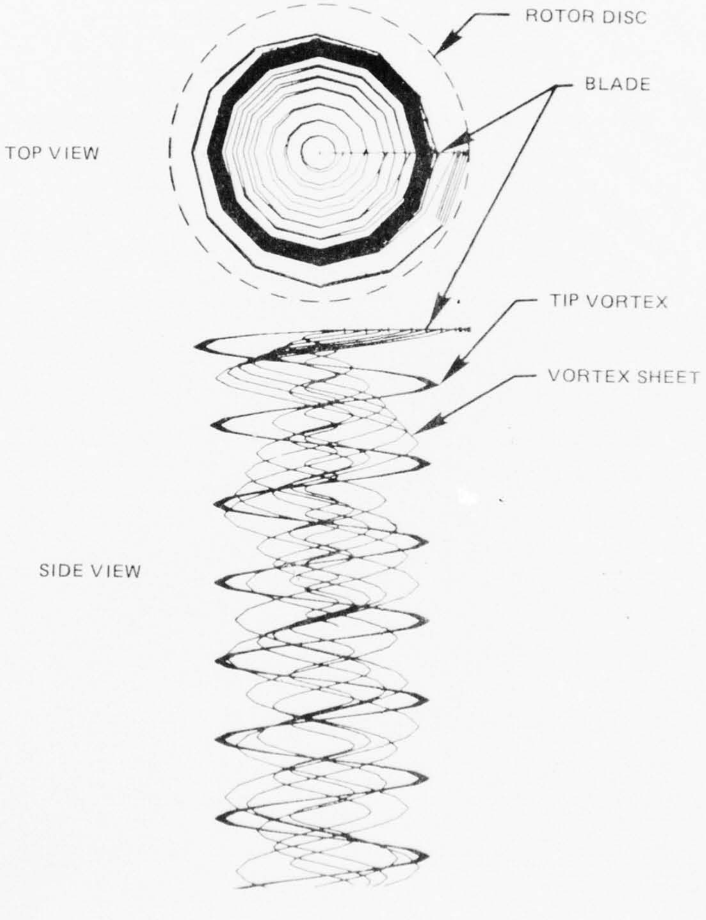

Figure 15. Computer Analysis Hovering Rotor Wake Representation for One Blade.

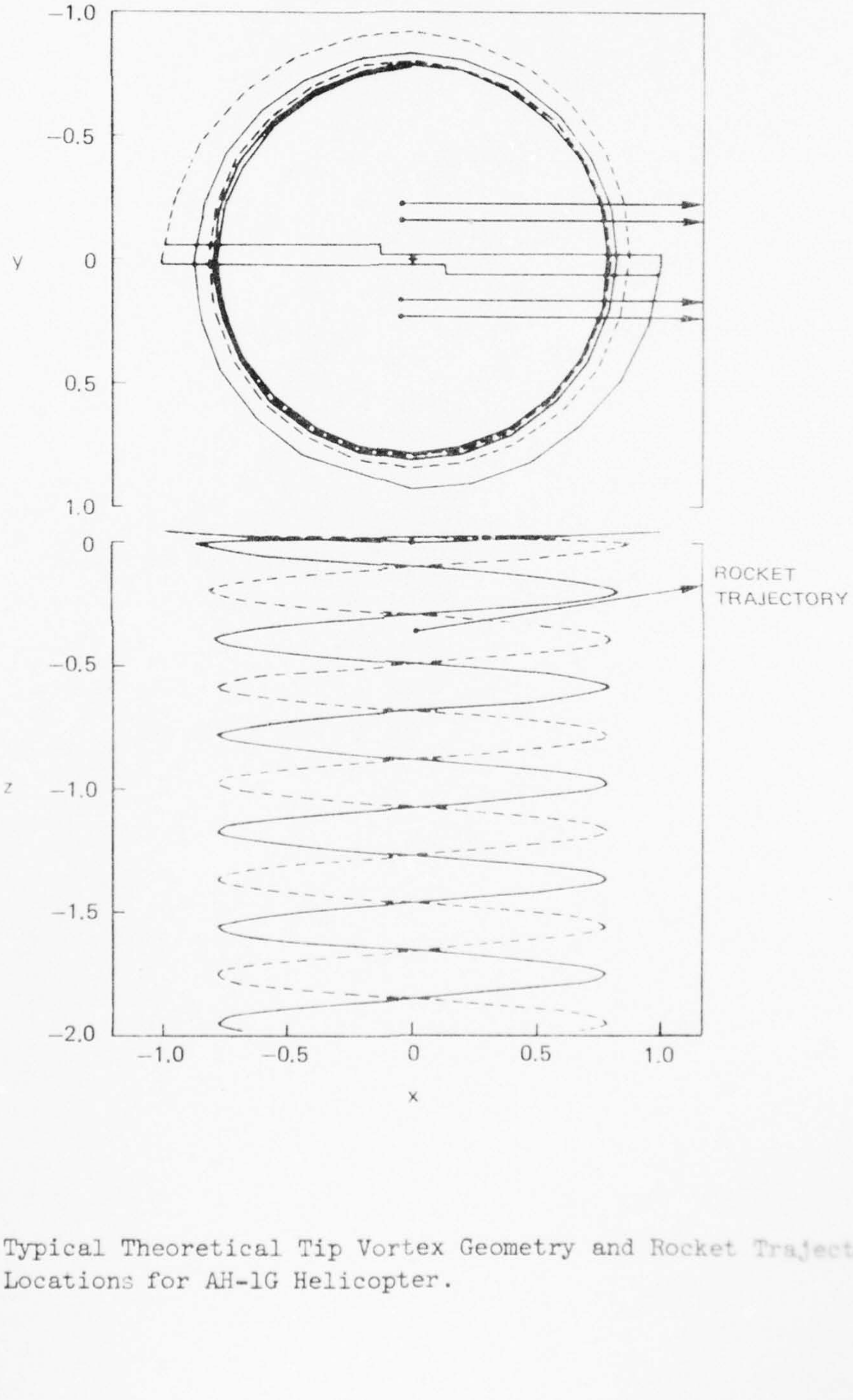

Figure 16. Typical Theoretical Tip Vortex Geometry and Rocket Trajectory Locations for AH-1G Helicopter.

AD-A042 554 UNITED TECHNOLOGIES RESEARCH CENTER EAST HARTFORD CONN F/G 20/4
INVESTIGATION OF THE AIRFLOW OF A HOVERING MODEL HELICOPTER AT --ETC(U)
JUL 77 A J LANDGREBE, J C BENNETT DAA21-76C-0151
UNCLASSIFIED UTRC-R77-912573-15 NL

2 OF 2
ADA042554

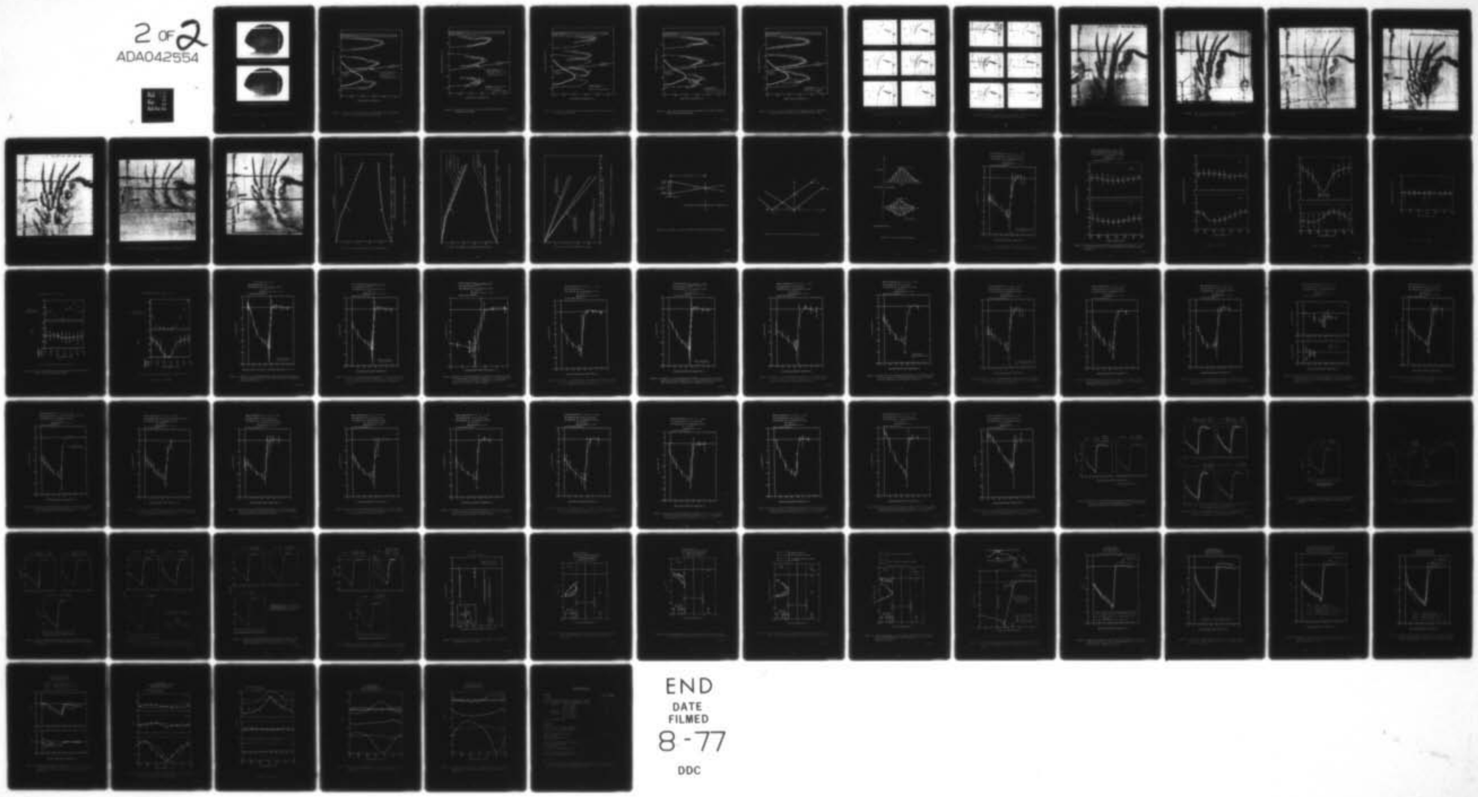

END
DATE
FILMED
8-77
DDC

2 OF 2

ADA042554

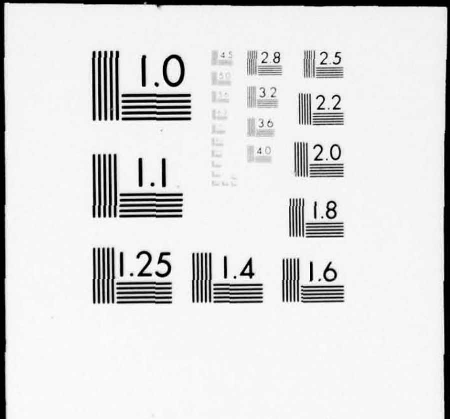

MICROCOPY RESOLUTION TEST CHART
NATIONAL BUREAU OF STANDARDS-1963-A

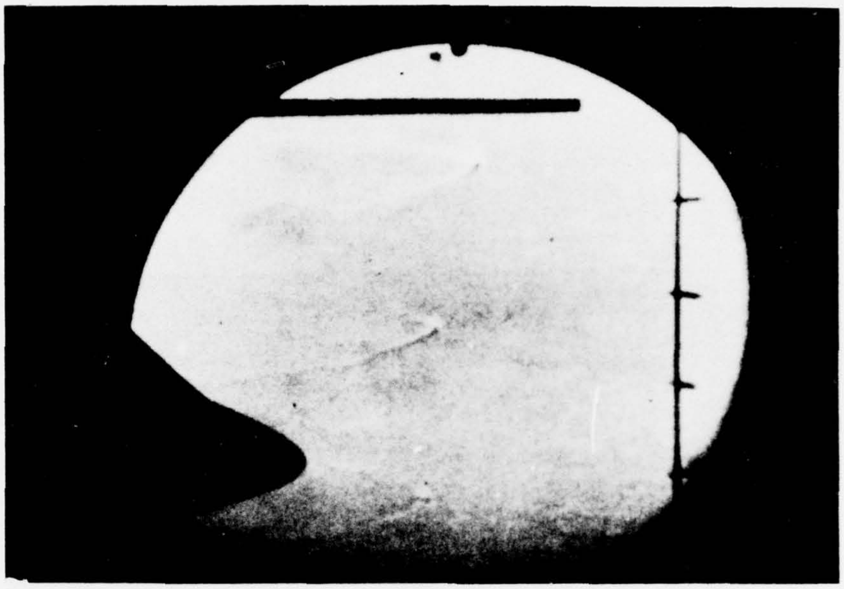

(a) REFERENCE CONFIGURATION AND CONDITION

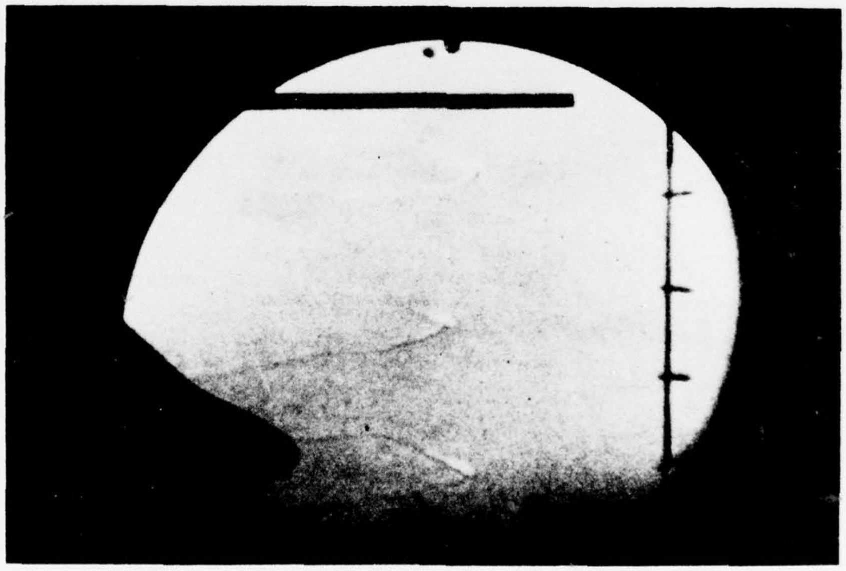

(b) IN-GROUND-EFFECT (SKID HEIGHT = 10 FT) CONDITION

Figure 17. Sample Frames from Schlieren Movies of Rotor Tip Vortices.

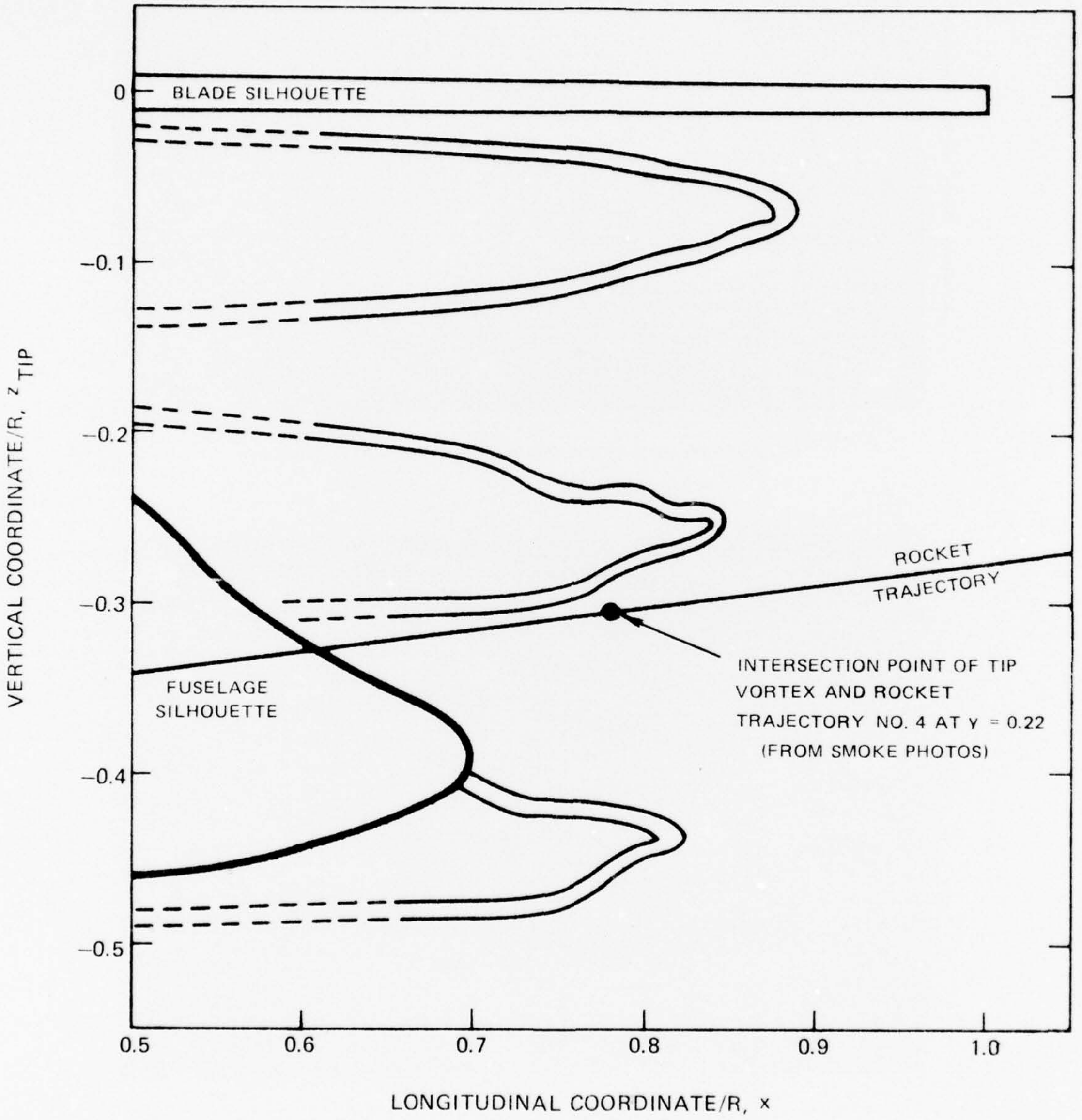

Figure 18. Locations of Tip Vortices for the Reference Test Configuration and Condition From a Schlieren Movie Frame.

77-07-23-6

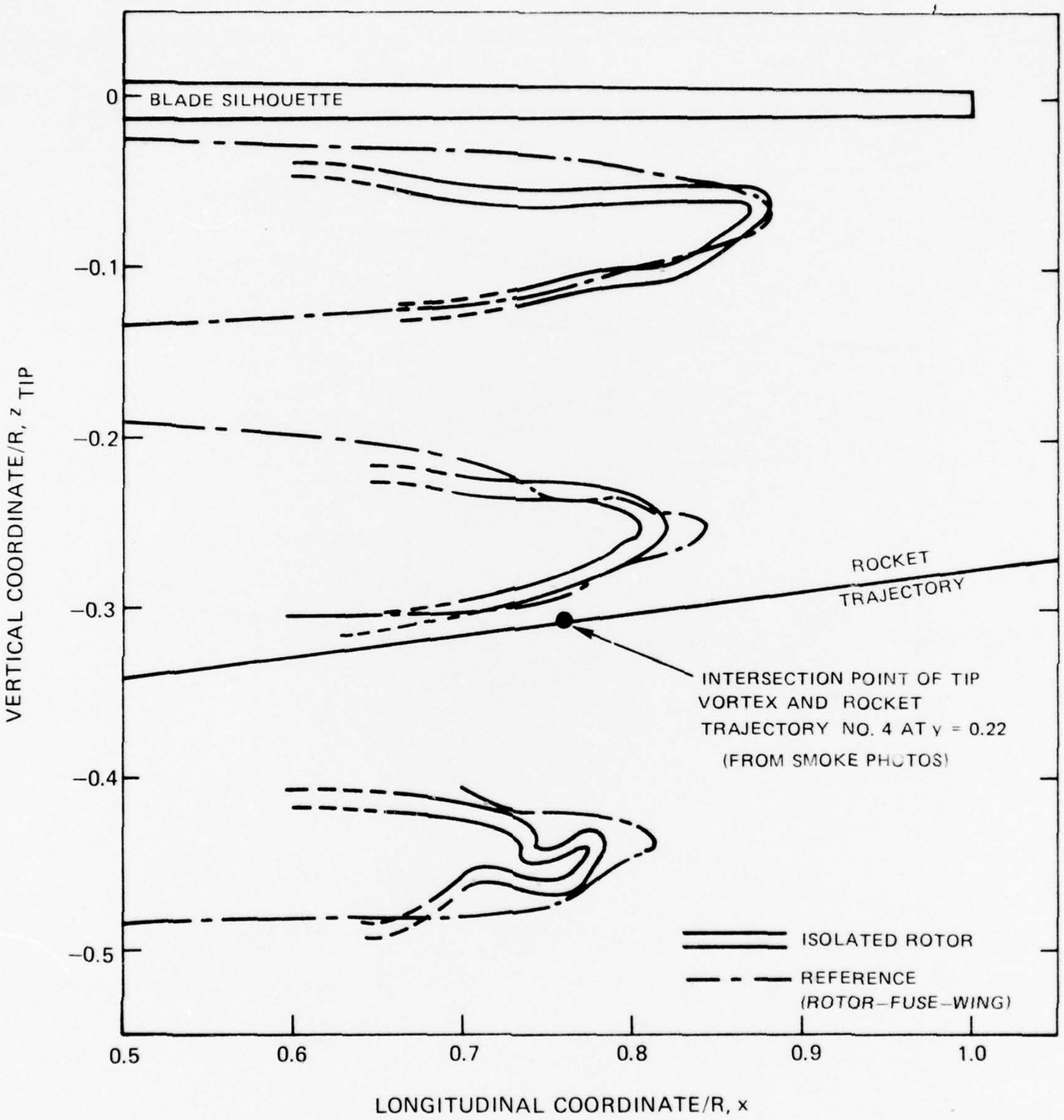

Figure 19. Locations of Tip Vortices from the Isolated Rotor from a Schlieren Movie Frame.

77–07–23–8

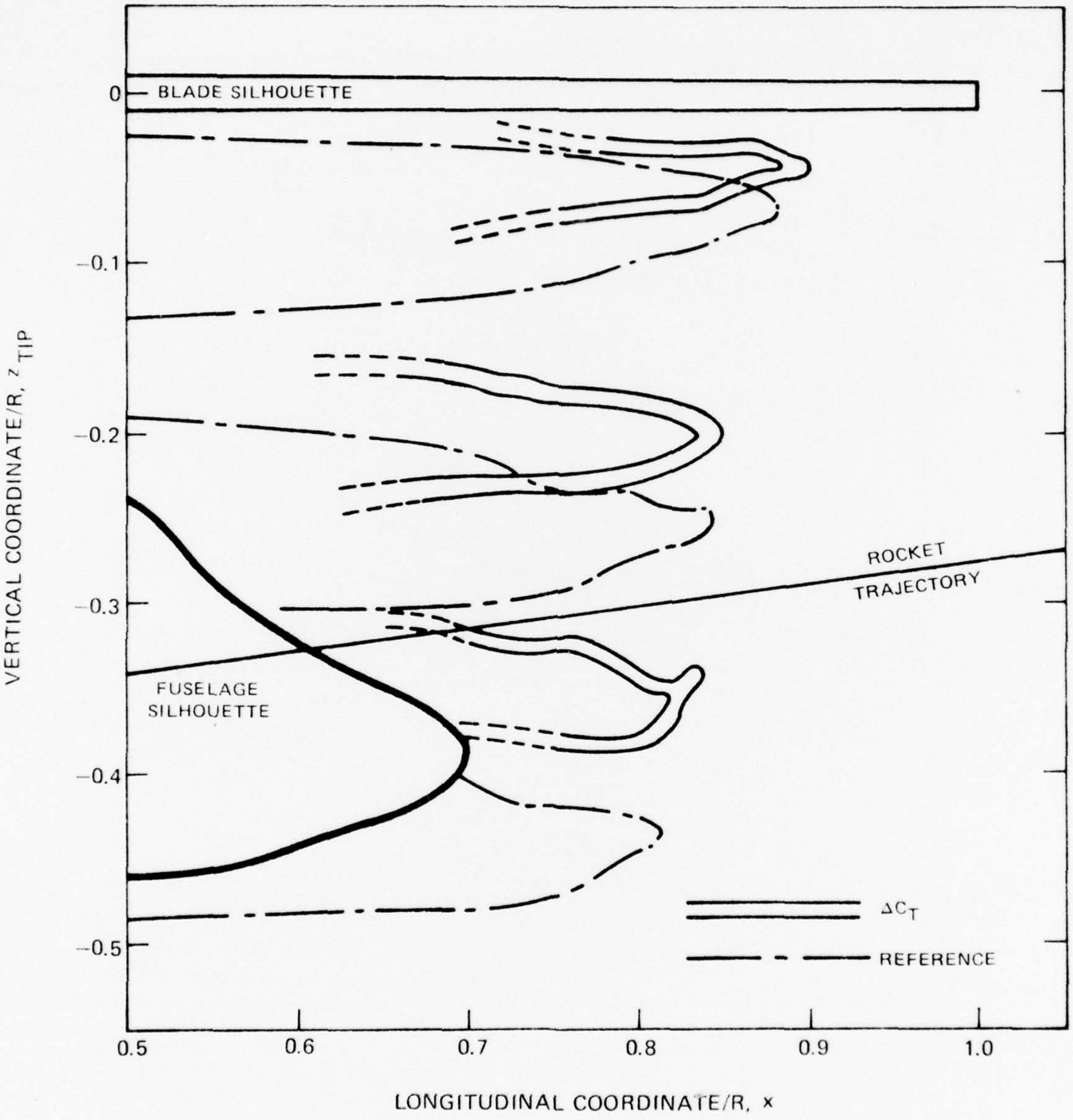

Figure 20. Locations of Tip Vortices for the Modified Thrust Condition from a Schlieren Movie Frame.

77-07-23-3

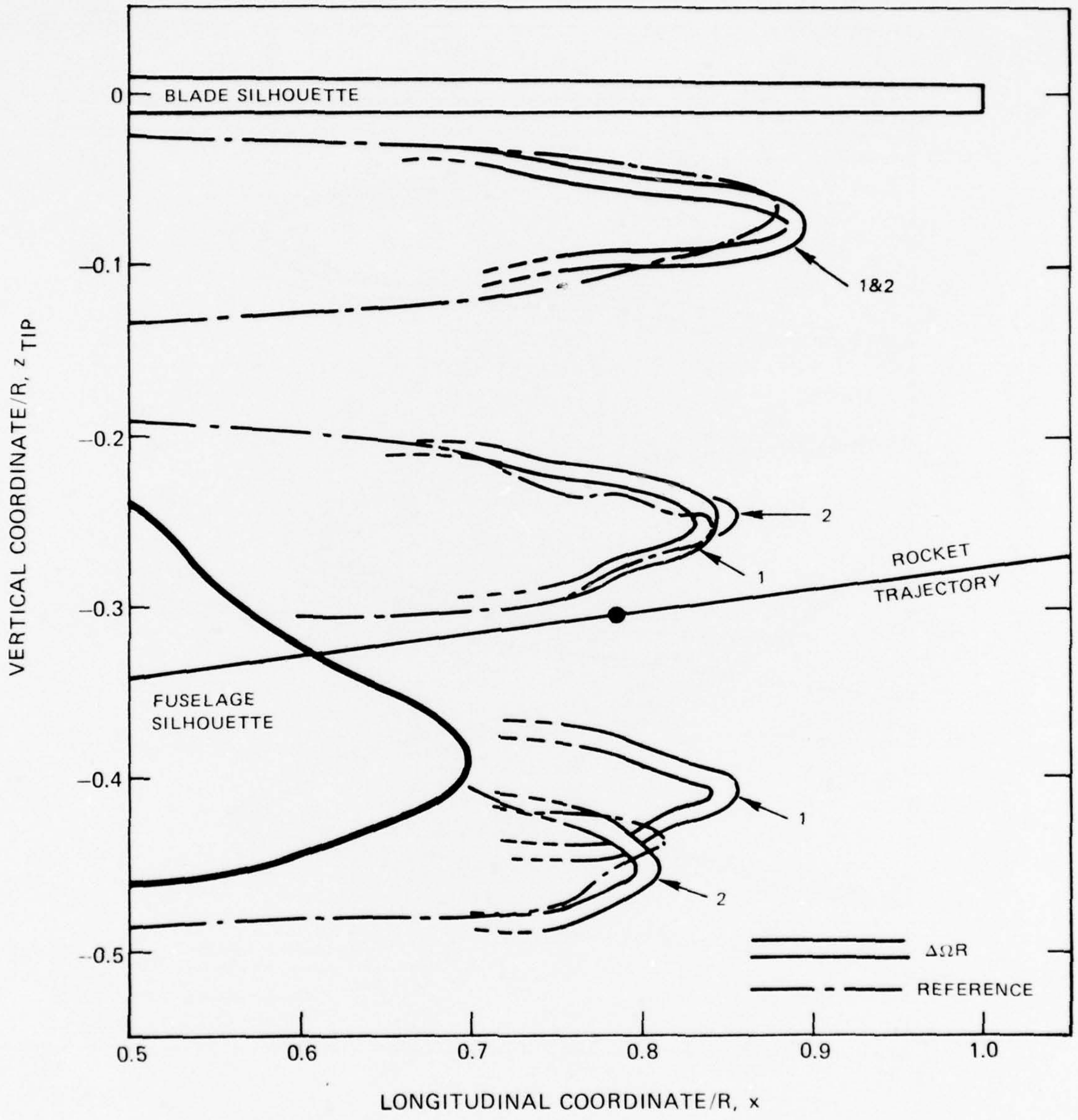

Figure 21. Locations of Tip Vortices for the Modified Tip Speed Condition From a Schlieren Movie Frame.

77–07–23–9

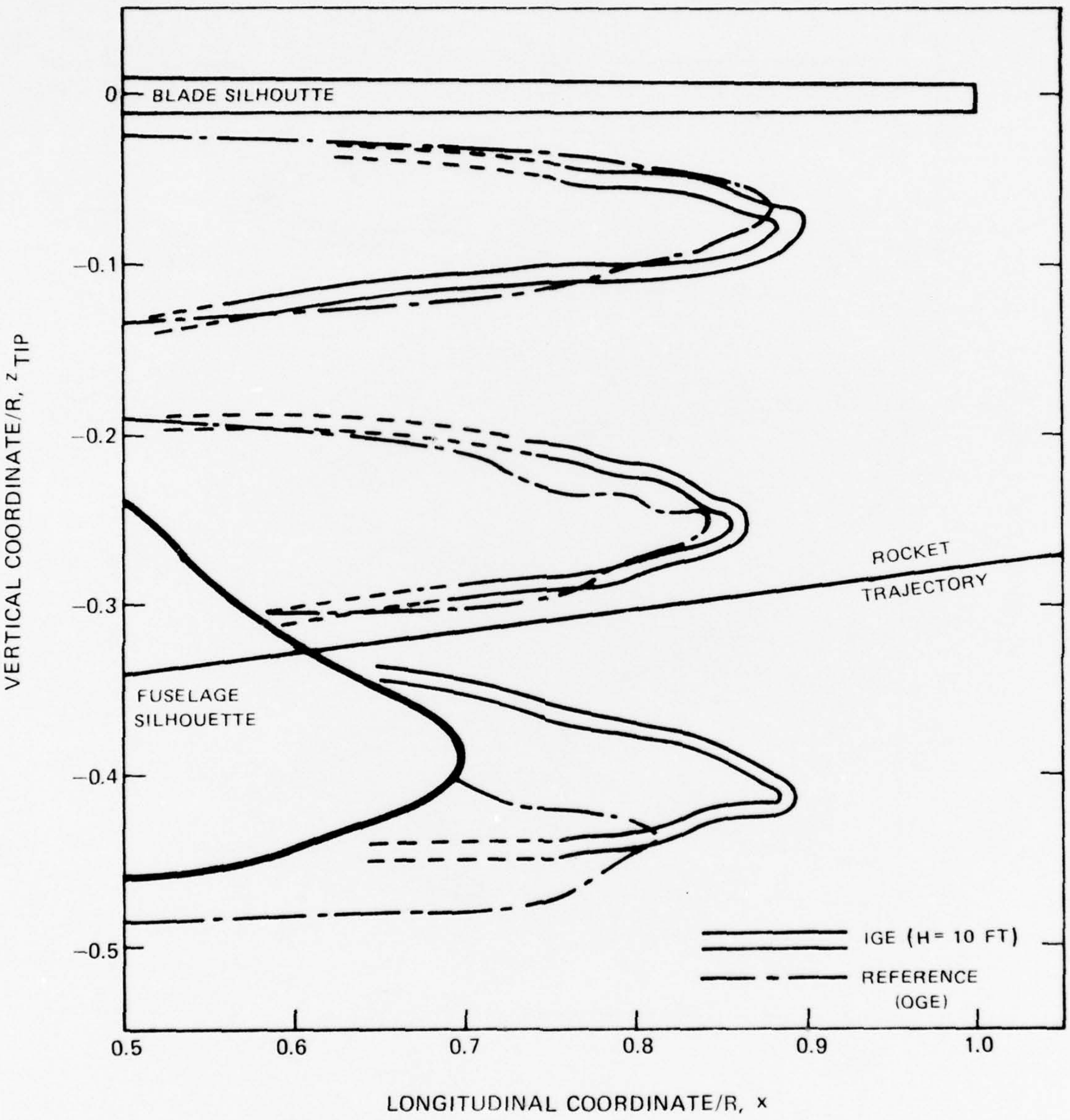

Figure 22. Locations of Tip Vortices for the Simulated 10 ft. Skid Height In-Ground-Effect Condition from a Schlieren Movie Frame.

77–07–23–7

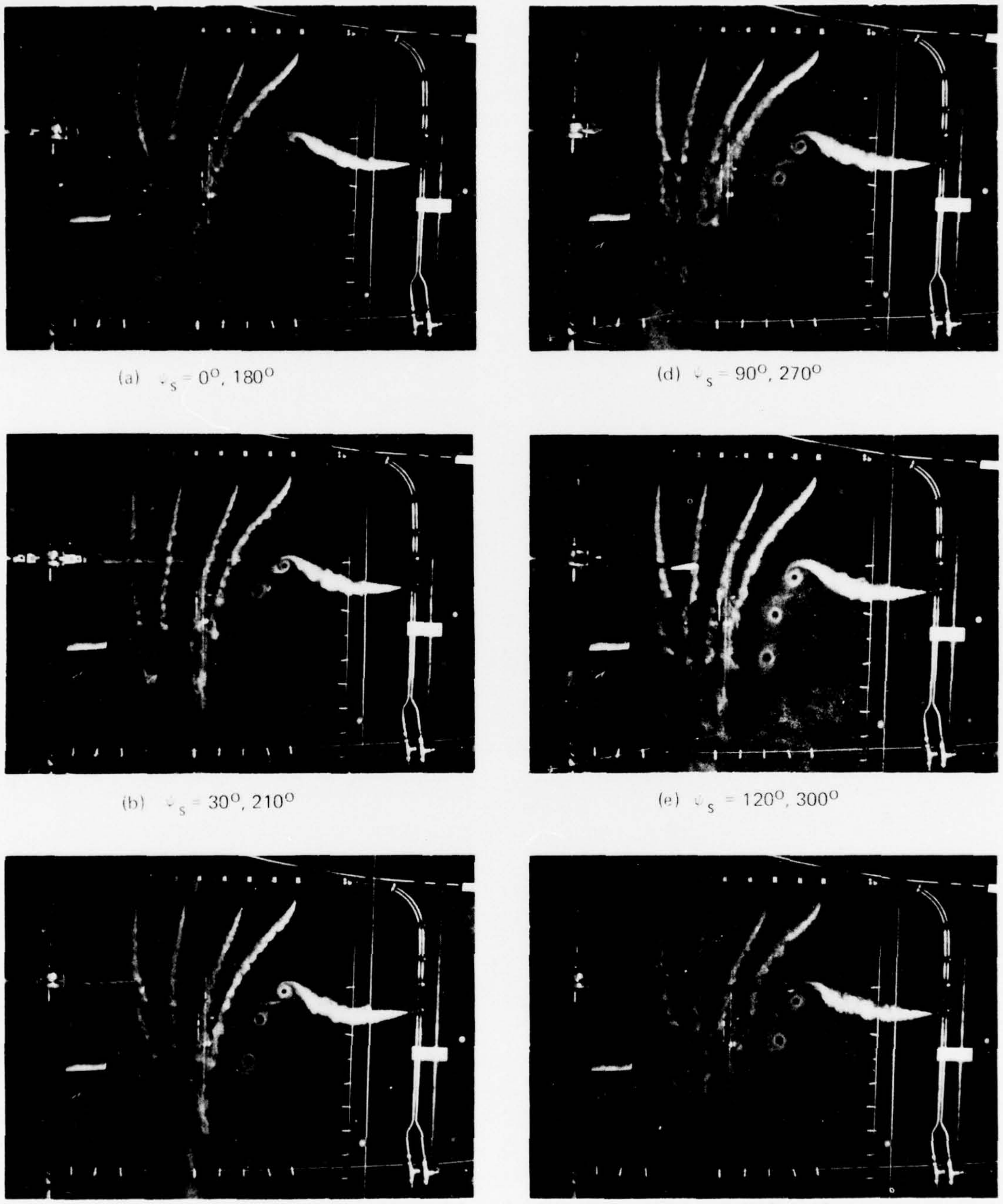

(a) $\psi_s = 0^\circ, 180^\circ$

(b) $\psi_s = 30^\circ, 210^\circ$

(c) $\psi_s = 60^\circ, 240^\circ$

(d) $\psi_s = 90^\circ, 270^\circ$

(e) $\psi_s = 120^\circ, 300^\circ$

(f) $\psi_s = 150^\circ, 330^\circ$

Figure 23. Smoke Flow Visualization Photographs of a Wake Cross Section for the Reference AH-1G Model Configuration and Test Condition for Varying Wake Azimuth Angles Relative to the Plane of Smoke.

77-06-177-1

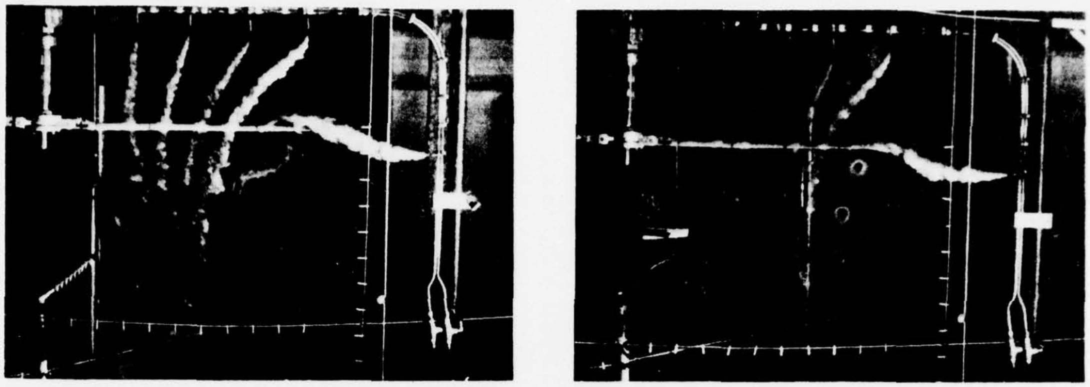

(a) ISOLATED ROTOR, REFERENCE CONDITION

(d) MODIFIED CANOPY

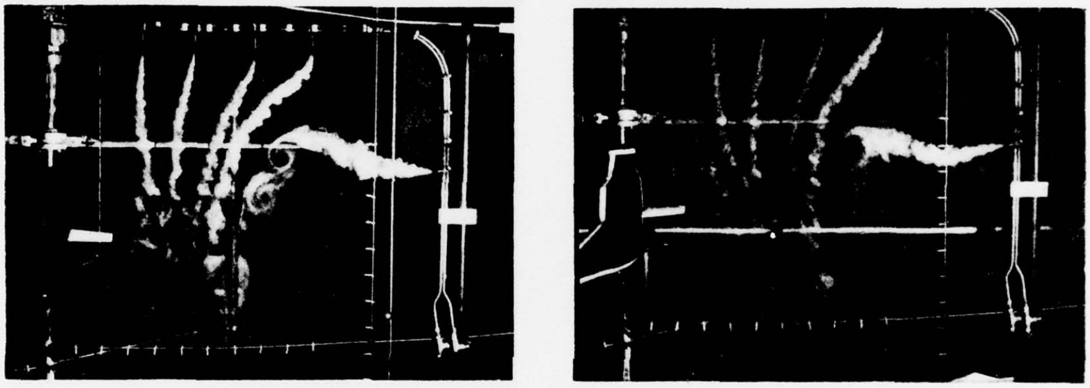

(b) $C_T = 0.75\, C_{T_{REF}}$

(e) IGE, H = 10 FT

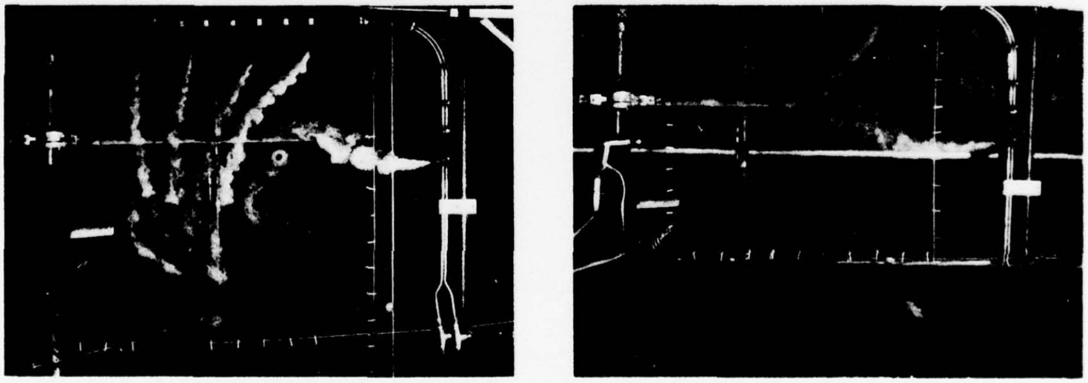

(c) $\Omega R = 0.75\, \Omega R_{REF}$

(f) IGE, H = 0

Figure 24. Smoke Flow Visualization Photographs of a Wake Cross Section for Various Test Configurations and Conditions.

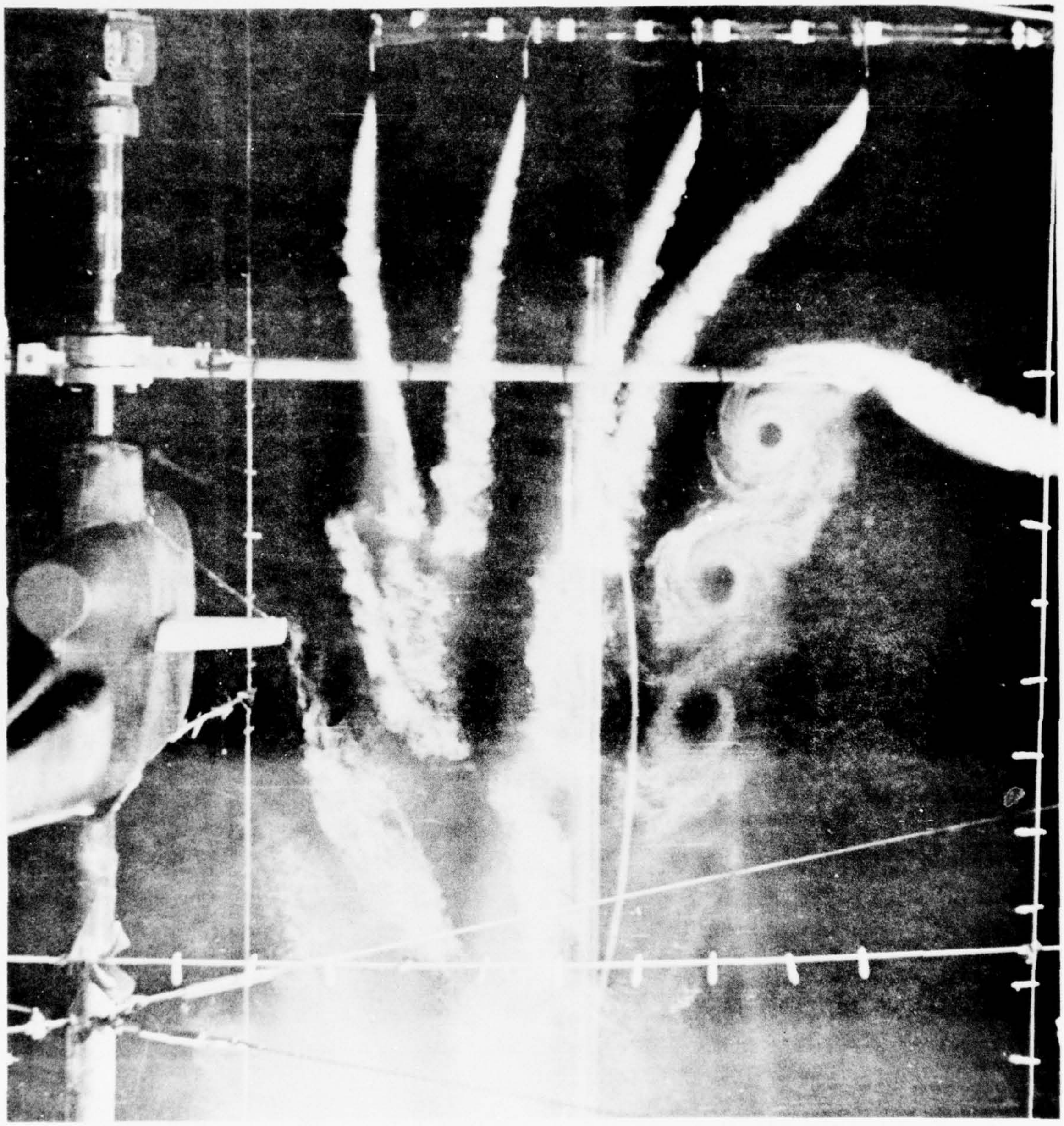

Figure 25. Smoke Flow Visualization Photograph of a Wake Cross Section for the Reference Configuration and Condition.

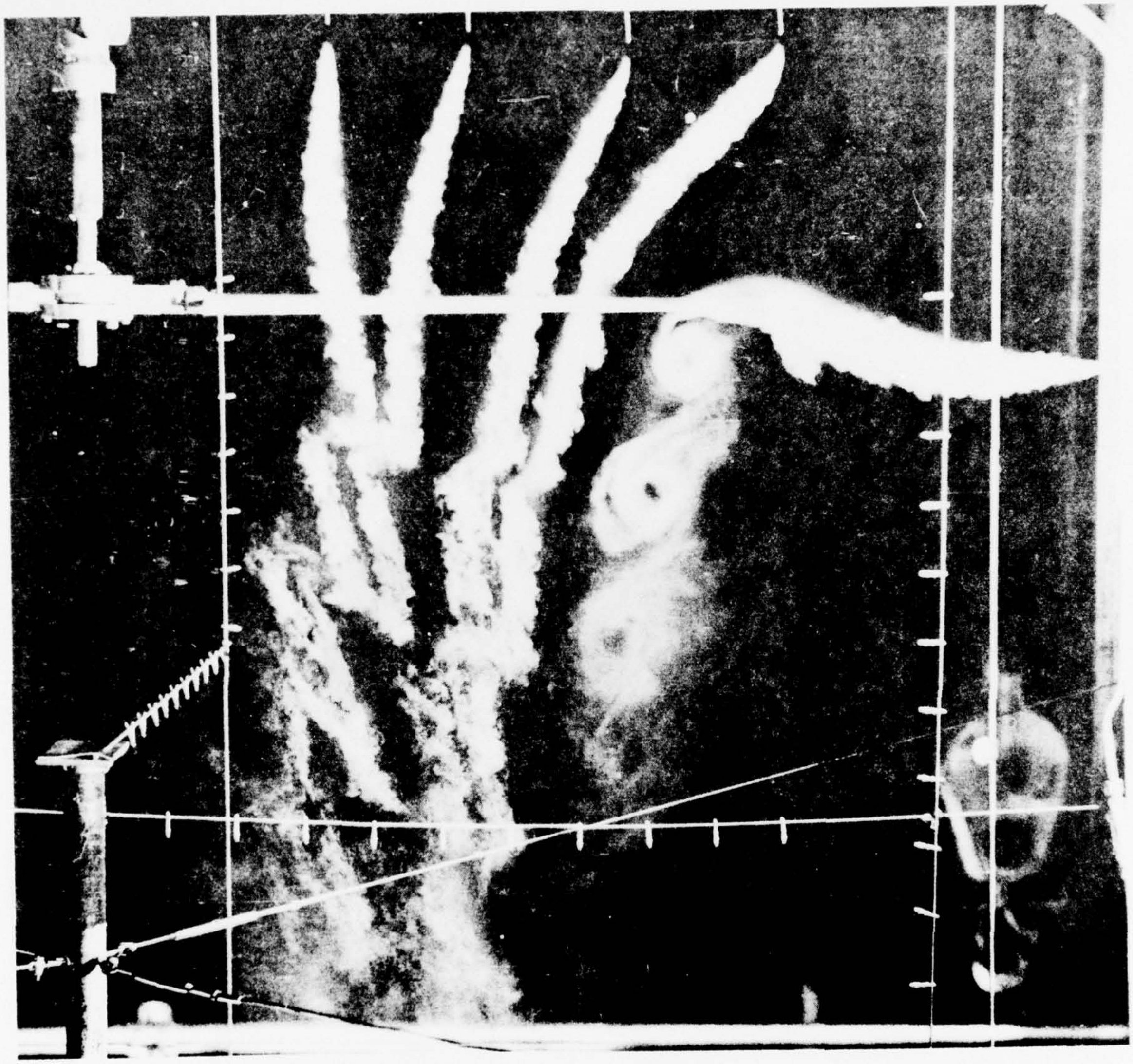

Figure 26. Smoke Flow Visualization Photograph of a Wake Cross Section for the Isolated Rotor and Reference Condition.

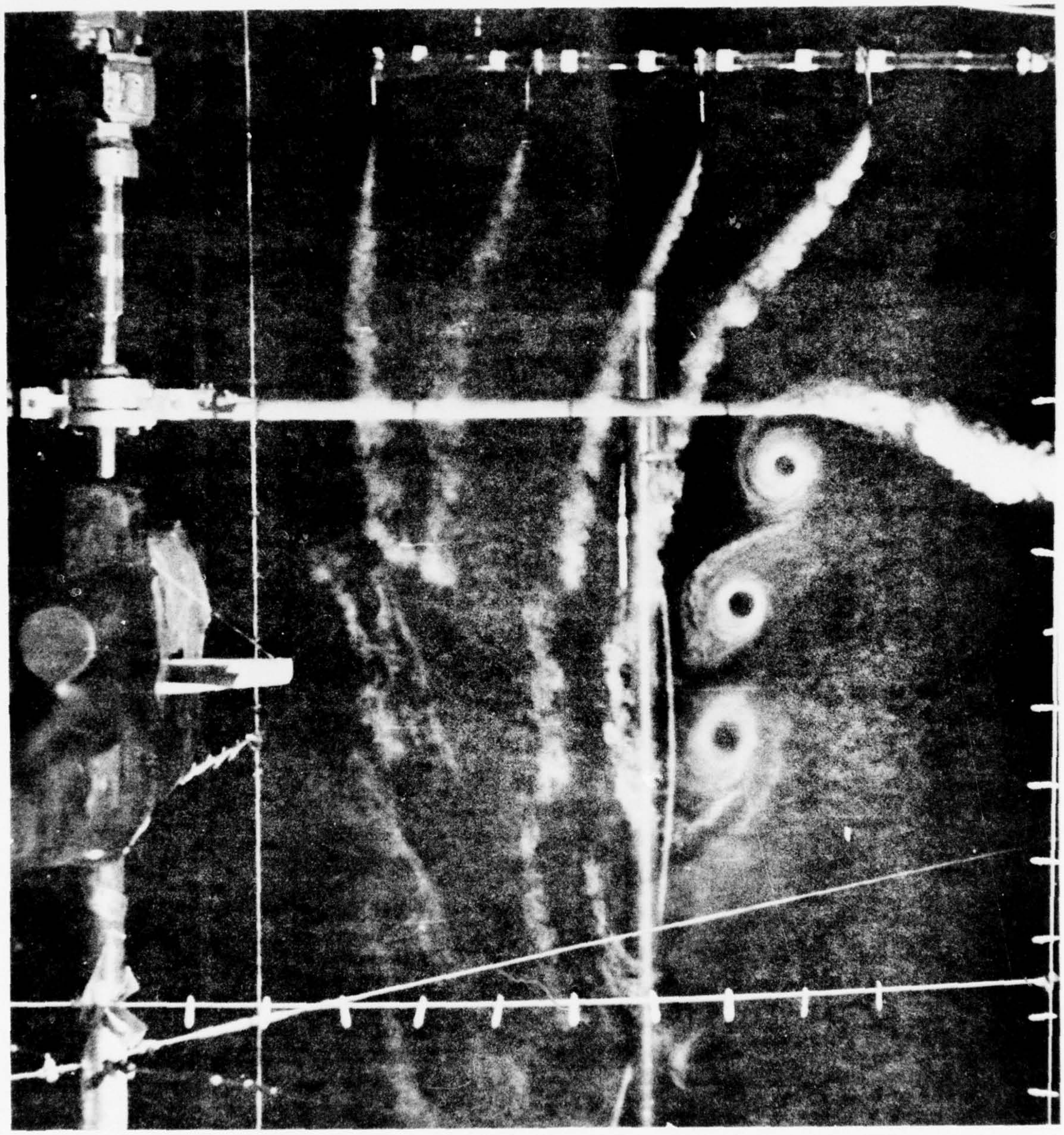

Figure 27. Smoke Flow Visualization Photograph of a Wake Cross Section for the Modified Canopy Configuration.

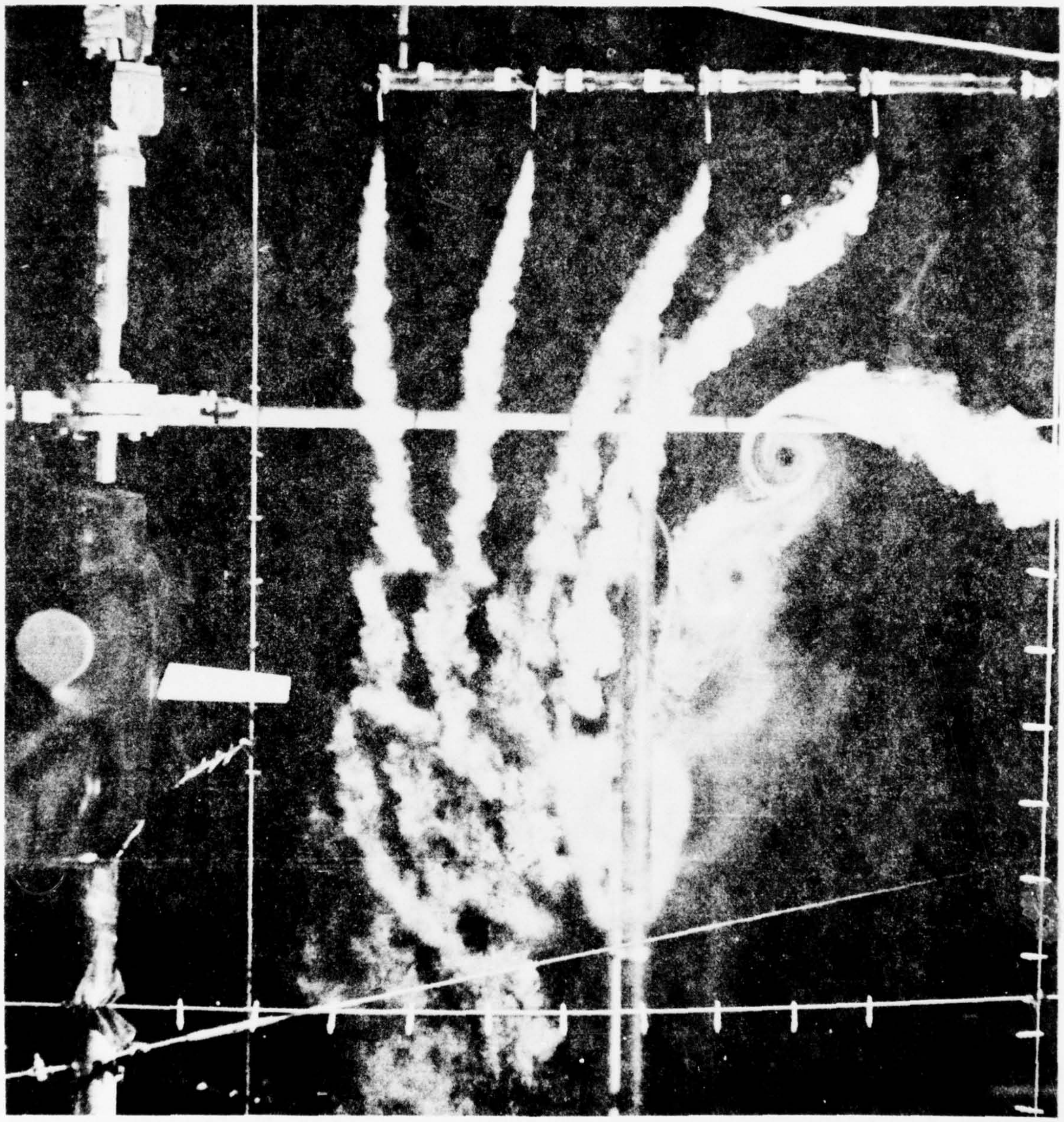

Figure 28. Smoke Flow Visualization Photograph of a Wake Cross Section for the Modified Thrust ($C_T = 0.75\ C_{T_{REF}}$) Condition.

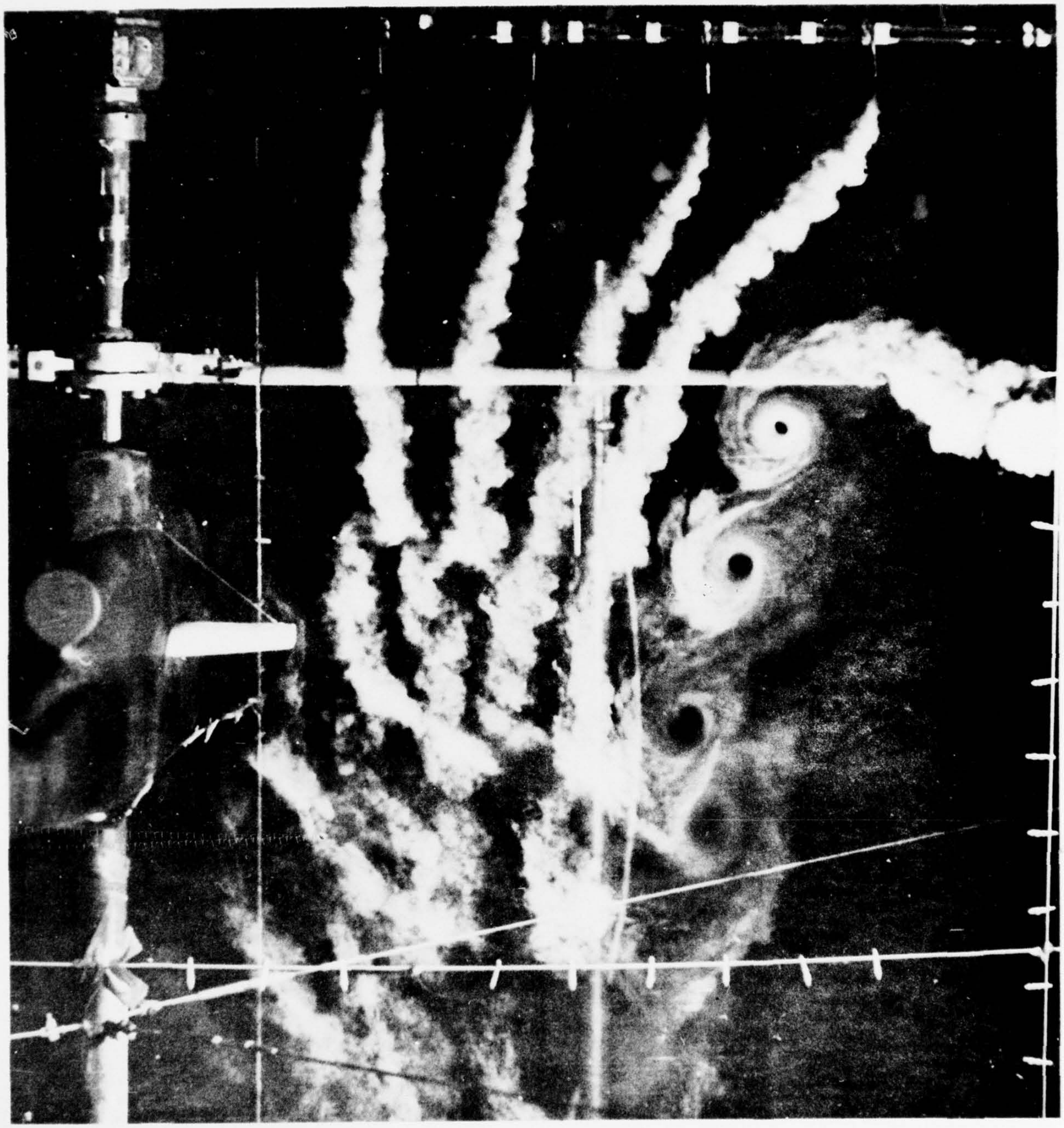

Figure 29. Smoke Flow Visualization Photograph of a Wake Cross Section for the Modified Tip Speed ($\Omega R = 0.75\ \Omega R_{REF}$) Condition.

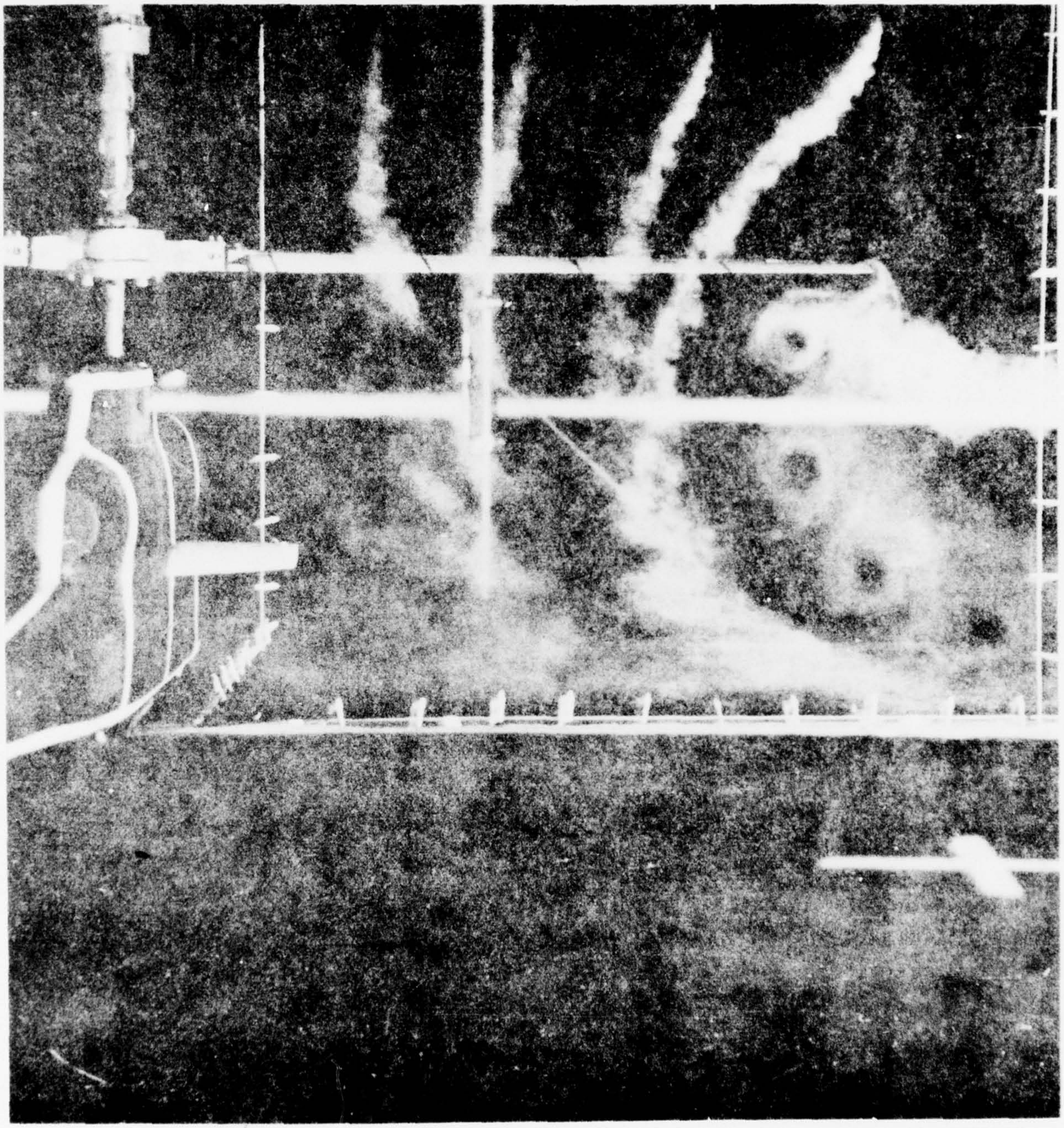

Figure 30. Smoke Flow Visualization Photograph of a Wake Cross Section for the In-Ground-Effect (Skid Height = 0) Condition.

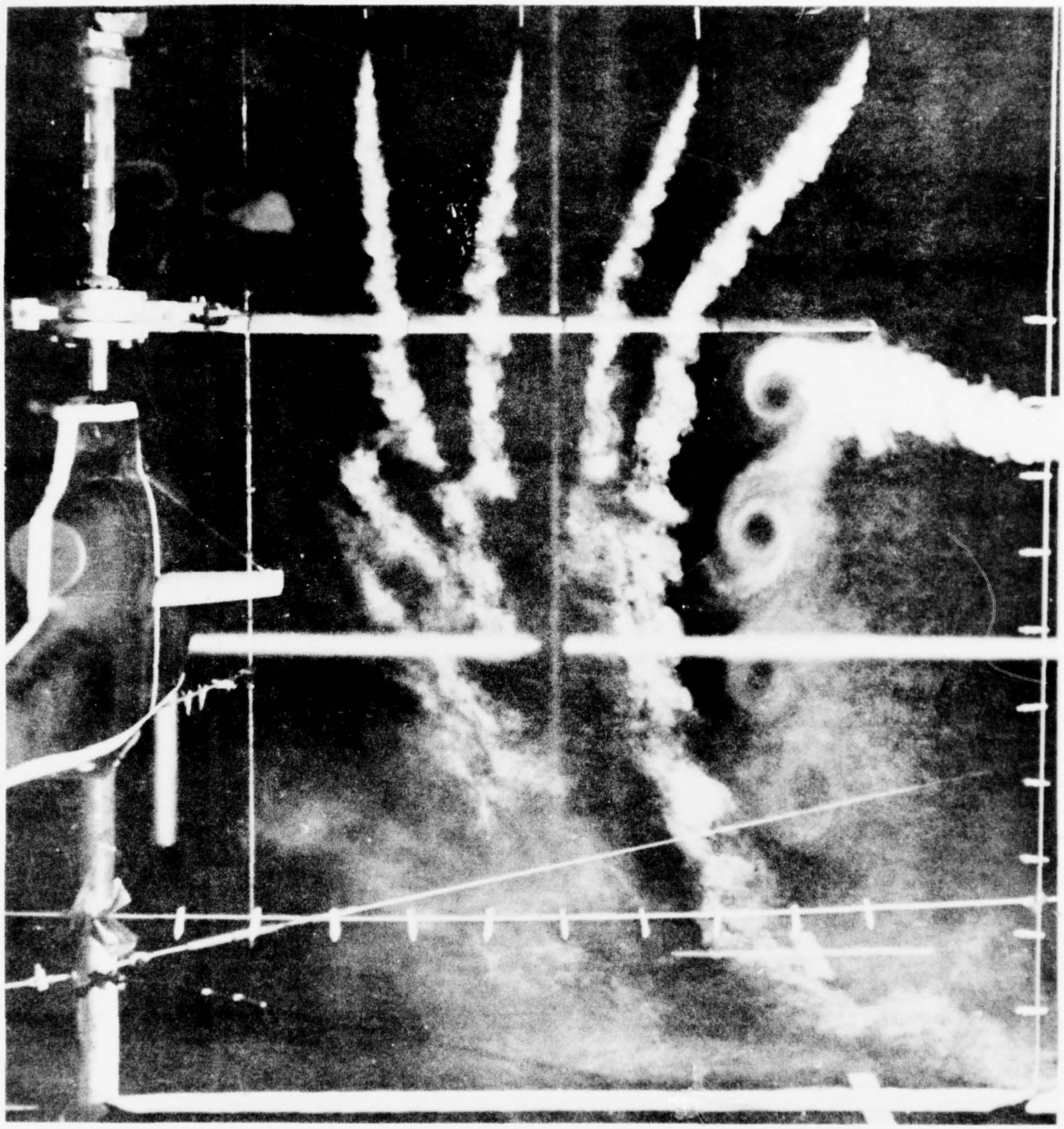

Figure 31. Smoke Flow Visualization Photograph of a Wake Cross Section for the In-Ground-Effect (Skid Height = 10 ft) Condition.

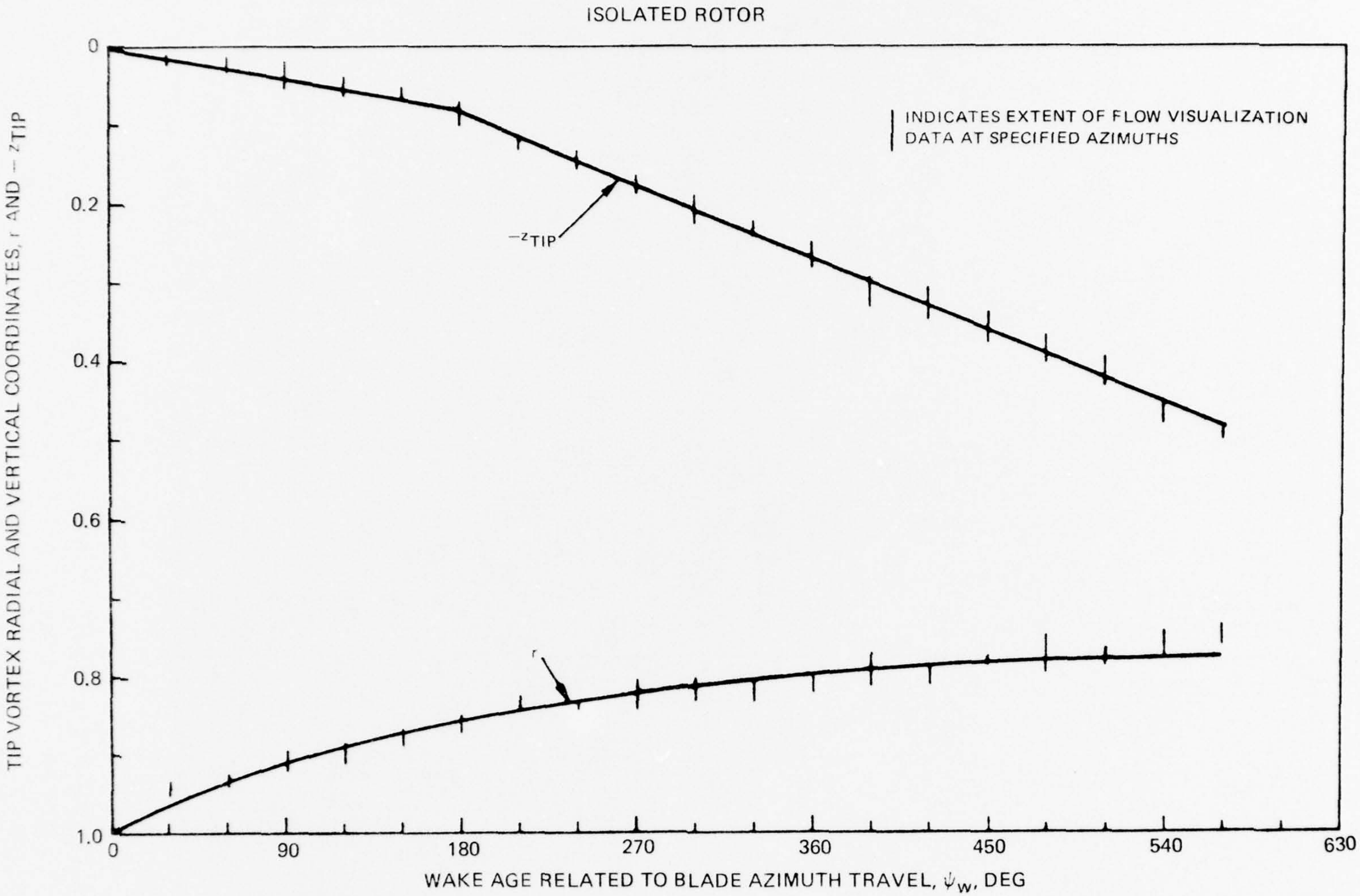

Figure 32. Tip Vortex Coordinates for Isolated Rotor.

77-07-92-1

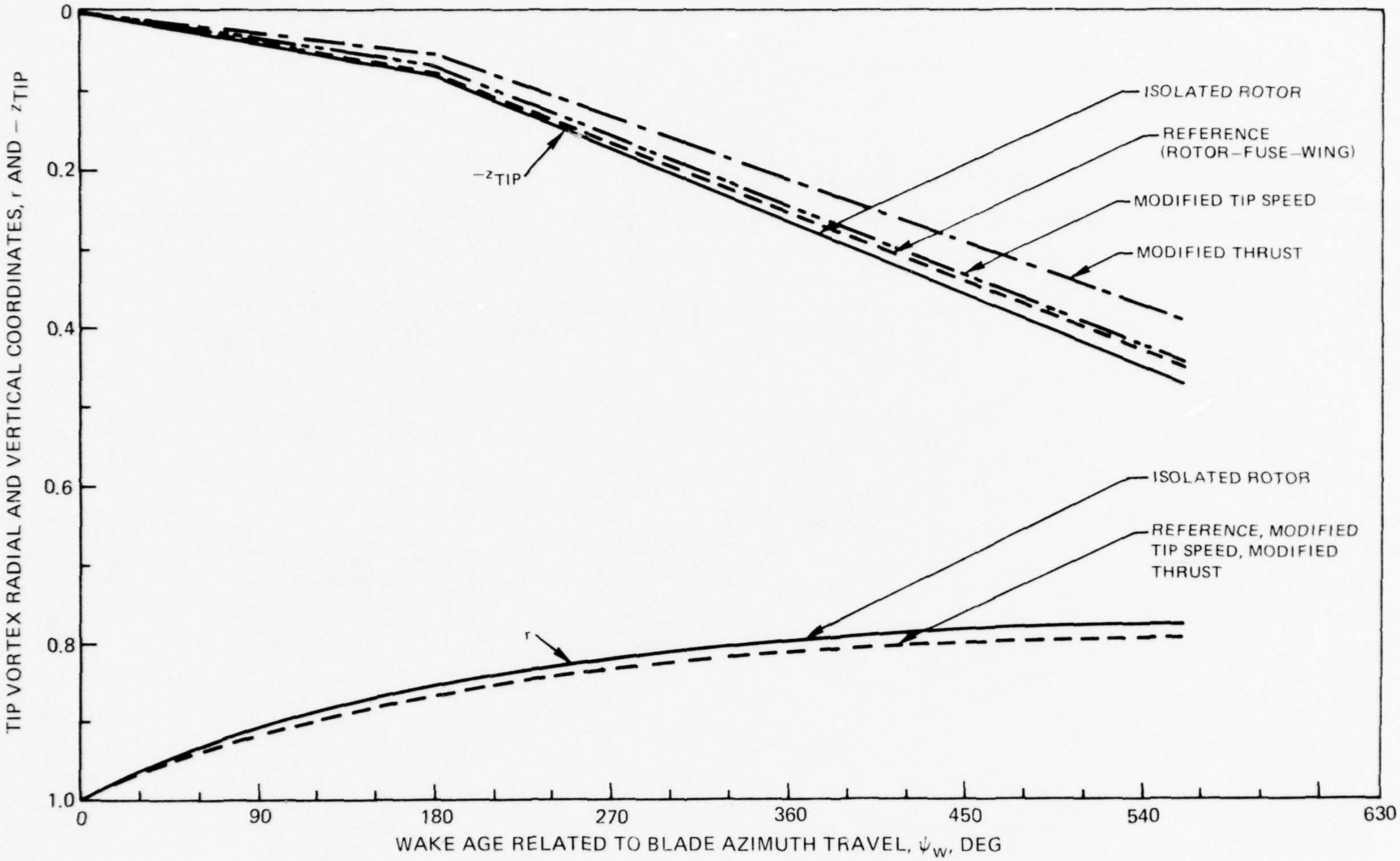

Figure 33. Tip Vortex Coordinates for Various Configurations and Conditions.

77–07–92–2

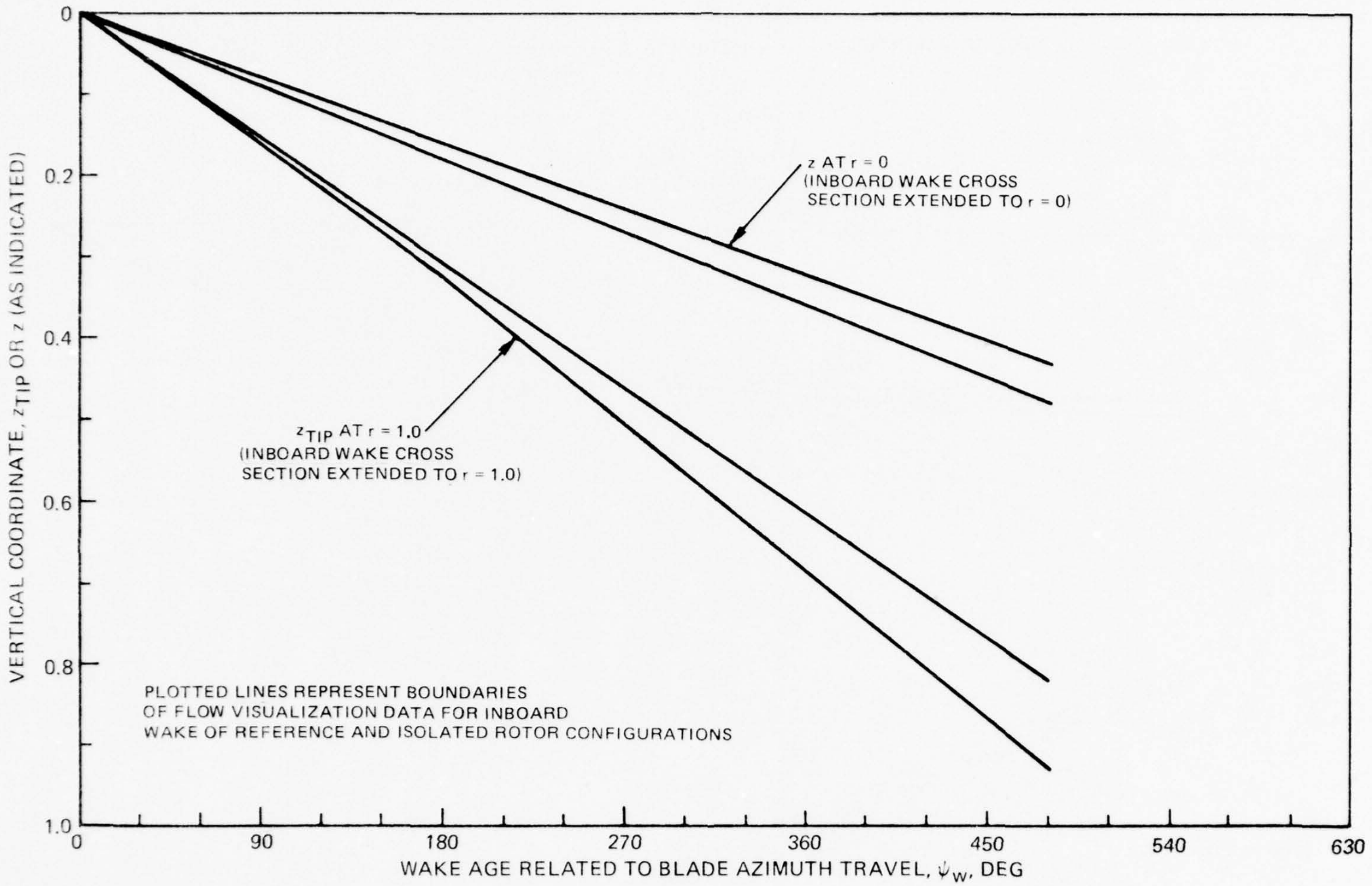

Figure 34. Inboard Vortex Sheet Coordinates for Reference and Isolated Rotor Configurations.

77-07-92-3

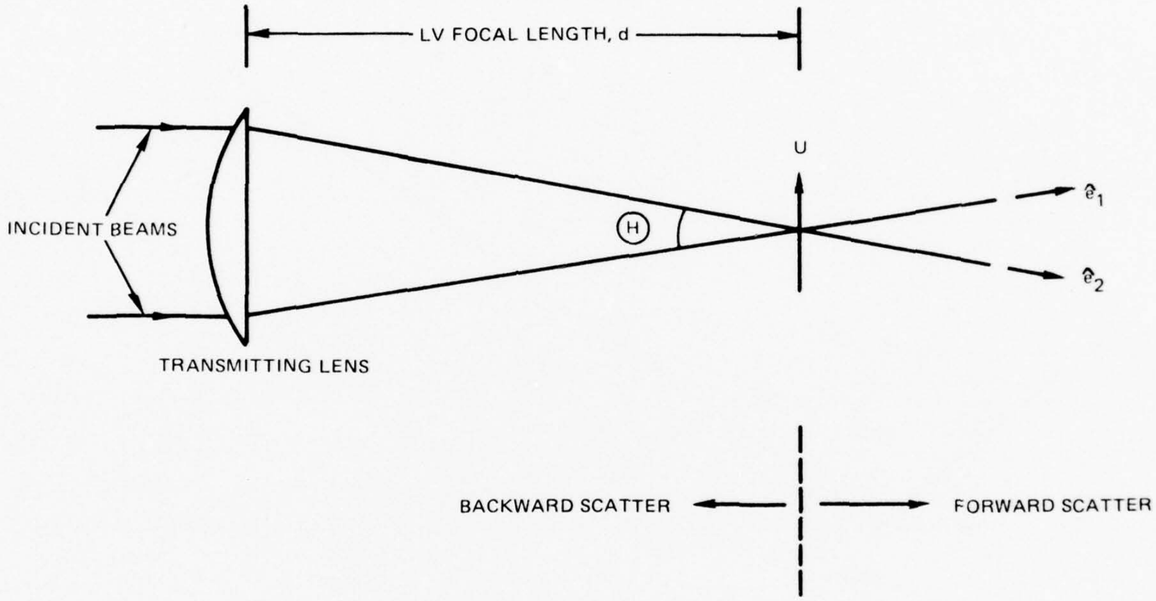

Figure 35. Schematic of Laser Velocimeter Dual-Scatter Transmitting Optics.

77-06-162-2

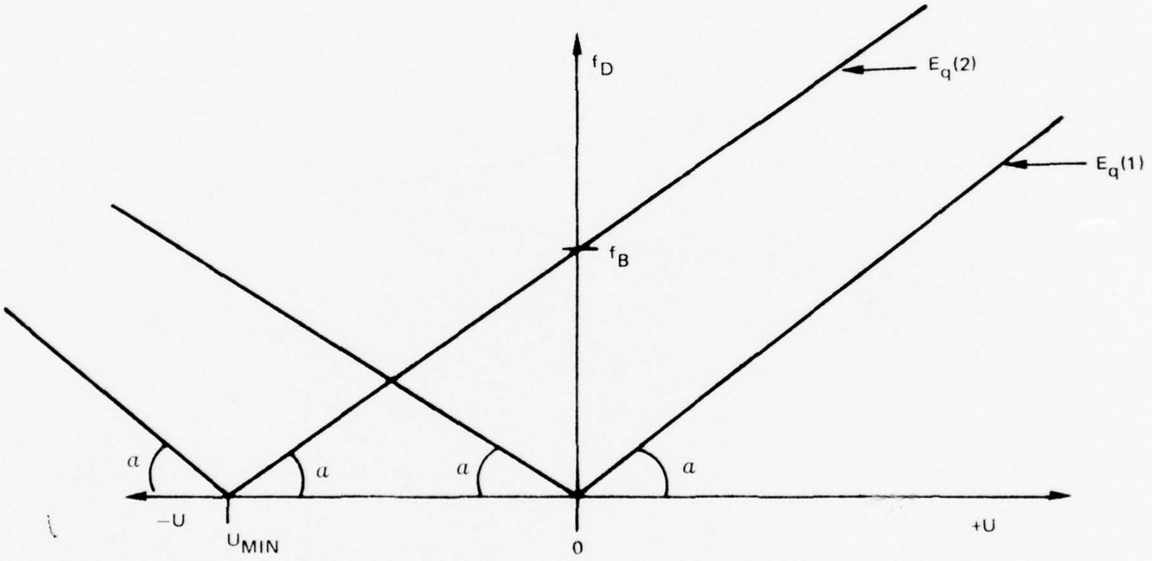

Figure 36. Laser Velocimeter Frequency-Velocity Calibration.

77-06-162-1

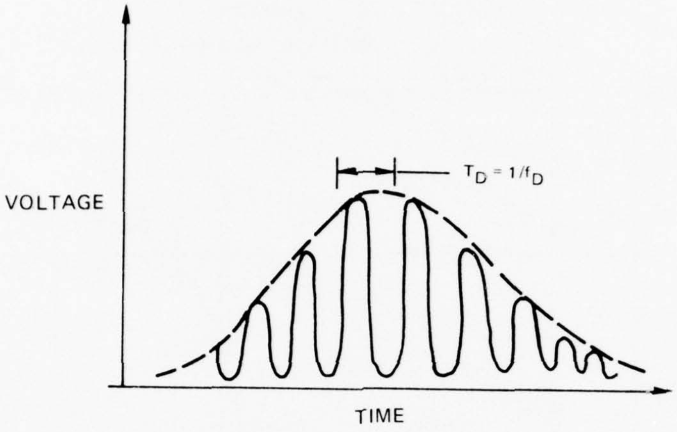

(a) PHOTOMULTIPLIER SIGNAL

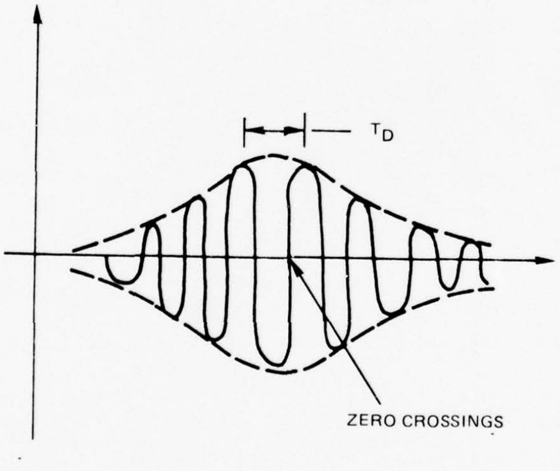

(b) PROCESSED SIGNAL

Figure 37. Laser Velocimeter Signals.

77-06-162-3

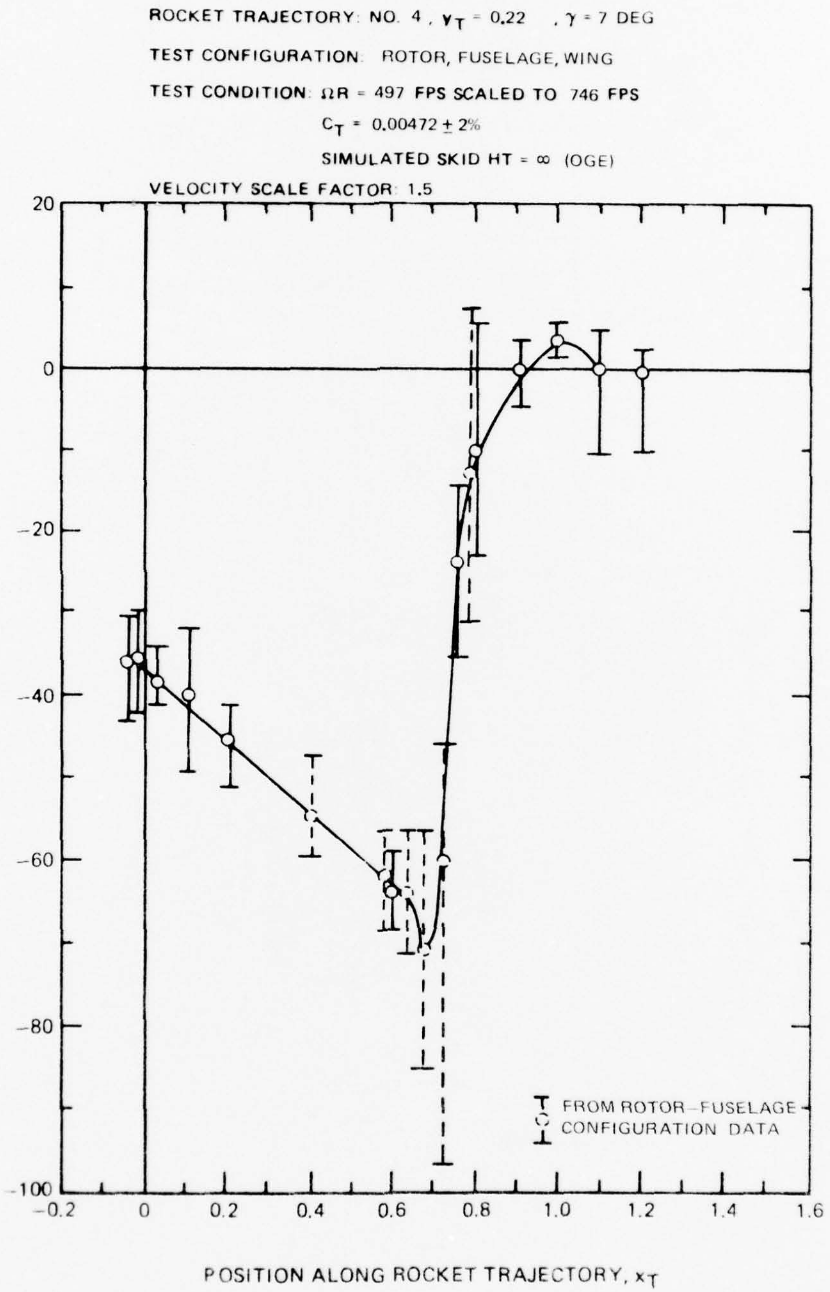

Figure 38. Sample Plot of the Time-Averaged and Peak v_{z_T} Flow Velocity Component for a Rocket Trajectory of the Reference Configuration and Condition.

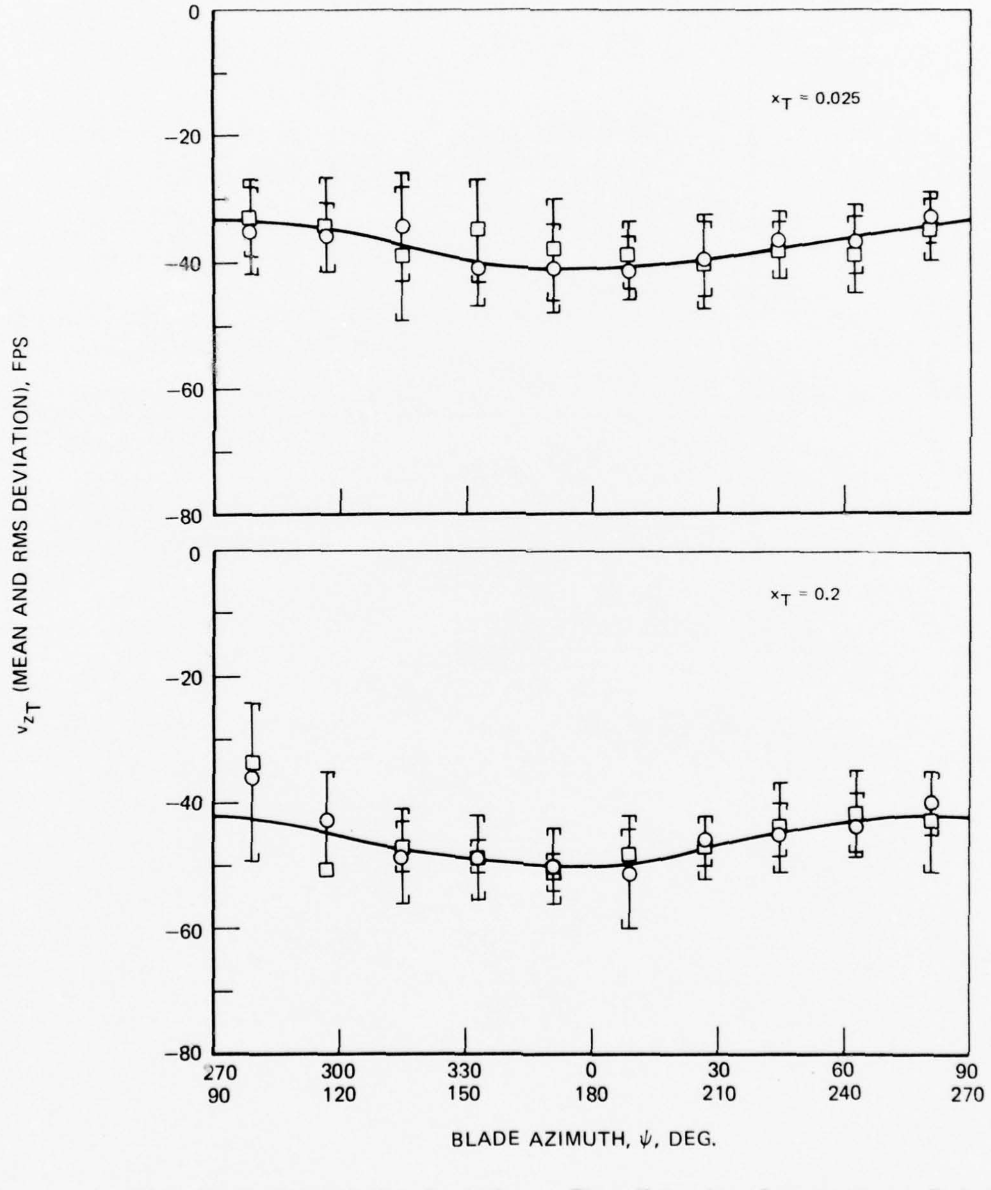

ROCKET TRAJECTORY: NO. 4, $v_T = 0.22$, γ = 7 DEG.

TEST CONFIGURATION: ROTOR–FUSELAGE–WING

TEST CONDITION: ΩR = 497 FPS SCALED TO 746 FPS

$C_T = 0.00472 \pm 2\%$

SIMULATED SKID HT = ∞ (OGE)

VELOCITY SCALE FACTOR: 1.5

Figure 39. Time Variation of the Scaled v_{z_T} Flow Velocity Component at Points on Rocket Trajectory No. 4 for the Reference Configuration and Condition.

77–06–233–3

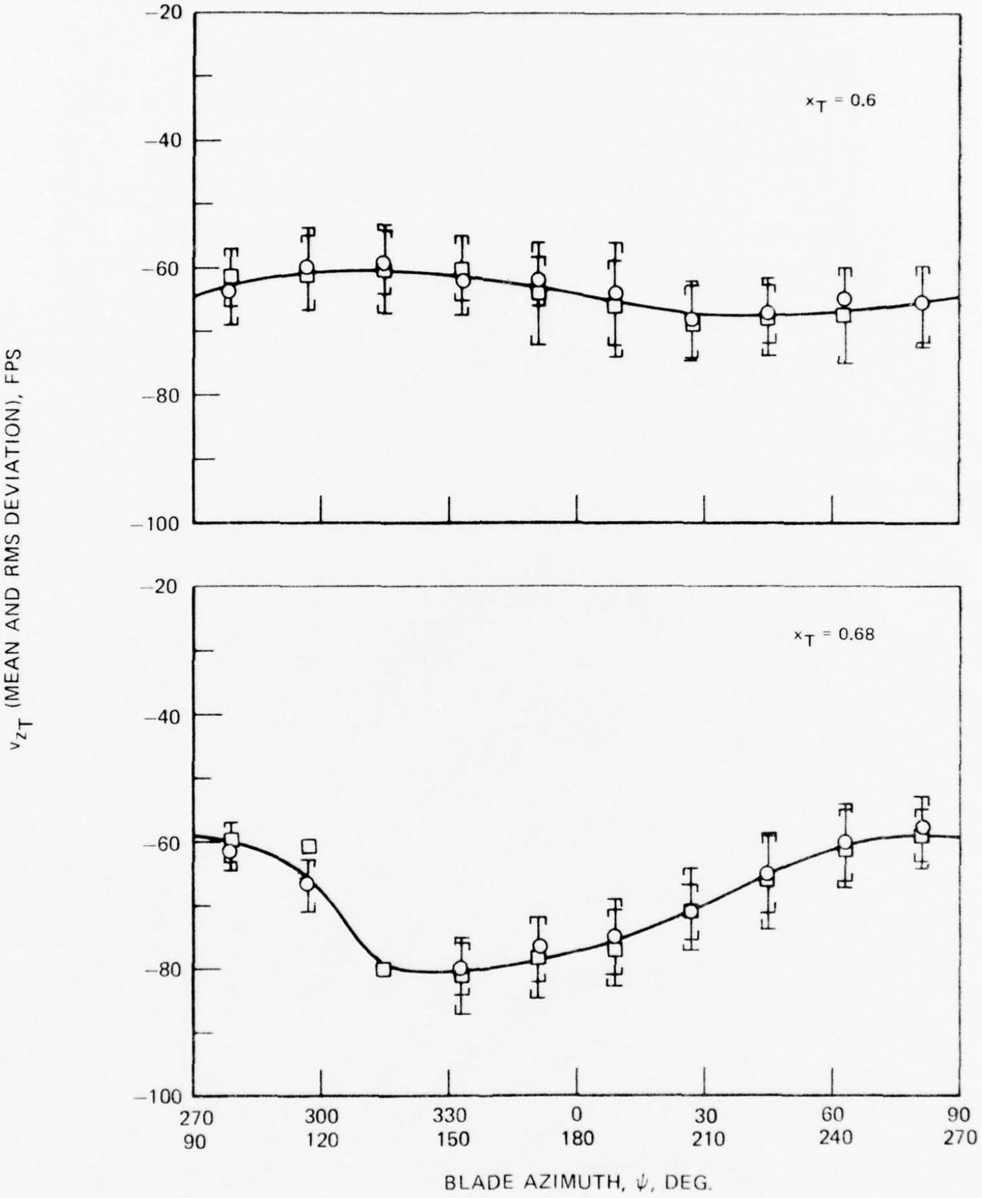

Figure 39. Continued.

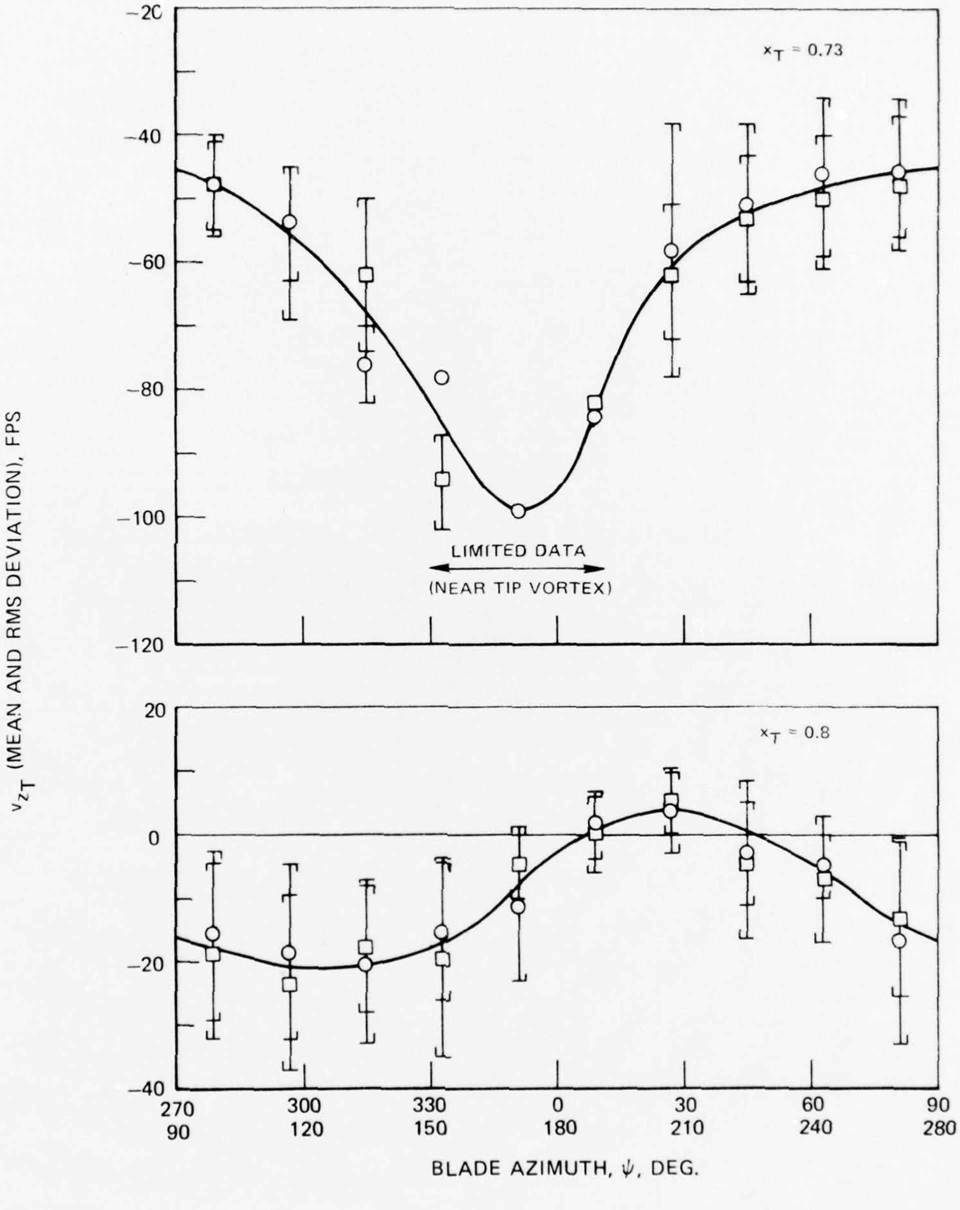

Figure 39. Continued.

77–06–233–4

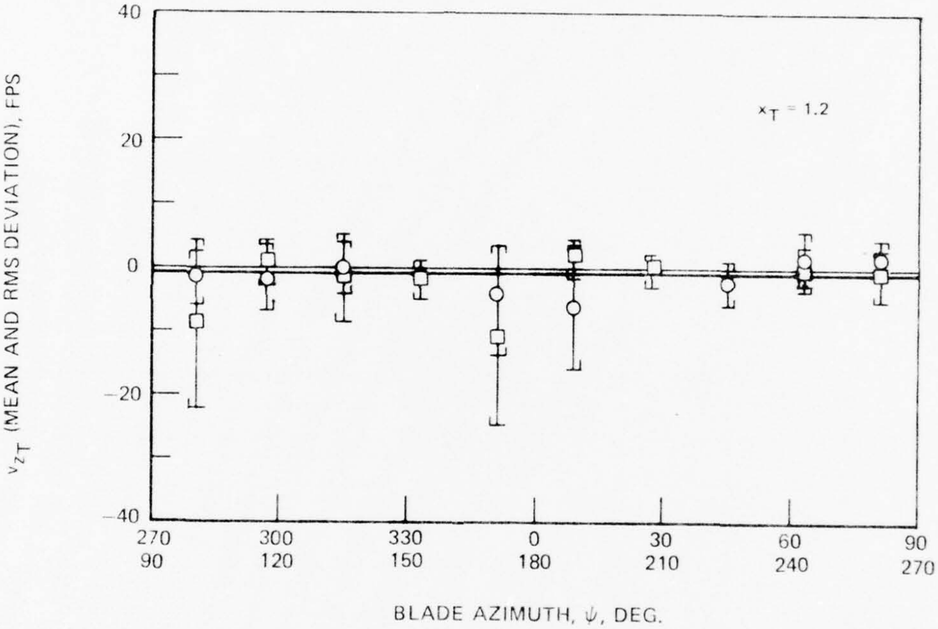

Figure 39. Concluded.

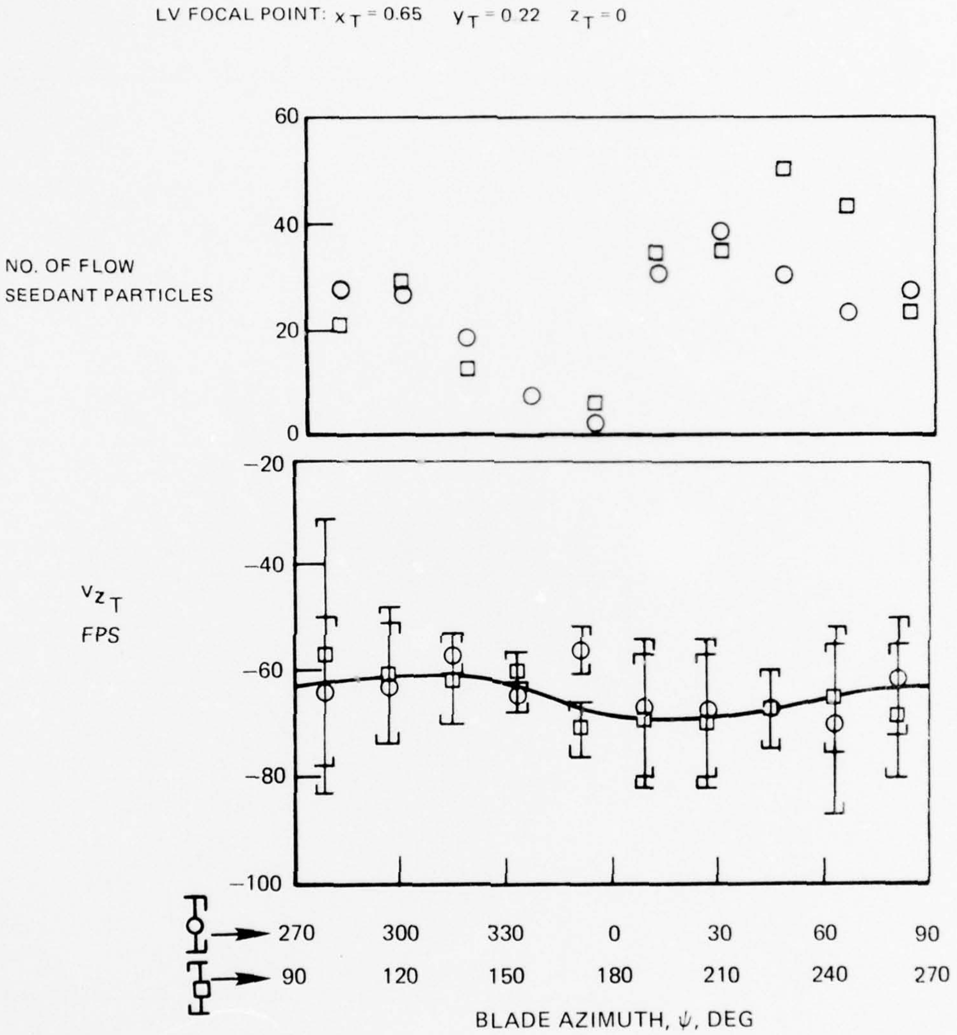

(a) At $x_T = 0.65$ (Inboard of Wake Boundary)

Figure 40. Sample Time Variations of Flow Velocity and Seedant Particles In the Vicinity of the Wake Boundary.

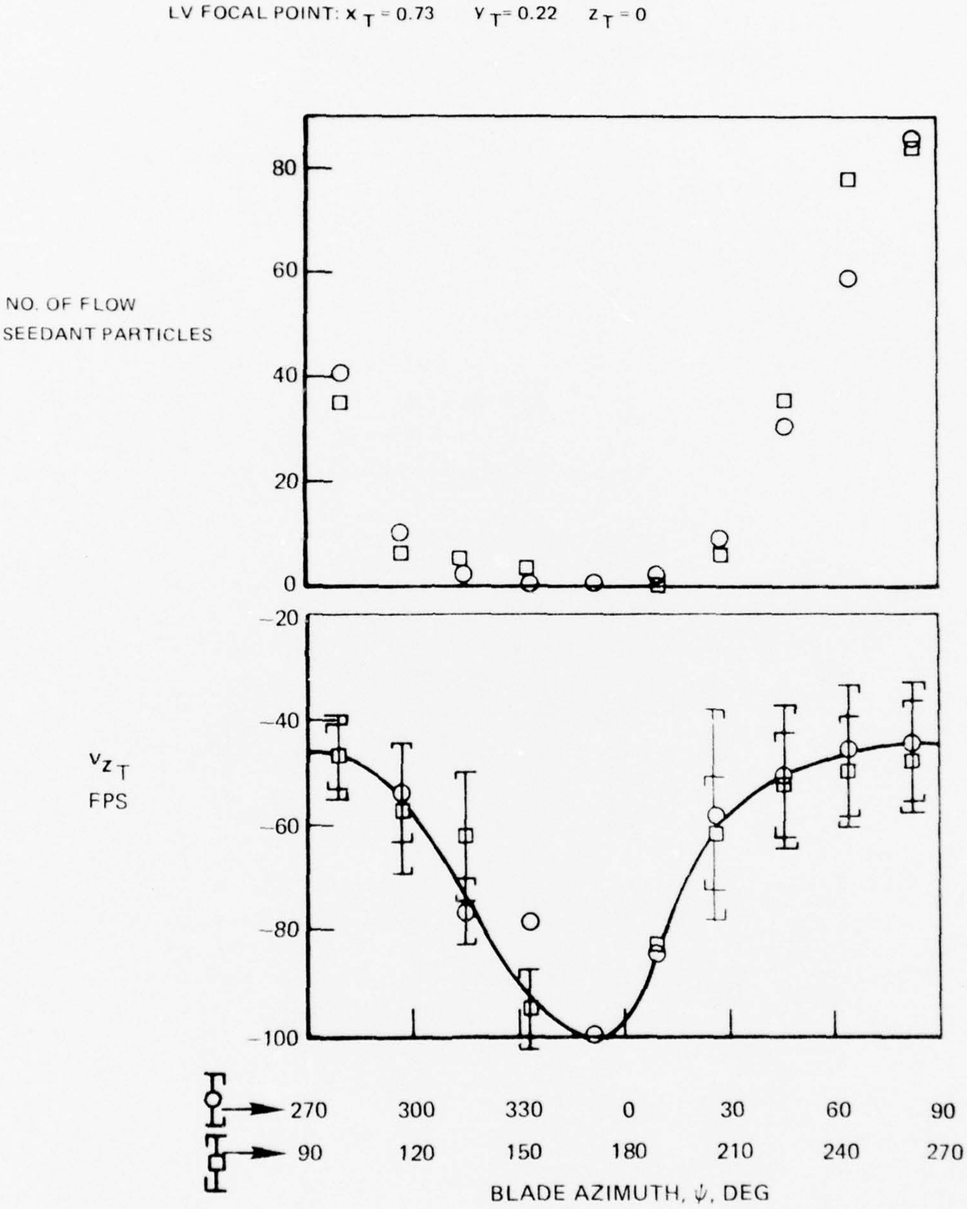

(b) At x_T = 0.73 (In Close Proximity to Wake Boundary)

Figure 40. Concluded.

LV TRAVERSE LINE: $y_T=0, \gamma=7^\circ$

TEST CONFIGURATION: ROTOR

TEST CONDITION: ΩR = 497 **FPS SCALED TO** 746 **FPS**

C_T = 0.00472 ± 2%

SIMULATED GROUND **HT** = ∞ (OGE)

VELOCITY SCALE FACTOR: 1.5

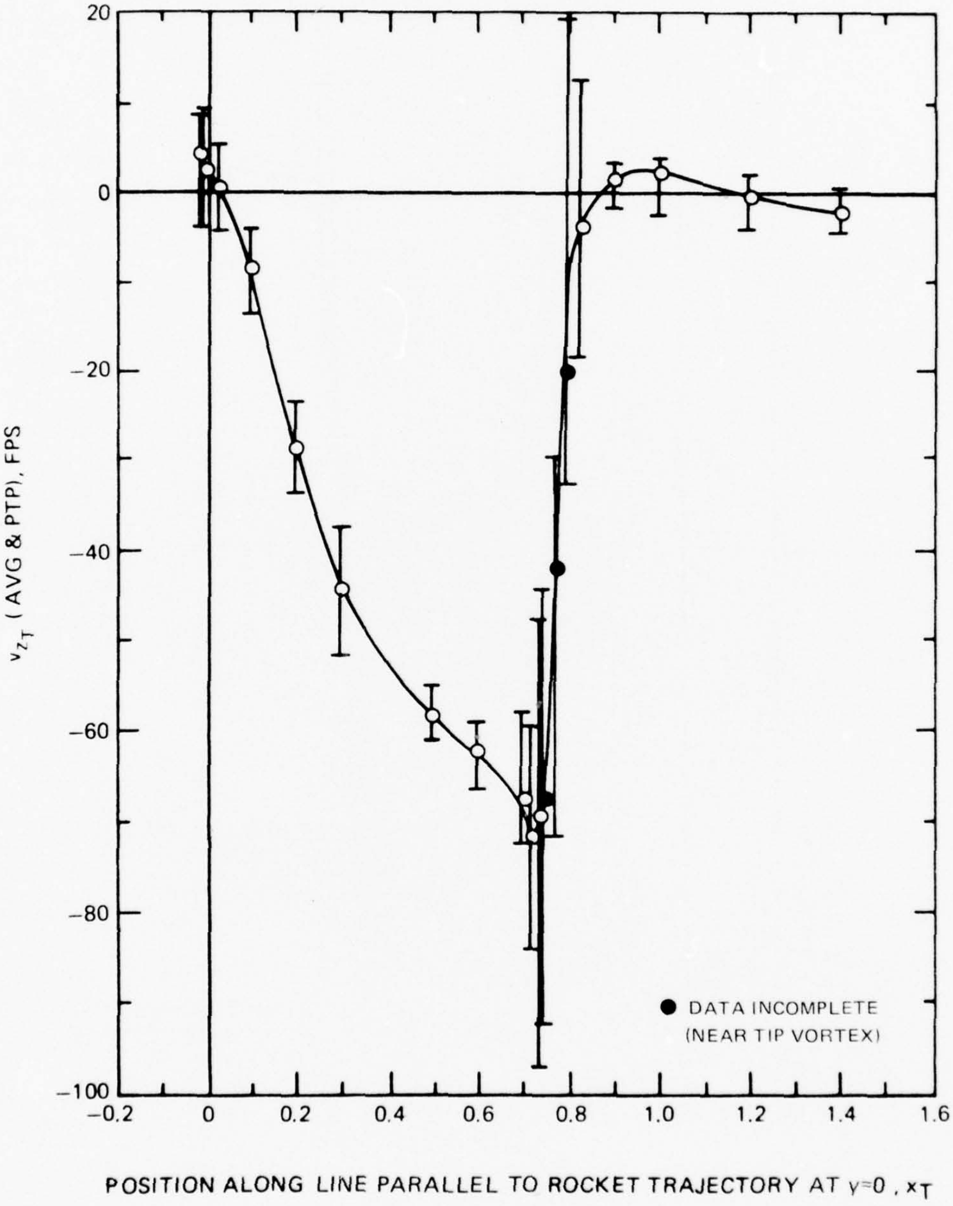

Figure 41. Variation of the Time-Average and Peaks of the Scaled v_{z_T} Flow Velocity Component at y_T = 0 For the Isolated Rotor Configuration and Reference Condition.

77-06-214-8

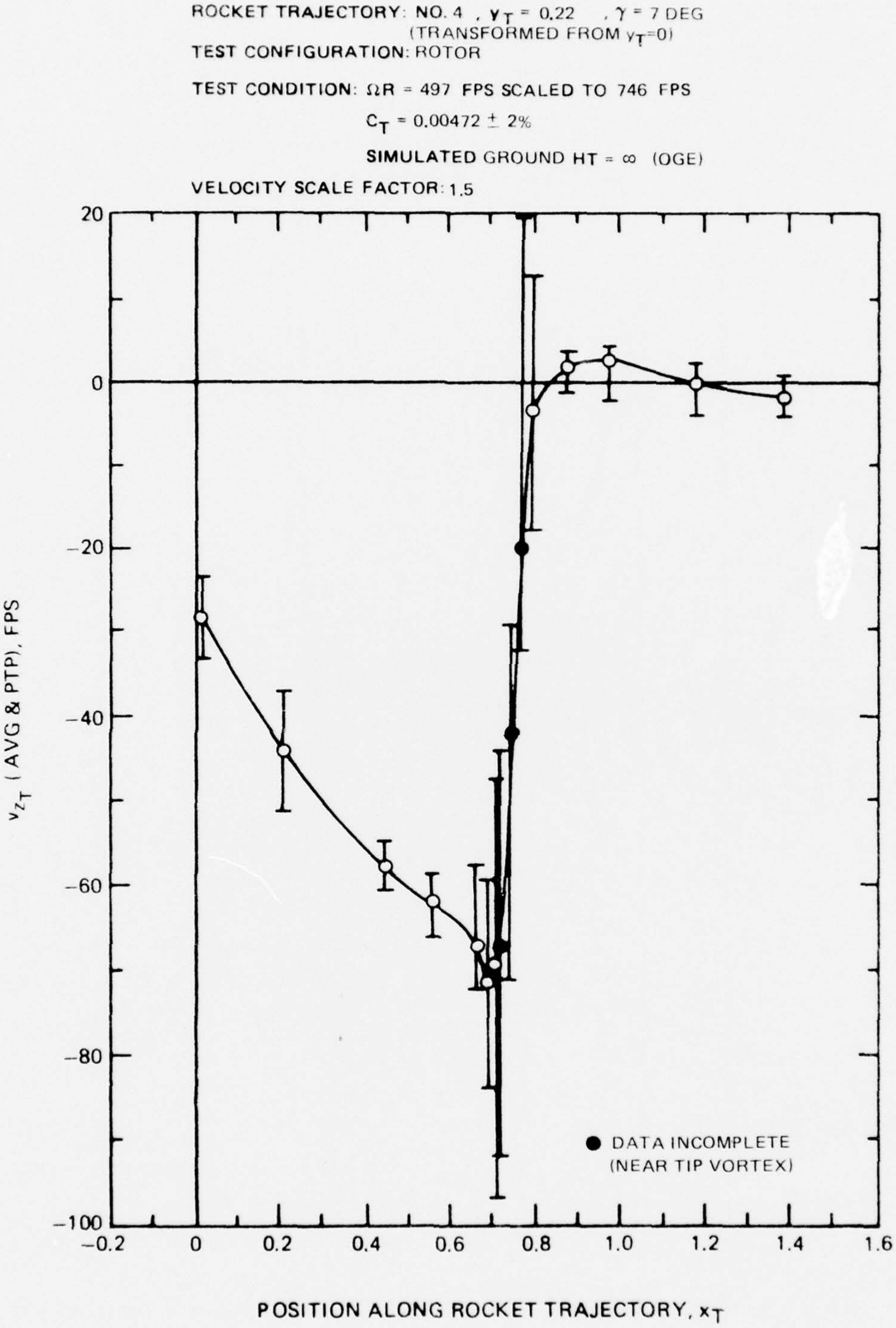

Figure 42. Variation of the Time-Average and Peaks of the Scaled v_{z_T} Flow Velocity Component at Rocket Trajectory No. 4 (Transformed From y_T = 0) For the Isolated Rotor Configuration and Reference Condition.

77–06–214–7

ROCKET TRAJECTORY: NO. 4 , y_T = 0.22 , γ = 7 DEG
(TRANSFORMED FROM y_T=0)
TEST CONFIGURATION: ROTOR
TEST CONDITION: ΩR = 497 **FPS SCALED TO** 746 **FPS**
C_T = 0.00472 ± 2%
SIMULATED GROUND **HT** = ∞ (OGE)
VELOCITY SCALE FACTOR: 1.5

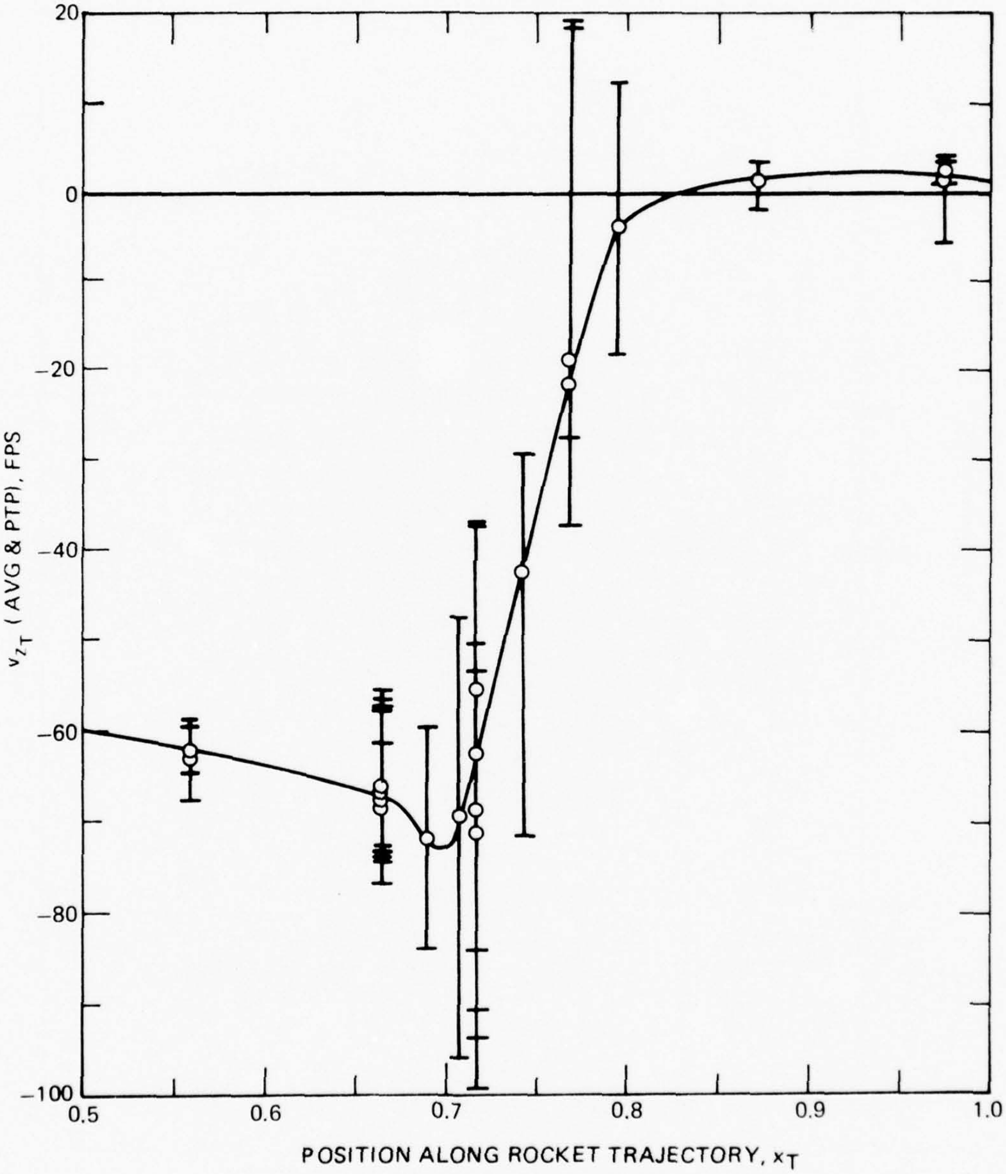

Figure 43. Variation of the Time-Average and Peaks of the Scaled v_{z_T} Flow Velocity Component at Rocket Trajectory No. 4 (Transformed From y_T = 0) For the Isolated Rotor Configuration and Reference Condition in Vicinity of Wake Boundary.

77-06-214-6

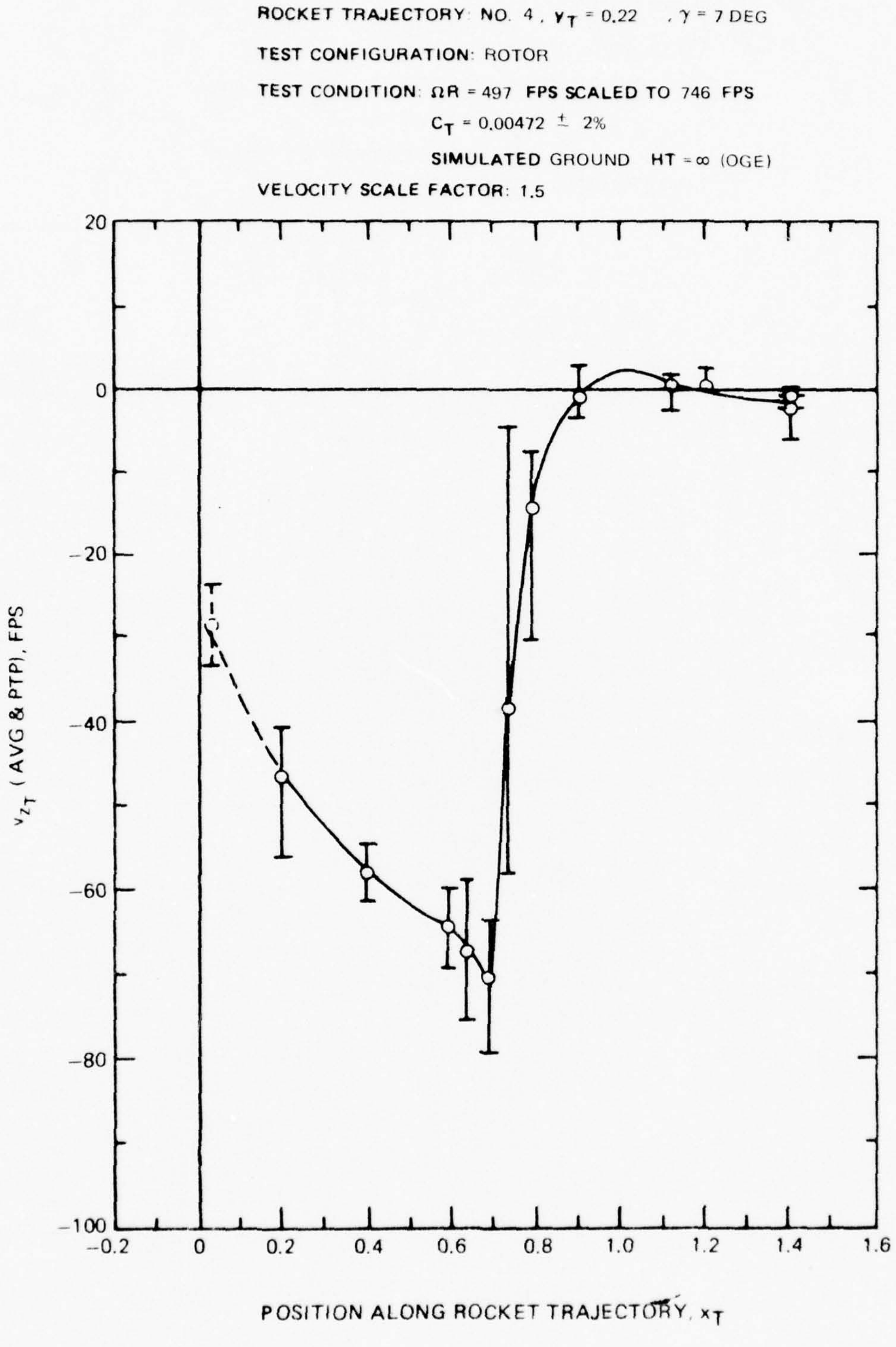

Figure 44. Variation of the Time-Average and Peaks of the Scaled v_{z_T} Flow Velocity Component at Rocket Trajectory No. 4 for the Isolated Rotor Configuration and Reference Condition.

77-06-214-2

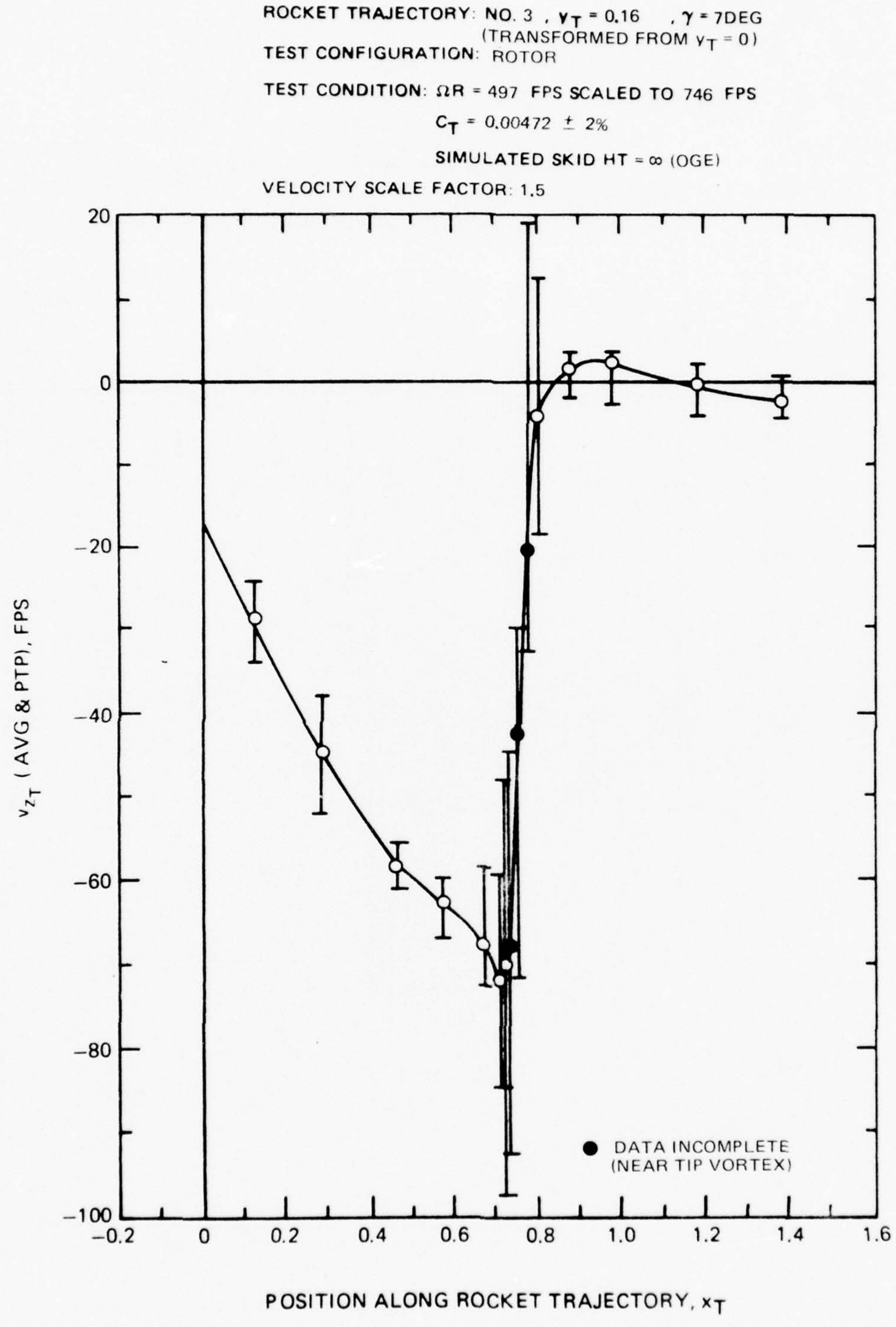

Figure 45. Variation of the Time-Average and Peaks of the Scaled v_{z_T} Velocity Component at Rocket Trajectory No. 3 (Transformed From y_T = 0) For The Isolated Rotor Configruation and Reference Condition.

77–06–214–3

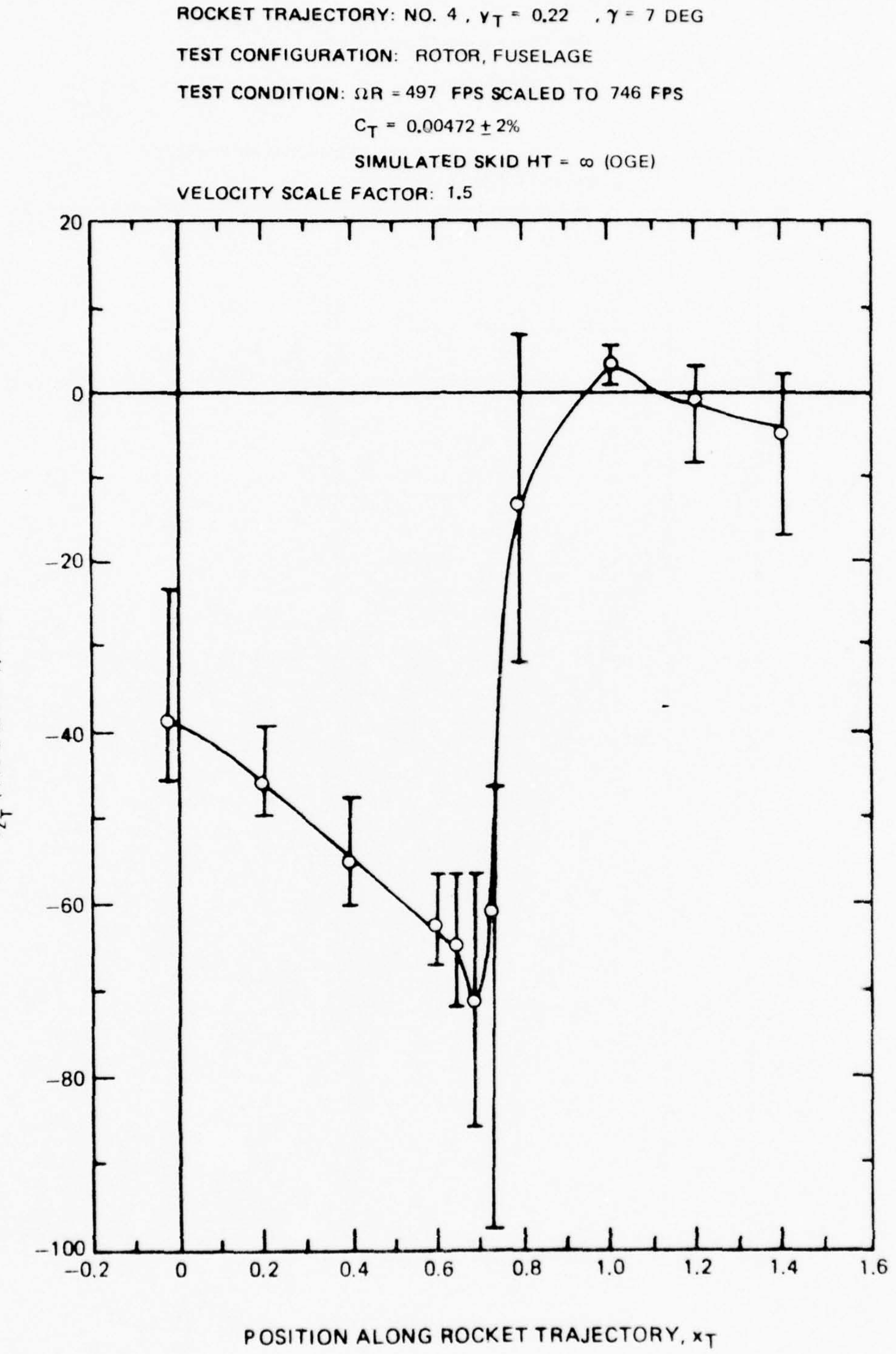

Figure 46. Variation of the Time-Average and Peaks of the Scaled v_{z_T} Flow Velocity Component at Rocket Trajectory No. 4 for the Rotor-Fuselage Configuration and Reference Condition.

77–06–187–15

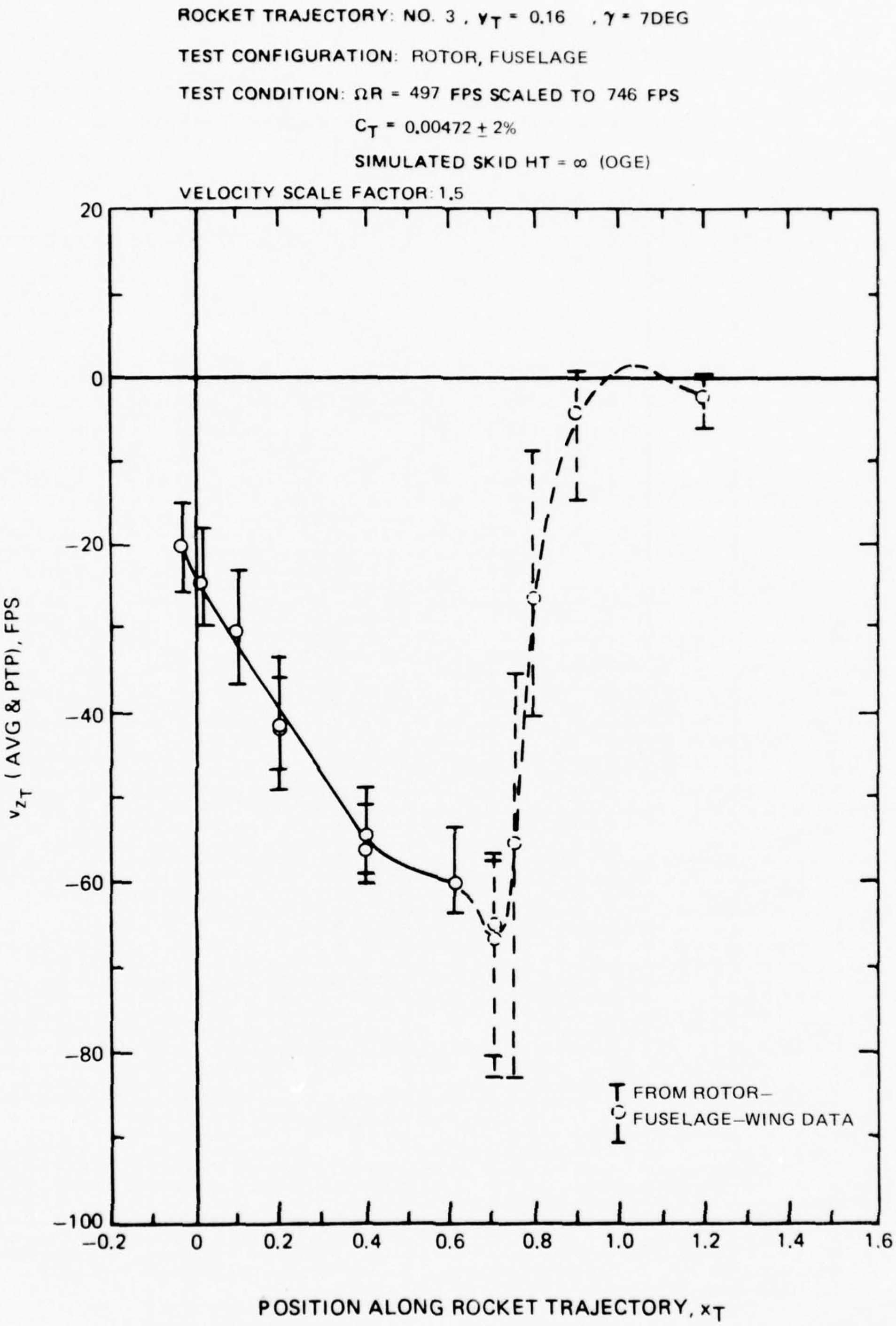

Figure 47. Variation of the Time-Average and Peaks of the Scaled v_{z_T} Flow Velocity Component at Rocket Trajectory No. 3 for the Rotor-Fuselage Configuration and Reference Condition.

77–06–187–4

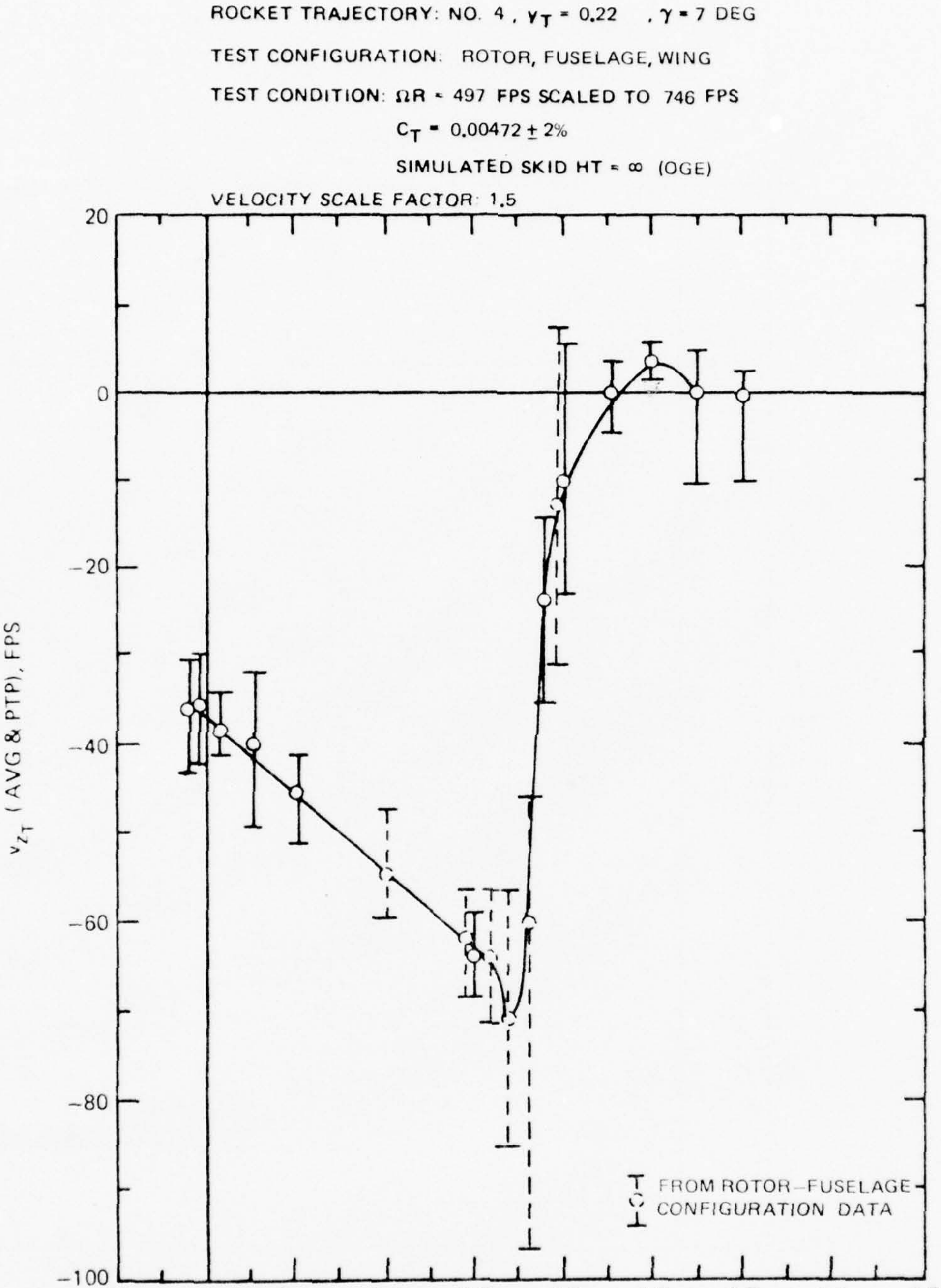

Figure 48. Variation of the Time-Average and Peaks of the Scaled v_{z_T} Flow Velocity Component at Rocket Trajectory No. 4 for the Reference Configuration and Reference Condition.

77–06–187–14

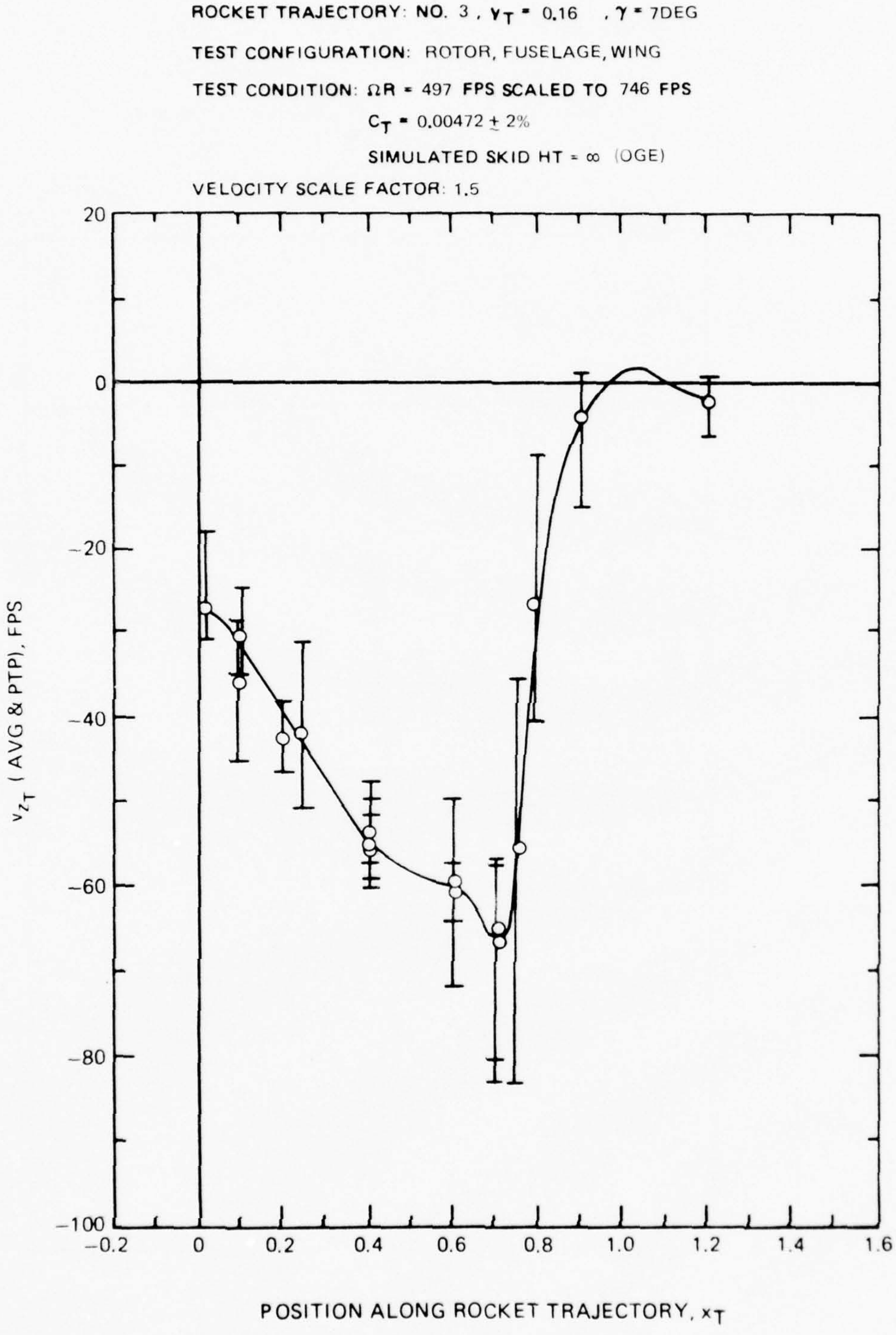

Figure 49. Variation of the Time-Average and Peaks of the Scaled v_{z_T} Flow Velocity Component at Rocket Trajectory No. 3 for the Reference Configuration and Reference Condition.

77-06-187-2

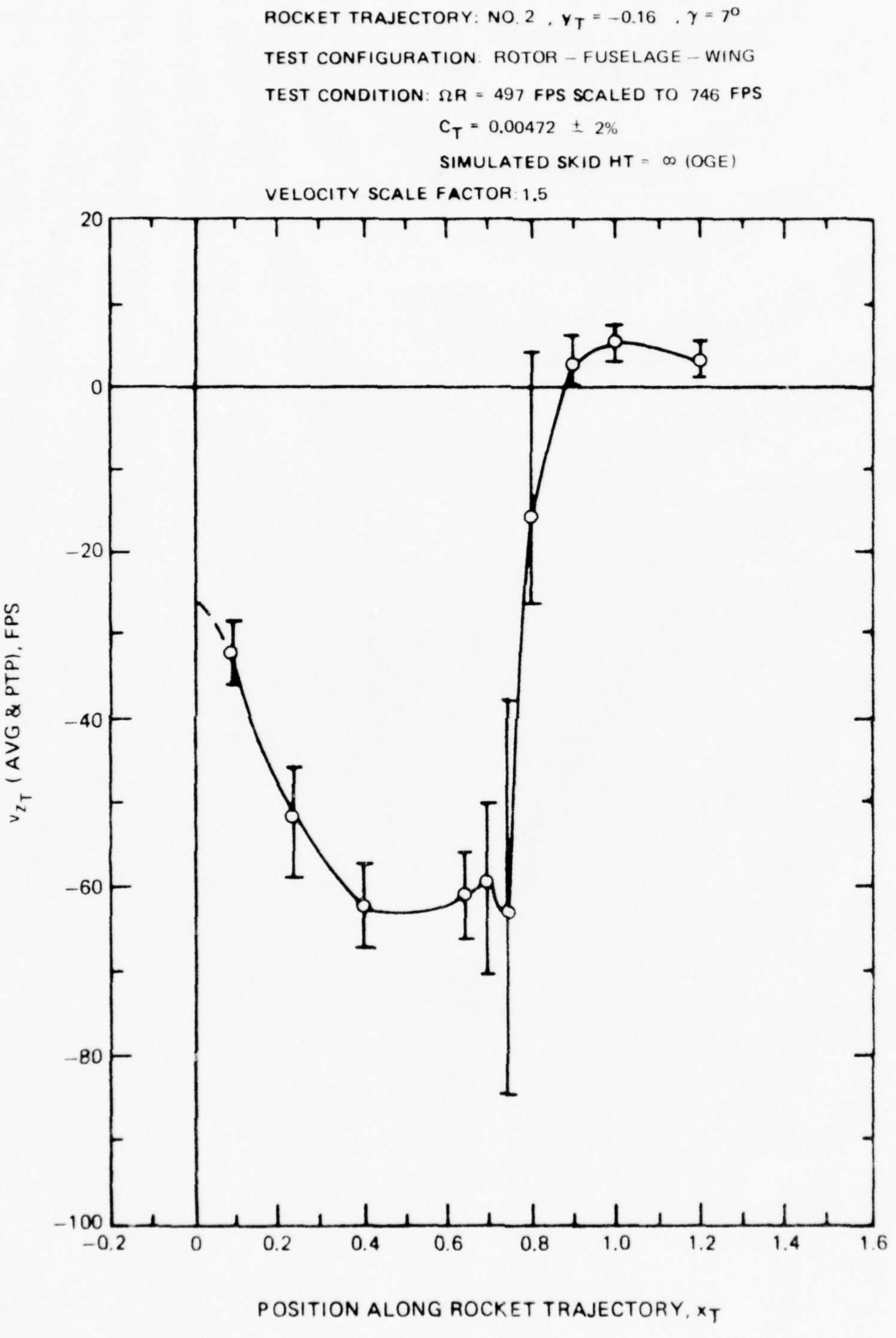

Figure 50. Variation of the Time-Average and Peaks of the Scaled v_{z_T} Flow Velocity Component at Rocket Trajectory No. 2 for the Reference Configuration and Reference Condition.

77–06–214–1

ROCKET TRAJECTORY: NO. 2, 3 $y_T = \pm 0.16$, $\gamma = 7$ DEG

TEST CONFIGURATION: ROTOR–FUSELAGE–WING

TEST CONDITION: ΩR = 497 FPS SCALED TO 746 FPS

C_T = 0.00472 ± 2%

SIMULATED SKID HT = ∞ (OGE)

VELOCITY SCALE FACTOR: 1.5

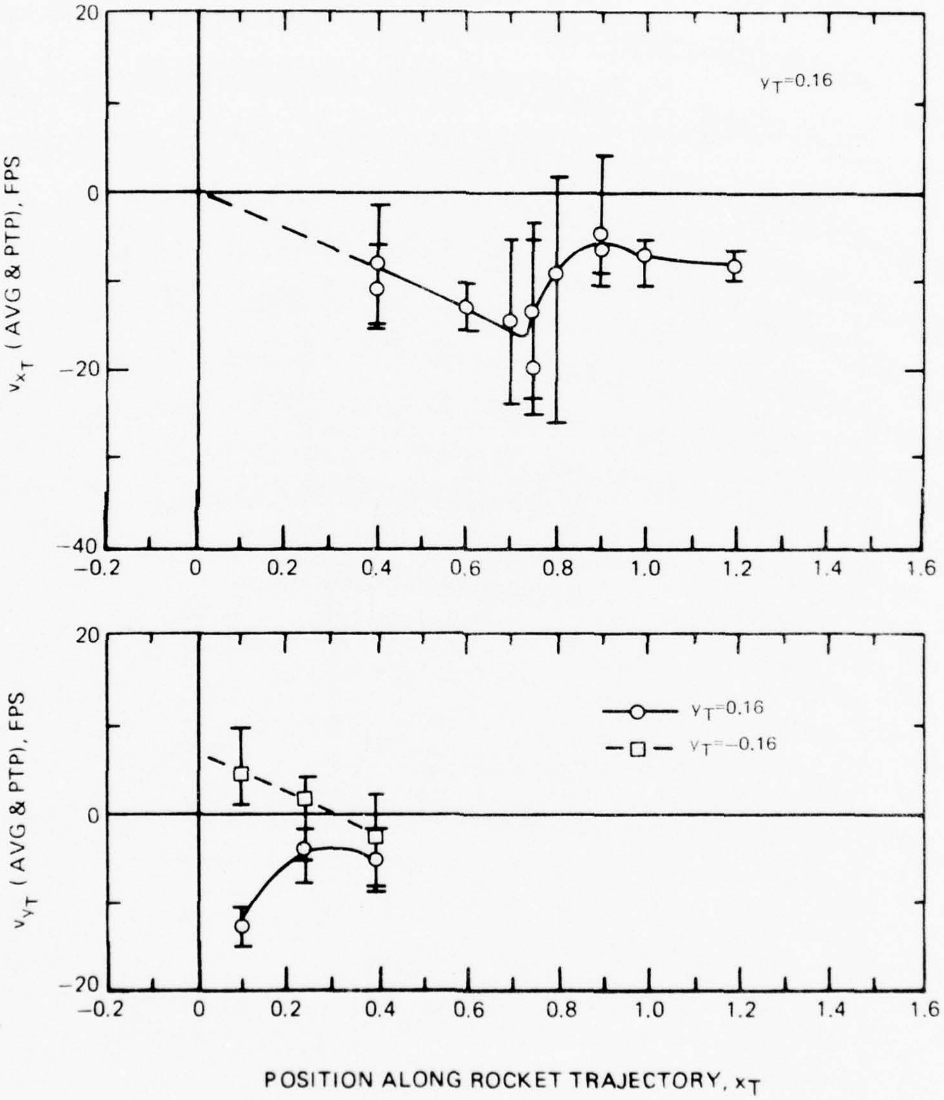

Figure 51. Variation of the Time-Average and Peaks of The Scaled v_{x_T} Flow Velocity Component at Rocket Trajectory No. 3 and the v_{y_T} Component at Trajectory Nos. 2 and 3 for the Reference Configuration and Reference Condition.

77–06–214–9

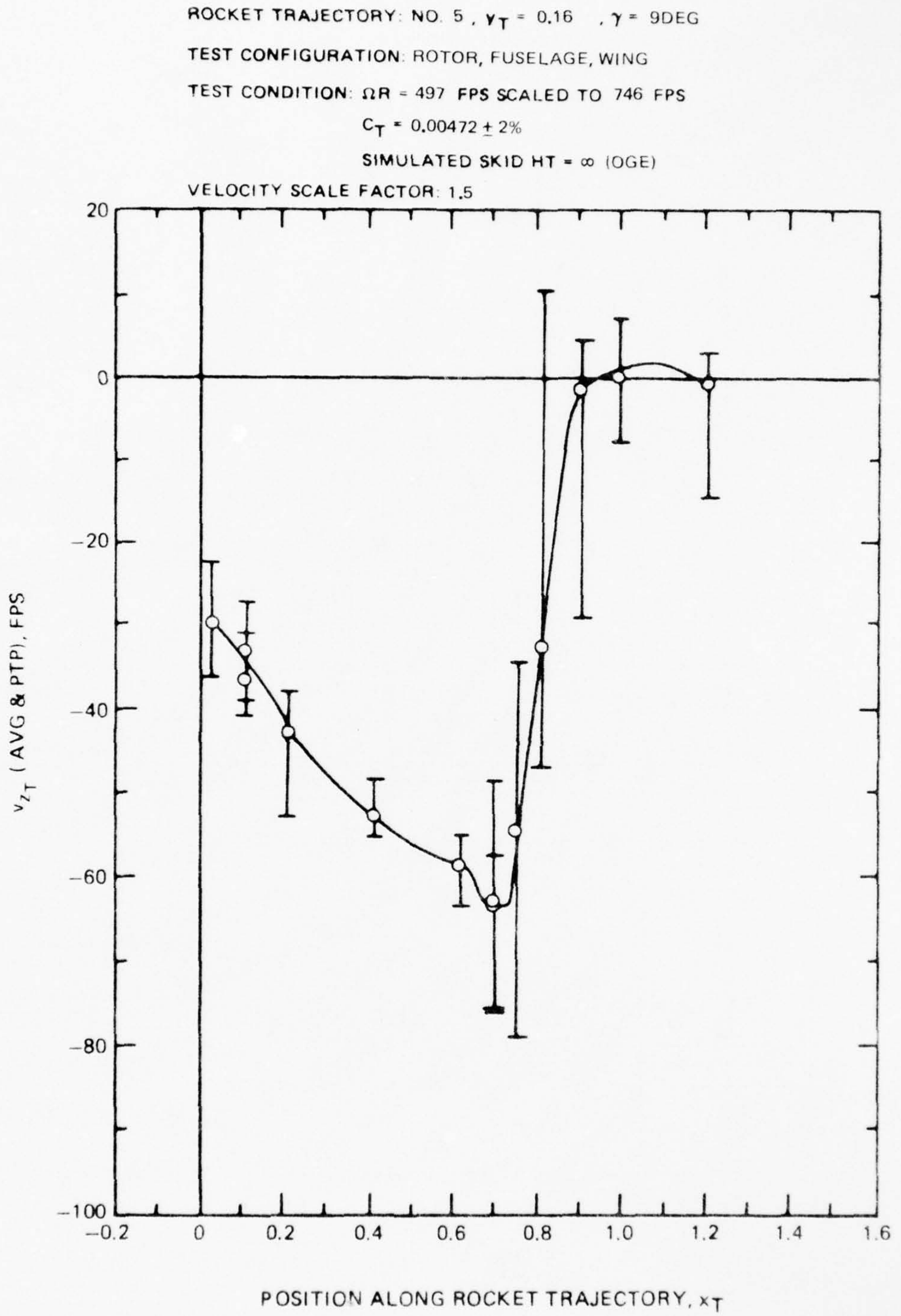

Figure 52. Variation of the Time-Average and Peaks of the Scaled v_{z_T} Flow Velocity Component at Rocket Trajectory No. 5 for the Reference Configuration and Reference Condition.

77-06-187-8

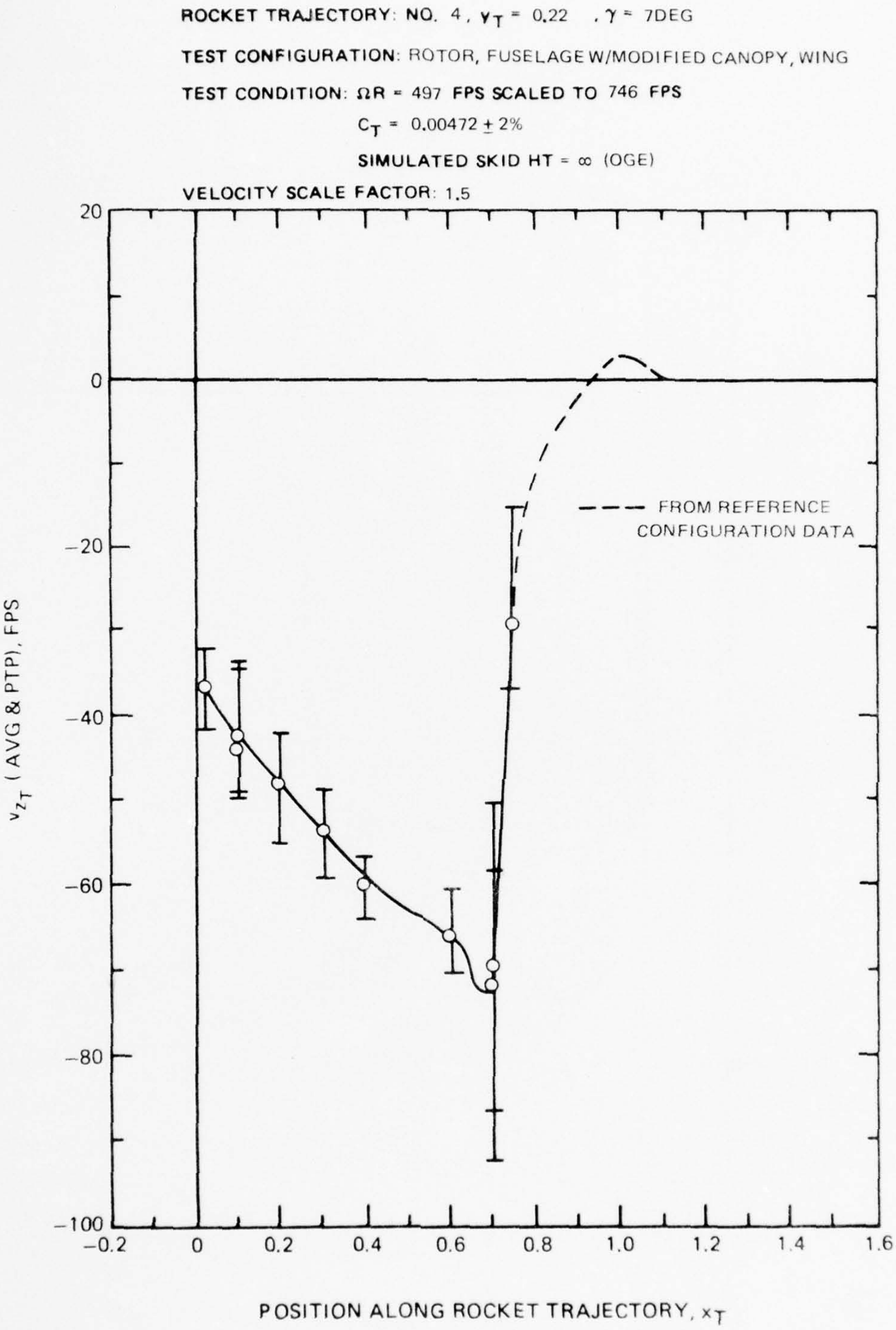

Figure 53. Variation of the Time-Average and Peaks of the Scaled v_{z_T} Flow Velocity Component at Rocket Trajectory No. 4 for the Modified Canopy Configuration and Reference Condition.

77–06–187–10

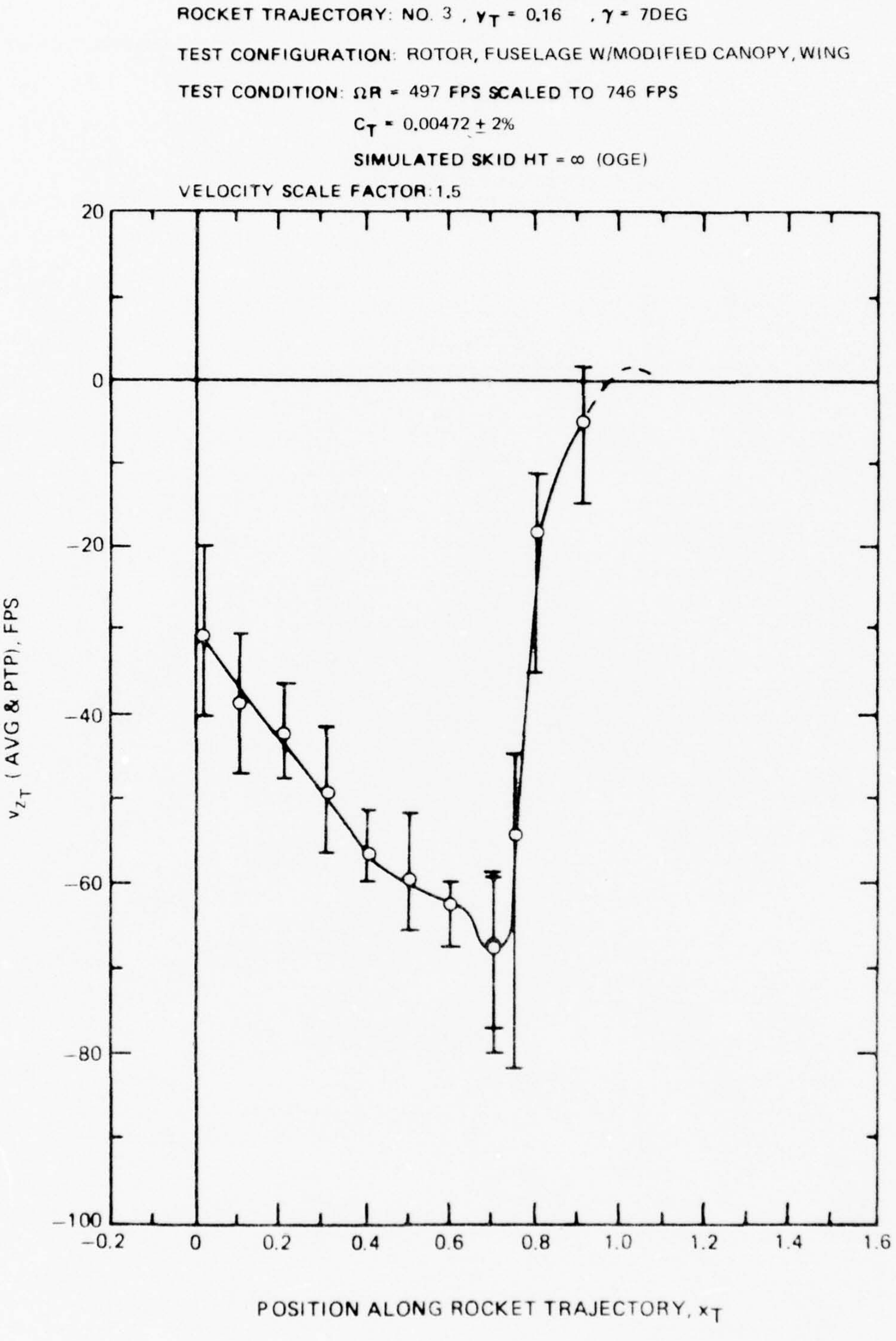

Figure 54. Variation of the Time-Average and Peaks of the Scaled v_{z_T} Flow Velocity Component at Rocket Trajectory No. 3 for the Modified Canopy Configuration and Reference Condition.

77–06–187–1

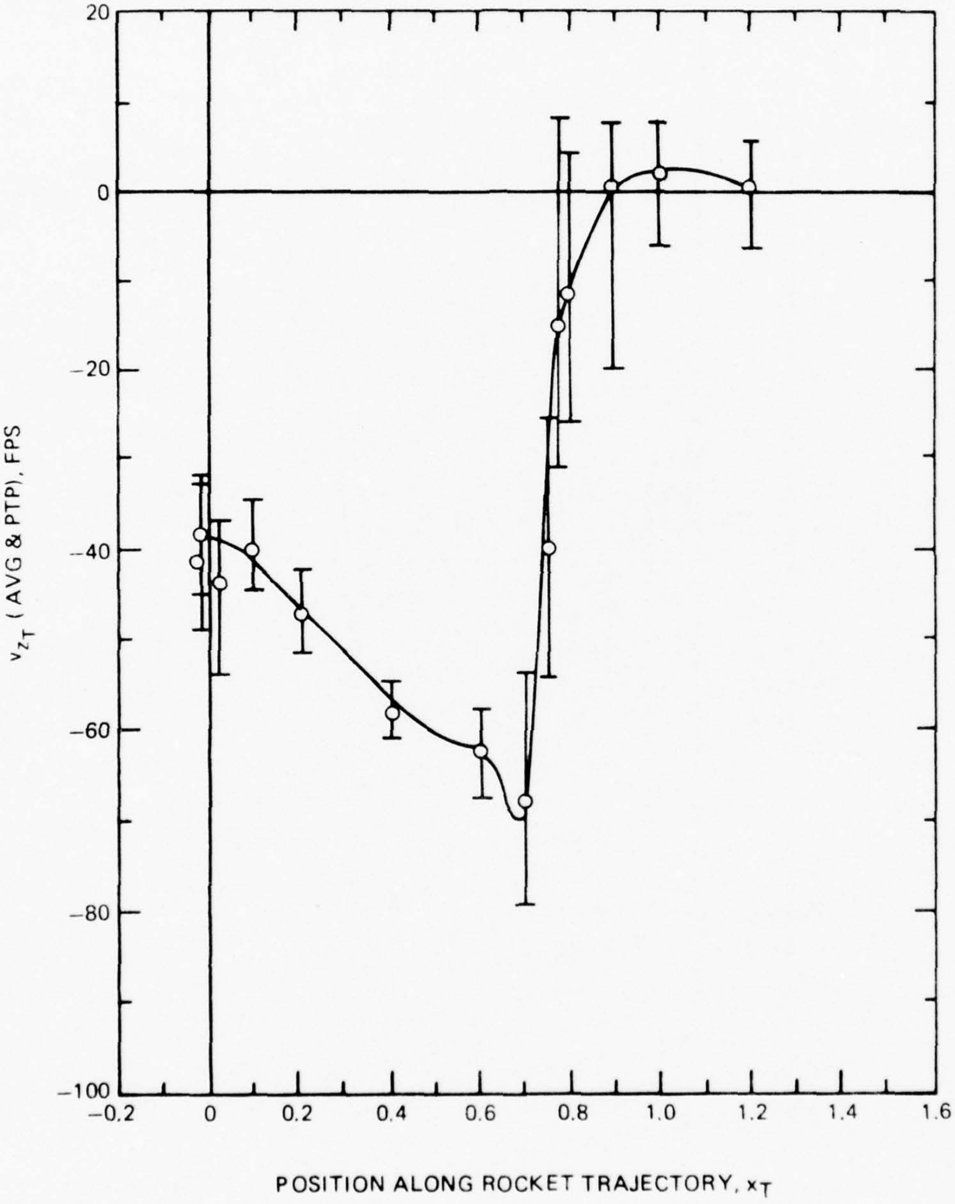

ROCKET TRAJECTORY: NO. 4, y_T = 0.22, γ = 7 DEG

TEST CONFIGURATION: ROTOR, FUSELAGE, WING

TEST CONDITION: ΩR = 497 FPS SCALED TO 746 FPS

C_T = 0.00354 ± 2% SCALED TO 0.00472

SIMULATED SKID HT = ∞ (OGE)

VELOCITY SCALE FACTOR: 1.73

Figure 55. Variation of the Time-Average and Peaks of the Scaled v_{z_T} Flow Velocity Component at Rocket Trajectory No. 4 for the Reference Configuration and Modified Thrust Condition.

77-06-187-13

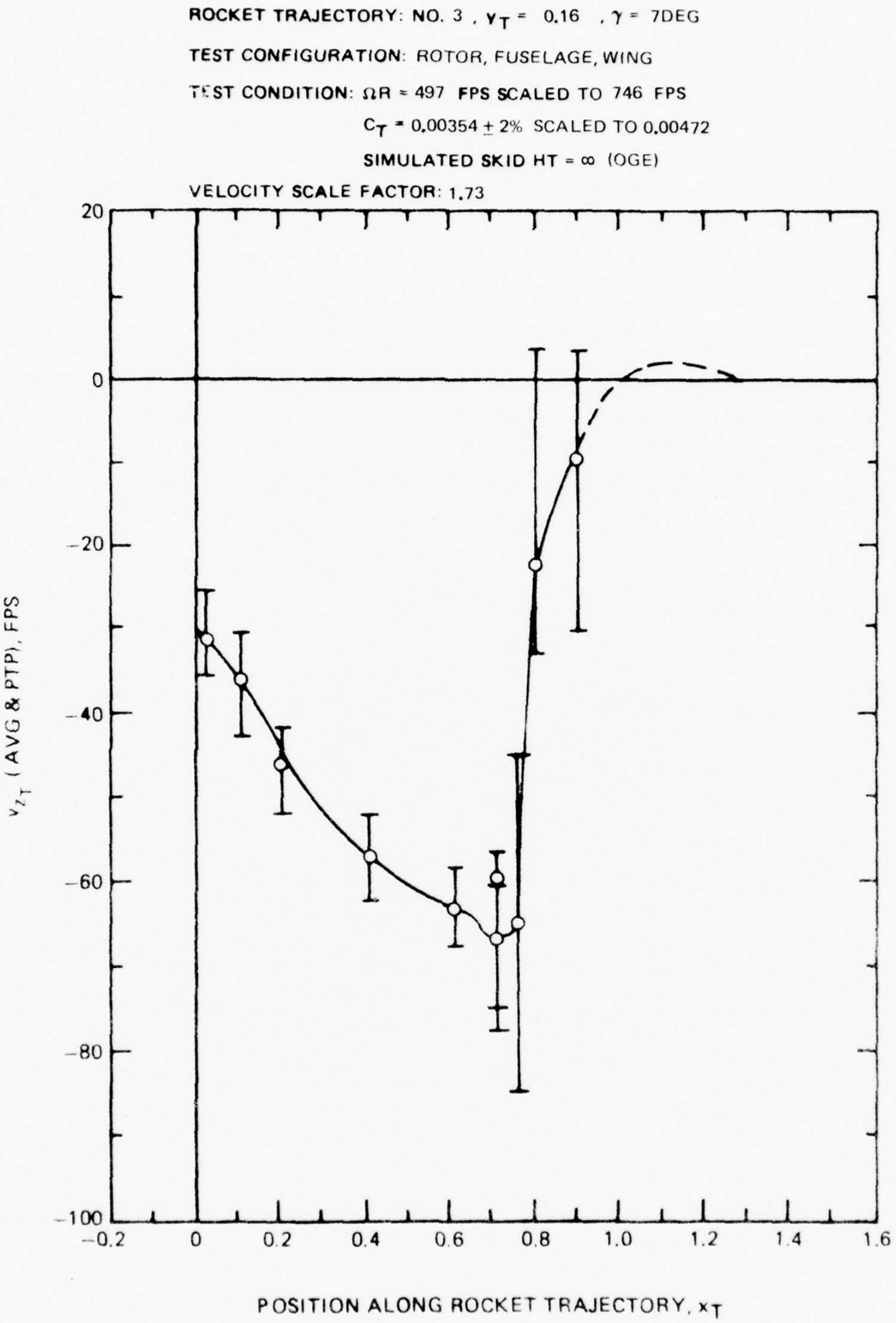

Figure 56. Variation of the Time-Average and Peaks of the Scaled v_{z_T} Flow Velocity Component at Rocket Trajectory No. 3 for the Reference Configuration and Modified Thrust Condition.

77-06-187-5

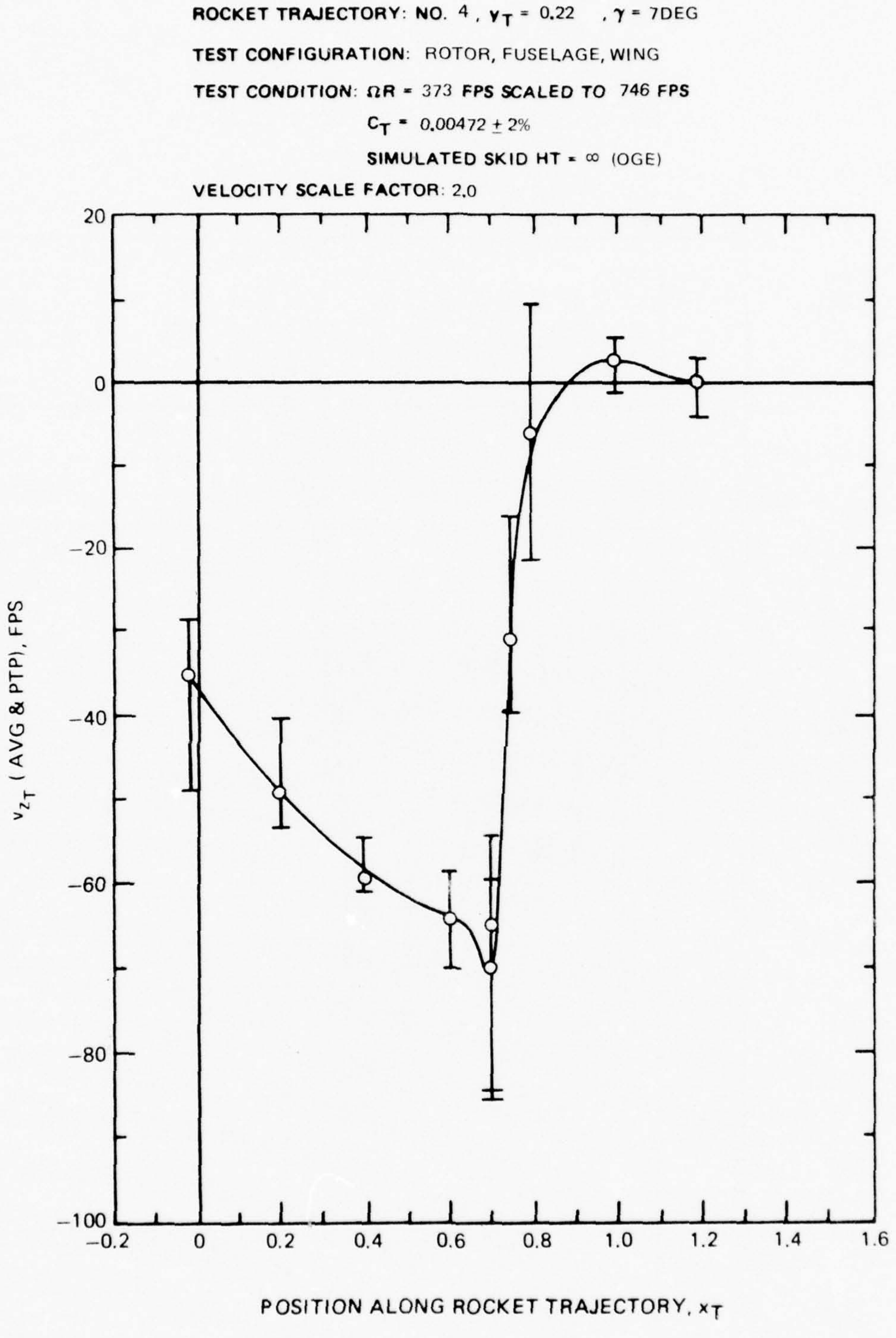

Figure 57. Variation of the Time-Average and Peaks of the Scaled v_{z_T} Flow Velocity Component at Rocket Trajectory No. 4 for the Reference Configuration and Modified Tip Speed Condition.

77-06-187-12

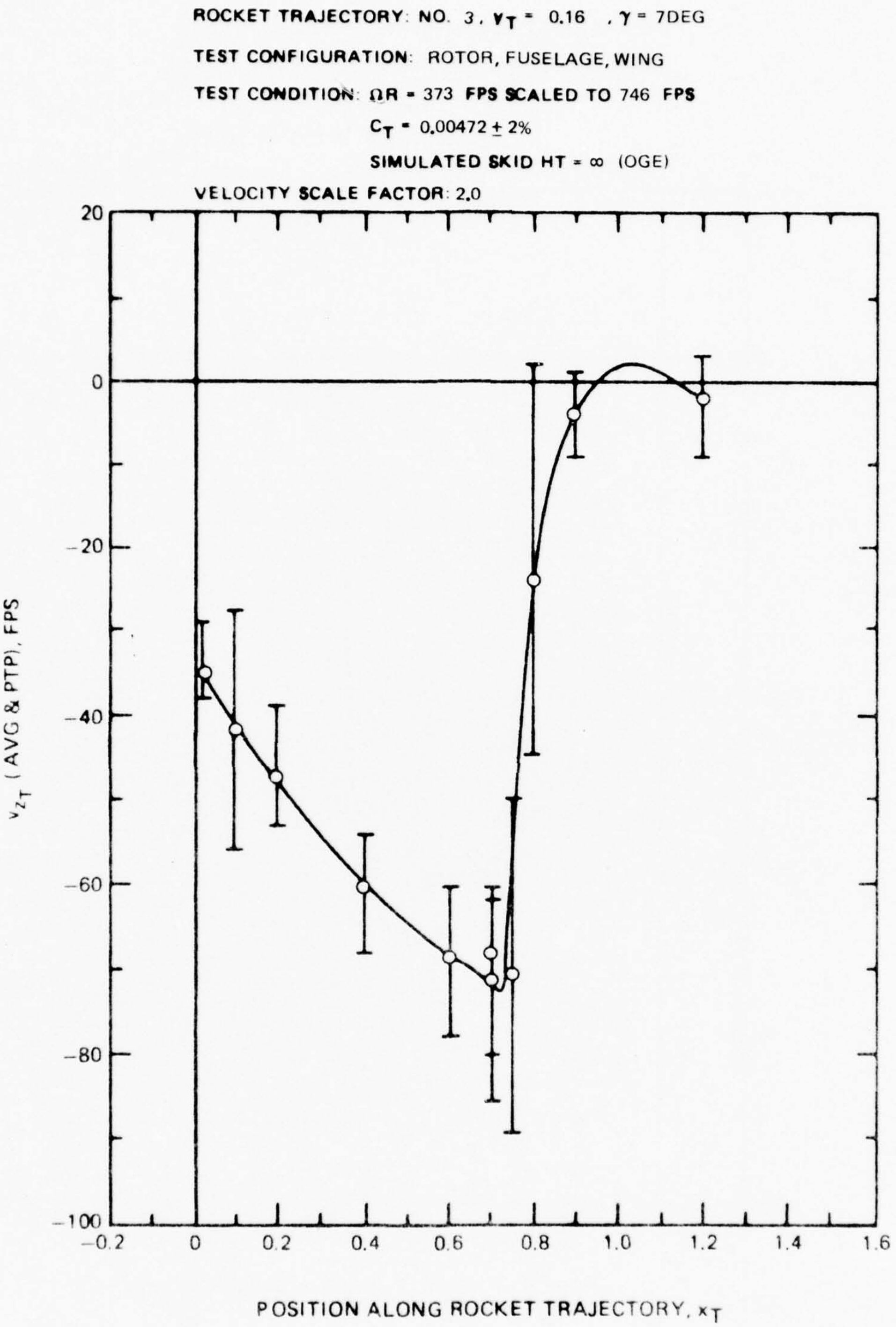

Figure 58. Variation of the Time-Average and Peaks of the Scaled v_{z_T} Flow Velocity Component at Rocket Trajectory No. 3 for the Reference Configuration and Modified Tip Speed Condition.

77-06-187-3

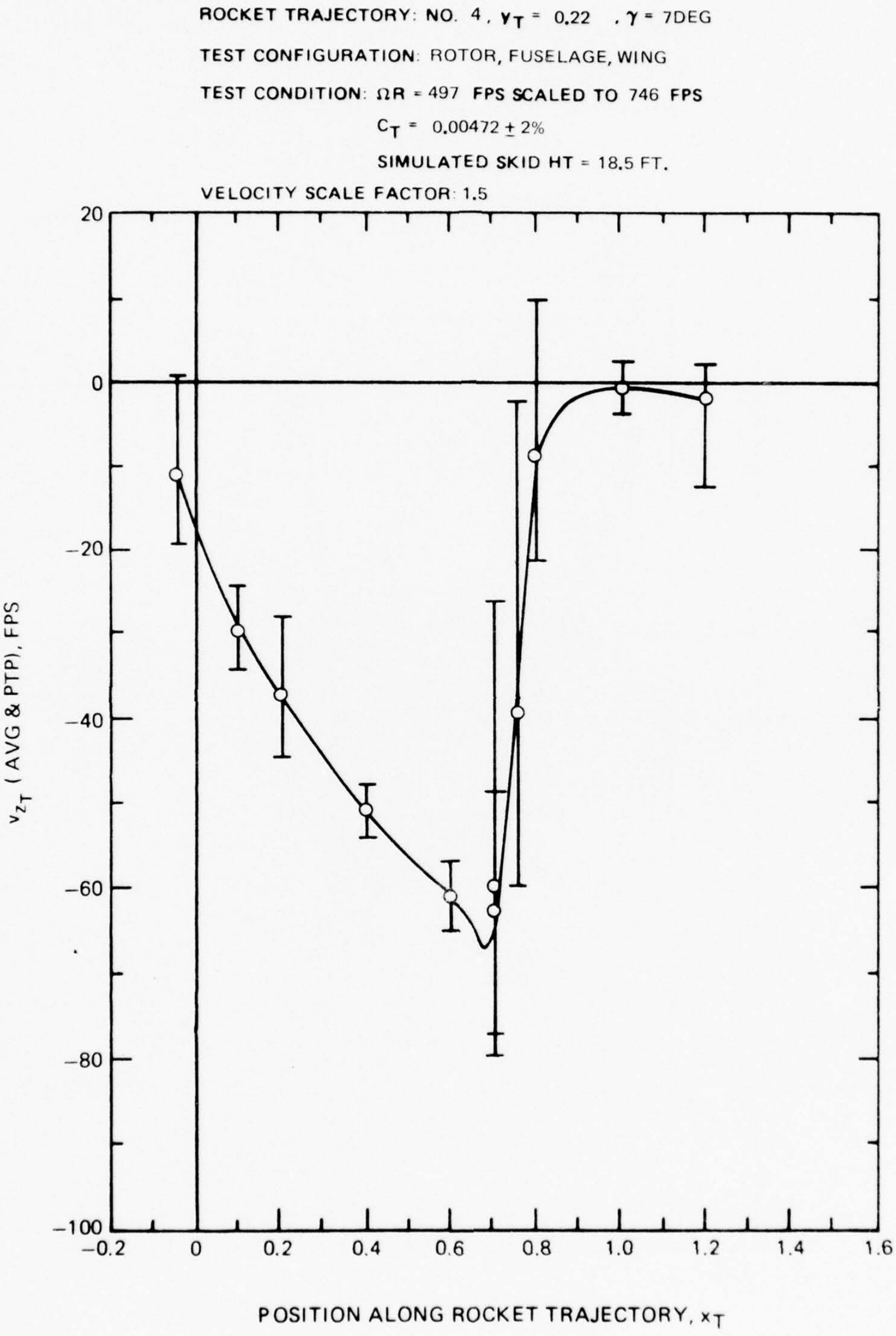

Figure 59. Variation of the Time-Average and Peaks of the Scaled v_{z_T} Flow Velocity Component at Rocket Trajectory No. 4 for the Reference Configuration and In-Ground-Effect (H = 18.5 ft) Condition.

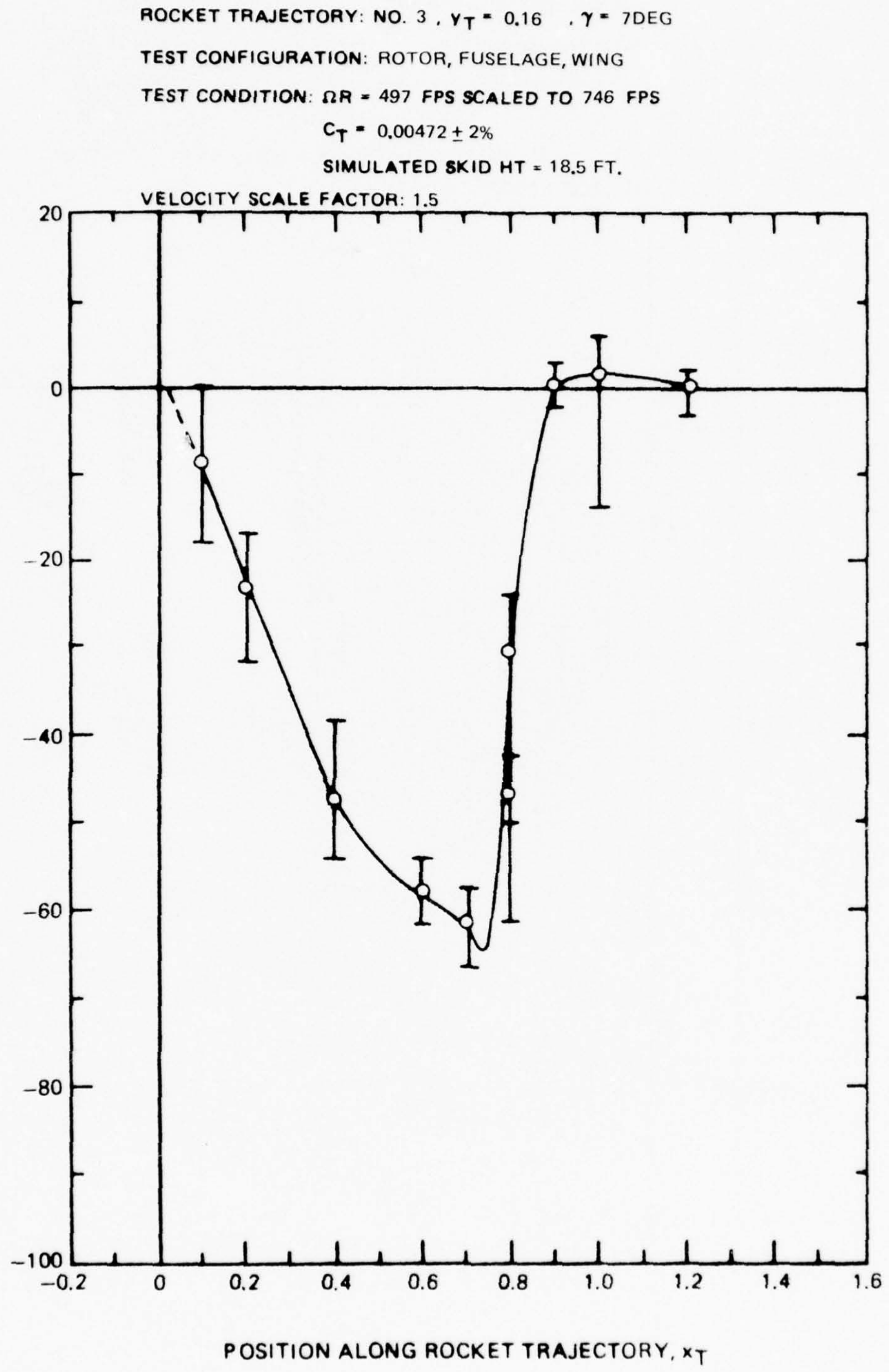

Figure 60. Variation of the Time-Average and Peaks of the Scaled v_{z_T} Flow Velocity Component at Rocket Trajectory No. 3 for the Reference Configuration and In-Ground-Effect (H = 18.5 ft) Condition.

77-06-187-6

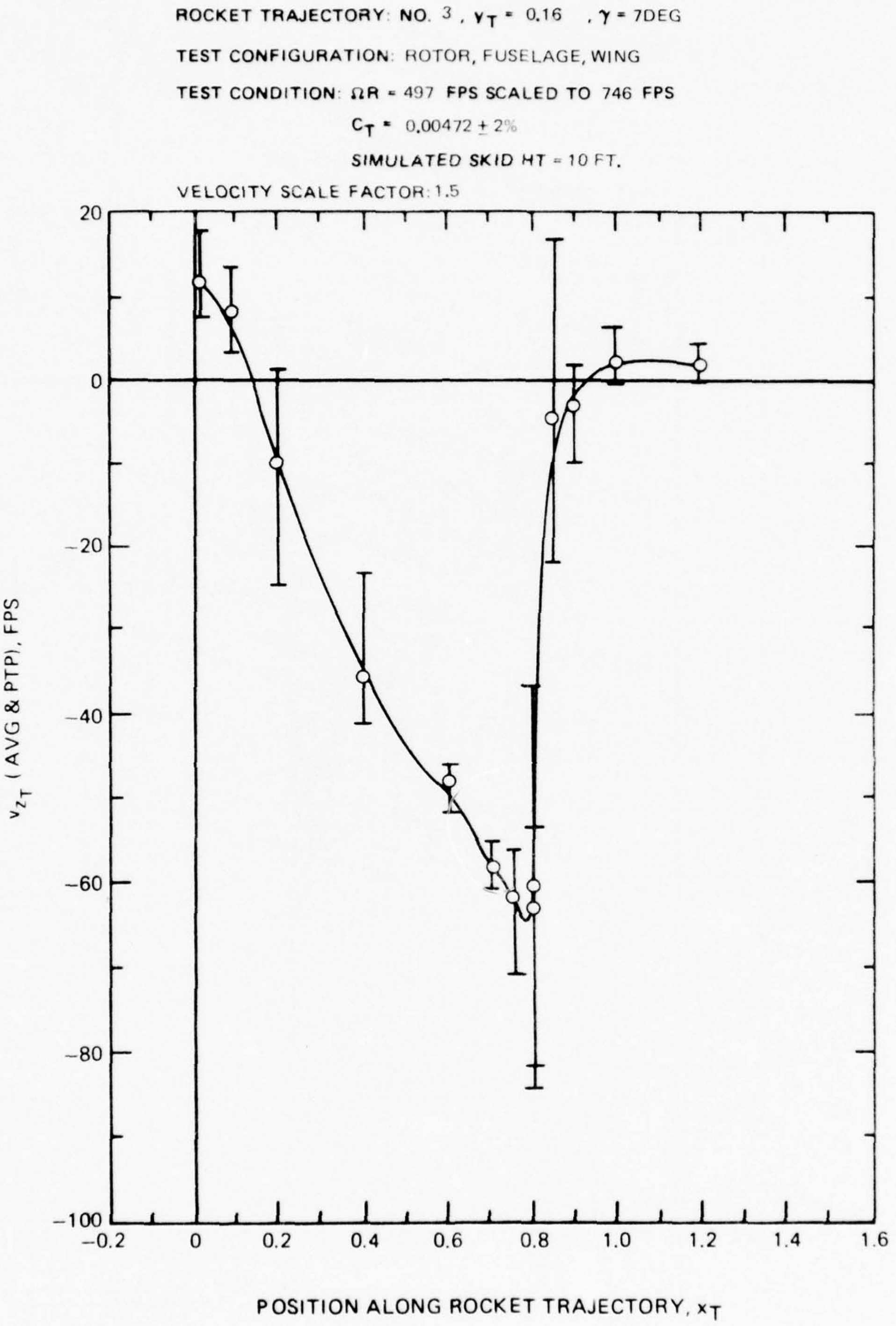

Figure 61. Variation of the Time-Average and Peaks of the Scaled v_{z_T} Flow Velocity Component at Rocket Trajectory No. 3 for the Reference Configuration and In-Ground-Effect (H = 10 ft) Condition.

77-06-187-7

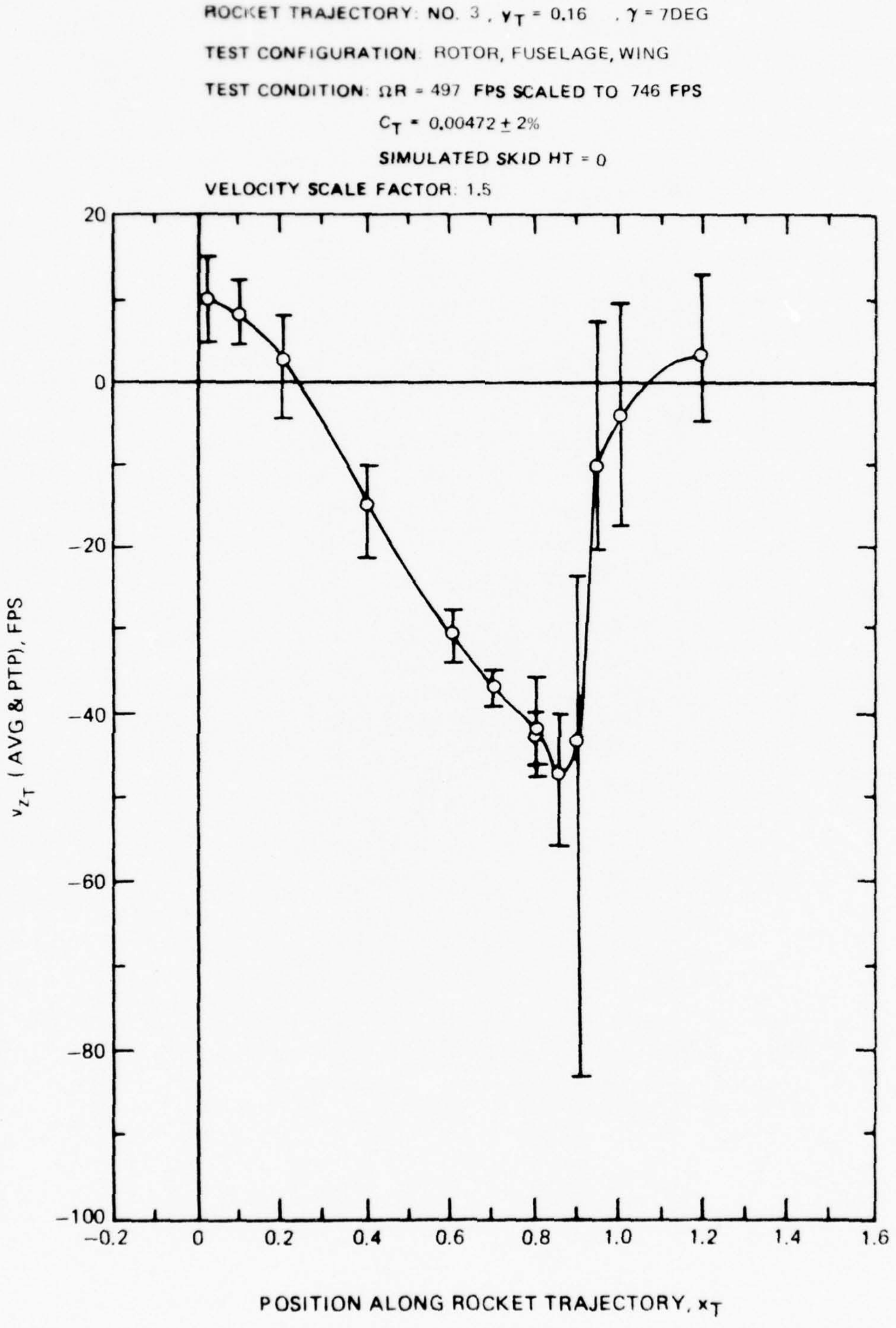

ROCKET TRAJECTORY: NO. 3 , γ_T = 0.16 , γ = 7DEG

TEST CONFIGURATION: ROTOR, FUSELAGE, WING

TEST CONDITION: ΩR = 497 FPS SCALED TO 746 FPS

C_T = 0.00472 ± 2%

SIMULATED SKID HT = 0

VELOCITY SCALE FACTOR: 1.5

Figure 62. Variation of the Time-Average and Peaks of the Scaled v_{Z_T} Flow Velocity Component at Rocket Trajectory No. 3 for The Reference Configuration and In-Ground-Effect (H = 0) Condition.

77-06-187-9

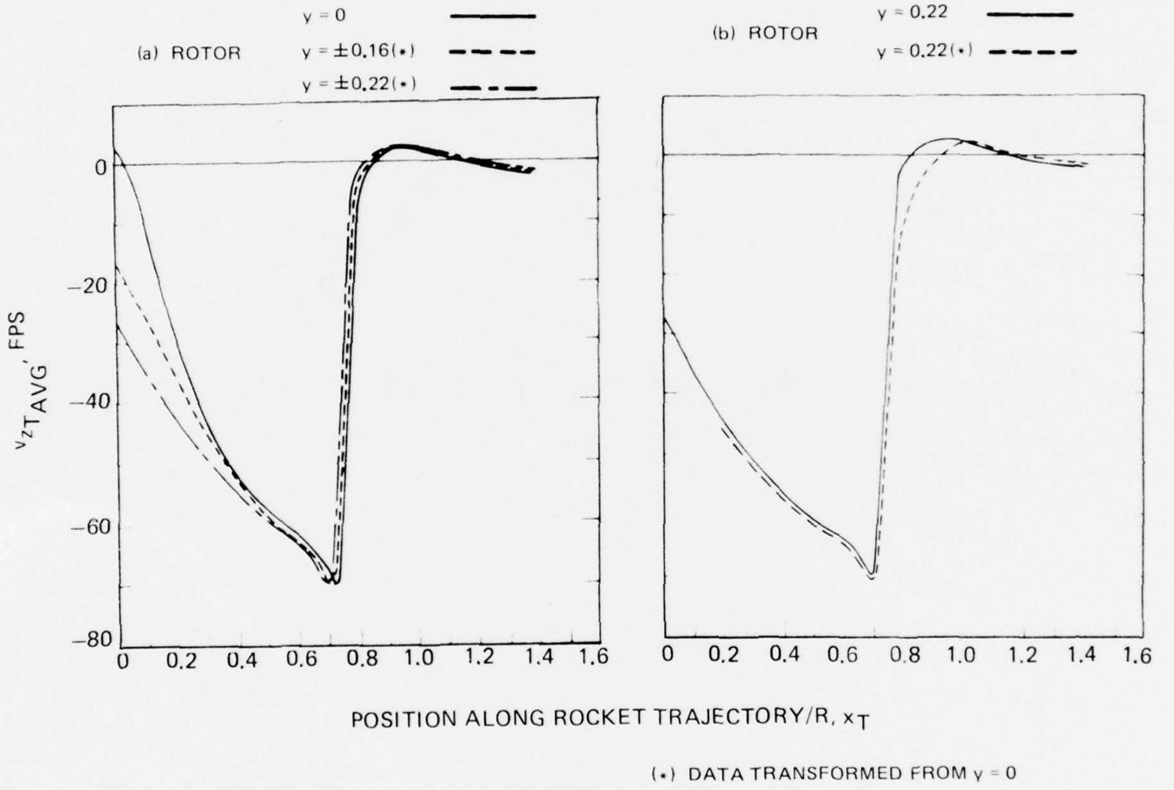

Figure 63. Effect of Rocket Trajectory Location and Transformation of Data From y_T = 0 On the Scaled Time-Averaged v_{z_T} Velocity Component for the Isolated Rotor and Reference Condition.

77–06–213–2

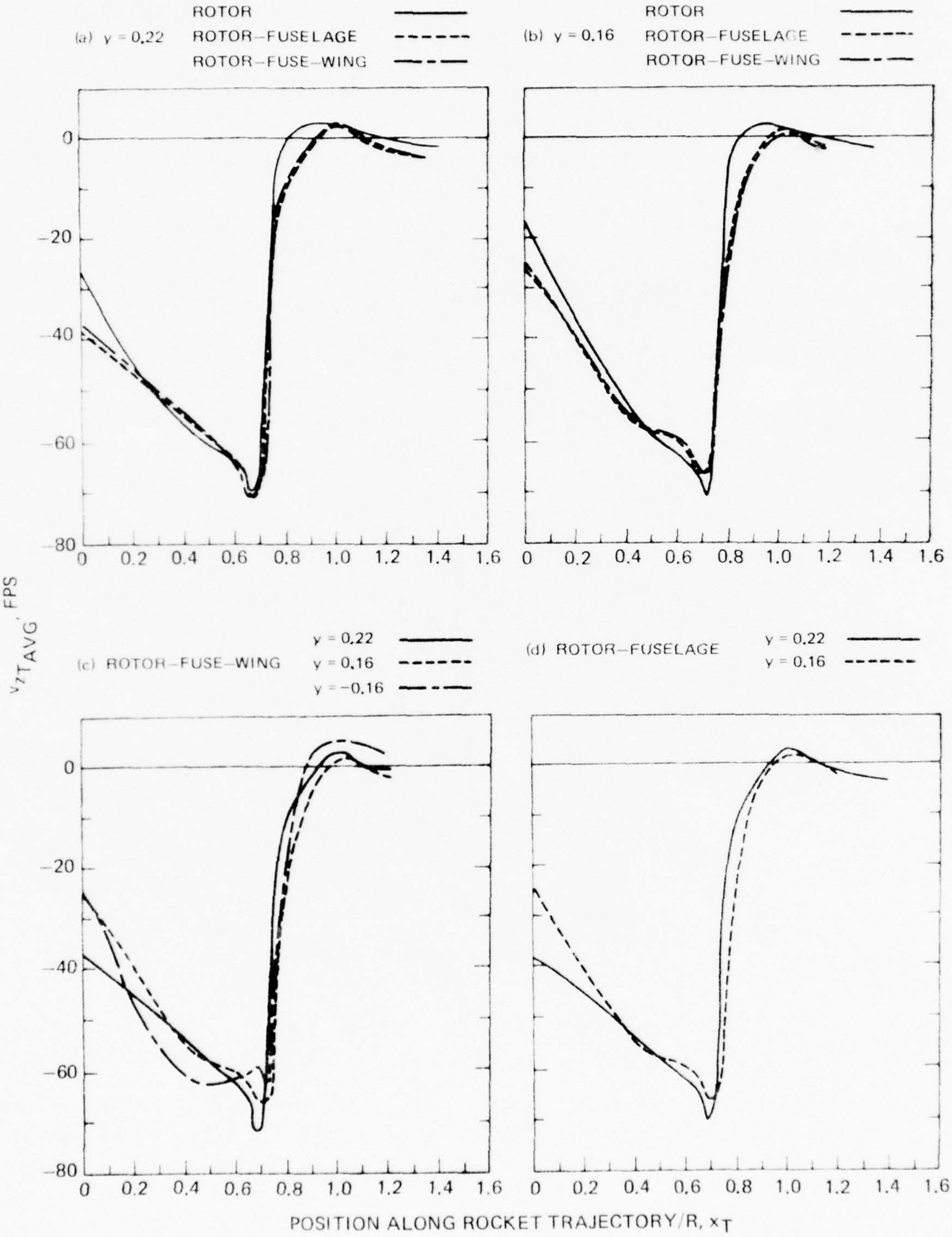

Figure 64. Effect of Configuration Components (Rotor, Fuselage, Wing) and Rocket Trajectory Location on The Scaled Time-Averaged v_{z_T} Velocity Component for the Reference Condition.

77–06–213–7

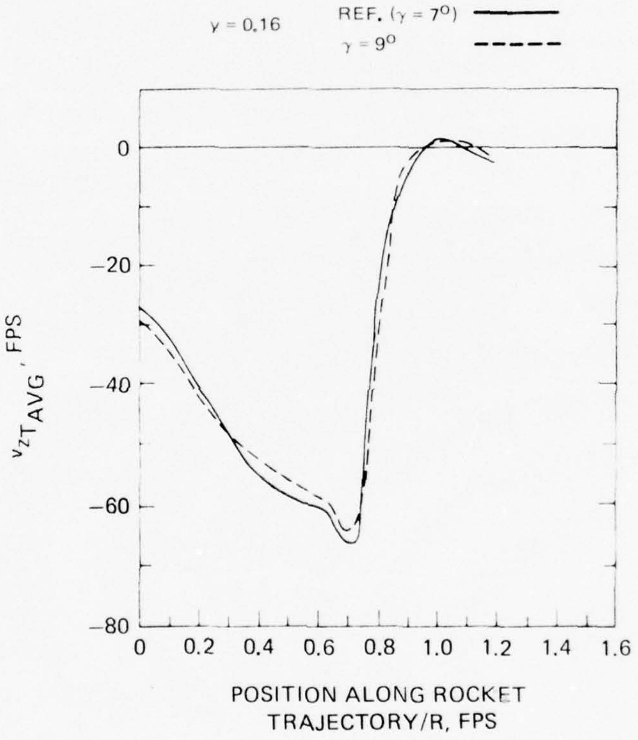

Figure 65. Effect of Rocket Attitude Variation on the Scaled Time-Average v_{z_T} Velocity Component for the Reference Configuration and Condition.

77–06–213–5

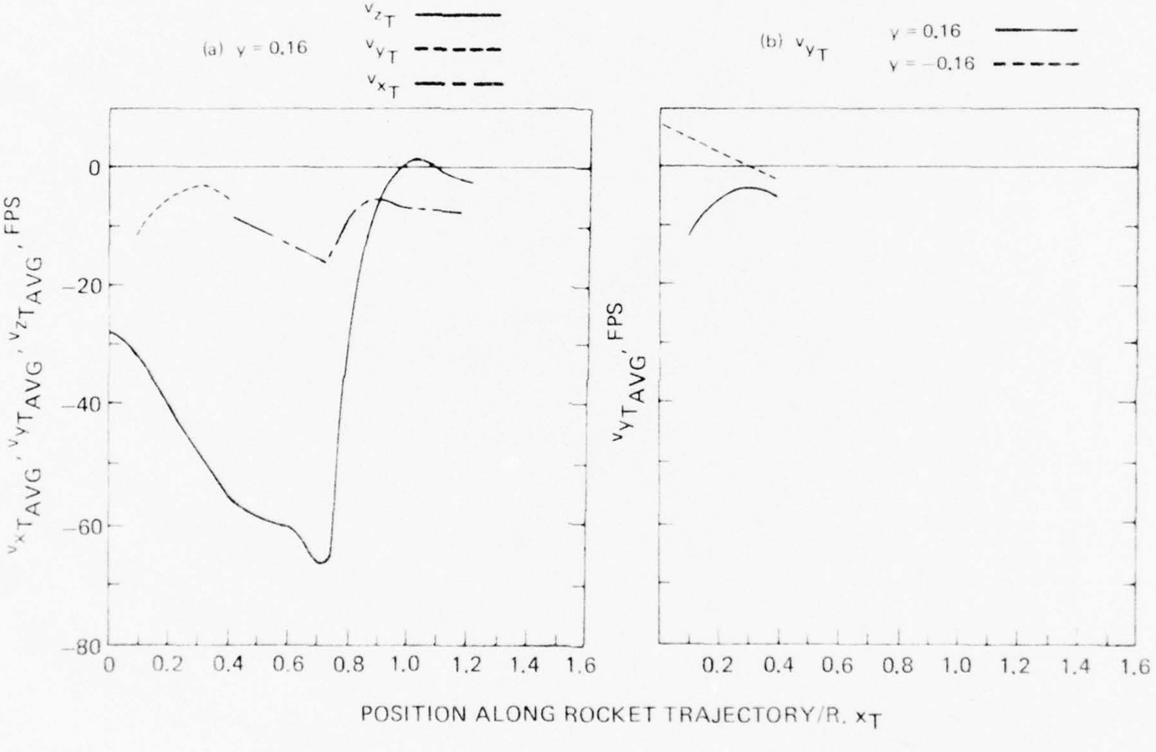

Figure 66. Comparison Of the Scaled Time-Average Velocity Components (v_{x_T}, v_{y_T}, v_{z_T}) for the Reference Configuration and Condition.

77-06-213-4

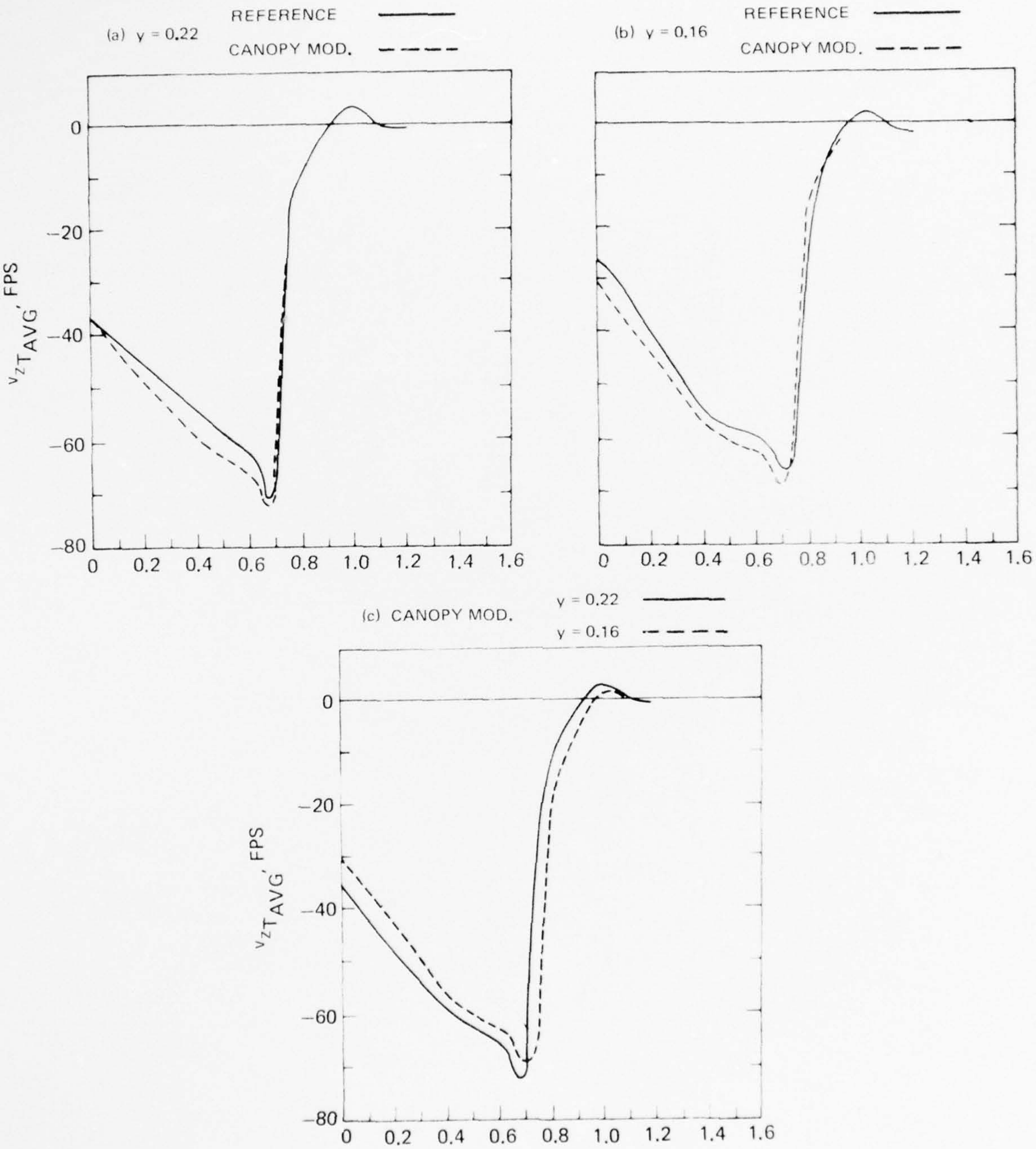

Figure 67. Effect of the Modified Canopy on the Scaled Time-Average v_{z_T} Velocity Component at Two Rocket Trajectories for the Reference Condition.

77-06-213-3

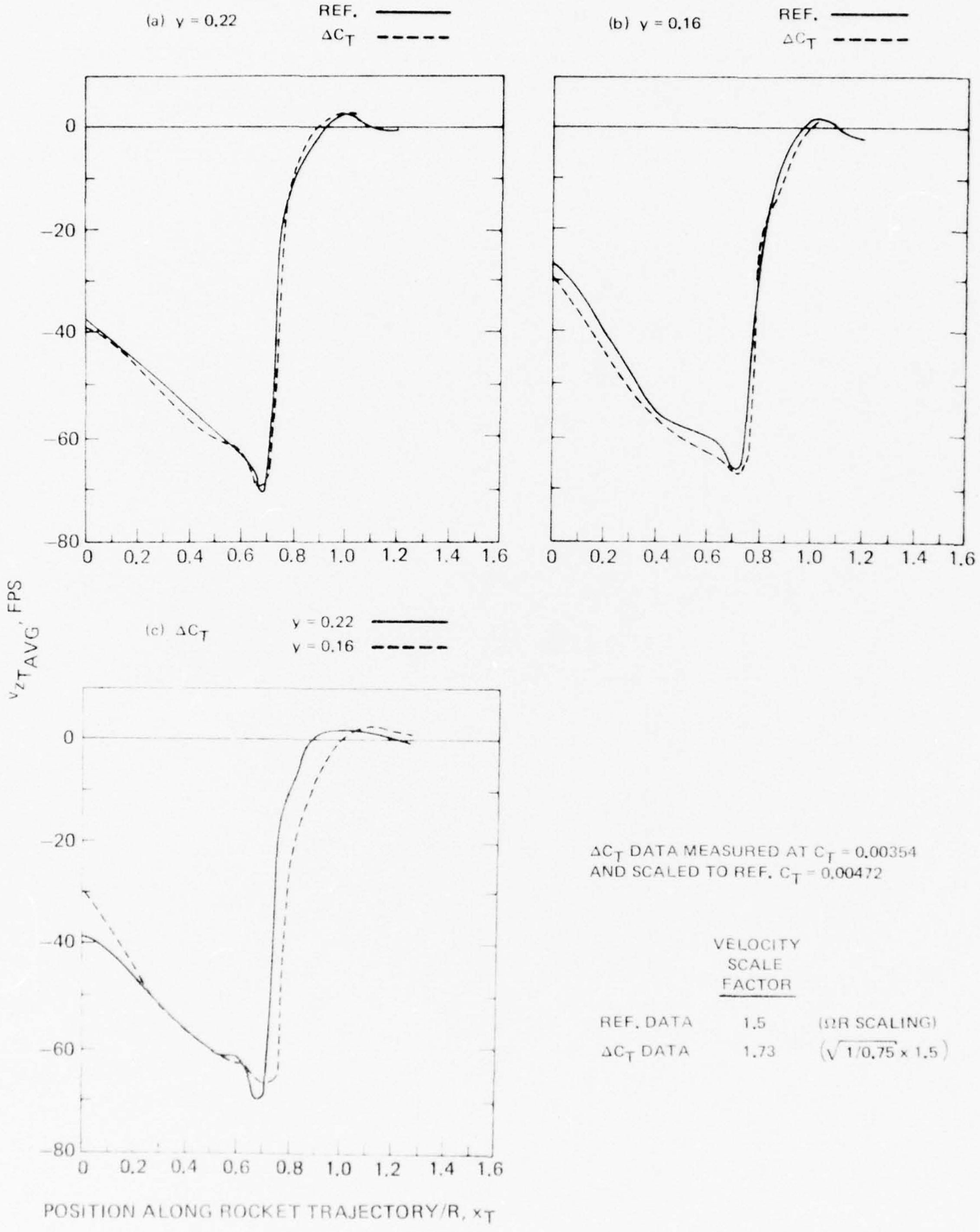

ΔC_T DATA MEASURED AT $C_T = 0.00354$ AND SCALED TO REF. $C_T = 0.00472$

	VELOCITY SCALE FACTOR	
REF. DATA	1.5	(ΩR SCALING)
ΔC_T DATA	1.73	$(\sqrt{1/0.75} \times 1.5)$

Figure 68. Comparison of the Time-Average v_{z_T} Velocity Component of the Modified Thrust and Reference Condtions at Two Rocket Trajectories When Scaled to the Same (Reference Full-Scale) Thrust Coefficient.

77-06-213-6

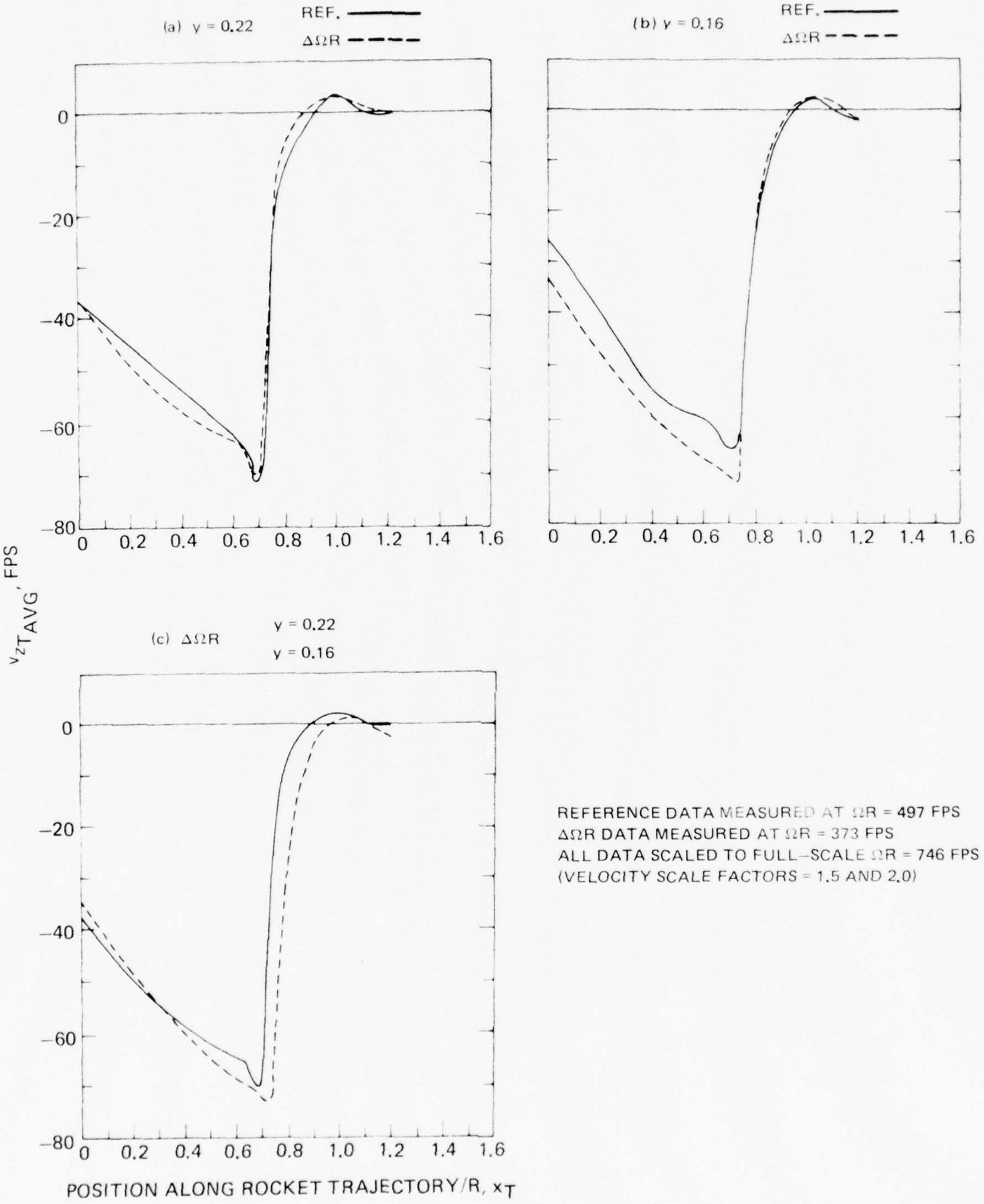

REFERENCE DATA MEASURED AT ΩR = 497 FPS
ΔΩR DATA MEASURED AT ΩR = 373 FPS
ALL DATA SCALED TO FULL-SCALE ΩR = 746 FPS
(VELOCITY SCALE FACTORS = 1.5 AND 2.0)

Figure 69. Comparison of the Time-Average v_{z_T} Velocity Component of the Modified Tip Speed and Reference Conditions at Two Rocket Trajectories When Scaled to the Same (Full-Scale) Tip Speed.

77-06-213-1

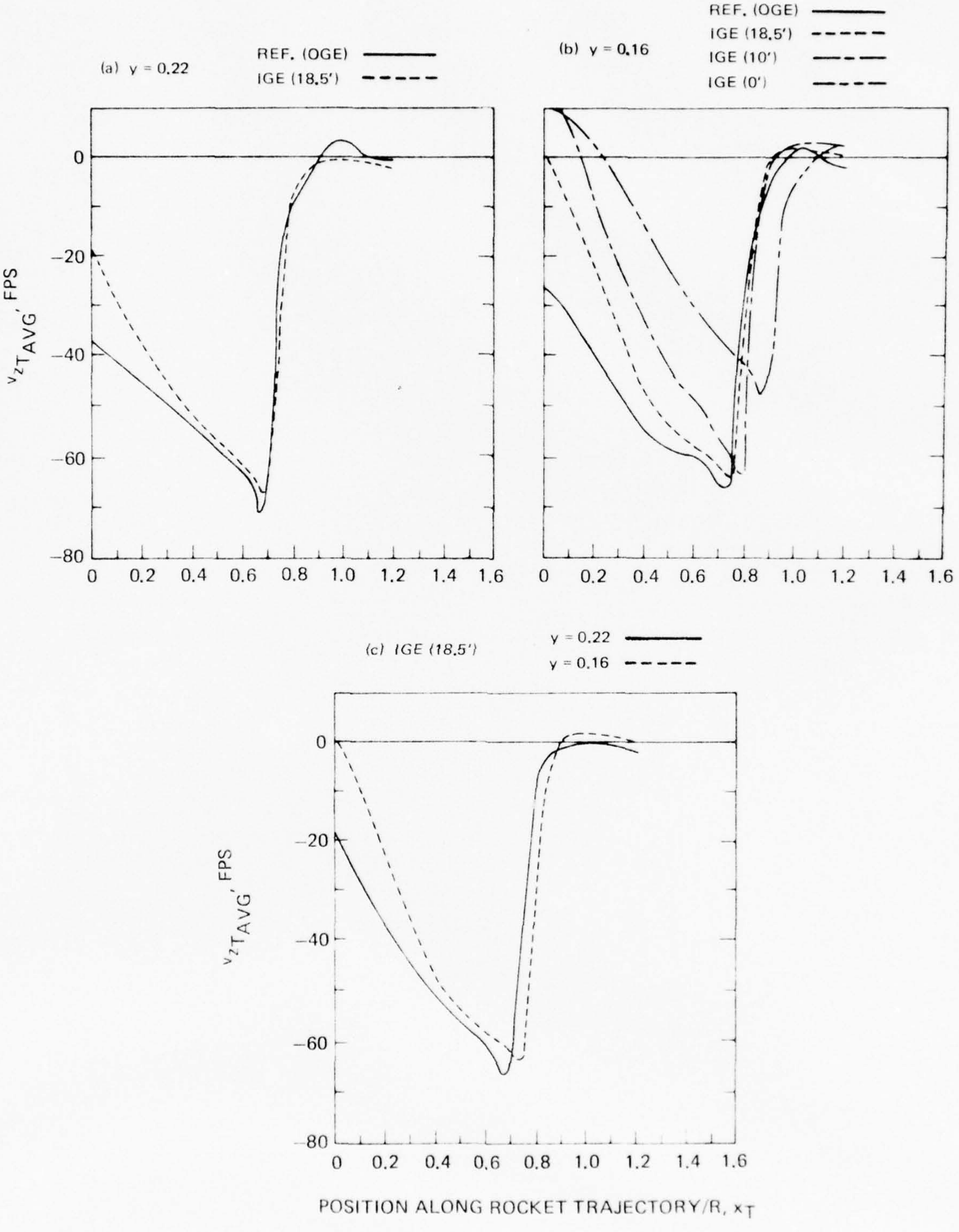

Figure 70. Ground Effect on the Scaled Time-Averaged v_{z_T} Velocity Component at Two Rocket Trajectories for Various Skid Heights Above Ground.

77-06-213-8

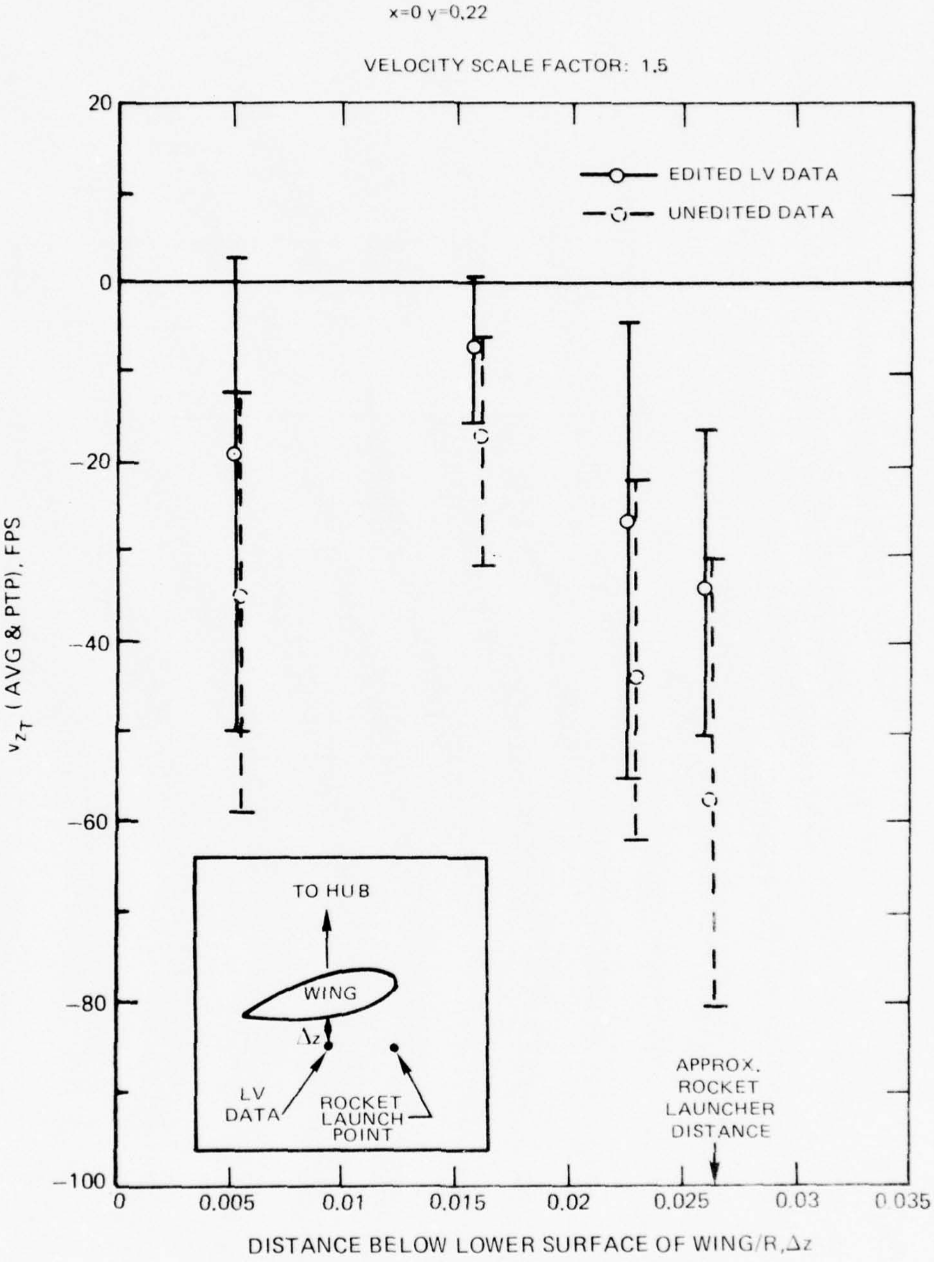

Figure 71. LV Data for Several Points Directly Beneath the Mid-Chord and Near the Tip of the Wing.

77–06–214–5

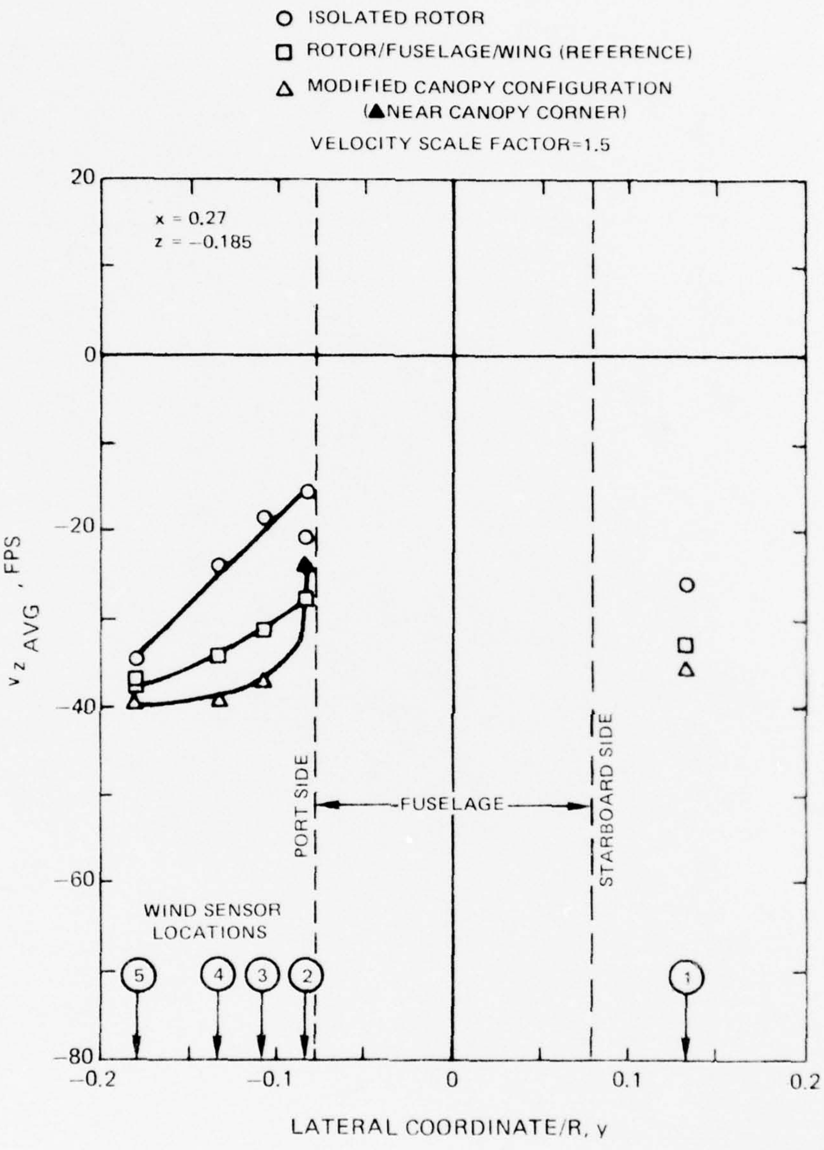

Figure 72. Scaled Time-Average v_z Data at Six Wind Sensor Locations Aside of the Canopy for Three Configurations and the Reference Condition.

77-06-148-2

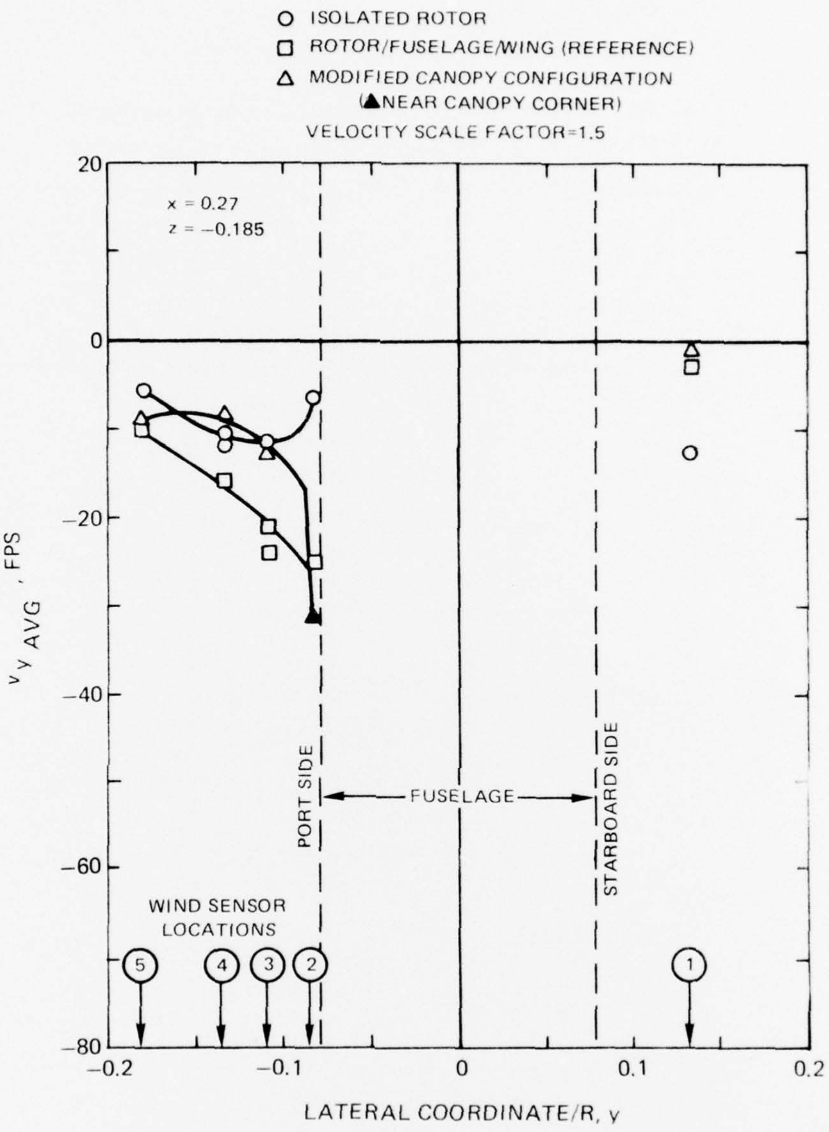

Figure 73. Scaled Time-Average v_y Data at Six Wind Sensor Locations Aside of the Canopy for Three Configurations and the Reference Condition.

77–06–148–3

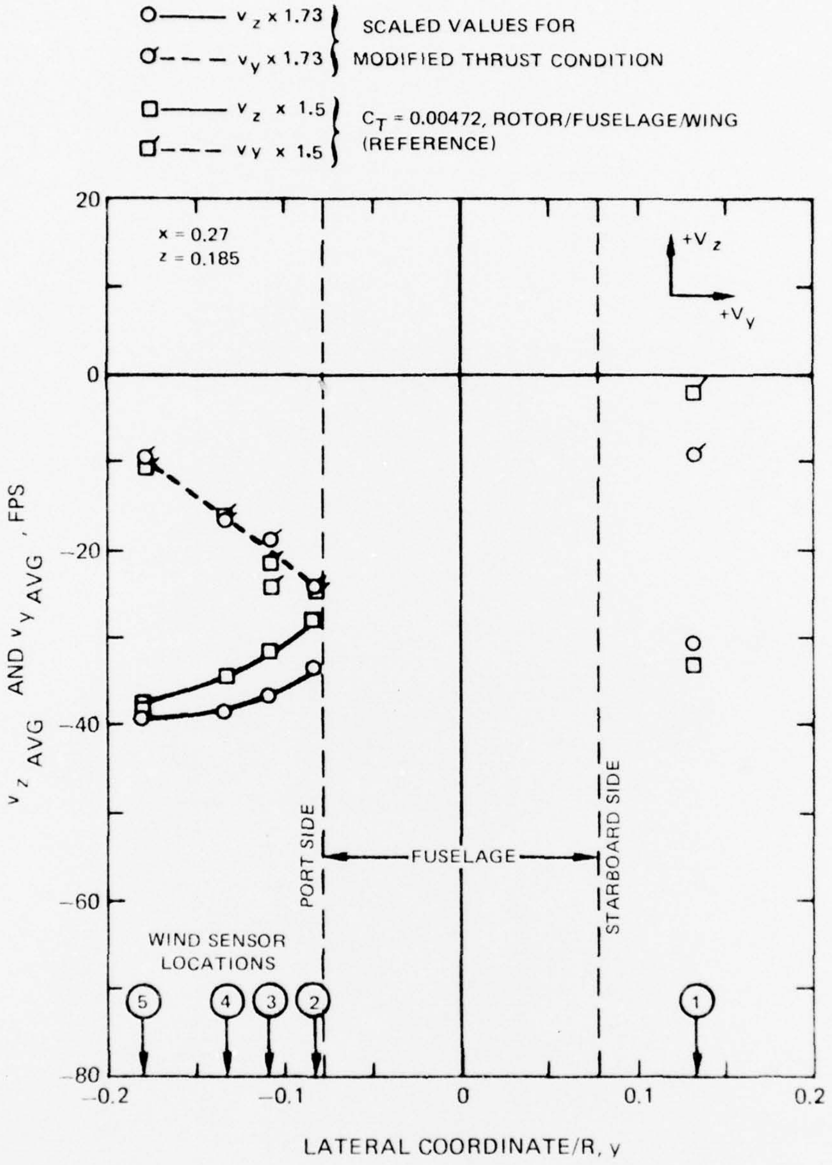

Figure 74. Scaled Time-Average v_y and v_z Data at Six Wind Sensor Locations Aside of the Canopy for the Modified Thrust and Reference Condition.

77–06–148–1

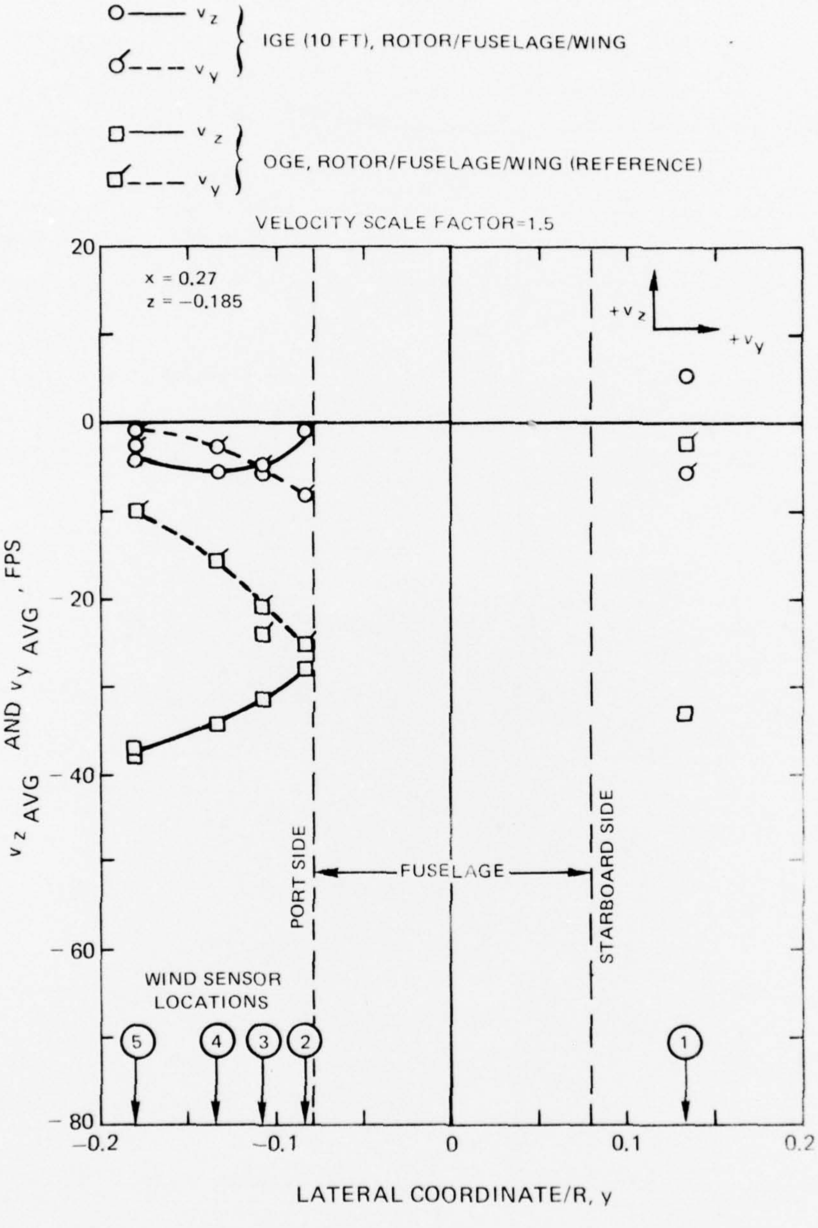

Figure 75. Scaled Time-Average v_y and v_z Data at Six Wind Sensor Locations Aside of the Canopy for the In-Ground-Effect (H = 10 ft) and Reference Conditions.

77-06-148-4

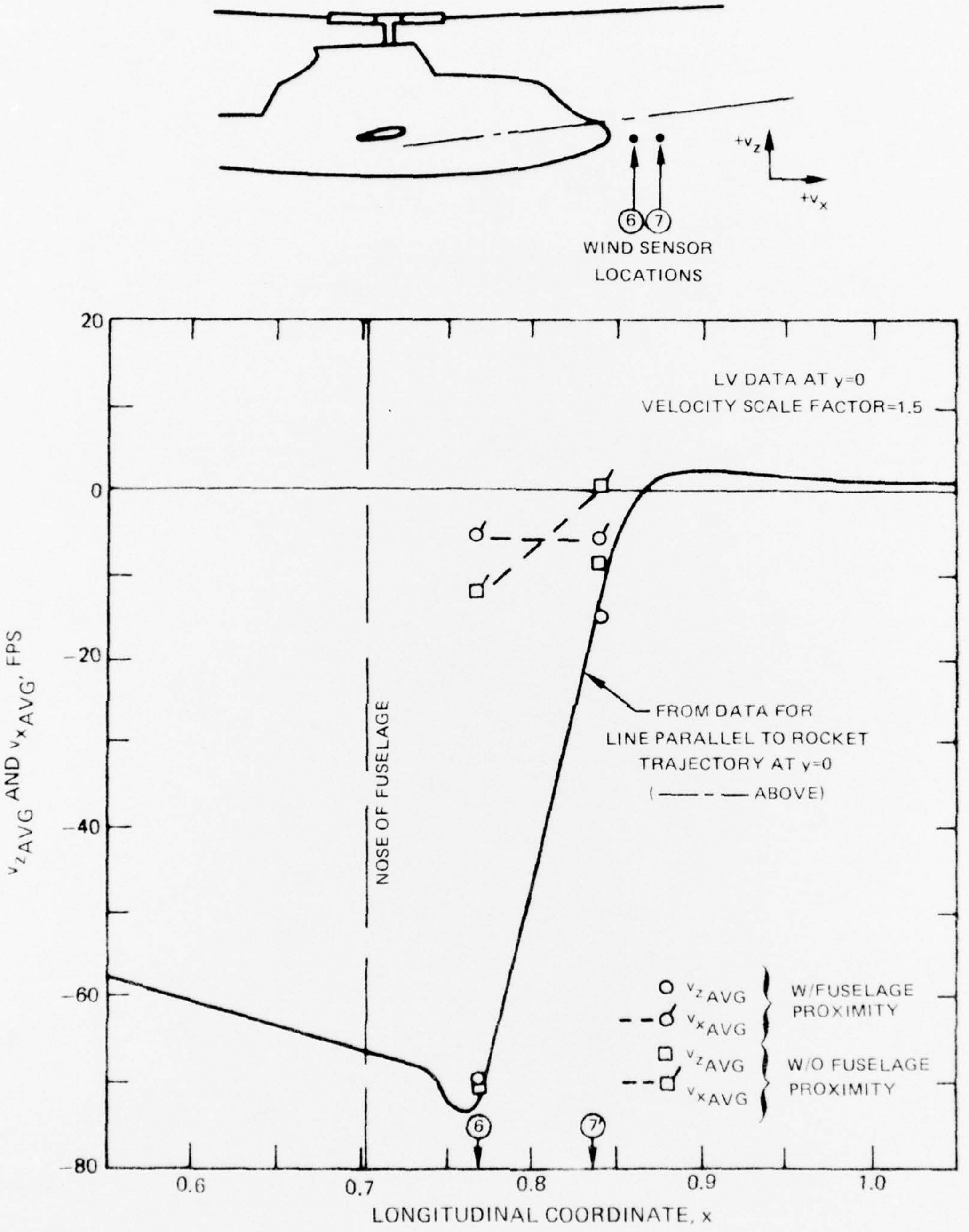

Figure 76. Scaled Time-Average v_x and v_z Data at Two Wind Sensor Locations In Front of the Fuselage Nose for the Reference Configuration and Condition.

77-06-214-4

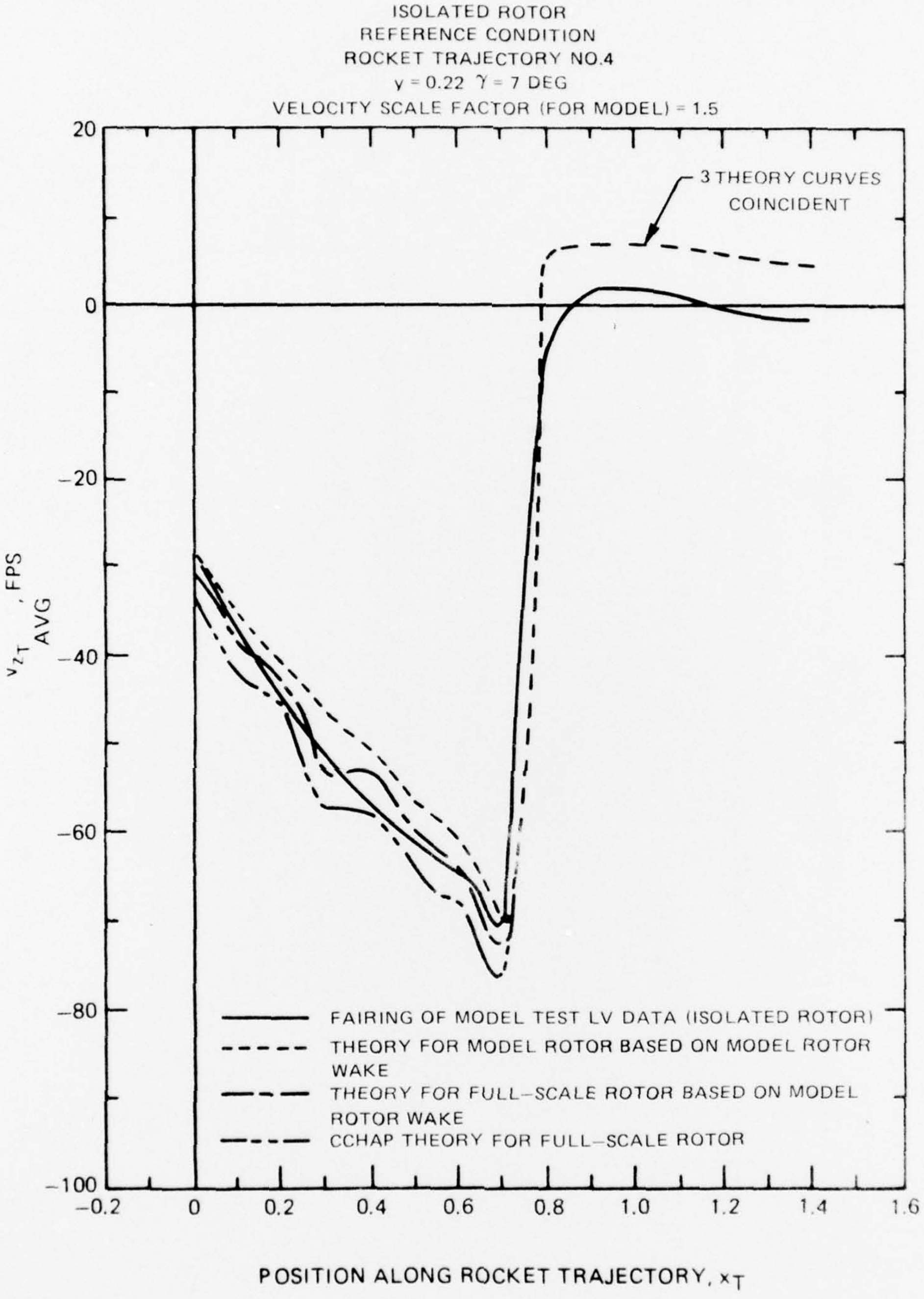

Figure 77. Comparison of Model and Full-Scale AH-1G Theoretical Results with Model LV Data for v_{z_T} (AVG) at Rocket Trajectory No. 4 for the Isolated Rotor, Reference Condition.

77-07-46-3

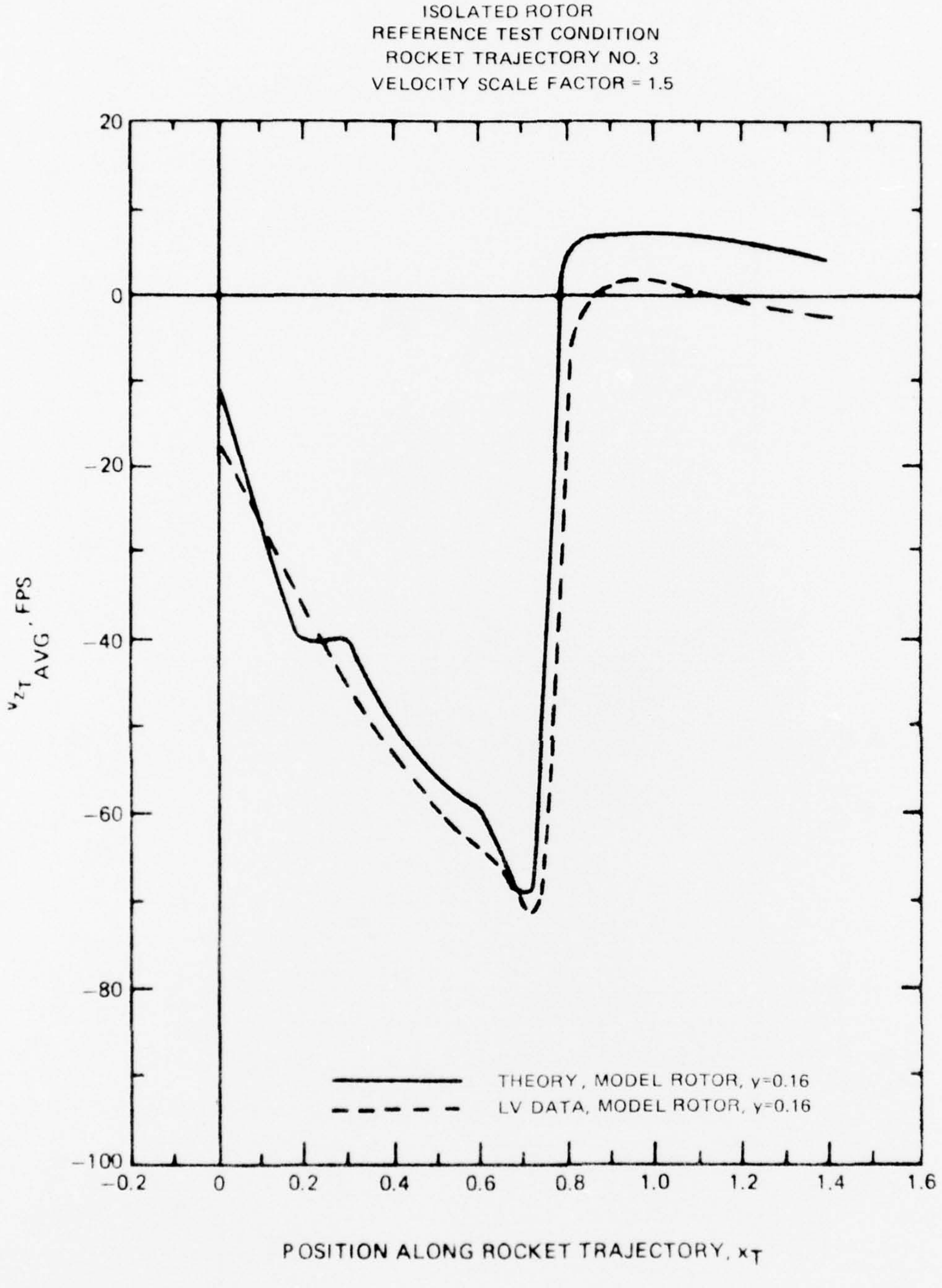

Figure 78. Comparison of Model Theoretical Results with Model LV Data for v_{z_T} (AVG) at Rocket Trajectory No. 3 for the Isolated Rotor, Reference Condition.

77-07-46-2

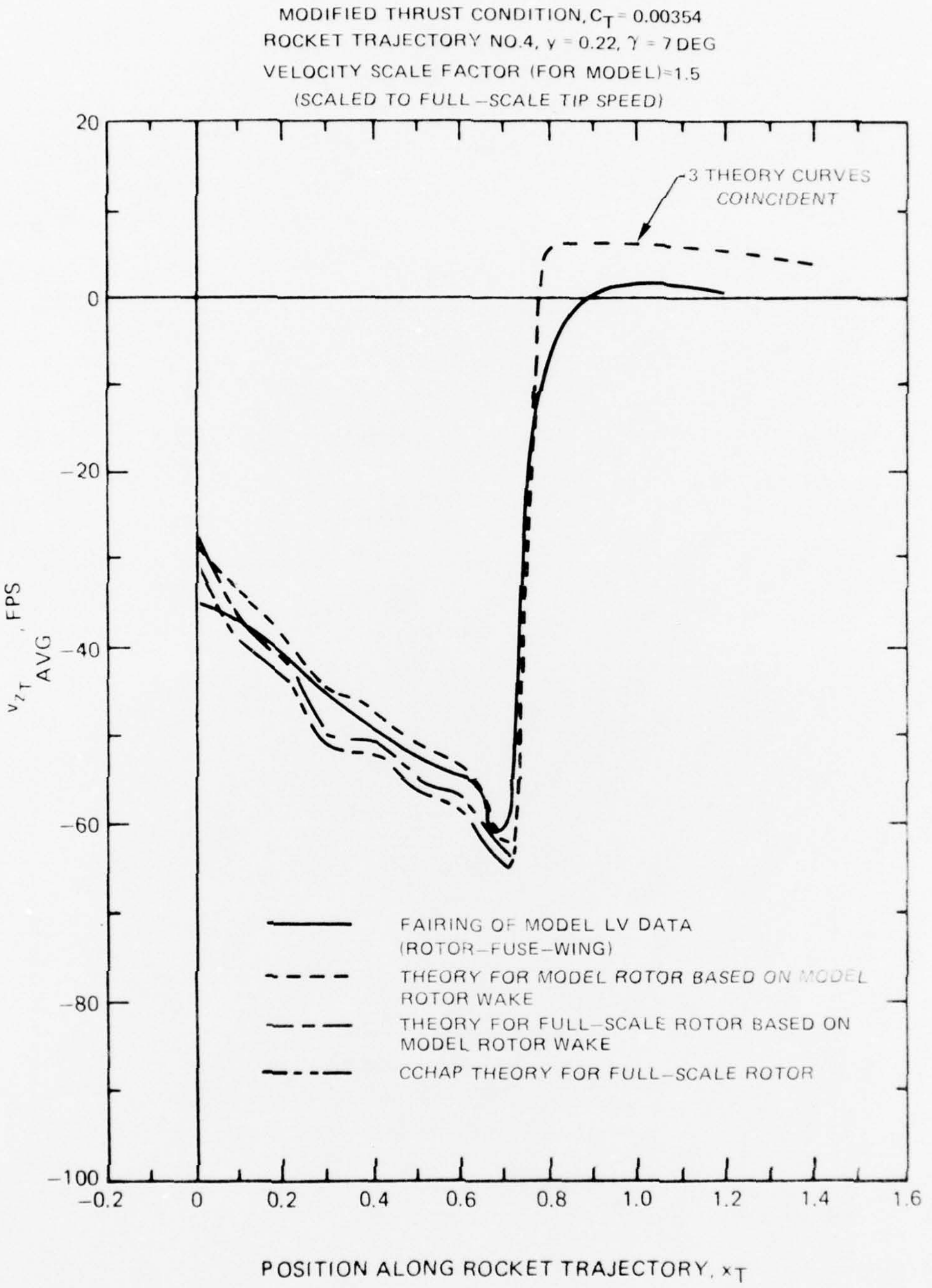

Figure 79. Comparison of Model and Full-Scale AH-1G Theoretical Results with Model LV Data for v_{z_T} (AVG) at Rocket Trajectory No. 4 for the Modified Thrust Condition.

77-07-46-4

REFERENCE TEST CONDITION
ROCKET TRAJECTORY NOS. 2&3
VELOCITY SCALE FACTOR = 1.5

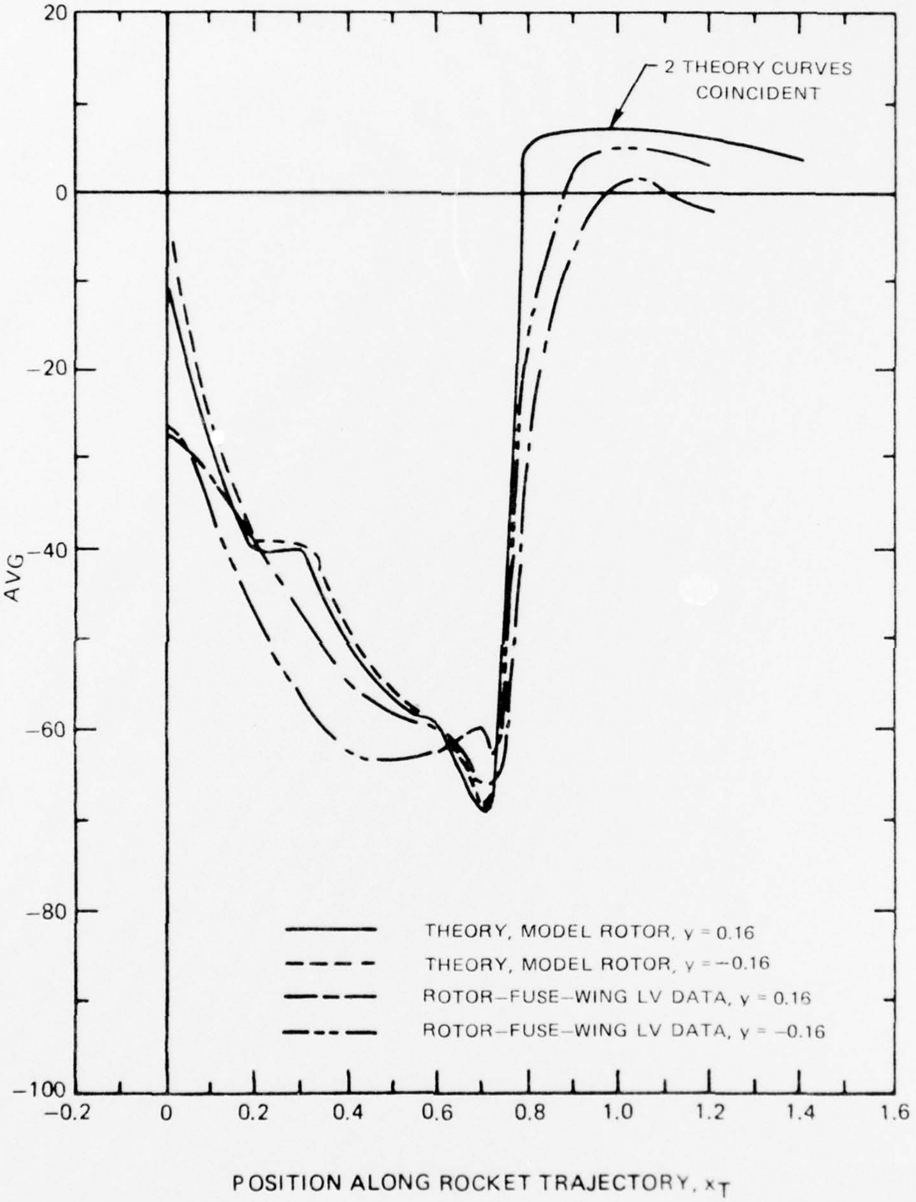

Figure 80. Comparison of Model Rotor Theoretical Results with Model Rotor-Fuselage-Wing (Reference Configuration) LV Data for v_{z_T} (AVG) at Rocket Trajectory Nos. 2 and 3 for the Reference Condition.

77–07–46–1

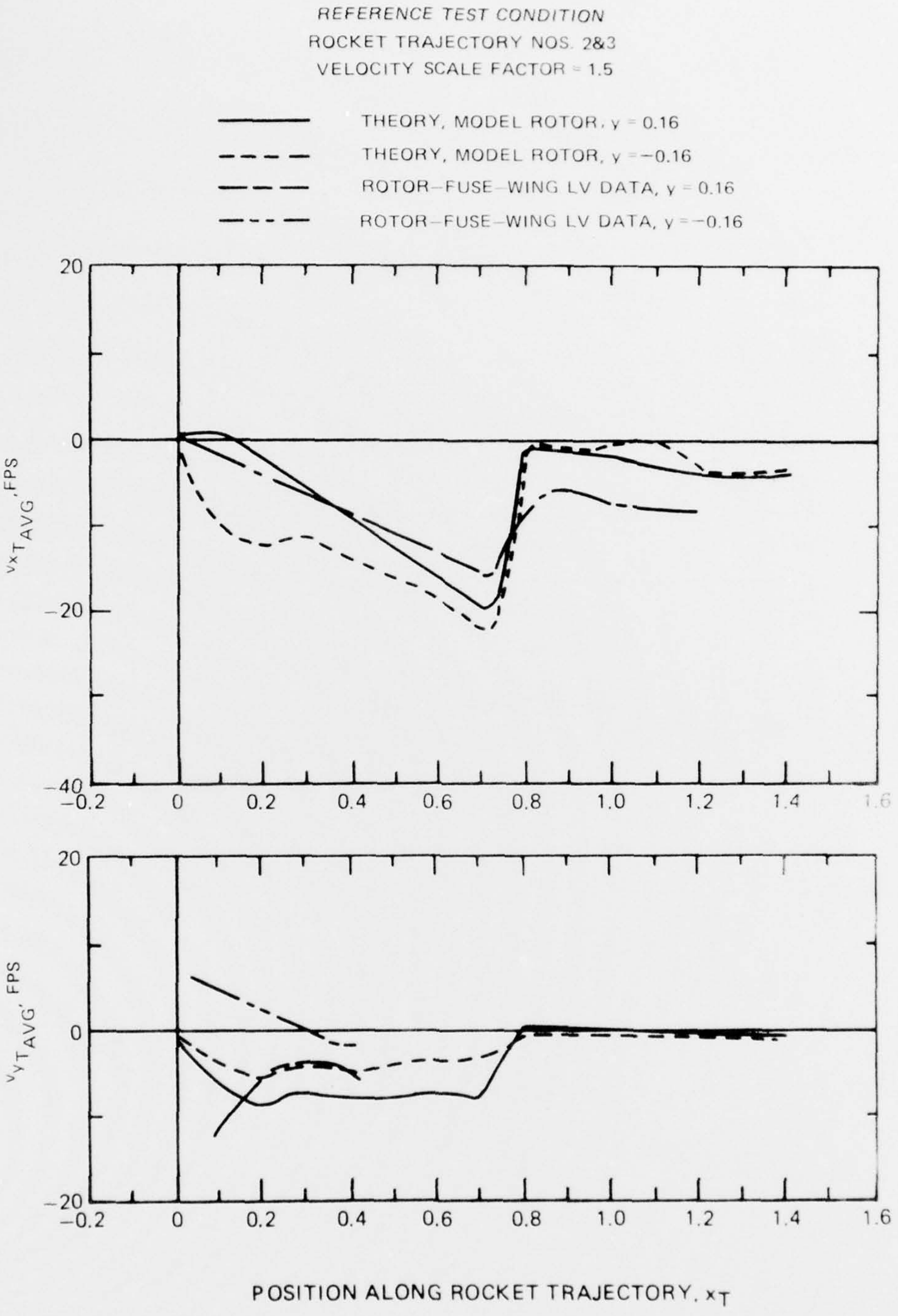

Figure 81. Comparison of Model Rotor Theoretical Results with Model Rotor-Fuselage-Wing (Reference Configuration) for v_{x_T} (AVG) and v_{y_T} (AVG) at Rocket Trajectory Nos. 2 and 3 for the Reference Condition.

77-0-46-5

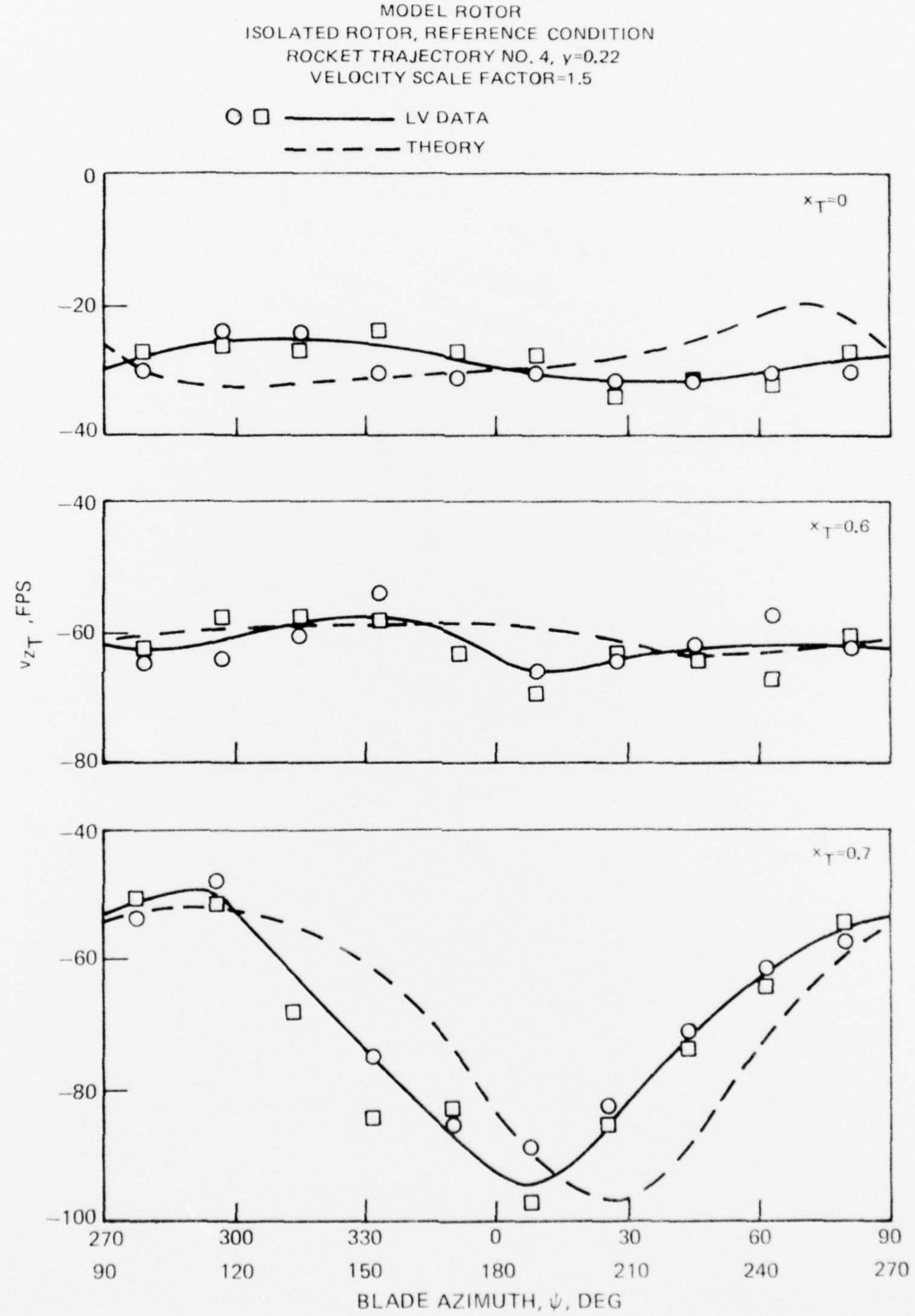

Figure 82. Comparison of Theoretical and Experimental (LV) Time Variations of v_{Z_T} at Several Points on Rocket Trajectory No. 4 for the Model Isolated Rotor, Reference Condition.

77-07-53-1

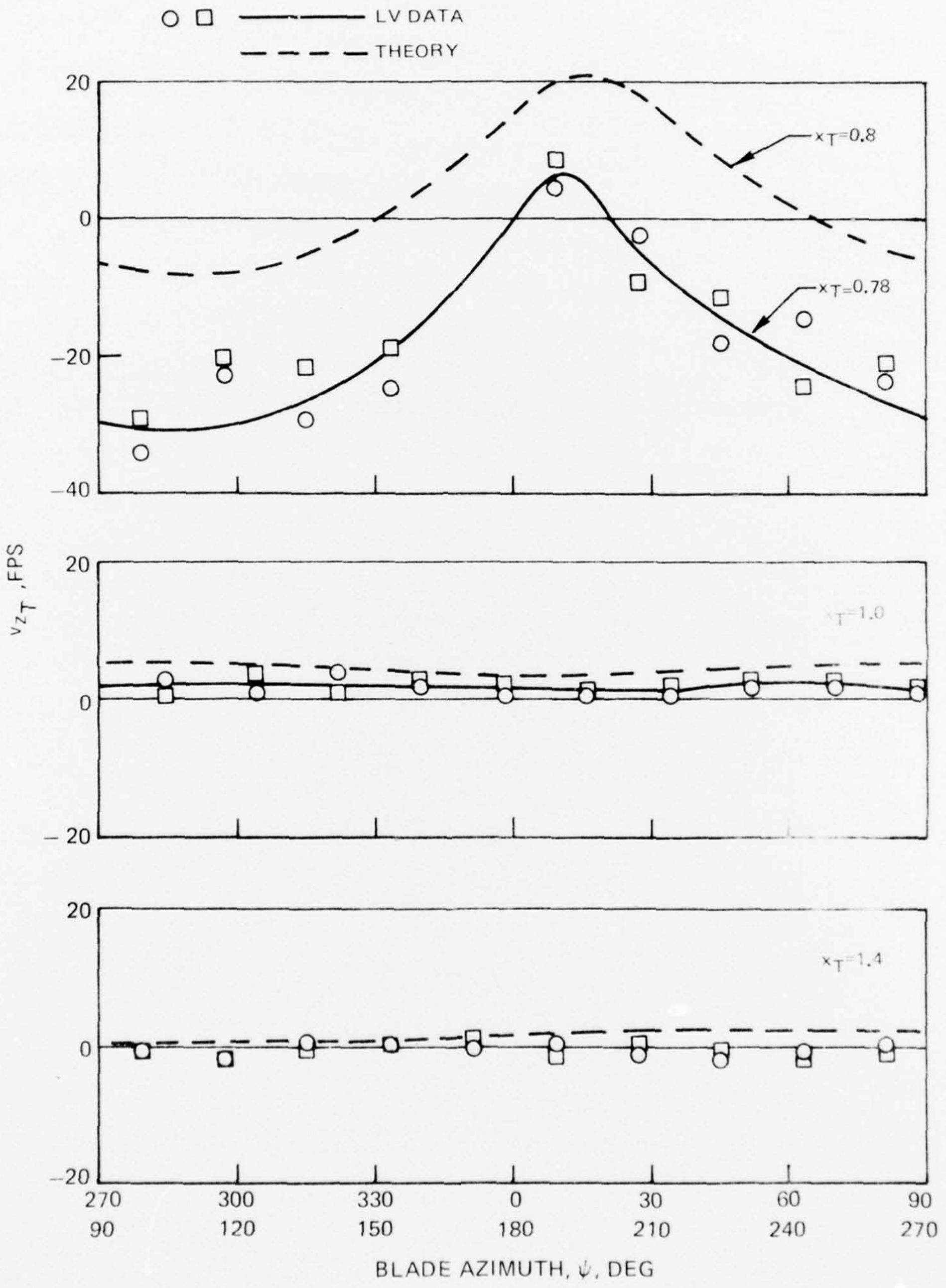

Figure 82. Concluded.

77-07-53-2

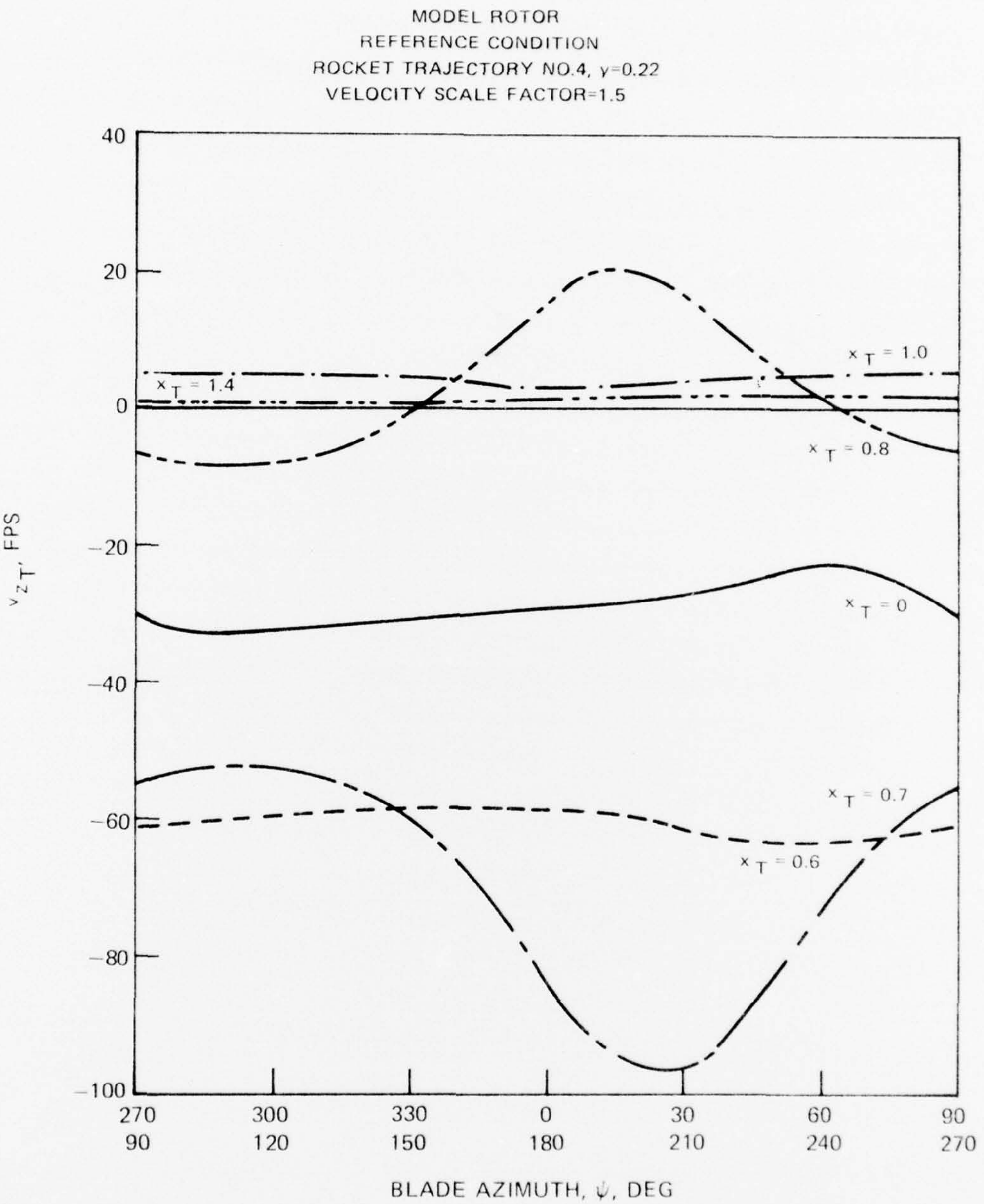

Figure 83. Theoretical Time Variations of v_{z_T} at Several Points on Rocket Trajectory No. 4 for the Model Isolated Rotor, Reference Condition.

77–07–23–4

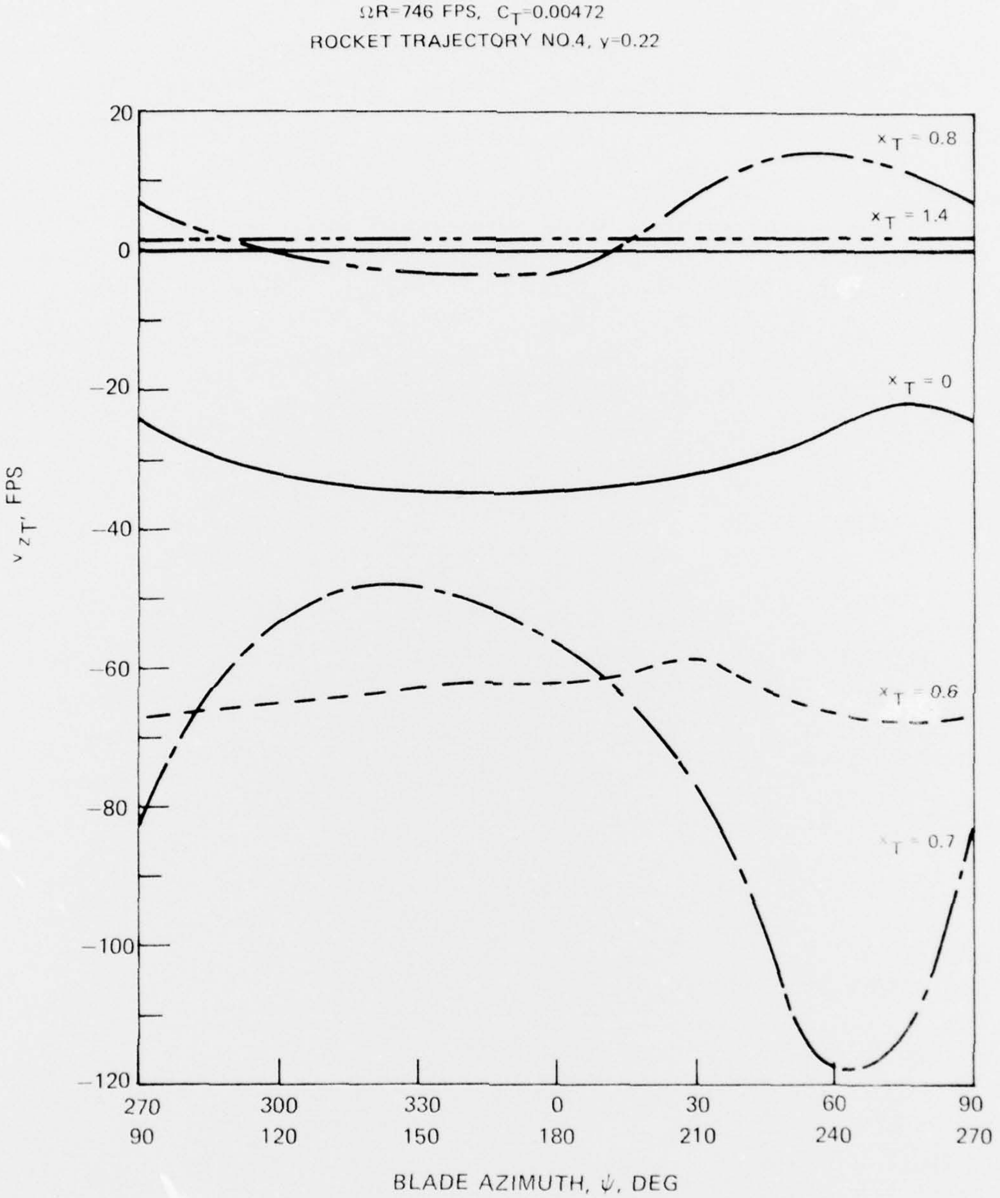

Figure 84. Theoretical Time Variations of v_{z_T} at Several Points on Rocket Trajectory No. 4 for the Full-Scale AH-1G Rotor, Reference Condition.

77-07-23-5

DISTRIBUTION LIST*

Address	No. of Copies
Commander	
U.S. Army Armament Research & Development Command	
Attn: Scientific & Technical Information Division	4
DRDAR-LC: Col. P. Kenyon	1
Dr. J. Frasier	1
Mr. A. Moss	1
DRDAR-LCA: Dr. E. Sharkoff	1
DRDAR-LCA-F: Mr. A. Loeb	1
Mr. D. Mertz	1
Mr. S. Wasserman	4
Dover, New Jersey 07801	
Commander	
MIRADCOM	
Attn: DRCPM-RK Mr. Robert Bergman	60
Redstone Arsenal, Alabama 35809	
Defense Documentation Center	12
Cameron Station	
Alexandria, Virginia 22314	
AFPRO, United Technologies Corporation	1
Pratt & Whitney Division	
400 Main Street	
East Hartford, Connecticut 06108	
United Technologies Research Center	75
East Hartford, Connecticut 06108	

---

*The above distribution list complies with the instructions of the Contract Project Officer. Additional distributions to both government agencies and industry will be conducted at MIRADCOM and UTRC.